

N8614356



DEVELOPMENT OF CONSTITUTIVE MODELS FOR CYCLIC PLASTICITY
AND CREEP BEHAVIOR OF SUPER ALLOYS AT HIGH TEMPERATURE

Final Report



Submitted by

Walter E. Haisler
Aerospace Engineering Department
Texas A&M University
College Station, Texas

to

NASA Lewis Research Center
Cleveland, Ohio

September 30, 1983

Research Foundation
Project 4246

Grant No. NAG 3-31

TABLE OF CONTENTS

ABSTRACT	1
SUMMARY OF RESEARCH	2
PUBLICATION LIST	15
APPENDIX (Selected Papers)	16



ABSTRACT

This report presents the Final Report on NASA Grant NAG 3-31 entitled "Development of Constitutive Models for Cyclic Plasticity and Creep Behavior of Super Alloys at High Temperature. An uncoupled constitutive model for predicting the transient response of thermal and rate dependent, inelastic material behavior has been developed. The uncoupled model assumes that there is a temperature below which the total strain consists essentially of elastic and rate insensitive inelastic strains only. Above this temperature, the rate dependent inelastic strain (creep) dominates. The rate insensitive inelastic strain component is modelled in an incremental form with a yield function, flow rule and hardening law. Revisions to the hardening rule permit the model to predict temperature-dependent kinematic-isotropic hardening behavior, cyclic saturation, asymmetric stress-strain response upon stress reversal, and variable Bauschinger effect. The rate dependent inelastic strain component is modelled using a rate equation in terms of back stress, drag stress and exponent n as functions of temperature and strain. A sequence of hysteresis loops and relaxation tests are utilized to define the rate dependent inelastic strain rate. Evaluation of the model has been performed by comparison with experiments involving various thermal and mechanical load histories on 5086 aluminum alloy, 304 stainless steel and Hastelloy X.



SUMMARY OF RESEARCH

Constitutive models may generally be grouped into three categories: microphenomenological, nonlinear viscoelastic, and classical plasticity. Each group can be further separated into unified and uncoupled theories, where the two differ in their approach to the treatment of rate independent and rate dependent inelastic deformation. The unified approach separates the total strain rate as

$$\dot{\epsilon} = \dot{\epsilon}^E + \dot{\epsilon}^I + \dot{\epsilon}^T \quad (1)$$

where $\dot{\epsilon}$ represents the total strain rate and superscripts E, I, and T represent the elastic, inelastic and thermal components, respectively. Alternatively, the uncoupled theories partition the inelastic strain into plastic and creep components. This can be expressed as

$$\dot{\epsilon} = \dot{\epsilon}^E + \dot{\epsilon}^P + \dot{\epsilon}^C + \dot{\epsilon}^T \quad (2)$$

where superscripts P and C represent the rate independent "plasticity" and rate dependent "creep" strain terms, respectively. Such uncoupling of the strain components provides for simpler theories to be developed (along with simple tests to define material constants) but does preclude any creep-plasticity interaction except through ad hoc rules. More complete discussions and literature reviews are provided in the papers and reports contained in the Appendix.

The constitutive model developed in this research is based on uncoupled strain components as written in equation (2). The model assumes that there is a temperature below which the total strain consists essentially of elastic and rate insensitive inelastic (plastic) strains only. Above this temperature, the rate dependent inelastic strain (creep) dominates. The rate insensitive plastic strain is modelled by an incremental model with a yield function, flow rule and hardening law. Provisions are made for cyclic saturation and variable Bauschinger effect. The rate dependent inelastic component is modelled using a rate equation in terms of back stress, drag stress, and exponent n as functions of temperature and strain. The rate dependent and independent inelastic components are selected so that their sum is always equal to the total inelastic strain at all temperatures.

Rate Insensitive Strain Component

The rate insensitive inelastic (plastic) strain component is modelled using a modified and improved incremental theory applicable to cyclic thermomechanical material response. The model makes use of four major components. For simplicity, the following equations will be presented in uniaxial form; their extension to multiaxial form is presented by Allen³.

First, we assume a relation between stress and elastic strain

$$\sigma = E \epsilon^E = E (\epsilon - \epsilon^P - \epsilon^C - \epsilon^T) \quad (3)$$

or in incremental form

$$\Delta\sigma = E^{t+\Delta t} (\Delta\varepsilon - \Delta\varepsilon^P - \Delta\varepsilon^C - \Delta\varepsilon^T) + \Delta E (\varepsilon^t - \varepsilon^{Pt} - \varepsilon^{Ct} - \varepsilon^{Tt}) \quad (4)$$

where σ is the uniaxial stress, E is elastic modulus, and ε is the uniaxial strain. Superscripts P, C, and T denote plastic, creep, and thermal components respectively while t denotes values at the start of the load step, and t+ Δt denotes values at the end of a load step.

The von Mises yield criterion is used herein in combination with a variable ratio isotropic-kinematic hardening law. The modified hardening rule used in this research permits the model to predict temperature dependent kinematic-isotropic hardening behavior, cyclic saturation, asymmetric stress-strain response upon stress reversal, and variable Bauschinger effect. The essential features of the hardening rule are described in the thesis by Cronenworth included in the Appendix.

While metals like aluminum exhibit a similar strain hardening behavior for reyield after the initial yield, some metals (stainless steels, for example) exhibit different forms of hardening behavior for each half cycle of loading even after several loading cycles, i.e., the stress-strain response is asymmetric. To account for the asymmetry, both halves of a stress-strain cycle are used as input to the model and the hardening ratio β is allowed to be a function of the direction of loading. Typical experimental data and the linearized representation are shown in Fig. 1. For temperature T_1 , curve ABC corresponds to the first half cycle of response while curve DE (or D'E') corresponds to the second half or reverse loading response.

For a combined hardening law, the hardening ratio, β , is the ratio of isotropic to kinematic hardening such that $\beta=0$ constitutes a kinematic hardening law where the yield surface retains its initial size, shape and orientation thus simply translating in principal stress space. Isotropic hardening, $\beta=1$, indicates that during plastic flow the yield surface expands uniformly about the origin and never translates. Using a values for the hardening ratio such as $0 \leq \beta \leq 1$ constitutes a combined hardening rule where the yield surface is allowed to both expand and translate. The hardening ratio may be variable if it is defined as a function of plastic strain and temperature using

$$\beta(\bar{\varepsilon}^P, T) = \frac{\sigma_r - (2\sigma_y - \sigma_0)}{(2\sigma_0 - 2\sigma_y)} \quad (5)$$

where the stress values are defined in Fig. 2 for each temperature. If β is a function of plastic strain as well as temperature, several cycles of stress-strain data are required to characterize this parameter. Typical curves for the hardening ratio are also shown in Fig. 2. As β approaches a limiting or asymptotic value with respect to plastic strain, we note that the cyclic hysteresis loops will saturate.

The growth law for the yield surface size K may be obtained from using

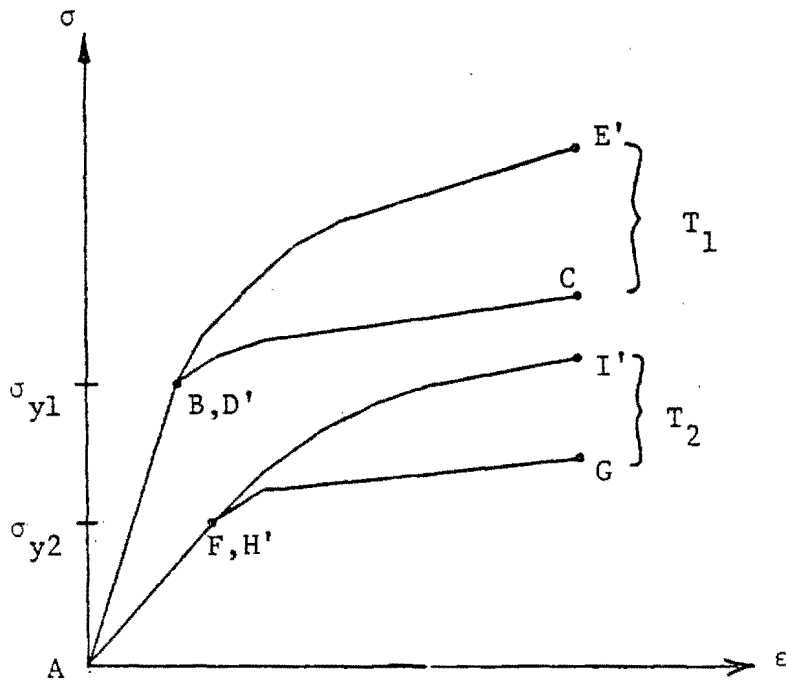
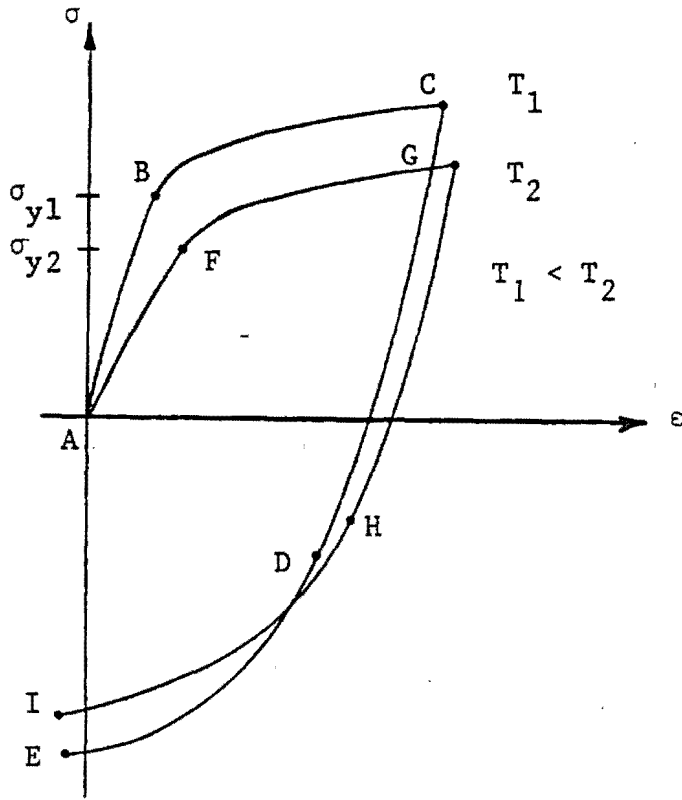


Fig. 1 Uniaxial isothermal single cycle reverse loading curves and their linear representations

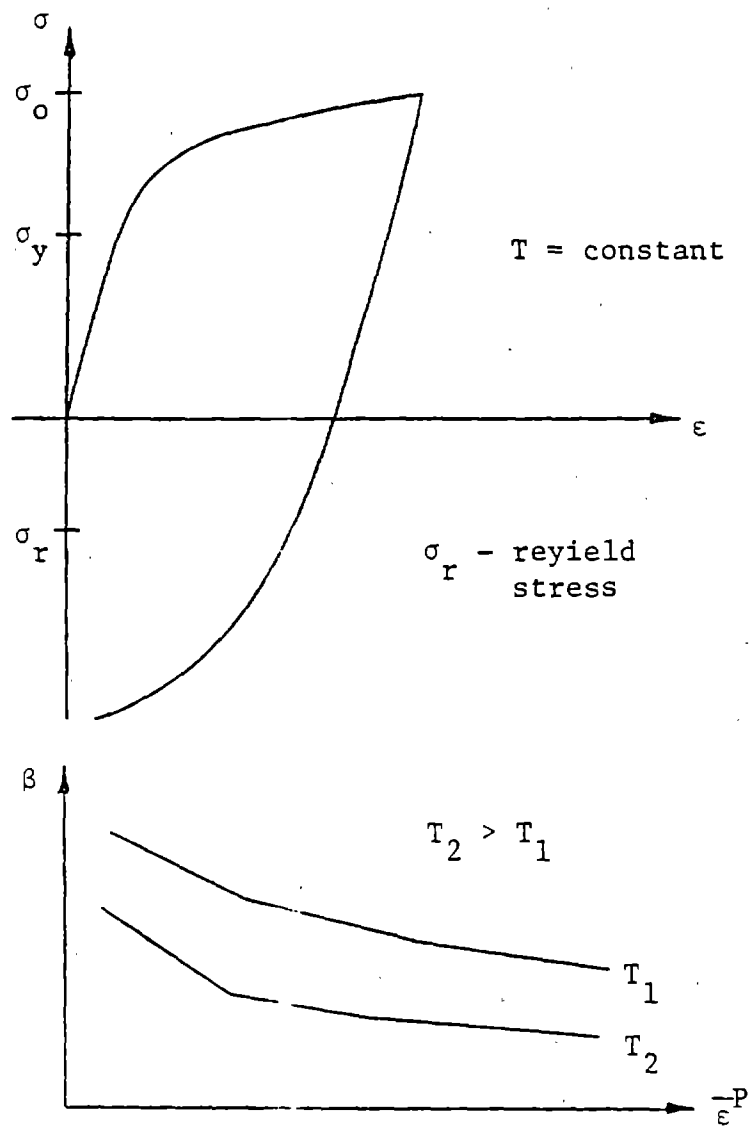


Fig. 2 Hardening ratio

$$K = \sigma_y + \beta (\sigma - \sigma_y) \quad (6)$$

where σ_y represents the yield stress and σ is the applied stress. In equation (6), $K = K(\bar{\epsilon}^P, T)$. For the case where loading and reverse loading response is different, we employ the following procedure at the reverse loading point. Consider that base diagrams of K vs $\bar{\epsilon}^P$ have been obtained as shown in Fig. 3. Recall that the "a" curves are the ones that result from reverse yielding while the "b" curves are from the virgin stress-strain curves. If a reverse yielding occurs at $\bar{\epsilon}^P = \bar{\epsilon}_0^P$, we assume the "b" curves are linked to the global diagram as shown at the bottom of Fig. 3, always linking-on the complete curve starting from zero plastic strain. When another reverse yielding takes place, either the "a" or "b" curves are linked to the global diagram at that particular value of plastic strain that has been accumulated. A similar procedure is carried out for the global uniaxial stress vs. plastic strain diagram.

The experimental requirements required to characterize the hardening law depend upon the metal. For the most general case, isothermal cyclic stress-strain tests are run till the hysteresis loops stabilize. Cyclic tests are required for several temperatures so that the temperature dependence can be adequately characterized. Loading rates must be selected so that time-dependent effects are negligible.

Rate Dependent Inelastic Strain Component

In the present, the rate sensitive strain component is obtained from hysteresis loops and stress relaxation tests at various temperatures. Fig. 4 shows a typical set of these tests and details how the rate dependent deformation is extracted from the saturated cyclic data. A reference temperature hysteresis loop is defined at a temperature below which the total strain consists essentially of elastic and rate insensitive plastic strains only. Above this temperature, the rate dependent inelastic strain (creep) dominates. Experimental tests conducted by Yuen (see Appendix) seem to indicate that such an uncoupling is feasible for Hastelloy X. The basic concept of decoupling strains according to Fig. 4 is to take that part of the inelastic strain which is strongly time dependent and call it $\dot{\epsilon}^C$; the remaining part is assumed to be all rate insensitive and incorporated into $\dot{\epsilon}^P$.

Micromechanical consideration suggest a model for the rate dependent inelastic strain of the form

$$\dot{\epsilon}^C = \text{sgn}(\sigma - \Omega) \left| \frac{\sigma - \Omega}{K} \right|^n \quad (7)$$

where $\dot{\epsilon}^C$ represents the rate dependent inelastic strain rate, Ω is the back stress, K is the drag stress, and n is a temperature-dependent "constant." The back stress, drag stress, and exponent n are generally function of temperature and strain (or stress). However, for some

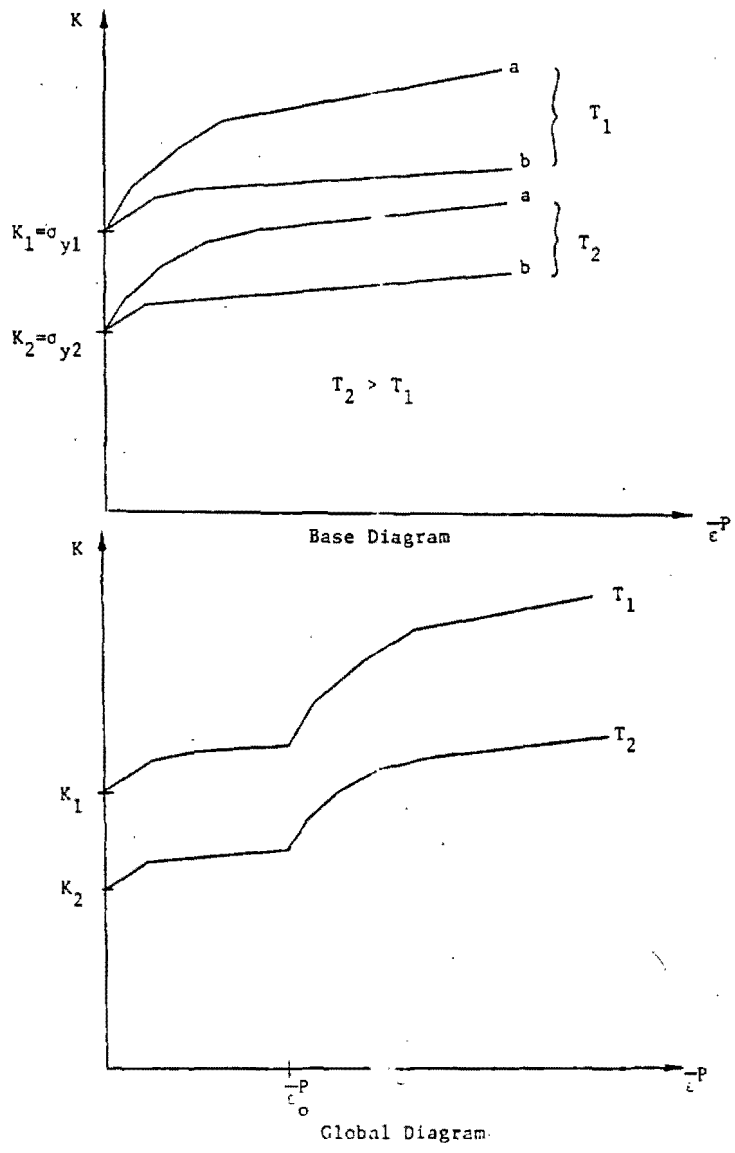


Fig. 3 Construction and evolution of K vs. ε^P diagrams

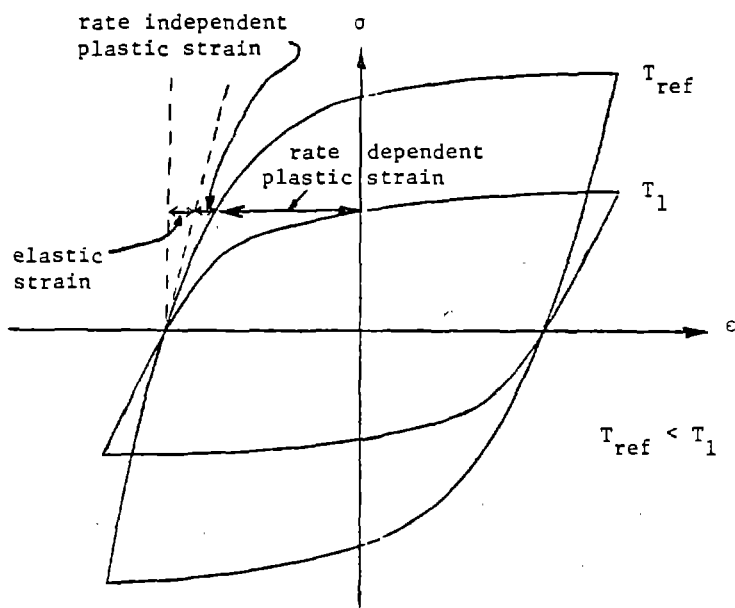
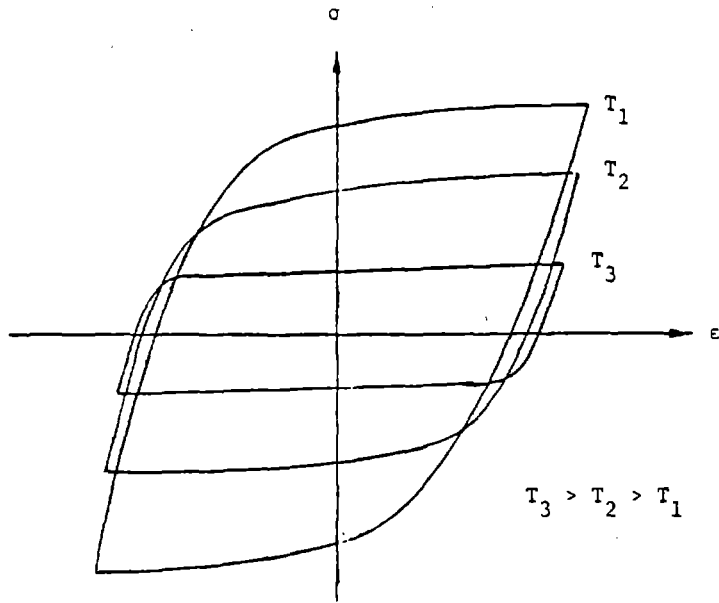


Fig. 4 Experimental characterization of the rate dependence of the model

materials a good assumption is that the drag stress and n are constant at sufficiently high temperatures. The experimental determination of Ω , K , and n is based on stress relaxation tests at low temperature and stress drop/strain transient test at high temperature. Details of these experiments are presented in the thesis by Yuen (see Appendix).

Evaluation of the Model

The capabilities of the constitutive model developed during this research have been evaluated through several hypothetical numerical experiments as well as by comparison with experimental results. Only a few of these results are presented here. More complete comparisons and details of the experiments, as well as experimental laboratory facilities developed during this research, are presented in the Appendix.

In the first example, we illustrate the effect of a change in strain hardening upon stress reversal, which is typical of many alloys. Figure 5 illustrates the stress-strain curves for a theoretical single cycle reverse load test. The input can be taken from either first or saturated cycle data. Curve B represents the initial strain hardening behavior while curve A represents the high rate of strain hardening seen upon stress reversal. If a single cycle reverse load test is performed with this theoretical data, the results will be similar to those shown as output in Fig. 5. The revised model using both halves of the cyclic stress-strain response (curves A and B) is a much more realistic representation of actually observed experimental behavior for many metals than the combined hardening rule previously used by the current researchers. Even the revised model representation using only curve B is an improvement over existing hardening rules which "square-off" the behavior upon reyield.

In the next example, we consider a hypothetical fully-reversed cyclic uniaxial strain history of $\pm 0.25\%$ strain with two different assumptions for the hardening law. In Fig. 6a, a combined hardening law with $\beta = 0.5$ was used while in Fig. 6b results are presented for a variable hardening ration given by $\beta = 0.5 - 41.7 \bar{\epsilon}^p$. It is seen that different rates and amounts of cyclic saturation are easily predicted by the model.

In the third example, we consider a uniaxial specimen subjected to a thermomechanical loading history as shown in Fig. 7. The stress-strain curves do not include any asymmetric hardening ($\beta = 0.5$), but are considered to be dependent on temperature as shown. Results from the constitutive model for modulus, strain hardening, and yield surface size as functions of plastic strain and temperature are shown in Fig. 8 (t_1 in Fig. 8 corresponds to t_1 in Fig. 7). It is interesting to note the change in yield surface size as a function of plastic strain. As discussed previously, the curves are modified each time there is a stress reversal which causes yield or reyield. This physically represents the rounded shape of the stress-strain curve after reverse yielding seen in experiment in terms of the mathematical modelling, this corresponds to the linking of the original yield surface curve onto

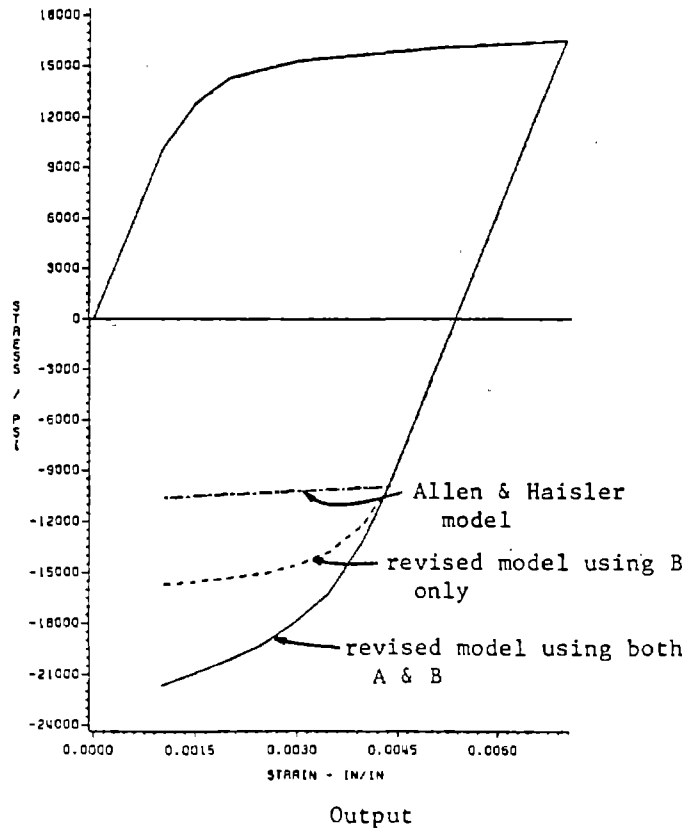
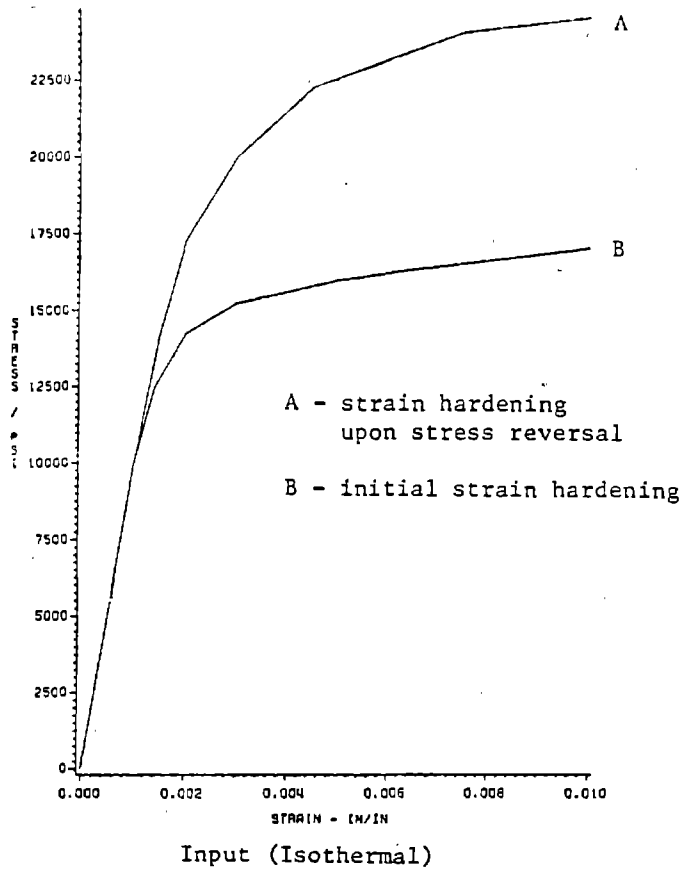
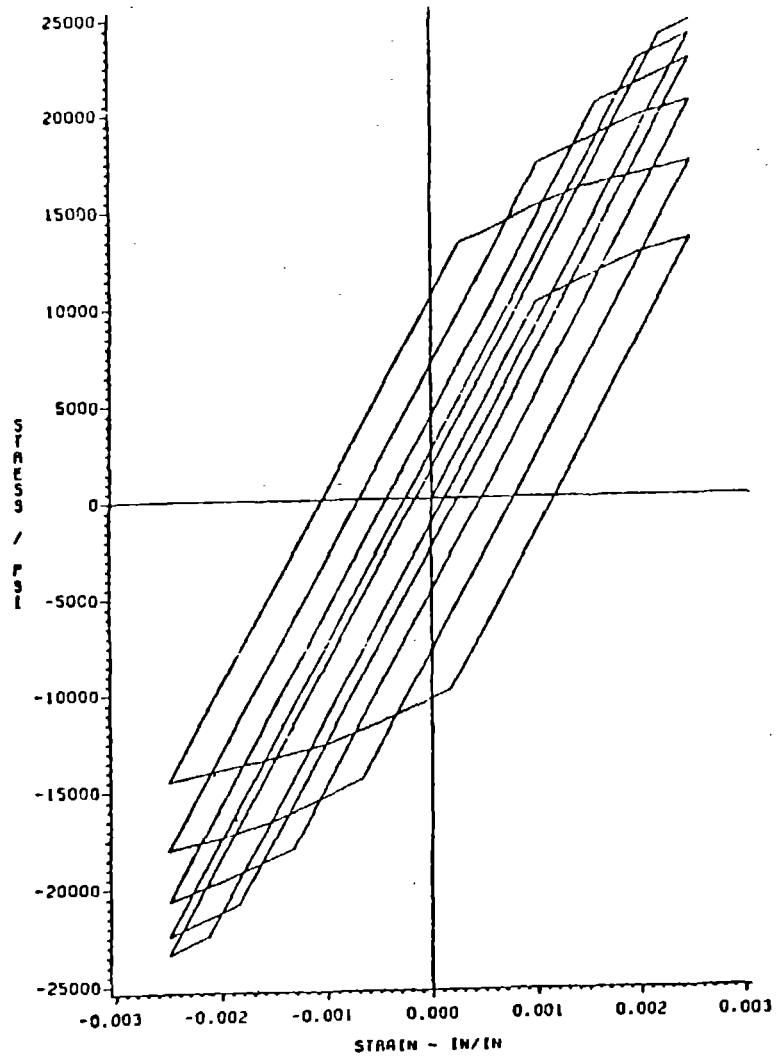
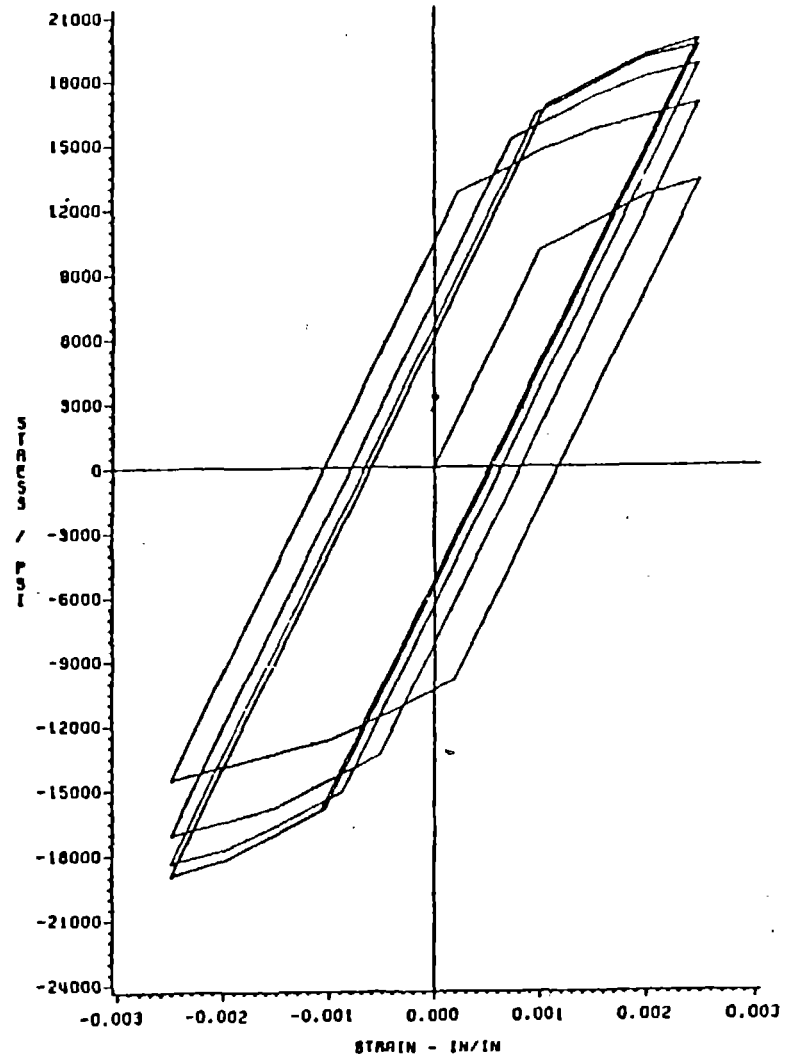


Fig. 5 Change of strain hardening with stress reversal



Combined hardening with β constant



Combined hardening with β a function of plastic strain

Fig. 6 Modeling of cyclic saturation using combined hardening law

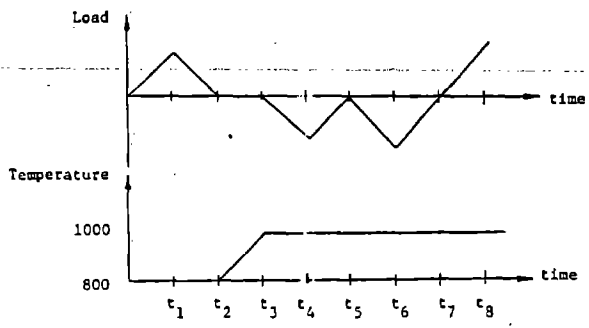
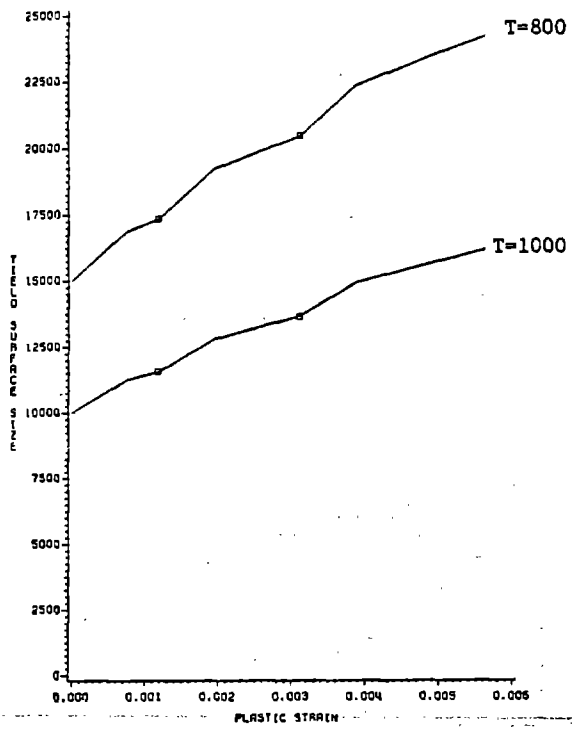
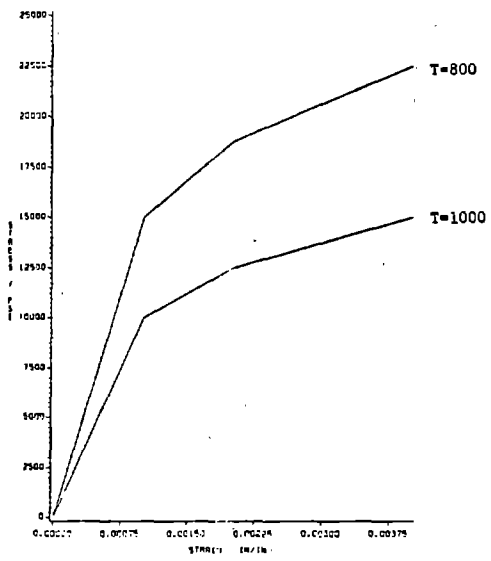


Fig. 7 Input for Example 3

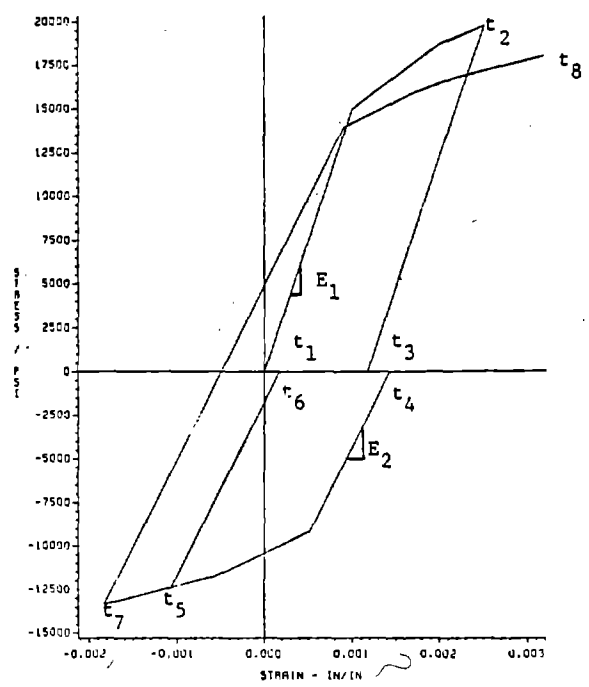


Fig. 8a Cyclic Thermomechanical loading

Fig. 8b Cyclic thermomechanical loading

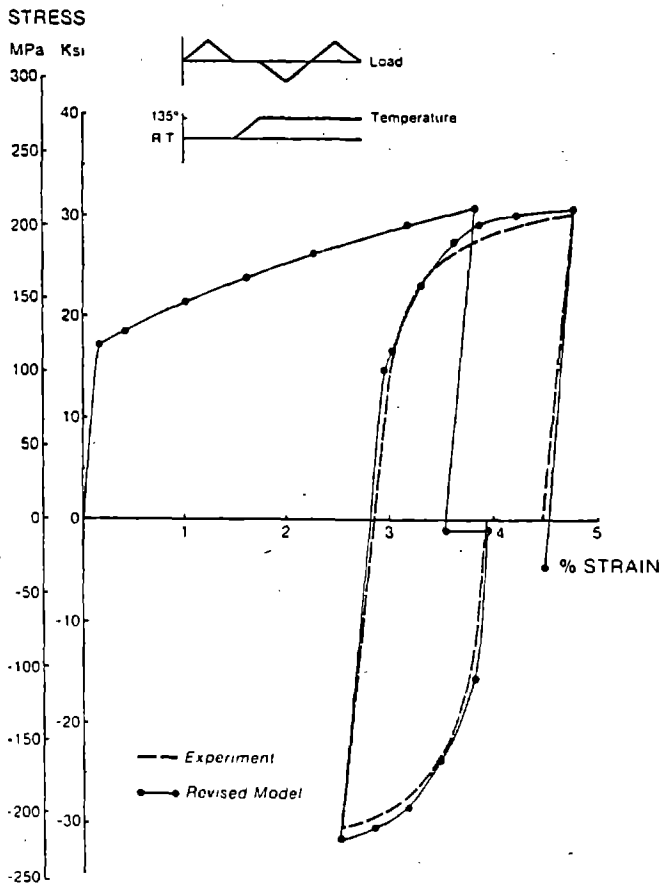


Fig. 9 Comparison of revised model to experiment for aluminum cyclic load test

the current global diagram. The squares in Fig. 8 point out where this process takes place each time.

The numerical experiments discussed above serve to indicate the potential response possible with the constitutive model. The model has also been compared to experiments involving several different materials and thermomechanical loading histories. Three of the comparisons are presented here. The first involves a uniaxial test of 5086 aluminum alloy between room temperature and 275°F. Stress-strain curves were obtained for one complete cycle (with asymmetric strain hardening accounted for) and, from experiment, the hardening ratio was found to be approximately 0.45 for the first loading cycle and approximately 0.0 (kinematic) for all reloading cycles. Figure 9 presents the cyclic loading and temperature history. We observe that the theoretical results are in very good agreement with experiment and the high rate of strain hardening during load reversal is modelled accurately.

In the next test, we attempt to model the evolution of hysteresis loops for a mechanically cycled 304 stainless steel specimen at 1,000°F. We note from Fig. 10 that the loading-reloading response is quite asymmetric and the difference alternates throughout many cycles. In this case, tension precedes compression; however, the same effect is observed if compression is applied first. From experiment, the hardening ratios were determined to be approximately 0.2 for the first quarter cycle and 0.35 for the second quarter cycle. Results for the first and fourth cycles indicate reasonably good correlation with experiment.

In the last case, we consider the prediction of cyclic saturation of Hastelloy X at room temperature when cycled between +/- 1.1% strain under strain control. Figure 11 presents the experimental results while Fig. 12 shows a comparison between theory and experiment. In Fig. 12, experimental data is shown only for the first one-half cycle and the last (saturated) cycle. The model results depict the gradual saturation response as well as the limiting response. A hardening ratio function given by $B = 0.075 + 2.375 \bar{\epsilon}^P$ was used in tension while that used for compression was $B = 0.10 - 0.5 \bar{\epsilon}^P$. Notice that as model predictions approach saturation, some fluctuation is seen on the compression side. This is thought to be due to increasing numerical error at this point as no equilibrium iterations are performed in the finite element analysis. Most of the difference in experiment and theory is due to difficulty in modeling of the second quarter cycle, otherwise the model predictions are reasonably good.

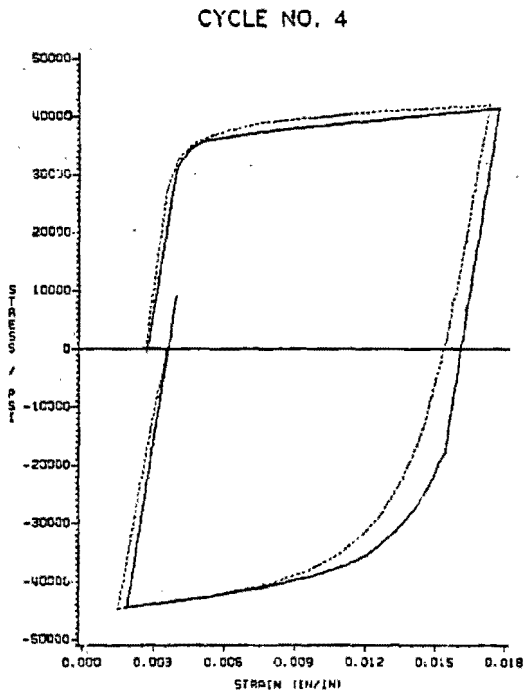
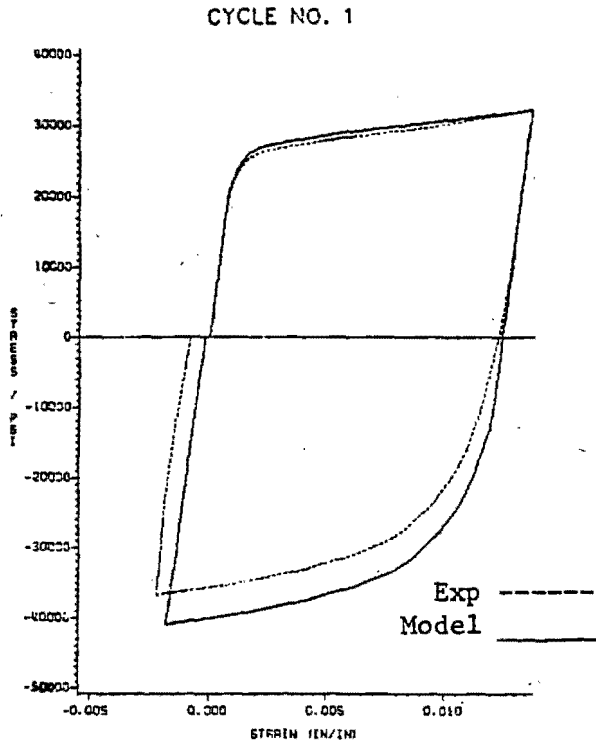


Fig. 10 Comparison of model and experiment for 304 stainless steel at 1000°F using first cycle data as input. A hardening ratio of 0.2 in tension and 0.35 in compression was used

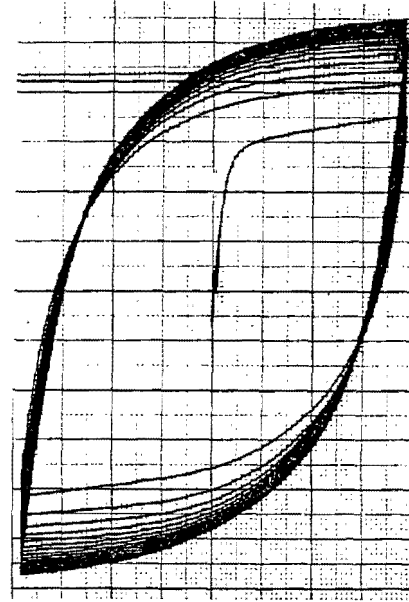


Fig. 11 Experimental hysteresis loops for Hastelloy-X at room temperature

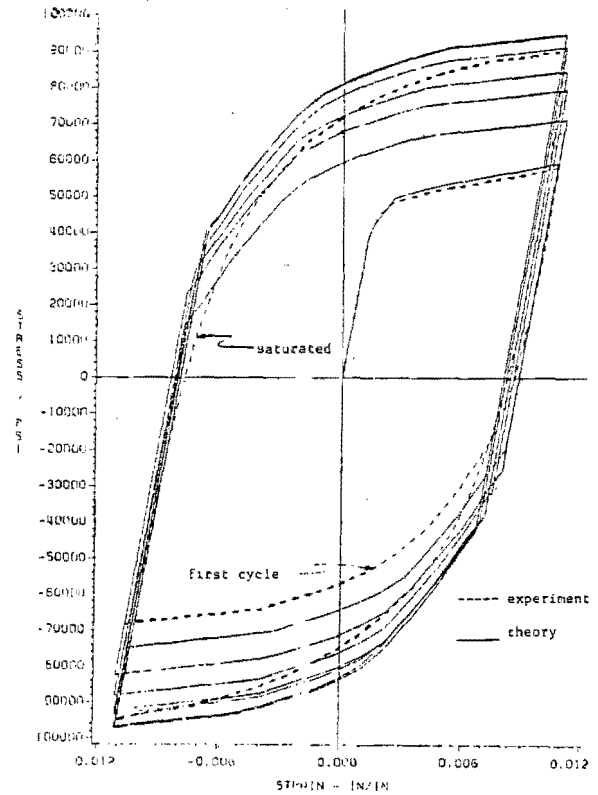


Fig. 12 Cyclic saturation of Hastelloy-X at room temperature

PUBLICATIONS LIST

Allen, D. H. and Haisler, W.E., "A Theory for Analysis of Thermoplastic Materials," Computers and Structures, Vol. 13, 1981, pp. 124-135.

Cronenworth, J., "Development and Evaluation of an Uncoupled, Incremental Constitutive Model for Elastic-Plastic Behavior at Elevated Temperature," Thesis, Texas A&M University, College Station, Texas, May 1982.

Bradley, W.L., "A New Uncoupled Viscoplastic Constitutive Model," presented at the Symposium on Nonlinear Constitutive Relations for High Temperature Applications, The University of Akron, Akron, Ohio, May 19-20, 1982.

Haisler, W., "Application of an Uncoupled Elastic-Plastic Creep Constitutive Model to Metals at High Temperatures," presented at the Symposium on Nonlinear Constitutive Relations for High Temperature Applications, The University of Akron, Akron, Ohio, May 19-20, 1982.

Yuen, S., "Development of an Uncoupled Viscoplastic Constitutive Model for Cyclic Plasticity of Hastelloy X at High Temperature," Thesis, Texas A&M University, College Station, Texas, May 1983.

Haisler, W.E. and Cronenworth, J., "An Uncoupled Viscoplastic Constitutive Model for Metals at Elevated Temperature," presented at the 24th AIAA Structures, Structural Dynamics and Materials Conference, Lake Tahoe, Nevada, May 2-4, 1983.

APPENDIX

(Selected Papers and Reports)

Haisler, W.E. and Cronenworth, J., "An Uncoupled Viscoplastic Constitutive Model for Metals at Elevated Temperature," presented at the 24th AIAA Structures, Structural Dynamics and Materials Conference, Lake Tahoe, Nevada, May 2-4, 1983.

CHAPTER I

INTRODUCTION

Modern computational methods for the stress analysis of structures are well established. For behavior that is linear and even geometrically nonlinear, the finite element method has proven to be a very capable tool for the structural engineer. However, nonlinear material analysis is much more difficult and not yet as fully developed as proven by the large amount of research done in this area in recent years. Of particular interest to this research, the solution of thermal and rate dependent elastic-plastic material behavior is quite difficult. Applications of this technology are needed in components such as nuclear reactor pressure vessels and gas turbine blades.

Historically, the study of plasticity of metals began in 1864 with the publishing by Tresca [1] of a preliminary account of experiments on punching and extrusion. This led him to state that a metal yielded plastically when the maximum shear stress attained a critical value. Application of Tresca's yield criterion was investigated by Saint-Venant [2] to determine stresses in cylinders and tubes. He also recognized that there was not a one-to-one relation between stress and total plastic strain. Levy in 1871 proposed multiaxial relations between stress and plastic strain [2].

Advancement to a more satisfactory yield criterion was constructed on the basis of purely mathematical considerations by von Mises [3]

This thesis follows the style and format of the Journal of Applied Mechanics.

in 1913. Further work was done in the 1920's by Prandtl [4], Nadai, Lode, and von Karman [2]. It was in the early 1930's that two important generalizations of the available theory were made. The first was made by Reuss in 1930 [5] who allowed for the elastic component of strain. The second was made by Schmidt (1932) and Odquist (1933) [2] who showed how to incorporate work hardening into the framework of the Levy-Mises equations. Thus by 1932 an elastic-plastic theory had been constructed to model these properties of an isotropic metal at room temperature [2].

Work in this area in the 1940's and beyond was done by several prominent researchers like Hill [2], Drucker [6], Prager [7], and Ziegler [8]. Recently, the basic trend has been to extend the rate independent theories to include rate effects by adding on a creep term. This leads to an uncoupled or partitioned theory, and many are now in use today in finite element structural analysis codes. Most recently with the recognition that the rate independent and rate dependent inelastic deformations are not autonomous phenomenon, a number of "unified" constitutive models have been developed and are still undergoing active development [9]. Present day efforts include the extension of classical plasticity to predict rate dependent behavior and the modification of linear viscoelasticity to model nonlinear material response [10]. Many theories are available but none have shown clear superiority over the others in modelling material behavior over wide ranges of temperature and load.

The purpose of this research is to extend the classical incremental theory of plasticity to develop and evaluate the uniaxial

constitutive relations necessary to model the nonlinear behavior of crystalline materials experiencing thermoelastic-plastic-creep. Among the requirements for a sound constitutive theory for the media mentioned above are that it incorporate the ability to model transient temperature response; cyclic behavior including cyclic saturation, the change in strain hardening upon stress reversal, and the Bauschinger effect; and rate dependence.

In fulfillment of these objectives, this thesis will proceed in the following manner. First, a brief literature review of the available theories is presented along with a discussion of the details of the constitutive model used in this research. Next, the development of the model is accomplished by derivation of the uniaxial theory including experimental data requirements and computational considerations. Several theoretical examples are presented along with comparison to experiments on several different metals at elevated temperature.



CHAPTER II

BACKGROUND

Present Status of Constitutive Modelling

To characterize the structural response of any general three-dimensional body, one must satisfy mechanics (conservation of mass and momentum, and kinematics), thermodynamics, and constitution. Since mechanics and thermodynamics are well established for most continua, it becomes the physical characteristics or constitution of a body that determines whether one can successfully analyze its structural response. Furthermore, because of the widely varying material properties and environments that structural media are subjected to, constitutive modelling is usually restricted to specific types of media. An all encompassing model that works equally well for all materials is simply not feasible. One such category of material response, and the one that this research will deal specifically with, is the elastic-plastic-rate-dependent crystalline material at elevated temperature.

The major types of constitutive laws available to model the material behavior discussed above can be grouped into three categories, microphenomenological, nonlinear viscoelastic, and classical plasticity. Also, there is an existing subdivision within the categories labeled unified and uncoupled theories, where the two differ in their approach to the treatment of rate independent and rate dependent inelastic deformation. The unified approach separates the total strain as

$$\epsilon = \epsilon^E + \epsilon^I + \epsilon^T, \quad (1)$$

where ϵ represents the total strain and superscripts E, I, and T represent the elastic, inelastic, and thermal components respectively. Alternatively, the uncoupled theories partition the inelastic strain into plastic and creep components. This can be expressed as

$$\epsilon = \epsilon^E + \epsilon^P + \epsilon^C + \epsilon^T, \quad (2)$$

where superscripts P and C represent the rate independent "plasticity" and rate dependent "creep" strain terms respectively. Researchers like Walker [9] and Krieg [11] question the partitioning as it has no underlying physical basis and does not account for creep and plasticity interaction.

The uncoupling of inelastic behavior into rate independent and rate dependent components is unsatisfactory to the material scientist because it is not microphysically justified [11]. Although many recent unified theories have been proposed, they still are not yet proven to be more successful overall than the uncoupled theories.

For example, Walker's theory [9] (considered one of the better unified models) reproduces cyclic stress-strain behavior at elevated temperatures very well. Unfortunately, the theoretical hysteresis loops at smaller strain rates or lower temperatures are too square in comparison with the actual experimental loops. Thus, Walker's theory does not characterize adequately the classical plasticity that is occurring in this load-temperature range. Walker also proposes an extension to include temperature dependence, but no attempt has been made to model transient temperature response [10]. His theory is restricted in its

use to an elevated temperature environment. The author does not want to leave the impression that Walker's theory is an inferior one as it is not. This discussion is simply to point out that the uncoupled theories are not necessarily inferior to the unified ones.

As discussed below, present theories attempt to model these physical mechanisms in a variety of ways.

Microphenomenological theories. The mechanisms for microphenomenological theories are discussed in detail by Allen [12]. These theories represent an element of material called a polycrystal as being composed of a large number of randomly oriented monocrystals. Statistical averages of the properties of each monocrystal and their interactions determine the behavior of the polycrystal [13]. These crystalline materials form lattice structures that contain many imperfections called dislocations which vary in density and location depending upon the processing used in manufacturing the material. Plastic deformation occurs by slip on certain crystallographic planes and is explained in terms of dislocation theory of plastic deformation. For example, dislocation interaction explains how strain hardening can occur in any crystal [14].

One example of a microphysically based constitutive law is an elastic-viscoplastic theory based on two internal state variables by Bodner, et al. [15]. The authors state the constitutive equations ability to represent the principal features of cyclic loading behavior including softening upon stress reversal, cyclic hardening or softening, cyclic saturation, cyclic relaxation, and cyclic creep. One limitation of the formulation though is that the computed stress-strain

curves are independent of the strain amplitude and therefore too "flat" or "square".

Another example is in the paper by Miller [16] on modelling of cyclic plasticity with unified constitutive equations. He also recognizes the shortcoming of many theories in predicting hysteresis loops which are "oversquare" in comparison to observed experimental behavior. Improvement is accomplished by making the kinematic work-hardening coefficient depend on the back stress and the sign of the nonelastic strain term. Results compare favorably with that observed in 2024-T4 aluminum alloy. Miller states his approach appears consistent with an existing physical explanation in terms of annihilation of previously-generated dislocation loops upon reversals in the direction of dislocation motion.

A theory that is similar in format to Miller's is by Krieg, Swearingen, and Rohde [11]. The model uses two internal state variables to reflect current microstructure and is based upon models for dislocation process in pure metals. It is an extension of an equation of state theory originally attributed to Kocks [17] where the inelastic flow rule is taken to be a power function incorporating a kinematic and isotropic internal variable. They assume that all the net mechanical effect of the complex dislocation processes can be contained by one or two readily measurable macroscopic variables. The theory cannot accurately model cyclic hardening or softening behavior and the strain hardening behavior is necessarily "square" in nature because of the power law assumption. Also, applications of the model over a wide range of homologous temperatures, or to alloys in general is not advised.

Nonlinear viscoelastic theories. Nonlinear viscoelastic or thermodynamically based theories are usually distinguished by their single integral or convoluted form. This type of constitutive model employs the first and second laws of thermodynamics along with physical constraints to complete the formulation [12]. A detailed review of several existing theories is presented in both [10] and [18].

One of the more promising theories is credited to Walker [9,18]. It is a unified integral viscoplastic theory developed by modifying the constitutive relation for a linear three parameter viscoelastic solid. The theory contains clearly defined material parameters, a rate dependent equilibrium stress, and a proposed multiaxial model. An important shortcoming of Walker's theory is its failure to model transient temperature conditions, but Allen and Milly [10] conclude that his theory is the best presently available for predicting cyclic response at elevated temperatures under isothermal conditions.

Other nonlinear viscoelastic theories discussed by Walker [18] are by Cernochy and Krempl, Valanis, and Chaboche.

Classical plasticity theories. The type of constitutive law considered in this research is derived from classical incremental plasticity. It is termed a macrophenomenological theory as it derives its state variables purely from experimental results without direct reference to the microstructure of the material. This type of constitutive law can be defined as one that attempts to describe the elastic-plastic behavior of a material based on properties obtained from a single stress state and then use them to establish relationships between the general stress and strain tensors [13]. Most incremental

plasticity theories have four major components: (1) a stress-elastic strain relation, (2) a yield function describing the onset of plastic deformation, (3) a hardening rule which prescribes the strain-hardening of the material and the modification of the yield surface during plastic flow, and (4) a flow rule which defines the component of strain that is plastic or nonrecoverable [19].

Research in this area is voluminous. The inviscid plasticity is well established while the extension to include rate and thermal effects is not. References [10,12] and [13] summarize some of the important research efforts in their field of study. Of the classical plasticity theories reviewed in [10], the most promising ones belong to Zienkiewicz and Corneau, and Allen and Haisler. The former is a rate dependent unified theory which allows for nonassociative plasticity and strain softening but does not model the Bauschinger effect or temperature dependence. The latter is an extension of classical plasticity to model both rate and thermal effects. It is a two state variable uncoupled theory with clearly defined material parameters and extension to multiaxial form. Still another example is a model proposed by Popov and Petersson [20,21]. Excellent agreement with experiment is shown in the isothermal, rate independent case. Snyder and Bathe [22] have proposed a modification to classical plasticity which does model both rate and thermal effects in the monotonic load case but is restricted to a kinematic hardening rule. Allen [12] suggests that the theory proposed by Yamada and Sakurai [23,24] may be the best for modelling the type of behavior described herein. Temperature dependence of material properties, a combined hardening rule, and an

CHAPTER III

DEVELOPMENT OF THE MODEL

The author gives the following justifications for using the uncoupled approach proposed by Allen and Haisler. One can partition the total inelastic strain into components as long as their sum yields the total nonrecoverable deformation without significant adverse effects [12]. The theory is able to model behavior over a wide range of load and temperature up to at least one-half the melting point for several metals. It is also one of only a few to address transient temperature conditions. Also, with the revised hardening law presented herein, the rate independent inelastic deformation is modeled as well as or better than the unified theories reviewed. Reasonable experimental data requirements are another strong point of this theory.

Derivation of the Constitutive Equations

The constitutive equations of the Allen and Haisler model are derived in a uniaxial incremental form relating the total stress increment to the total strain increment. Development of the theory in this form is a logical approach as it lends itself to much simpler evaluation without introducing unnecessary complications of a multiaxial theory. Many components of the work required are much more easily done in uniaxial form such as the computer code development and experimental model verification.

As stated earlier, most classical plasticity theories have four major components. First, there is a relation between stress and elastic strain

$$\sigma = E\epsilon^E = E(\epsilon - \epsilon^P - \epsilon^C - \epsilon^T), \quad (3)$$

or in incremental form

$$\Delta\sigma = E^{t+\Delta t}(\Delta\epsilon - \Delta\epsilon^P - \Delta\epsilon^C - \Delta\epsilon^T) + \Delta E(\epsilon^t - \epsilon^P{}^t - \epsilon^C{}^t - \epsilon^T{}^t) \quad (4)$$

where σ is the uniaxial stress, E is the elastic modulus, and ϵ is the uniaxial strain. Superscripts P, C, and T denote plastic, creep, and thermal components respectively while t denotes values at the start of the load step, and $t + \Delta t$ denotes values at the end of a load step. Note that the elastic modulus is measured at the end of the step because the time step is finite rather than infinitesimal as described by Allen [12]. A graphical decomposition of the total strain is shown in Fig. 1. The term "zero time" denotes a loading input short enough to negate any time dependent deformation but long enough to disregard inertial effects (a few seconds for many metals) [12]. Conversely, the long time curve characterizes the rate dependent deformation. Recall that there is no physical basis for uncoupling the inelastic deformation, but it is valid as long as coupling effects are insignificant or the uncoupling is done properly.

Secondly, a yield function describes the onset of plastic deformation. A possible functional form, supported by experiment, is given by

$$F(\sigma - \alpha) = K^2 \left(\int d\epsilon^P, T \right) \quad (5)$$

where α and K represent the center and radius of the yield surface respectively, $\int d\epsilon^P$ is the history of the equivalent uniaxial plastic

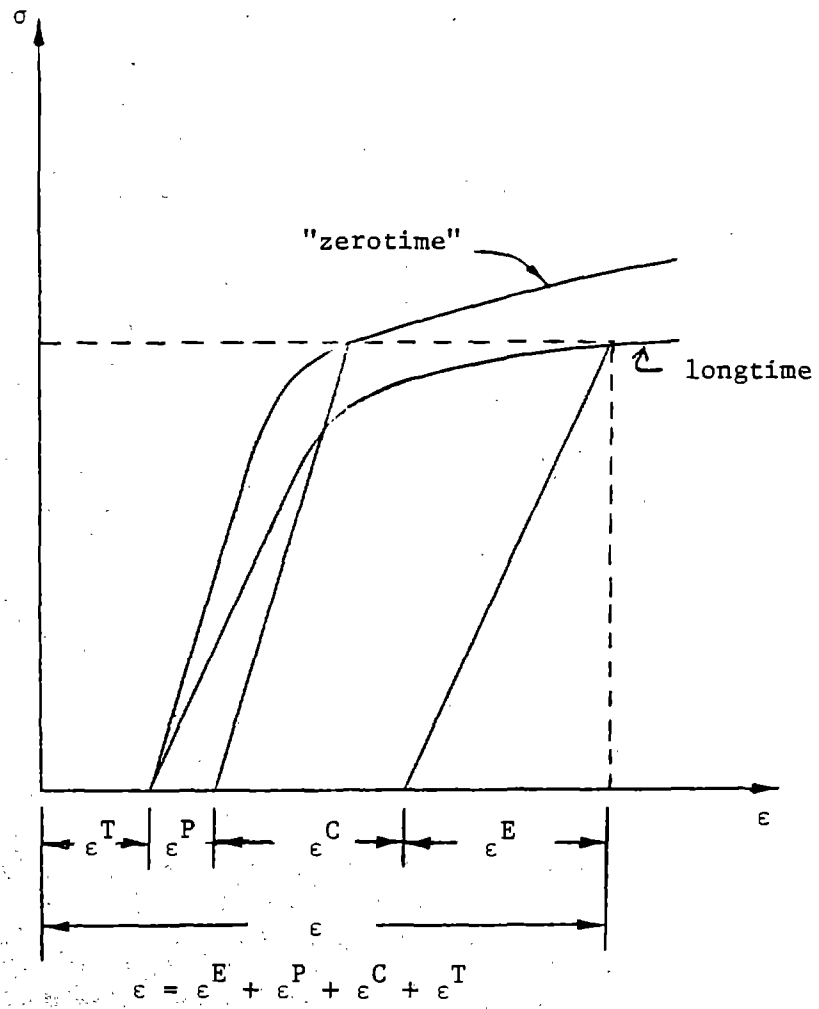


Fig. 1 Total strain decomposition

strain and T is the temperature. Note that microphysically α is a state variable combining the effects of the back and drag stresses while $d\epsilon^P$ is a second state variable representing the dislocation arrangement. This arrangement of dislocations and dislocation loops will be discussed later as to their effect on reyield and strain hardening behavior upon reyield.

A hardening rule prescribes the strain hardening of the material and the modification of the yield surface during plastic flow and can be stated in a combined isotropic-kinematic form as

$$d\alpha = d\mu(\sigma - \alpha) \quad (6)$$

where $d\mu$ is a scalar. Lastly, if yielding does occur we need further information concerning the rate of deformation to complete the description of the material behavior. This information is provided by the flow rule which defines the component of strain that is plastic or nonrecoverable and can be written as

$$d\epsilon^P = d\lambda \frac{\partial F}{\partial \sigma} \quad (7)$$

where $d\lambda$ is a scalar determined from material data. Equation (7) is called an associated flow rule because it is the less general case containing the partial derivative of the yield function rather than a general plastic potential. It is also known as a normality condition because it can be interpreted as requiring the normality of the plastic strain increment "vector" to the yield surface in n stress dimensions [26].

Differentiation of (5) is the first step in deriving the constitutive equations and will yield

$$\frac{\partial F}{\partial \sigma} d\sigma - \frac{\partial F}{\partial \alpha} d\alpha = 2K \frac{\partial K}{\partial \epsilon} d\epsilon^{-P} + 2K \frac{\partial K}{\partial T} dT. \quad (8)$$

The above consistency condition requires that loading from a plastic state must lead to another plastic state [27]. Substitution of (7) into (4)

$$d\sigma = E^{t+\Delta t} (d\epsilon - d\lambda \frac{\partial F}{\partial \sigma} - d\epsilon^C - d\epsilon^T) + dE(\epsilon^t - \epsilon^{P^t} - \epsilon^{C^t} - \epsilon^{T^t}) \quad (9)$$

and then (9) into (8) yields

$$\begin{aligned} \frac{\partial F}{\partial \sigma} \{E^{t+\Delta t} (d\epsilon - d\lambda \frac{\partial F}{\partial \sigma} - d\epsilon^C - d\epsilon^T) + dE(\epsilon^t - \epsilon^{P^t} - \epsilon^{C^t} - \epsilon^{T^t})\} \\ - \frac{\partial F}{\partial \alpha} d\alpha = 2K \frac{\partial K}{\partial \epsilon} d\epsilon^{-P} + 2K \frac{\partial K}{\partial T} dT. \end{aligned} \quad (10)$$

Solving for $d\lambda$ from above

$$\begin{aligned} d\lambda = \{ \frac{\partial F}{\partial \sigma} [E^{t+\Delta t} (d\epsilon - d\epsilon^C - d\epsilon^T) + dE(\epsilon^t - \epsilon^{P^t} - \epsilon^{C^t} - \epsilon^{T^t})] - \frac{\partial F}{\partial \alpha} d\alpha \\ - 2K \frac{\partial K}{\partial \epsilon} d\epsilon^{-P} - 2K \frac{\partial K}{\partial T} dT \} / (\frac{\partial F}{\partial \sigma} E^{t+\Delta t} \frac{\partial F}{\partial \sigma}) \end{aligned} \quad (11)$$

and substituting (11) into (4) yields

$$\begin{aligned} d\sigma = E^{t+\Delta t} \{ \{ d\epsilon - [\frac{\partial F}{\partial \sigma} [E^{t+\Delta t} (d\epsilon - d\epsilon^C - d\epsilon^T) + dE(\epsilon^t - \epsilon^{P^t} - \epsilon^{C^t} - \epsilon^{T^t})] \\ - \frac{\partial F}{\partial \alpha} d\alpha - 2K \frac{\partial K}{\partial \epsilon} d\epsilon^{-P} - 2K \frac{\partial K}{\partial T} dT] / (\frac{\partial F}{\partial \sigma} E^{t+\Delta t} \frac{\partial F}{\partial \sigma}) \} \frac{\partial F}{\partial \sigma} \\ - d\epsilon^C - d\epsilon^T \} + dE(\epsilon^t - \epsilon^{P^t} - \epsilon^{C^t} - \epsilon^{T^t}). \end{aligned} \quad (12)$$

Rearranging the last equation to obtain

$$\begin{aligned}
d\sigma &= E^{t+\Delta t} (d\varepsilon - d\varepsilon^C - d\varepsilon^T) + dE(\varepsilon^t - \varepsilon^P - \varepsilon^C - \varepsilon^T) \\
&= \frac{E^{t+\Delta t} \frac{\partial F}{\partial \sigma} \frac{\partial F}{\partial \sigma} E^{t+\Delta t} (d\varepsilon - d\varepsilon^C - d\varepsilon^T)}{\frac{\partial F}{\partial \sigma} E^{t+\Delta t} \frac{\partial F}{\partial \sigma}} \\
&+ \frac{E^{t+\Delta t} \frac{\partial F}{\partial \sigma} \frac{\partial F}{\partial \sigma} dE(\varepsilon^t - \varepsilon^P - \varepsilon^C - \varepsilon^T)}{\frac{\partial F}{\partial \sigma} E^{t+\Delta t} \frac{\partial F}{\partial \sigma}} \\
&+ E^{t+\Delta t} \frac{\partial F}{\partial \sigma} \left[\frac{-\frac{\partial F}{\partial \sigma} d\alpha - 2K \frac{\partial K}{\partial \varepsilon} \frac{d\varepsilon^P}{d\varepsilon} - 2K \frac{\partial K}{\partial T} dT}{\frac{\partial F}{\partial \sigma} E^{t+\Delta t} \frac{\partial F}{\partial \sigma}} \right] \quad (13)
\end{aligned}$$

Using the normality condition (7) one can write

$$-E^{t+\Delta t} \frac{\partial F}{\partial \sigma} = -E^{t+\Delta t} \frac{d\varepsilon^P}{d\lambda} \quad (14)$$

Then equation (4) can be rewritten as

$$-E^{t+\Delta t} \frac{d\varepsilon^P}{d\lambda} = \frac{d\sigma}{d\lambda} - \frac{1}{d\lambda} [E^{t+\Delta t} (d\varepsilon - d\varepsilon^C - d\varepsilon^T) + dE(\varepsilon^t - \varepsilon^P - \varepsilon^C - \varepsilon^T)], \quad (15)$$

and equation (13) can also be rewritten as

$$\begin{aligned}
\theta d\sigma &= E^{t+\Delta t} (d\varepsilon - d\varepsilon^C - d\varepsilon^T) \theta - E^{t+\Delta t} \frac{\partial F}{\partial \sigma} \frac{\partial F}{\partial \sigma} E^{t+\Delta t} (d\varepsilon - d\varepsilon^C - d\varepsilon^T) \\
&+ dE(\varepsilon^t - \varepsilon^P - \varepsilon^C - \varepsilon^T) - E^{t+\Delta t} \frac{\partial F}{\partial \sigma} \frac{\partial F}{\partial \sigma} E(\varepsilon^t - \varepsilon^P - \varepsilon^C - \varepsilon^T), \quad (16)
\end{aligned}$$

where

$$\theta = \frac{\partial F}{\partial \sigma} \frac{d\alpha}{d\lambda} + 2K \frac{\partial K}{\partial \varepsilon} \frac{d\varepsilon^P}{d\lambda} + 2K \frac{\partial K}{\partial T} \frac{dT}{d\lambda} + E^{t+\Delta t} \frac{\partial F}{\partial \sigma} \frac{\partial F}{\partial \sigma} \quad (17)$$

Rearrange above to obtain

$$d\sigma = \left[E^{t+\Delta t} - \frac{E^{t+\Delta t} \frac{\partial F}{\partial \sigma} \frac{\partial F}{\partial \sigma} E^{t+\Delta t}}{\theta} \right] (d\varepsilon - d\varepsilon^C - d\varepsilon^T) \\ + \left[dE - \frac{E^{t+\Delta t} \frac{\partial F}{\partial \sigma} \frac{\partial F}{\partial \sigma} dE}{\theta} \right] (\varepsilon^t - \varepsilon^P - \varepsilon^C - \varepsilon^T) \quad (18)$$

Now make the assumption made by Hunsaker [28] that

$$(d\sigma - C d\varepsilon^P) \frac{\partial F}{\partial \sigma} = 0 \quad (19)$$

which defines C as a scaling parameter requiring $(d\sigma - C d\varepsilon^P)$ to be perpendicular to the yield surface outer normal. The verification of this assumption is discussed by Allen [29]. Rewrite equation (8)

$$\frac{\partial F}{\partial \sigma} d\sigma = \frac{\partial F}{\partial \sigma} d\alpha + 2K \frac{\partial K}{\partial \varepsilon} d\varepsilon^P + 2K \frac{\partial K}{\partial T} dT \quad (20)$$

and equate with (19) to obtain

$$C d\varepsilon^P \frac{\partial F}{\partial \sigma} = \frac{\partial F}{\partial \sigma} d\sigma = \frac{\partial F}{\partial \sigma} d\alpha + 2K \frac{\partial K}{\partial \varepsilon} d\varepsilon^P + 2K \frac{\partial K}{\partial T} dT \quad (21)$$

Also, substitute the normality condition (7) into (21) will give

$$Cd\lambda \frac{\partial F}{\partial \sigma} \frac{\partial F}{\partial \sigma} = \frac{\partial F}{\partial \sigma} d\sigma = \frac{\partial F}{\partial \sigma} d\alpha + 2K \frac{\partial K}{\partial \varepsilon} d\varepsilon^P + 2K \frac{\partial K}{\partial T} dT \quad (22)$$

or

$$C \frac{\partial F}{\partial \sigma} \frac{\partial F}{\partial \sigma} = \frac{1}{d\lambda} \frac{\partial F}{\partial \sigma} d\sigma = \frac{\partial F}{\partial \sigma} \frac{d\alpha}{d\lambda} + 2K \frac{\partial K}{\partial \varepsilon} \frac{\partial \varepsilon^P}{d\lambda} + 2K \frac{\partial K}{\partial T} \frac{\partial T}{d\lambda} \quad (23)$$

Using the relations in (23), equation (17) can now be rewritten as

$$\theta = C \frac{\partial F}{\partial \sigma} \frac{\partial F}{\partial \sigma} + E^{t+\Delta t} \frac{\partial F}{\partial \sigma} \frac{\partial F}{\partial \sigma} \quad (24)$$

where

$$C = \frac{\frac{\partial F}{\partial \sigma} d\sigma}{d\lambda \frac{\partial F}{\partial \sigma} \frac{\partial F}{\partial \sigma}} = \frac{d\sigma}{d\lambda \frac{\partial F}{\partial \sigma}} \quad (25)$$

Applying (7), the above becomes

$$C = \frac{d\sigma}{d\varepsilon^{-P}} \quad (26)$$

Physically, C is the slope of the uniaxial stress vs. equivalent uniaxial plastic strain diagram during an isothermal load increment.

However, during a nonisothermal load step

$$d\sigma = \frac{\partial \sigma}{\partial \varepsilon^{-P}} d\varepsilon^{-P} + \frac{\partial \sigma}{\partial T} dT = c d\varepsilon^{-P} + \frac{\partial \sigma}{\partial T} dT \quad (27)$$

or

$$C = \frac{d\sigma}{d\varepsilon^{-P}} + \frac{\partial \sigma}{\partial T} \frac{dT}{d\varepsilon^{-P}} = H' + \frac{\partial \sigma}{\partial T} \frac{dT}{d\varepsilon^{-P}} \quad (28)$$

The above statement is required because the uniaxial stress is a function of both the plastic strain history and temperature during nonisothermal loading.

Finally, substitute (24) and (28) into equation (18) to obtain

$$d\sigma = \left[E^{t+\Delta t} - \frac{E^{t+\Delta t} \frac{\partial F}{\partial \sigma} \frac{\partial F}{\partial \sigma} E^{t+\Delta t}}{H' \frac{\partial F}{\partial \sigma} \frac{\partial F}{\partial \sigma} + E^{t+\Delta t} \frac{\partial F}{\partial \sigma} \frac{\partial F}{\partial \sigma}} \right] (d\varepsilon - d\varepsilon^C - d\varepsilon^T)$$

$$\begin{aligned}
& + \left[dE - \frac{E^{t+\Delta t} \frac{\partial F}{\partial \sigma} \frac{\partial F}{\partial \sigma} dE}{H' \frac{\partial F}{\partial \sigma} \frac{\partial F}{\partial \sigma} + E^{t+\Delta t} \frac{\partial F}{\partial \sigma} \frac{\partial F}{\partial \sigma}} \right] (\epsilon^t - \epsilon^P{}^t - \epsilon^C{}^t - \epsilon^T{}^t) \\
& + \left[\frac{E^{t+\Delta t} \frac{\partial F}{\partial \sigma} \frac{\partial F}{\partial \sigma} \frac{\partial \sigma}{\partial T}}{H' \frac{\partial F}{\partial \sigma} \frac{\partial F}{\partial \sigma} + E^{t+\Delta t} \frac{\partial F}{\partial \sigma} \frac{\partial F}{\partial \sigma}} \right] dT. \tag{29}
\end{aligned}$$

Now for the yield surface translation scalar, substitute (6) into (8) and solve for $d\mu$ as follows

$$\frac{\partial F}{\partial \sigma} d\sigma - \frac{\partial F}{\partial \sigma} [d\mu(\sigma - \alpha)] = 2K \frac{\partial K}{\partial \epsilon^P} + 2K \frac{\partial K}{\partial T} dT \tag{30}$$

$$d\mu \frac{\partial F}{\partial \sigma} (\sigma - \alpha) = \frac{\partial F}{\partial \sigma} d\sigma - 2K \frac{\partial K}{\partial \epsilon^P} d\epsilon^P - 2K \frac{\partial K}{\partial T} dT \tag{31}$$

$$d\mu = \frac{\frac{\partial F}{\partial \sigma} d\sigma - 2K \frac{\partial K}{\partial \epsilon^P} d\epsilon^P - 2K \frac{\partial K}{\partial T} dT}{\frac{\partial F}{\partial \sigma} (\sigma - \alpha)} \tag{32}$$

An outline for the uniaxial computer program utilizing the above equations is contained in the Appendix.

Yield Function

The von Mises yield criterion is used herein and can be written in terms of principal stresses σ_i as

$$F(\sigma_i) = \frac{1}{2} \{ (\sigma_1 - \sigma_2)^2 + (\sigma_2 - \sigma_3)^2 + (\sigma_3 - \sigma_1)^2 \} = K^2 \tag{33}$$

where K represents the current yield surface size. It has been shown to be in excellent agreement with experiment for many ductile metals,

for example aluminum, cold-worked mild steel, medium carbon and alloy steels [2]. The von Mises yield criterion can be written in uniaxial form (with the use of a combined isotropic-kinematic hardening law) as

$$F(\sigma-\alpha) = (\sigma-\alpha)^2 = K^2 \quad (34)$$

where α is the yield surface center.

Note that the assumed yield function is dependent only on the second deviatoric stress invariant, i.e., independent of hydrostatic stress and with the assumption of initially isotropic materials. Also, the temperature dependence is handled through thermally dependent material properties and is isotropic in nature, but there is no rate dependence in this form of the yield function.

Hardening Rule

Laws governing the influence of plastic deformation on the yield surface and strain hardening of a material are called hardening rules. A significant amount of research has been done in this area, and there are many different rules in use.

Consider Fig. 2 as a comparison of several hardening rules for a given isothermal load history. Although isotropic hardening will successfully model loading histories in which stress reversals do not occur, it is not satisfactory to model the Bauschinger effect or cyclic phenomenon. Conversely, kinematic hardening will model the Bauschinger effect, but neither hardening rule predicts the increased strain hardening upon reyield as their "square" hysteresis loop predictions show. Oak Ridge (ORNL) [30] and combined hardening rules predict overall

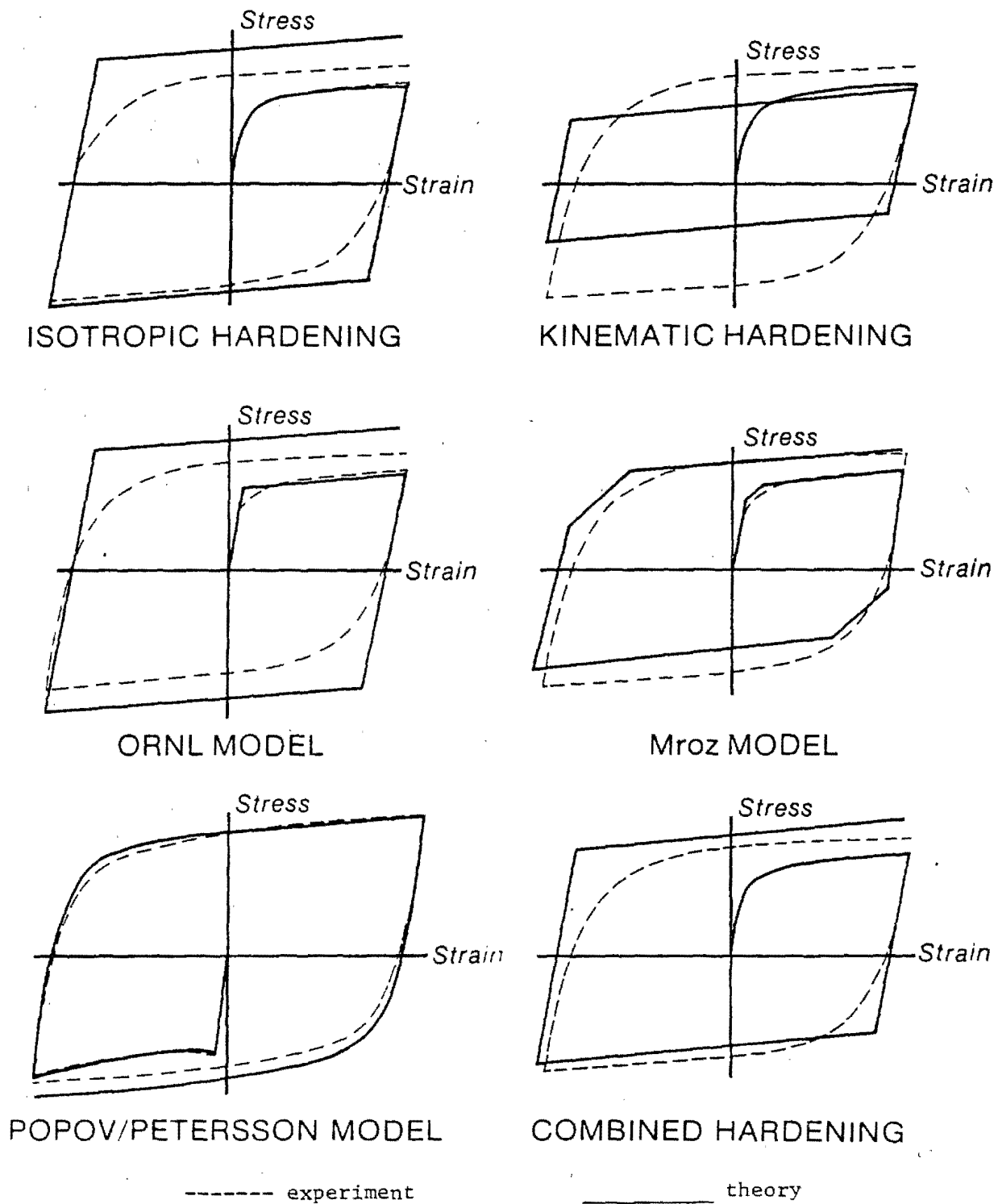


Fig. 2 Plasticity models

response somewhat better. Hunsaker [13] suggests the mechanical sub-layer model for loadings in which stress reversals may occur. Of all the plasticity models displayed in Fig. 2, the multisurface approach of Petersson and Popov [20,21] clearly gives the best theoretical representation of the experiment.

Thus, if one is interested in the exact stress-strain behavior over the entire load history and not just an end result, a hardening law which accounts for increased strain hardening upon reyield becomes a necessity.

At temperatures below roughly one-half the melting point for many metals, a change of loading direction in stress space plays a very important role. In many hardening rules emphasis is placed on how to describe the evolution of the yield surface while little has been done as to how the plastic modulus is affected by stress reversals in cyclic loading [31]. Above this temperature the stress-strain behavior is controlled by rate dependent deformation and experimentally observed hysteresis loops are relatively "square". Thus the simulation of the strain hardening is not as critical.

Many authors mention the "oversquareness" of predicted hysteresis loops. Among these are Miller [16], Dafalias and Popov [31], Walker [9], and Popov and Petersson [20,21]. It seems that this phenomenon is of some interest to the researchers in this field. Miller improves his unified time-dependent constitutive equations by making the kinematic work-hardening coefficient a function of the back stress and the sign of the nonelastic strain rate and shows favorable agreement with that observed in 2024-T4 aluminum alloy. Another approach by

Dafalias and Popov which was extended by Petersson and Popov involves enclosing the initial yield surface within a larger bounding surface. Both surfaces are allowed to translate and deform in stress space, and the proximity of the two determines the plastic moduli. Two other hardening rules which provide for a high strain-hardening rate upon reyielding are the Mroz and mechanical sublayer models [13].

Since Miller's theory [16] is microphenomenologically based, he seeks to make his model consistent with existing microphysical explanations. He states that dislocations moving in a given direction will form dislocation loops by interaction with precipitate particles, and when the direction of dislocation motion is reversed a dislocation can annihilate a nearby loop which was previously left behind. A relatively rapid change of strain in the nature of the stress field encountered by the reversing dislocation would result and lead to a large value of the slope $d\sigma/d\epsilon$. As the strain continues to reverse, dislocations will no longer be encountering such oppositely-signed loops and $d\sigma/d\epsilon$ will gradually decrease. Miller models this by associating the directionality of the dislocation debris with the back stress R and the direction of current dislocation motion with the sign of the difference $\sigma/E-R$. A similar argument is given by Polakowski and Rippling [14].

Although the combined isotropic-kinematic hardening rule used by Allen and Haisler [25] cannot represent the high rate of strain hardening accompanying stress reversals which cause yielding, it does account for thermally dependent material properties and the Bauschinger effect. Thus it was felt that with some modifications, all cyclic characteristics could be modeled. To summarize, the two important

shortcomings of their hardening law in representing cyclic behavior are its failure to account for the high rate of strain hardening upon reyielding after a stress reversal and cyclic saturation.

In terms of actual modelling of the two shortcomings discussed above, several revisions and improvements have been added to the model. First as discussed in regards to experimental data requirements, additional stress-strain input is required to characterize various strain hardening rates. Metals like aluminum exhibit a similar strain hardening behavior for reyield after the initial yield. Conversely, stainless steel can exhibit two different forms of hardening behavior even after several loading cycles. A program flag controls which input stress-strain curve to use to generate hardening parameters depending on the material being modeled and the yield (load) history. Secondly, the hardening ratio was allowed to be a function of plastic strain and in some cases the direction of loading. This allows modelling of cyclic saturation.

More specifically, the hardening rule revisions can be explained in two different discussions. The first deals with strain hardening upon reyield and the second with cyclic saturation.

Use of the combined hardening law in Allen and Haisler [25], predicts cyclic behavior like that shown in Fig. 3. The hardening ratio, β is the ratio of isotropic to kinematic hardening. Setting $\beta=0$ constitutes a kinematic hardening law where the yield surface retains its initial size, shape, and orientation thus simply translating in principal stress space. Isotropic hardening, $\beta=1$, means that during plastic flow the yield surface expands uniformly about the origin and

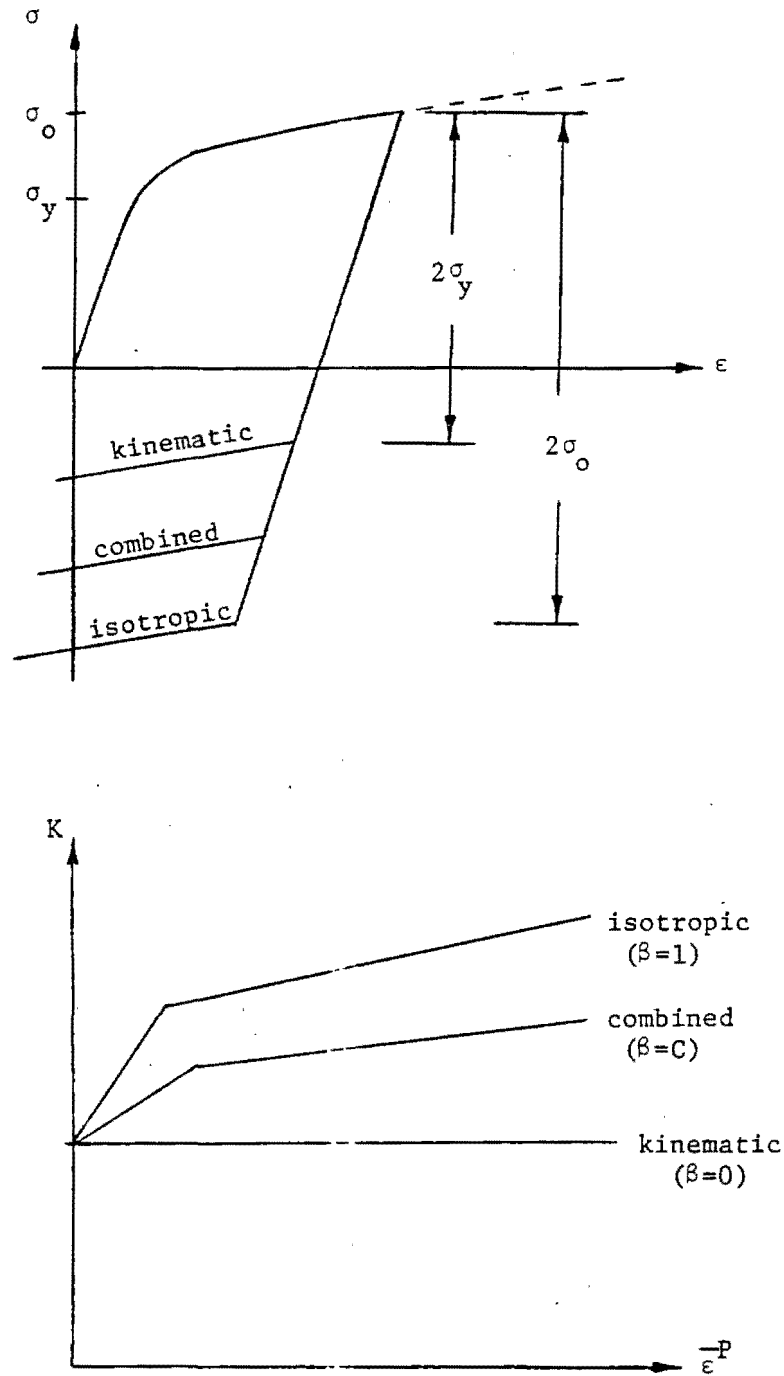


Fig. 3 Definition of standard hardening rules

never translates. Using a value for the hardening ratio such as $0 \leq \beta \leq 1$ constitutes a combined hardening rule where the yield surface is allowed to both expand and translate.

Notice in Fig. 3 that the reyielded strain hardening behavior is "squared-off" as discussed above. The revised model has the ability to reproduce strain hardening behavior that is dependent on direction or history of yielding. This is observed in experiment as the high rate of strain hardening upon stress reversal in a cyclic load test. In other words, the material demonstrates two distinct forms of behavior as shown in Fig. 4. Initial strain hardening character is usually quite "sharp" in comparison with the rounded shape of the reverse loading curve. Popov and Petersson [21] found it essential in dealing with cyclic steel behavior to use two stress-strain curves as input. The first is from a monotonic test on virgin material and the second is from a hysteresis loop which develops after several loading cycles.

For a large number of common metals, a cyclic load history leads to a limiting periodic response in which the stress-strain curve for each consecutive cycle is the same. This is termed cyclic saturation and is illustrated in Fig. 5 [32]. Capability to portray this phenomenon is not contained in many common hardening laws. With the addition of a hardening ratio that is a function of plastic strain and in some cases direction of loading into the existing model, this phenomenon can be modeled much more successfully than a combined hardening rule with a constant hardening ratio.

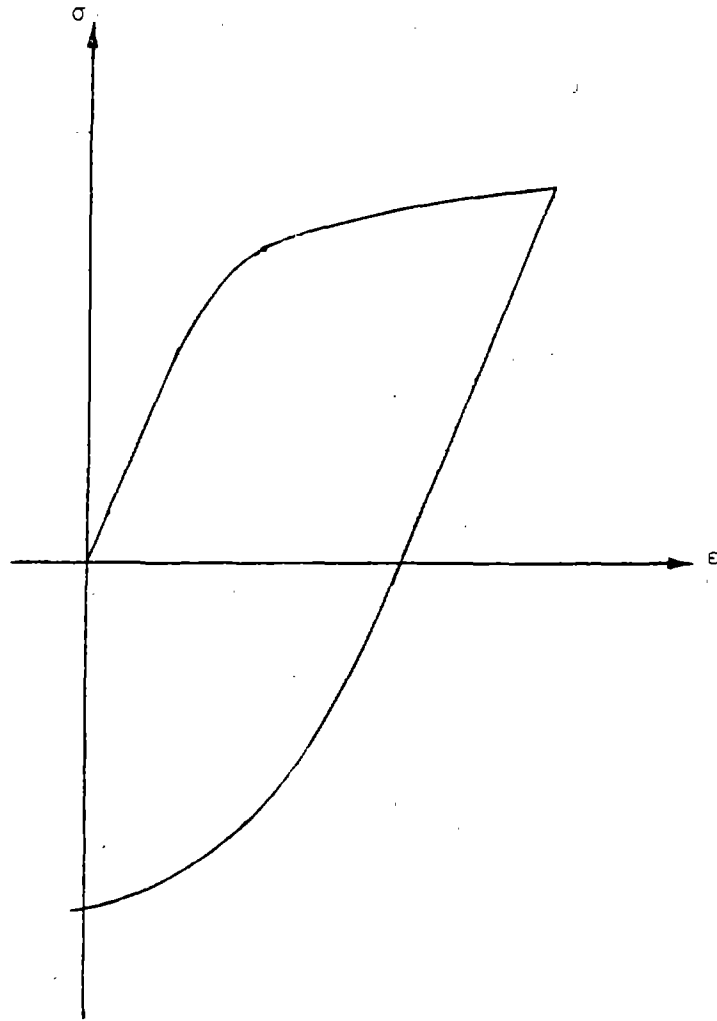


Fig. 4 Typical experimental results showing difference in first and second quarter cycle response

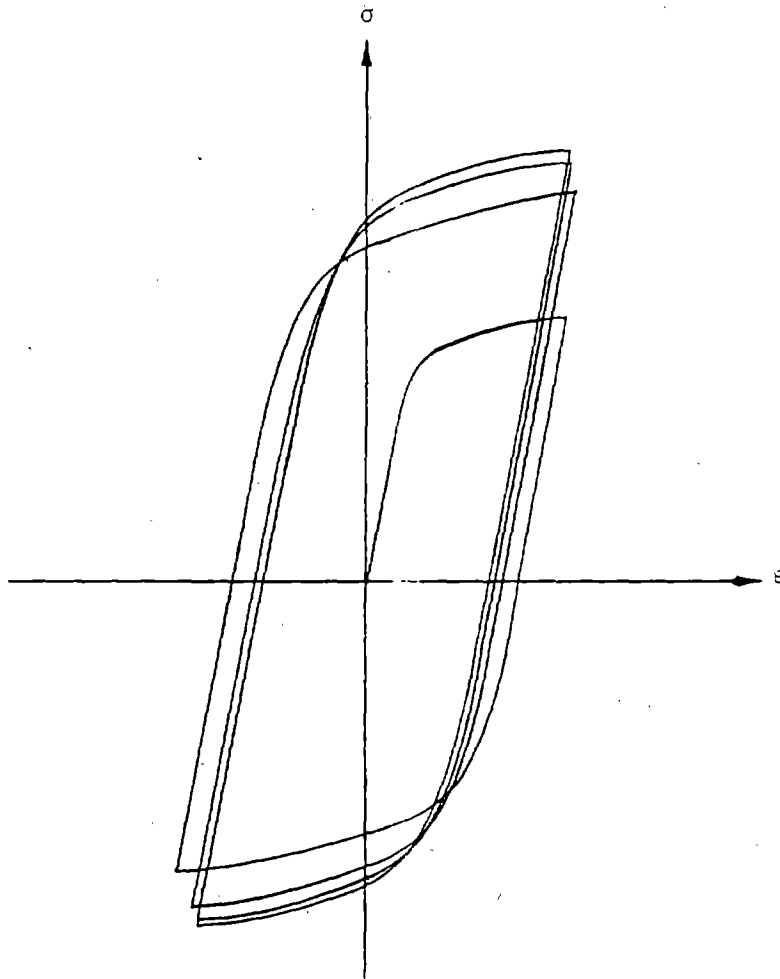


Fig. 5 Mechanical response of typical ductile metal exhibiting cyclic saturation in cyclic loading

The reader is referred to the sections on experimental data requirements and theoretical examples for more details concerning the above discussion.

Creep Strain Increment

The creep strain is defined as the uncoupled rate dependent inelastic deformation in the present theory. Several methods are available to characterize this strain component. Traditional characterization has been based on the use of standard creep tests run at constant stress and temperature. Creep strain (or creep strain rate) is written as a function of time, stress, and temperature through the use of power law functions, exponentials, hyperbolic functions, etc. obtained by appropriate curve fitting techniques. Additional ad hoc creep hardening rules have been devised to model rate dependent behavior during reverse and cyclic loading. Oak Ridge National Laboratory used such models for 304 stainless steel with some success [33]. In many cases it is more expedient to use tabulated creep strain data as opposed to curve fitted data; although this requires numerical interpolation between a set of isothermal, constant stress creep curves.

In the present research, an alternate approach has been taken involving hysteresis loops and stress relaxation tests at various temperatures. Fig. 6 shows a typical set of these tests and details how the rate dependent deformation is extracted from them.

A reference temperature hysteresis loop is defined at a temperature below which the total strain consists essentially of elastic and rate independent plastic strains only. Above this temperature, the

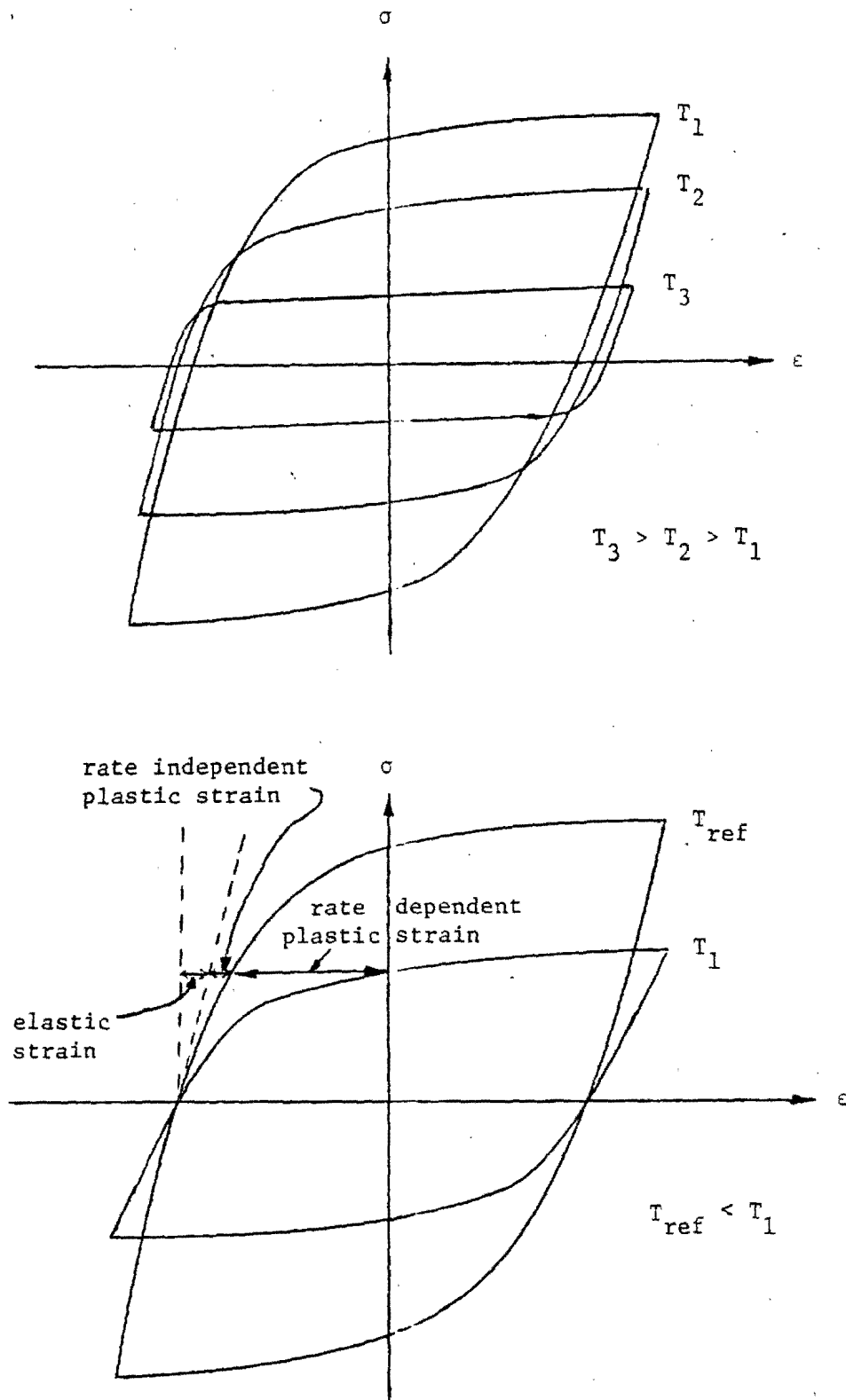


Fig. 6 Experimental characterization of the rate dependence of the model

rate dependent inelastic strain (creep) dominates. Experimentally, Bradley and Haisler [34,35] have shown for Hastelloy-X that such an uncoupling appears feasible.

Micromechanical considerations suggest a model for the rate dependent inelastic strain of the form

$$\dot{\epsilon}^C = \left(\frac{\sigma - \Omega}{K_0} \right)^n, \quad (35)$$

where $\dot{\epsilon}^C$ represents the rate dependent inelastic strain rate, Ω is the back stress, K_0 is the drag stress, and n is a constant. The back stress, drag stress, and exponent n are generally functions of temperature and strain. However, for some materials a good assumption is that the drag stress and n are constant at sufficiently high temperatures.

At the tips of the hysteresis loops, the stress and back stress have reached maximum values σ_{\max} and Ω_{\max} respectively. If we let σ_1 and σ_2 denote the maximum stress values at two different strain rates $\dot{\epsilon}_1$ and $\dot{\epsilon}_2$, then the value of n can be computed as

$$n = \ln(\dot{\epsilon}_1 / \dot{\epsilon}_2) / \ln[(\sigma_1 - \Omega_{\max}) / (\sigma_2 - \Omega_{\max})] \quad (36)$$

where Ω_{\max} is assumed to be constant between $\dot{\epsilon}_1$ and $\dot{\epsilon}_2$. Similarly, the constant K_0 can be determined by rewriting (35) in the form

$$K_0 = (\sigma_1 - \Omega_{\max}) \dot{\epsilon}_1^{-1/n} \quad (37)$$

It should be noted that a number of the unified models reviewed in Chapter II (for example, Walker's [9]) utilized similar functional

forms and experimental characterizations of the inelastic strain component compared to that used in this research for rate dependent inelastic strain. Although the functional forms used to model the unified inelastic strain give excellent agreement at high temperature (where rate dependence dominates), they give overly square stress-strain response at low temperature (where rate independent plasticity dominates). This is due primarily to the failure of the present unified models to account properly for rate independent behavior. In the present research, this difficulty is hopefully overcome by modeling the rate dependent inelastic and rate independent inelastic strain more accurately with appropriate definition of a temperature range where each is applicable.

Experimental Data Requirements

One of the requirements for a good constitutive model is that it have reasonable experimental data requirements. Characterization of model parameters should follow easily from standard tests.

All experimental data tests are performed at sufficient levels of the primary variables (strain and temperature) in order to bracket their magnitudes in the particular test of interest. Consideration is also given to allow accurate linear interpolation between temperatures.

The first set of tests required is uniaxial isothermal single cycle reverse loading tests like those shown in Fig. 7. These tests are performed at fast enough strain rates so that the rate dependent component of deformation is negligible. Characterization of both

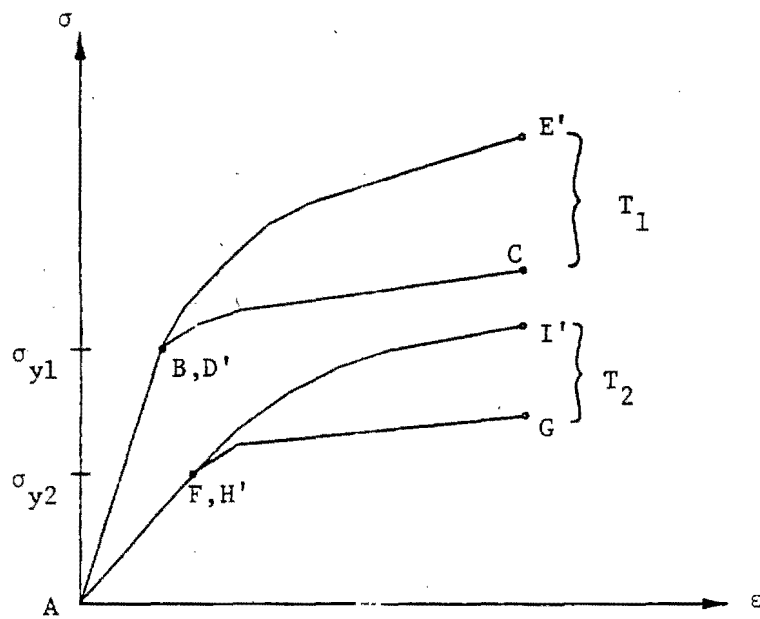
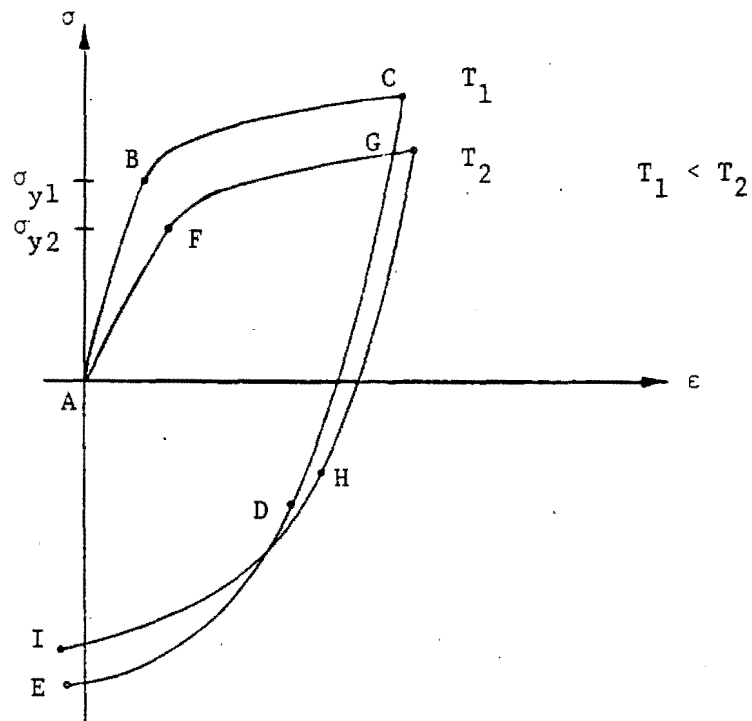


Fig. 7 Uniaxial isothermal single cycle reverse loading curves and their linear representations input to the model

initial and subsequent strain hardening behavior is the reason for the reverse loading tests. Piecewise linear representations of the data obtained from experiment are input into the model with the number of linear segments used depending on the accuracy desired.

For example as shown in Fig. 7 at $T=T_1$, the initial elastic-plastic behavior is characterized by curve ABC. Similarly the subsequent elastic-plastic behavior is characterized by curve DE. The piecewise linear representations become curve ABC and D'E' where D'E' was obtained by shifting curve DE to the yield point B. A similar procedure is performed for all other temperatures as required. Note that if the difference in strain hardening behavior is not considered critical, (the difference between curves ABC and DE is insignificant) only curves ABC and AFG would be required input.

If the hardening ratio is constant with respect to plastic strain, it can also be determined from the above tests using the relation

$$\beta = \frac{\sigma_r - (2\sigma_y - \sigma_o)}{(2\sigma_o - 2\sigma_y)}, \quad (38)$$

where stress values are defined in Fig. 8 for each temperature. If β is a function of plastic strain as well as temperature, several cycles of stress-strain data would be required to characterize this parameter. Typical input curves for the hardening ratio are also shown in Fig. 8.

A piecewise linear description of the temperature dependence of the coefficient of thermal expansion is also required if it varies significantly for the temperature range of interest.

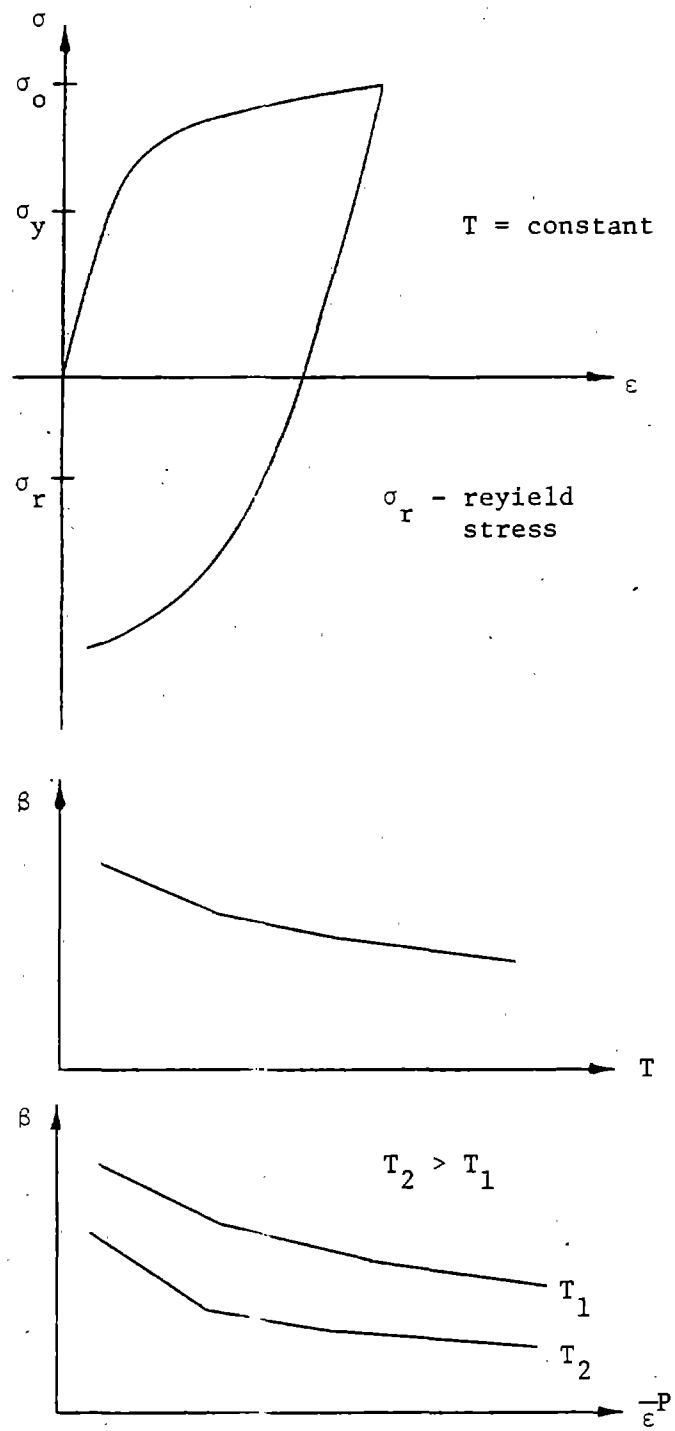


Fig. 8 Hardening ratio

Experimental characterization of the rate dependent terms is the same as for Walker's model [9]. Steady state hysteresis loops at different strain rates under fully reversed strain controlled conditions as shown previously in Fig. 6 (p. 30) are required. These are all performed until saturated values are established. Also required are stress drop creep and relaxation tests from initial point on a steady state hysteresis loop. All constants are a function of temperature and require the above tests to be performed at all temperatures of interest unless interpolation is used.

For comparative purposes, a brief description of the experimental data requirements for several other constitutive models is presented.

The first tests required by Krieg, et al. [11] are stress-drop tests during steady state creep. This means that a fraction of the applied stress is removed rapidly, and then this reduced stress is held constant until the accrued strain is sufficient to permit the strain rate immediately after the drop to be obtained by extrapolation. The stress is then increased to its original value to re-establish steady state creep. This procedure allows the response of a specimen to drop tests of various magnitudes to be obtained from a single creep stress. For full characterization, this test procedure must be repeated at several nominal creep stress levels and temperatures. Steady state and primary creep data must also be utilized.

Miller [16] states that with a general purpose constitutive equation a fairly wide variety of data is required. Calculation of a complete set of material constants for an alloy on which hysteresis loop data are available can be a very lengthy task with a substantial

amount of experimentation required for his model.

The characterization of model parameters for the theory of Bodner, et al. [15] requires two monotonic stress-strain curves at different steady strain rates. For cyclic loading an additional constant is required, but determination of that constant is unclear in their presentation.

Construction of Yield Surface Size and Stress vs. Equivalent Uniaxial Plastic Strain Diagrams

Calculation of the yield surface size and equivalent uniaxial stress is accomplished by constructing K and $\bar{\sigma}$ vs. $\bar{\epsilon}^P$ diagrams and interpolating on these diagrams at known values of $\bar{\epsilon}^P$ and T . From a piecewise linear representation of a "zero time" stress-strain curve, the equivalent uniaxial plastic strain is given by

$$\bar{\epsilon}_i^P = \epsilon_{x_i} - \sigma_{x_i} / E \quad (39)$$

The yield surface size and equivalent uniaxial stress are given by

$$K_i = \sigma_y + \beta(\sigma_{x_i} - \sigma_y) \quad (40)$$

$$\bar{\sigma}_i = \sigma_{x_i} \quad (41)$$

where σ_y represents the yield stress.

For the revised hardening law, two each of the above diagrams are required. The first diagrams for each case (K and $\bar{\sigma}$) will be labeled base diagram and are simply the functions calculated from equations (39) - (41) for the input stress-strain curves. These change only if

the hardening ratio is a function of plastic strain. The second set or global diagrams evolve throughout the solution process. They are initialized to equal the base diagrams but are modified each time a load reversal which causes yielding occurs. The modification process consists of linking the base curves to the global curves at the values of $\bar{\epsilon}^P$, K and $\bar{\sigma}$ corresponding to the yield stress of interest. Inputting two stress-strain curves at each temperature comes into play as their exists for example two K vs. $\bar{\epsilon}^P$ base diagrams at each input temperature. Factors such as type of material and load history determine which base curve is linked to the global diagram. All program interpolation for calculation of model parameters is done on the global diagrams.

The above procedure is best explained by a figurative example. Using Fig. 7 (p. 33) as the input stress-strain curves, the K vs. $\bar{\epsilon}^P$ base diagram for a constant hardening ratio is shown at the top of Fig. 9. Recall that the "a" curves are the ones that result from reverse yielding while the "b" curves are from the virgin stress-strain curves. Note that the Allen and Haisler model uses only the "b" curves. A reverse yielding occurs at $\bar{\epsilon}^P = \epsilon_o^P$ causing the "b" curves to be linked to the global diagram as shown at the bottom of Fig. 9. When another reverse yielding takes place, either the "a" or "b" curves are linked to the global diagram at that particular value of $\bar{\epsilon}^P$. A similar procedure is carried out for the global $\bar{\sigma}$ vs. $\bar{\epsilon}^P$ diagram.

Computational Considerations

For completeness of the theoretical presentation, the gradients, transition step, thermal strain increment, and elastic strain

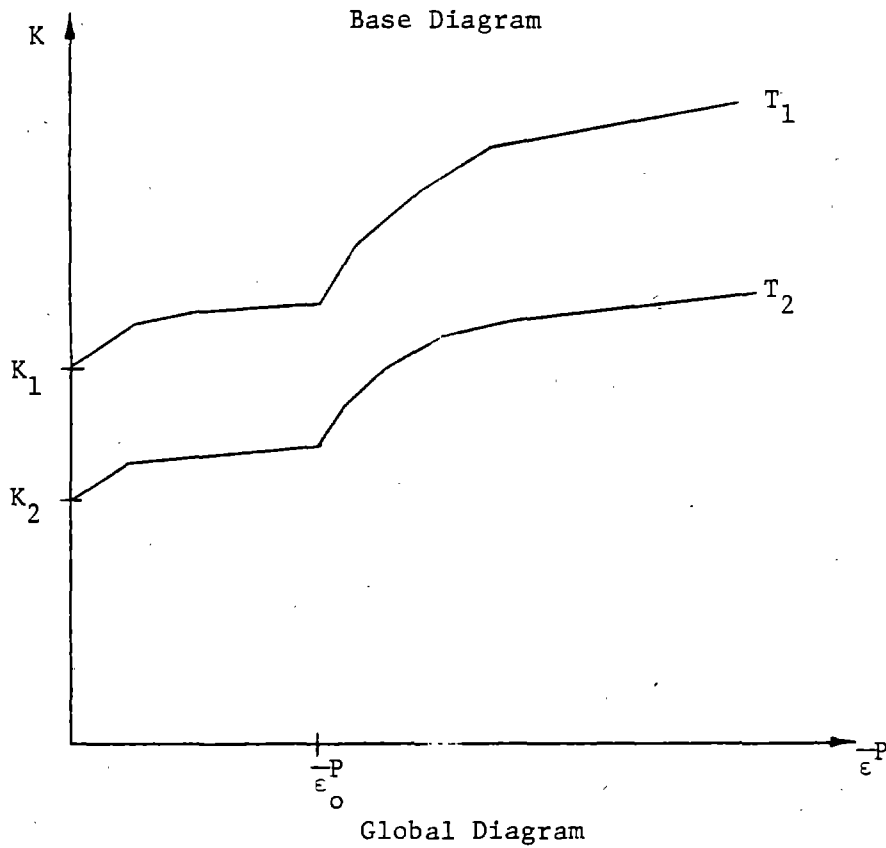
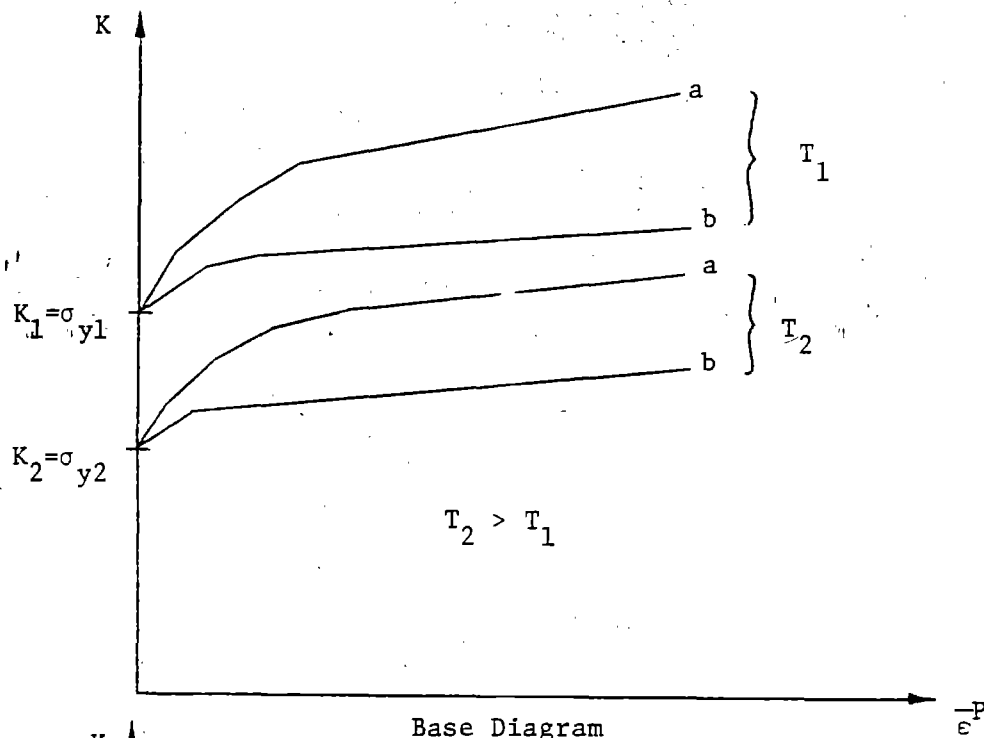


Fig. 9 Construction and evolution of K vs. $\frac{P}{\epsilon}$ diagrams

increment are all discussed below with regards to computational considerations. They are also presented by Allen [36].

Gradients. Linear interpolation is performed to compute values between input temperatures. The yield surface temperature gradient can be obtained by

$$\frac{\partial K}{\partial T} = \frac{K_H - K_L}{T_H - T_L} \quad (42)$$

where the subscripts H and L denote the values of a particular variable for the temperatures above and below the current temperature T.

Similarly

$$\frac{\partial \bar{\sigma}}{\partial T} = \frac{\bar{\sigma}_H - \bar{\sigma}_L}{T_H - T_L} \quad (43)$$

where the stress values are obtained from the $\bar{\sigma}$ vs. $\bar{\epsilon}^P$ diagram. The slope of the K vs. $\bar{\epsilon}^P$ diagram can be obtained by

$$\frac{\partial K}{\partial \bar{\epsilon}^P} = \left(\frac{\partial K}{\partial \bar{\epsilon}^P} \right)_H - \left\{ \left(\frac{\partial K}{\partial \bar{\epsilon}^P} \right)_H - \left(\frac{\partial K}{\partial \bar{\epsilon}^P} \right)_L \right\} \frac{(T_H - T)}{(T_H - T_L)} \quad (44)$$

and the slope of the $\bar{\sigma}$ vs. $\bar{\epsilon}^P$ diagram by

$$H' = (H')_H - \left\{ (H')_H - (H')_L \right\} \frac{(T_H - T)}{(T_H - T_L)} \quad (45)$$

Transition step. Special treatment must be given to the transition step from elastic to elastic-plastic behavior. The portion of the assumed elastic stress increment $d\sigma$ which will cause yielding is $\zeta d\sigma$ and the strain increment to bring the total strain to the

yield surface is ndc. Thus for the transition step, the stress and strain status are modified to become

$$\sigma \rightarrow \sigma + \zeta d\hat{\sigma} \quad (46)$$

$$\varepsilon \rightarrow \varepsilon + nd\varepsilon \quad (47)$$

where

$$\zeta = \frac{-B + \sqrt{B^2 - 4AC}}{2A} \quad (48)$$

$$A = d\hat{\sigma}d\hat{\sigma}$$

$$B = 2(\sigma - \alpha)d\hat{\sigma} \quad (49)$$

$$C = (\sigma - \alpha)(\sigma - \alpha) - (K^{t+\Delta t})^2$$

$$\eta = \frac{\sigma^t + \zeta d\hat{\sigma} - E^{t+\Delta t} \varepsilon^t}{E^{t+\Delta t} d\varepsilon^t} \quad (50)$$

The above equations are presented here for completeness of the theory.

A full derivation of them is given by Allen [12].

Thermal and elastic strain increments. The thermal strain increment is given by [36]

$$d\varepsilon^T = \alpha_T^{t+\Delta t} (T_{t_2} - T_R) - \alpha_T^t (T_{t_1} - T_R), \quad (51)$$

where $\alpha_T^{t+\Delta t}$ and α_T^t are the coefficients of thermal expansion at the beginning and end of a load step respectively, T_{t_1} and T_{t_2} are the temperatures at the beginning and end of a load step respectively, and T_R is the reference temperature for the unstrained state.

The elastic strain increment is calculated by [36]

$$d\epsilon^E = \frac{1}{E^{t+\Delta t}} \{d\sigma - dE(\epsilon^t - \epsilon^{P^t} - \epsilon^{C^t} - \epsilon^{T^t})\} \quad (52)$$

Extension to Multiaxial Theory

The approach used to derive the uniaxial constitutive equations makes it very simple to extend them to the multiaxial case. For example, equation (29) could be simplified considerably by, for instance, dividing out terms like $\partial F/\partial \sigma$. This is not done, however, to retain generality and ease of extension to the multiaxial case. To convert equation (29) to a three dimensional form simply let uniaxial values of stress and strain become the respective stress and strain tensors. Recall the yield function is stated in terms of principal stresses in equation (33). The general elastic constitutive matrix is then substituted for the elastic modulus.

Gradients are still determined from uniaxial input stress-strain data, in fact the only additional experimental data required is Poisson's ratio. The equivalent uniaxial plastic strain is

$$d\bar{\epsilon}^P = \frac{2}{3} d\epsilon_{ij}^P d\epsilon_{ij}^P \quad (53)$$

in tensor notation. In engineering notation this equation can be written as

$$d\bar{\epsilon}^P = \left\{ \frac{2}{9} [(d\epsilon_x^P - d\epsilon_y^P)^2 + (d\epsilon_y^P - d\epsilon_z^P)^2 + (d\epsilon_z^P - d\epsilon_x^P)^2 + 6(d\epsilon_{xy}^P)^2 + 6(d\epsilon_{xz}^P)^2 + 6(d\epsilon_{yz}^P)^2] \right\}^{1/2} \quad (54)$$

A full derivation of the multiaxial theory is contained in reference [12].

CHAPTER IV

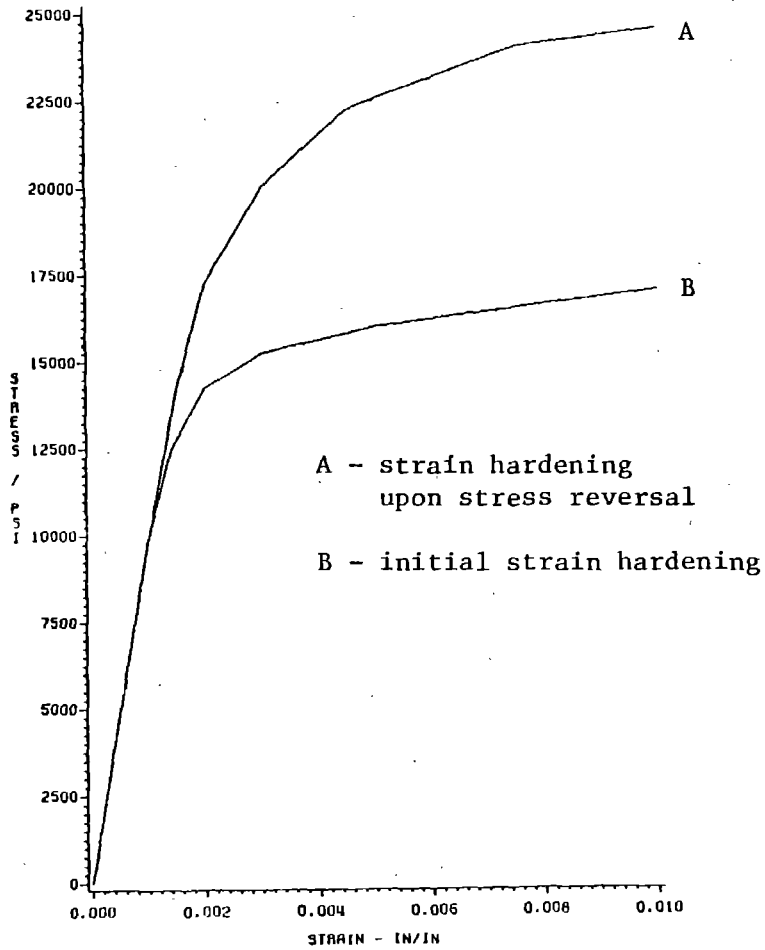
EVALUATION OF THE MODEL

Evaluation of the constitutive model detailed in this thesis is now performed. A section on theoretical model capabilities is presented followed by evaluation against experiment.

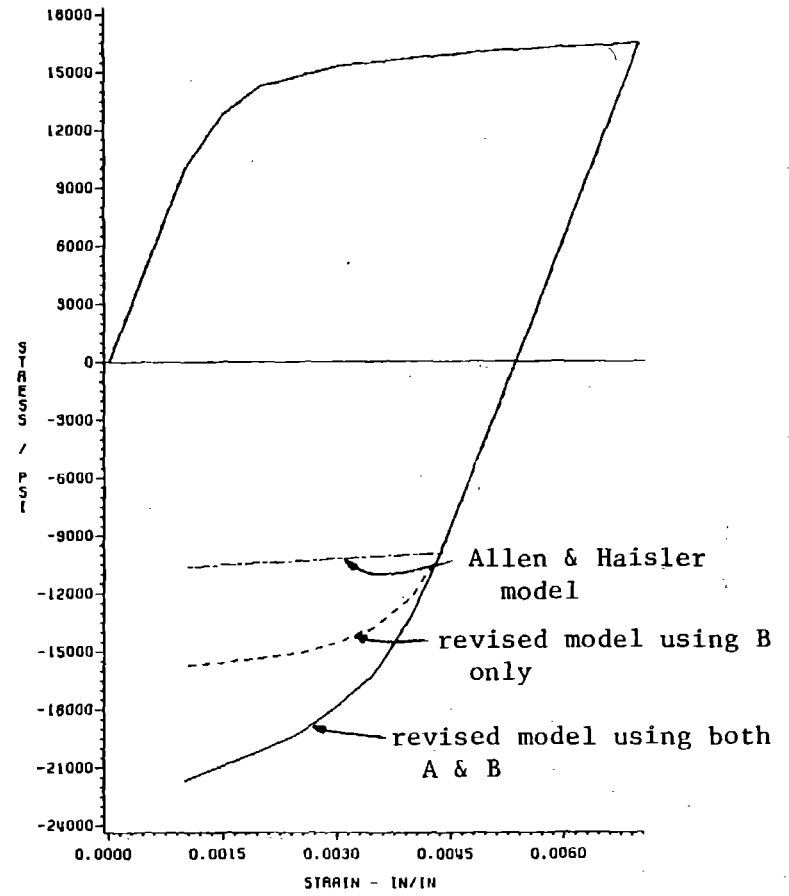
Theoretical Model Capabilities

Several examples of the capabilities of the model proposed by Allen and Haisler are given in references [36] for the uniaxial case and [12] for the multiaxial case. The purpose of the following examples is to demonstrate the improvements in the revised model by using theoretical illustrations of experimentally observed behavior.

Example 1 - Change of strain hardening with stress reversal. The revised model has the ability to reproduce strain hardening behavior that is dependent on direction of yielding. Fig. 10 illustrates the input stress-strain curves for a theoretical single cycle reverse load test. The input can be taken from either first or saturated cycle data. On the input diagram curve B represents the initial strain hardening behavior while curve A represents the high rate of strain hardening seen upon stress reversal. If a single cycle reverse load test is performed with this theoretical data, the results will be similar to those shown as output in Fig. 10. The revised model using curves A and B is a much more realistic representation of actually observed experimental behavior for many metals than the combined hardening rule of Allen and Haisler. Even the revised model



Input (Isothermal)



Output

Fig. 10 Change of strain hardening with stress reversal

representation using only curve B is an improvement over existing hardening rules which "square-off" the behavior upon reyield.

Example 2 - Cyclic saturation. A hypothetical fully reversed cyclic strain history of $\pm 0.25\%$ strain was considered using four different values for the hardening ratio. The values used are shown in Fig. 11 following the discussion on hardening rules in Chapter III. An allowance for cyclic saturation is made by letting β be a function of plastic strain. This corresponds physically to allowing the yield surface to first translate and expand and then gradually saturate to a constant size as observed in experiment. Input stress-strain data is the same as the first one-quarter cycle input.

The results for isotropic and kinematic hardening are shown in Fig. 12. Kinematic hardening will model the limiting periodic response, but there is no cyclic hardening of the material in achieving the saturated hysteresis loop. Conversely, isotropic hardening predicts that the material will eventually cycle to a limiting purely elastic response as the yield surface expands without bound. This same behavior is also predicted by a combined hardening law using a constant hardening ratio. It takes somewhat longer to cycle to the elastic response because of the component of kinematic hardening present. This is shown in Fig. 13.

Successful modelling of cyclic saturation is accomplished by letting the hardening ratio in the combined hardening law be a function of plastic strain. For this example, the linear relationship shown in Fig. 11 was assumed with results as shown in Fig. 13. Both the cyclic hardening and limiting periodic responses are depicted.

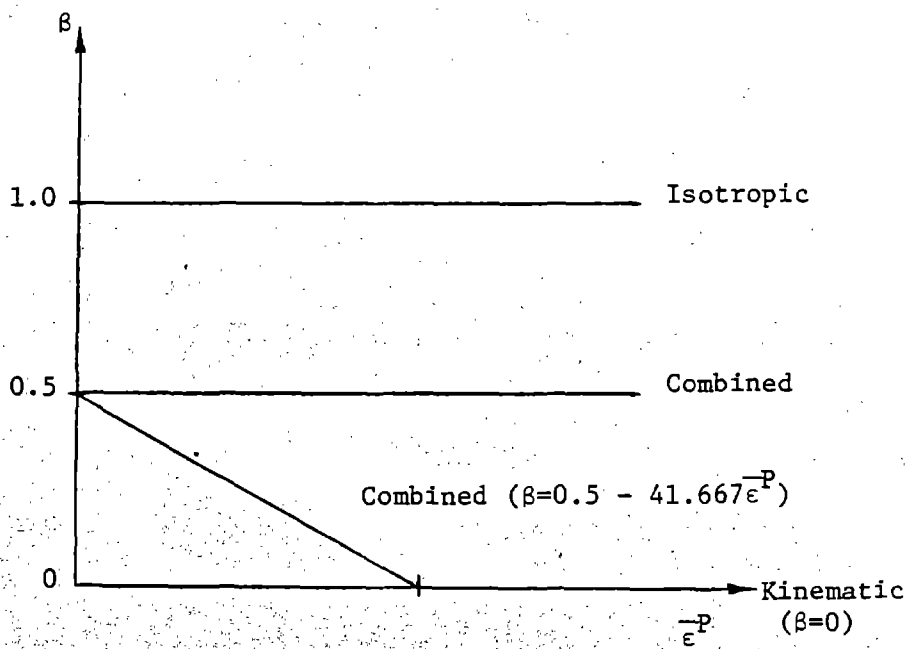
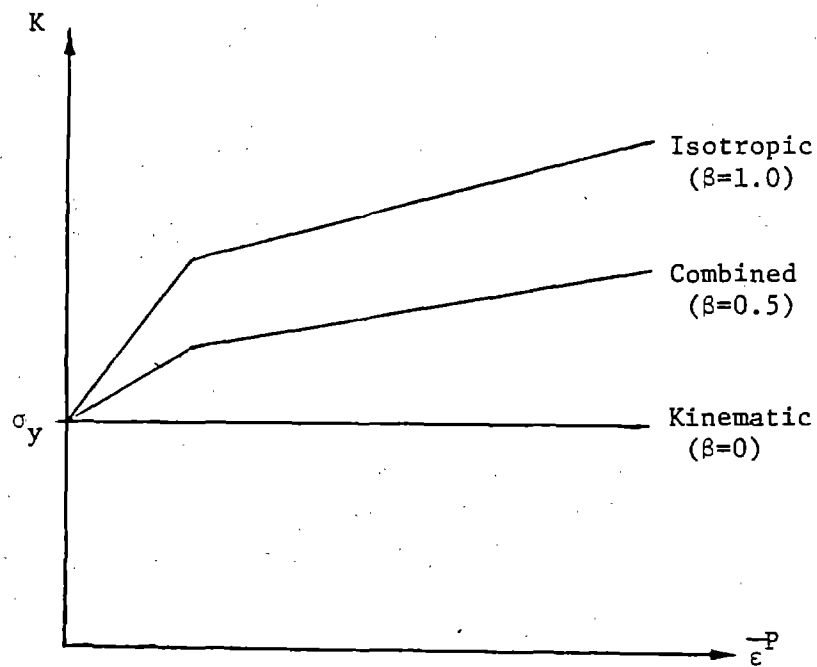
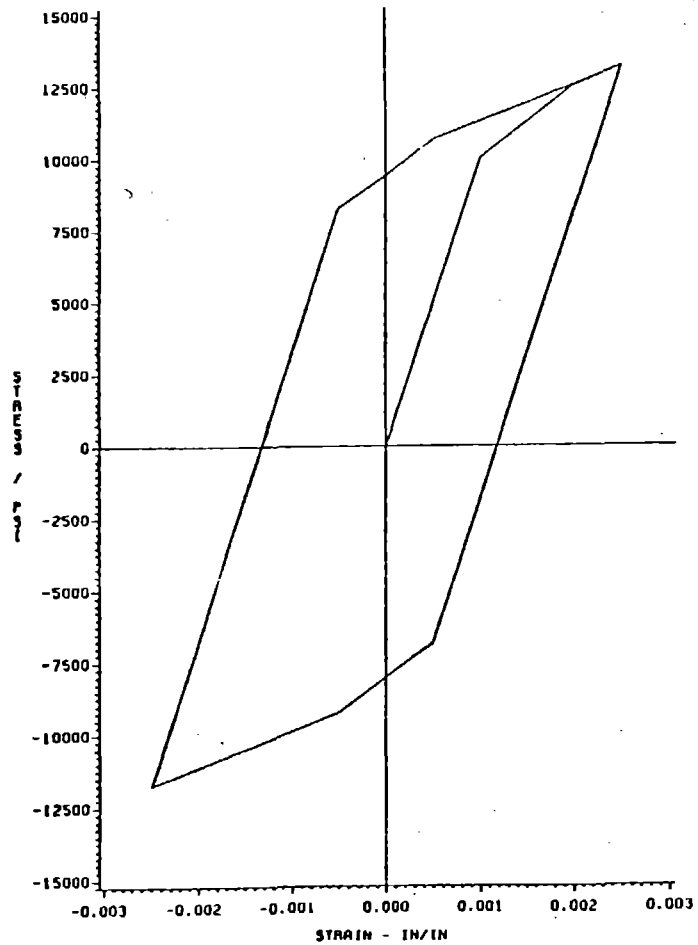
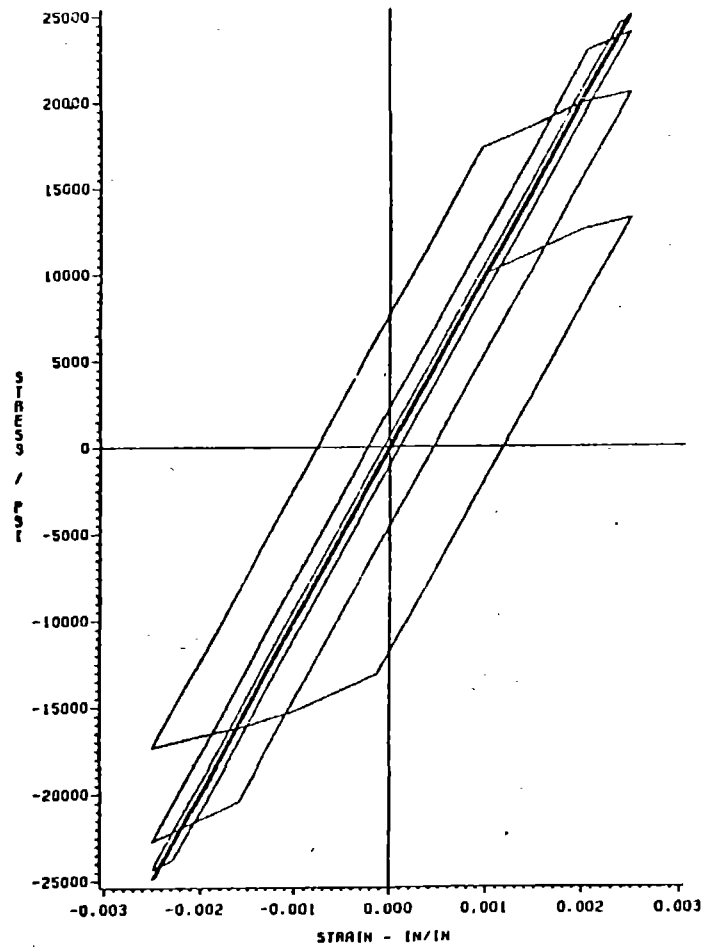


Fig. 11 Hardening rules used in Example 2

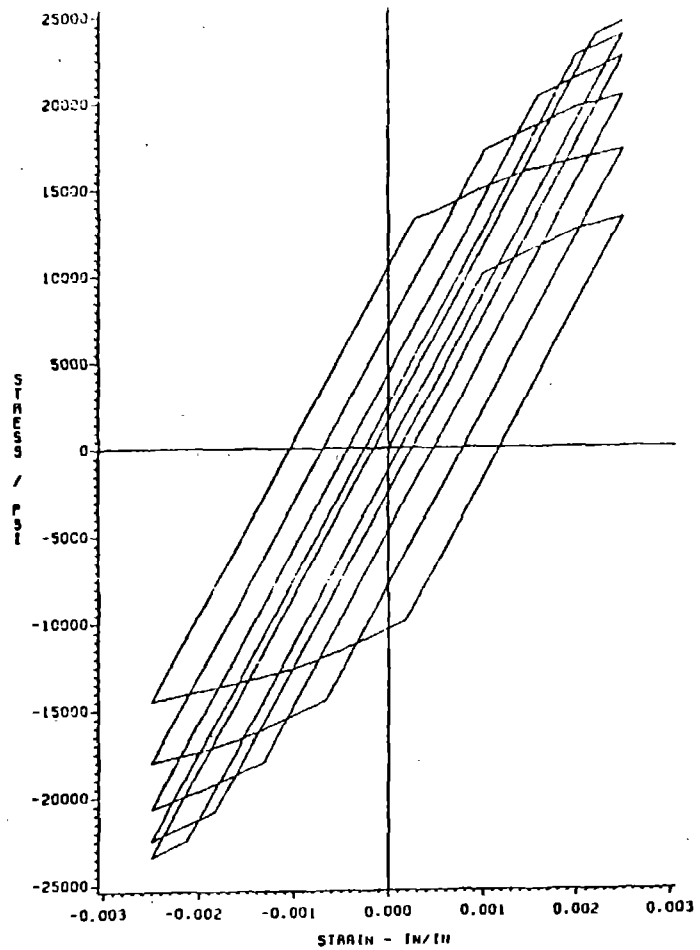


Kinematic Hardening

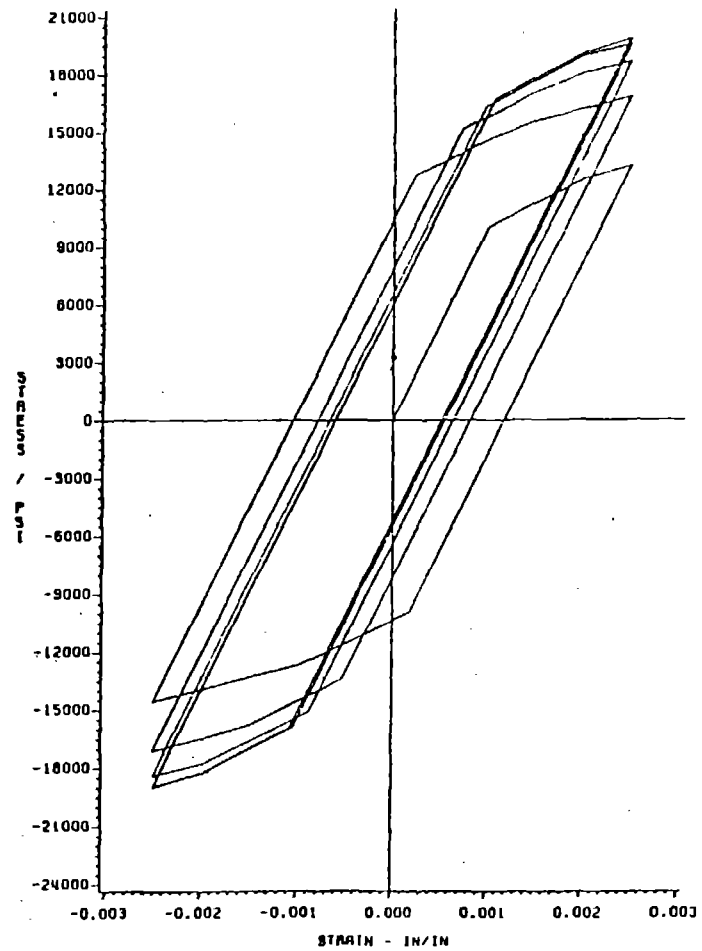


Isotropic Hardening

Fig. 12 Modeling of cyclic saturation using kinematic and isotropic hardening laws



Combined hardening with β constant



Combined hardening with β a function of plastic strain

Fig. 13 Modeling of cyclic saturation using combined hardening law

Example 3 - Cyclic thermomechanical loading. This example is similar to one in reference [25] but is still applicable here to show the increased capabilities of the revised model in predicting the strain hardening behavior and also in reiterating its nonisothermal aspects. Depicted in Fig. 14 are the input stress-strain curves and thermomechanical load history for a hypothetical test. Note that these curves do not include the capacity for variable hardening in order to maintain clarity of the example. The hardening ratio is a constant one-half.

Results from the constitutive model are shown in Fig. 15 where t_i in this figure corresponds to t_i in Fig. 14. Modulus, strain hardening, and yield surface size changes with temperature are all shown.

It is also interesting to look at the resulting yield surface size vs. plastic strain diagram for this example also shown in Fig. 15. As discussed previously in construction of these diagrams, the curves are modified everytime there is a stress reversal which causes yield. This physically represents the rounded shape of the stress-strain curve after reverse yielding seen in experiment. In terms of modelling, this corresponds to "linking" the original K vs. $\bar{\epsilon}^p$ curves onto the current global diagram also explained in the section on construction of these diagrams. The squares in Fig. 15 point out where this process takes place each time. The curves at each temperature are modified for linear interpolation purposes.

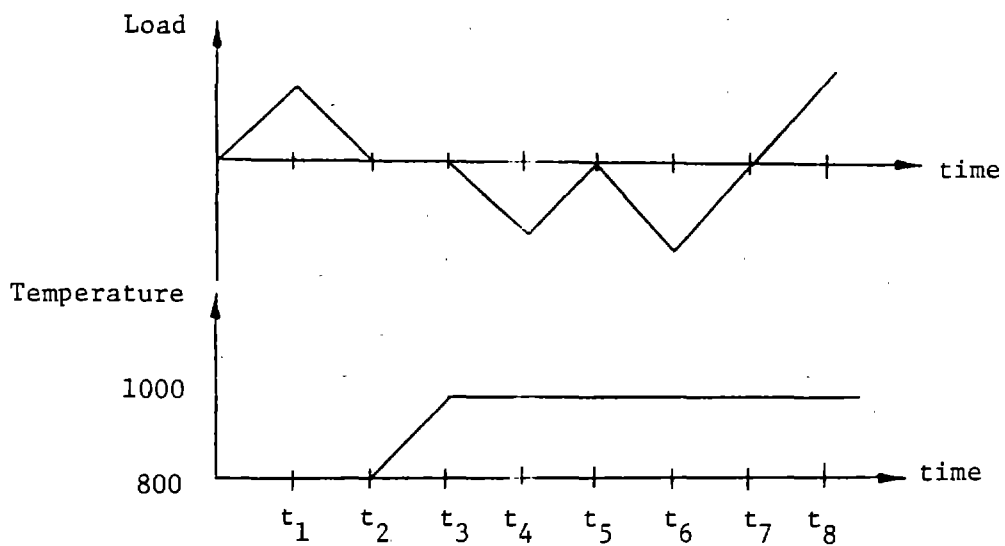
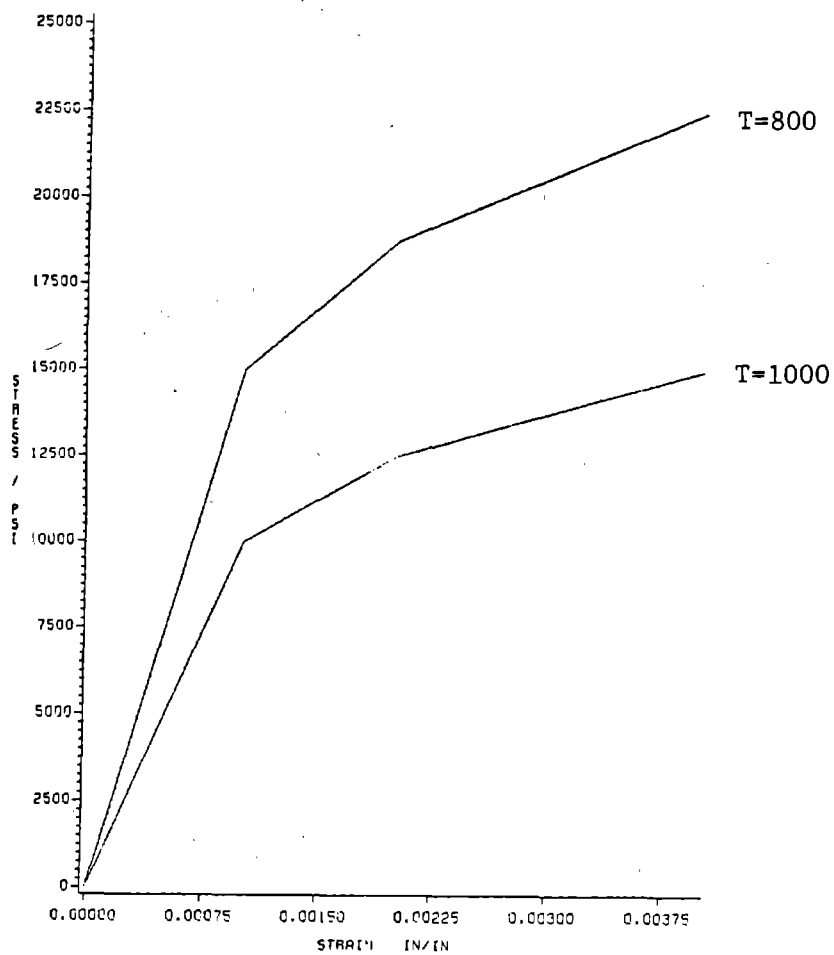


Fig. 14 Input for Example 3

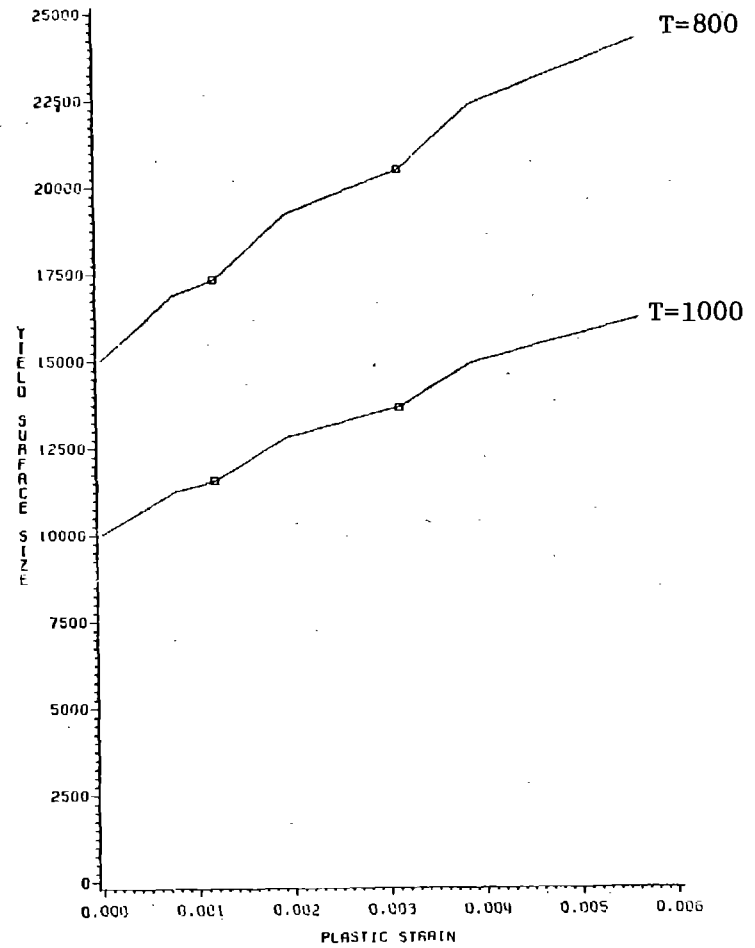
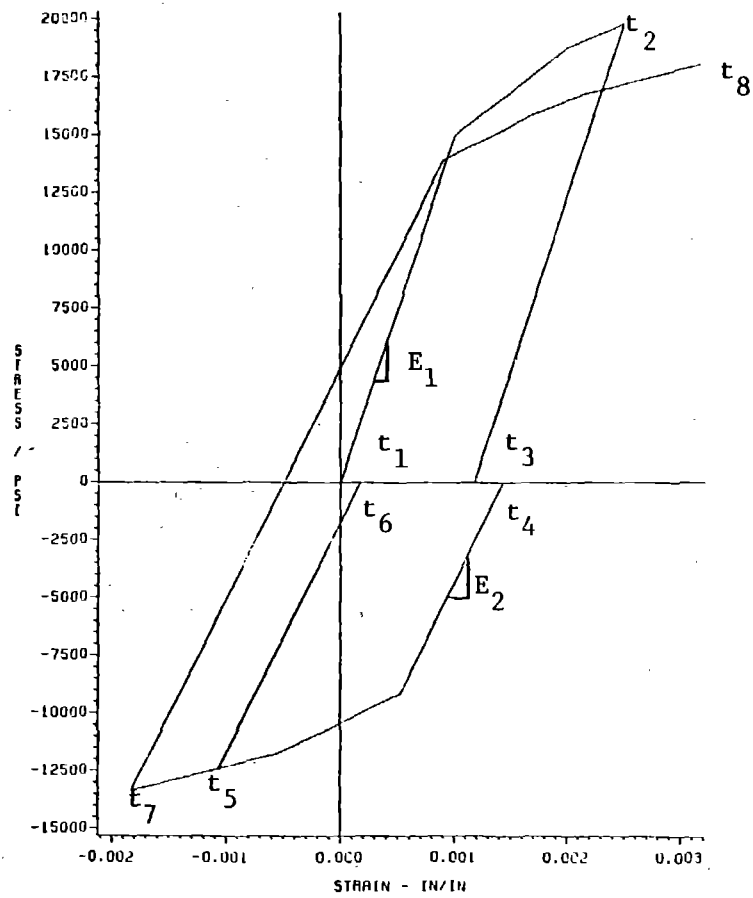


Fig. 15 Cyclic thermomechanical loading

Comparison with Experiment

As discussed earlier, characteristics of metals such as the high rate of strain hardening upon yield reversal are much more pronounced at high strain rates and temperatures below one-half the melting point. Modelling of this phenomenon is less critical at more elevated temperatures where plastic deformation is more fully rate controlled. More importantly, there is an intermediate temperature range where the coupling of plasticity and rate effects is the most critical test of the constitutive model. To evaluate the models capabilities in all of these environments, specific areas of testing are: (1) elevated temperature tests that evaluate the rate independent capabilities of the model, (2) cyclic load tests that evaluate the modelling of the Bauschinger effect, the change in strain hardening upon stress reversal, yield surface evolution, and cyclic saturation, (3) transient temperatures tests that evaluate the modelling of thermally dependent material properties, (4) high temperature tests that evaluate the rate dependent capabilities of the model, and (5) thermoelastic-plastic-creep tests that evaluate the capabilities in the intermediate temperature range.

The high temperature materials testing laboratory in the mechanical engineering department of Texas A&M University was used to run all tests. A Mechanical Testing Systems (MTS) machine along with an induction heating coils and generator, optical and thermocouple type temperature controllers, high temperature tension-compression grips, a high temperature diametral strain extensometer, and constant stress creep frames fully outfitted for high temperature testing are the main components available in this lab.

Cyclic thermomechanical load test on 5086 aluminum alloy. The first experimental evaluation is for a thermomechanical load history applied to a 5086 aluminum alloy. This test is very similar to Example 3. Fig. 16 shows the results of comparing the Allen and Haisler model using several different constant hardening ratios to experiment. One can observe both of the shortcomings of the model discussed earlier. The theoretical strain hardening behavior upon reyield is much too flat or square and the cyclic hardening predictions are inadequate. By inputting a second stress strain curve to characterize the more rounded strain hardening behavior and making the hardening ratio a function of plastic strain as in the revised model, this experiment can be modeled very well. The actual function of plastic strain used for β is that $\beta=0.45$ (constant) for the first quarter cycle and since the isotropic component of the yield surface saturated very quickly in the observed experimental results, the second quarter cycle was treated as being kinematic in nature. These results are shown in Fig. 17.

Cyclic loading of 304 stainless steel at 1000°F. Several other model features are demonstrated by this test. As seen in Fig. 18, the compressive strain hardening behavior in the first cycle is more rounded in shape than the tensile behavior. It is believed that the same behavior would be seen on the first and second quarter cycles if compression preceded tension. Unlike the previous test on aluminum, this difference seems to alternate throughout all four cycles presented in Fig. 18. Thus one must alternate between first quarter and second quarter cycle input stress-strain data to model this test well.

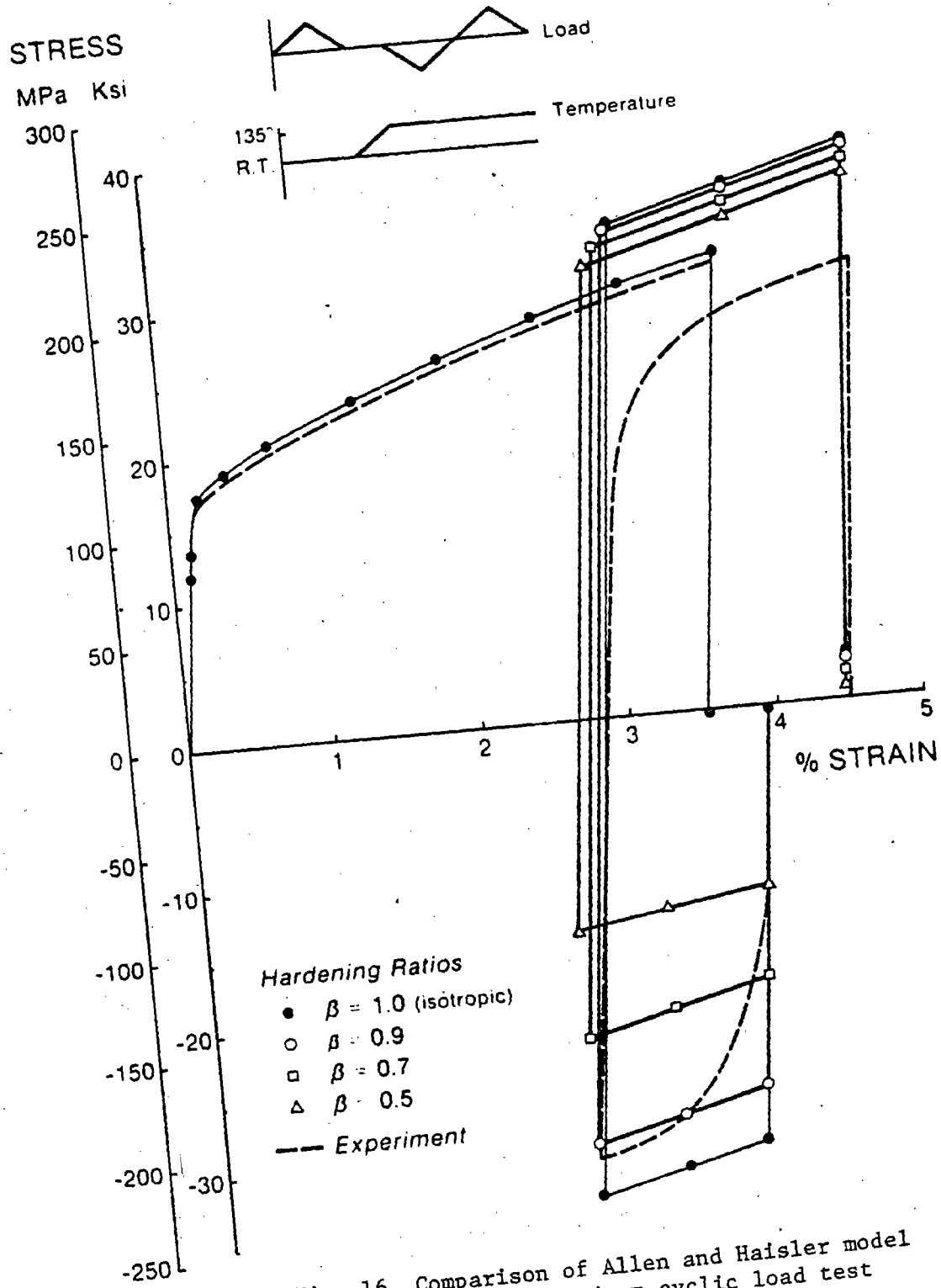


Fig. 16 Comparison of Allen and Haisler model to experiment for aluminum cyclic load test

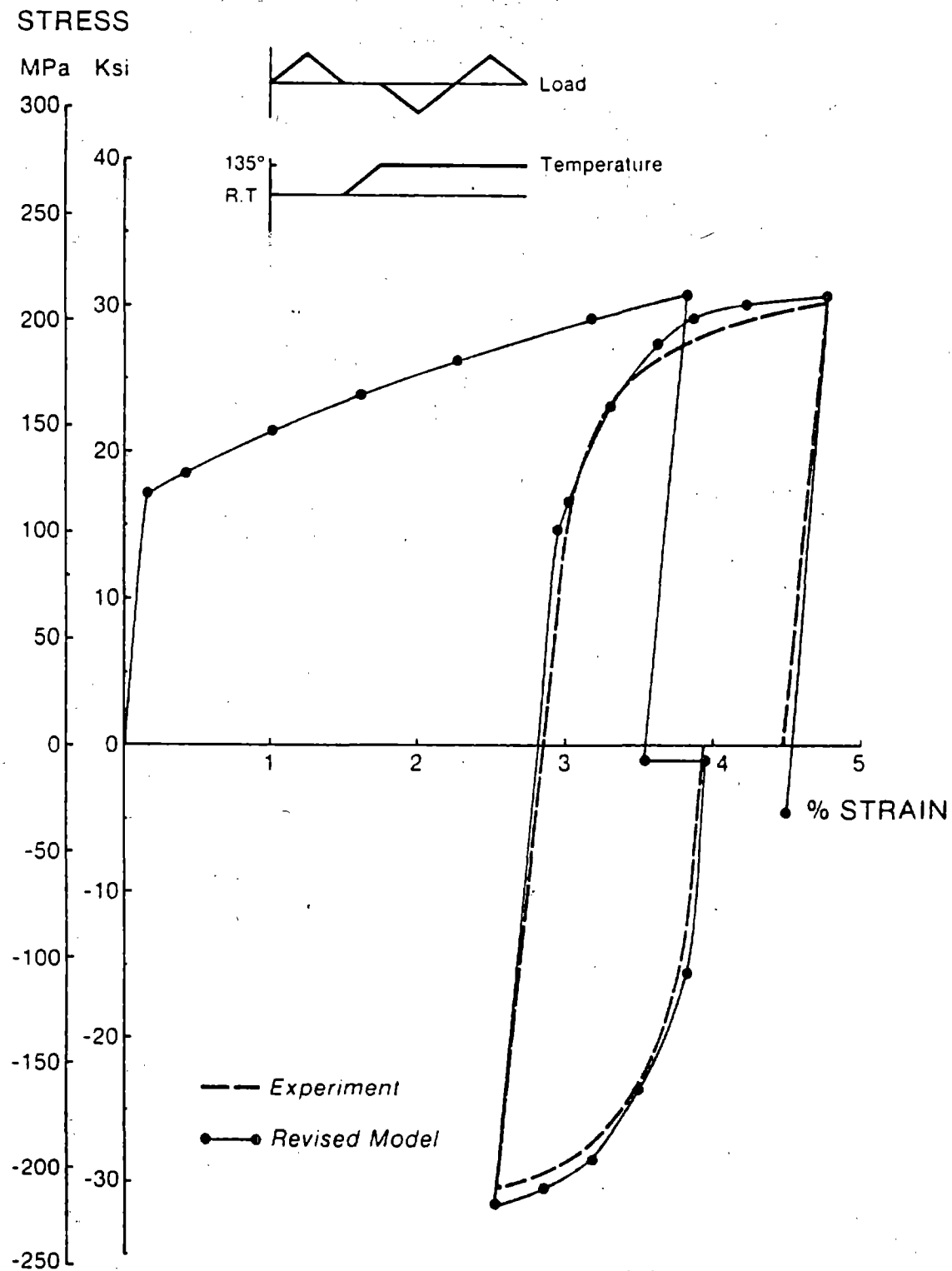


Fig. 17 Comparison of revised model to experiment for aluminum cyclic load test

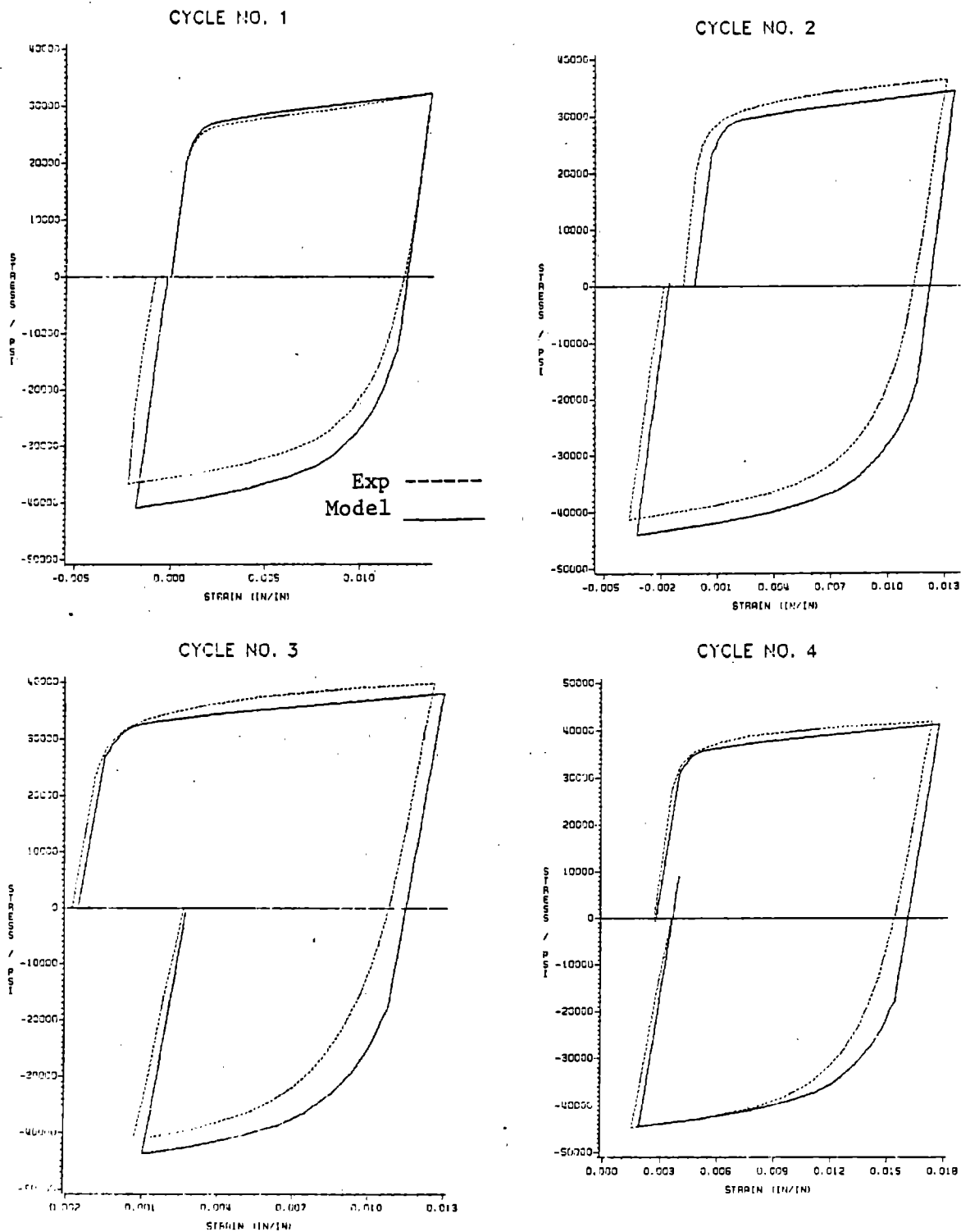


Fig. 18 Comparison of model and experiment for 304 stainless steel at 1000°F using first cycle data as input. A hardening ratio of 0.2 in tension and 0.35 in compression was used

One possible explanation for this alternating strain hardening behavior could be that the initial yield sets up an asymmetric microstructure. This phenomenon could also be explained by reasoning that there is less resistance to grain boundary sliding in tension as compared to compression. It is clear that a similar test needs to be performed with the initial yield in compression and then alternating tension and compression.

Next, the ability to vary the hardening ratio between alternating quarter cycles is demonstrated. In addition, Fig. 19 shows the results of using fourth cycle data as input. Both Fig. 18 and Fig. 19 show good correlation of the model with experiment. An interesting observation is that the elastic modulus during unloading decreases slightly in the experimental results. This is not taken into account by the constitutive model and is the reason for most of the discrepancy between experiment and model predictions.

Cyclic saturation of hastelloy-X. In Chapter 3, there was a discussion concerning cyclic saturation. Recall that cyclic saturation is the limiting periodic response in which the stress-strain curve for each consecutive cycle is the same as shown in Fig. 5 (p. 28). Although most materials show a gradual hardening during this saturation process, some materials may cyclically soften. Microphysically this corresponds to the movement of dislocations from a random orientation into a cell structure which stabilizes their movement. This results in the limiting response of the material. At more elevated temperatures, the saturation effect naturally becomes faster as the mobility of the dislocation increases with increasing temperature. Hastelloy-X

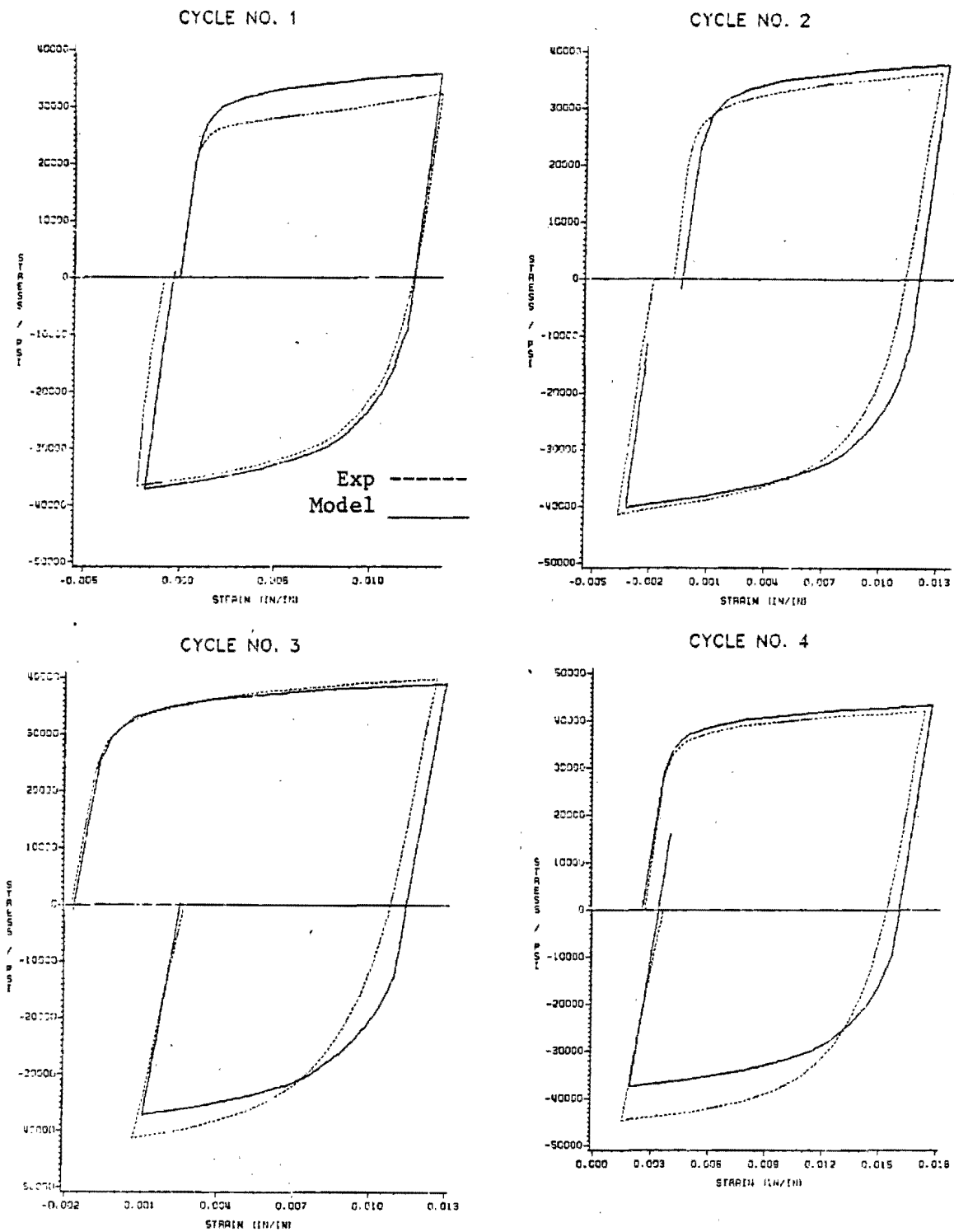


Fig. 19 Comparison of model and experiment for 304 stainless steel at 1000°F using fourth cycle data as input. A hardening ratio of 0.15 in tension and 0.28 in compression was used

displays cyclic saturation as shown in Figs. 20-25. These curves are actual experimental results of load vs. diameter change from the MTS machine. The abrupt drops in stress at various points are not due to machine problems but are rather due to dynamic strain aging of the material.

The center diagram in Fig. 20 shows the cyclic saturation discussed above. Uniaxial specimens were cycled under strain control (diametral strain) between equal tension and compression strain ranges until saturation occurred. In order to observe strain rate effects, most tests were run at three rates corresponding to test times of 10, 30, and 300 seconds per quarter cycle. During the test the diameter change rate was constant so that actual axial strain rate was variable during the cycle; however, the above test times correspond to average axial strain rates of 1.1×10^{-3} , 3.67×10^{-4} , and 3.67×10^{-5} in/in/sec. These rates were chosen because they are typical of strain rates seen under normal operating conditions of hot gas turbines. Notice that at room temperature, the rate dependent inelastic strain is negligible as the hysteresis loops do not change with different diameter change rates. Fig. 21 and Fig. 22 show the results for the same strain history at 500°F and 900°F, respectively. To define the rate dependent inelastic strain, a reference hysteresis loop is utilized as was outlined in Chapter 3. Comparing Figs. 22 and 23, it is seen that rate dependence of the saturated hysteresis loops is insignificant below 900°F for the rates considered. Consequently, the reference temperature is chosen as 900°F.

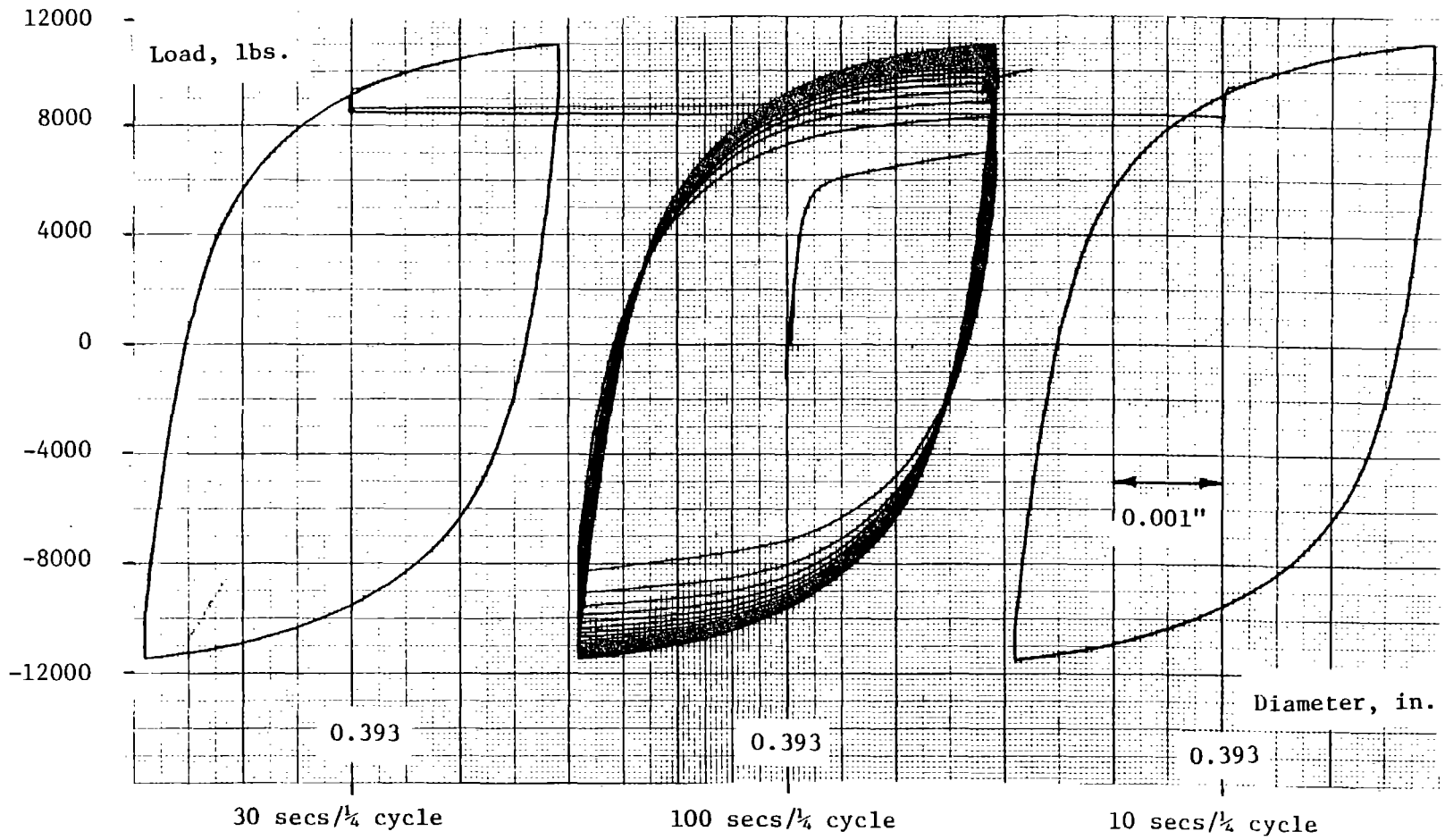


Fig. 20 Experimental hysteresis loops for hastelloy-X at room temperature

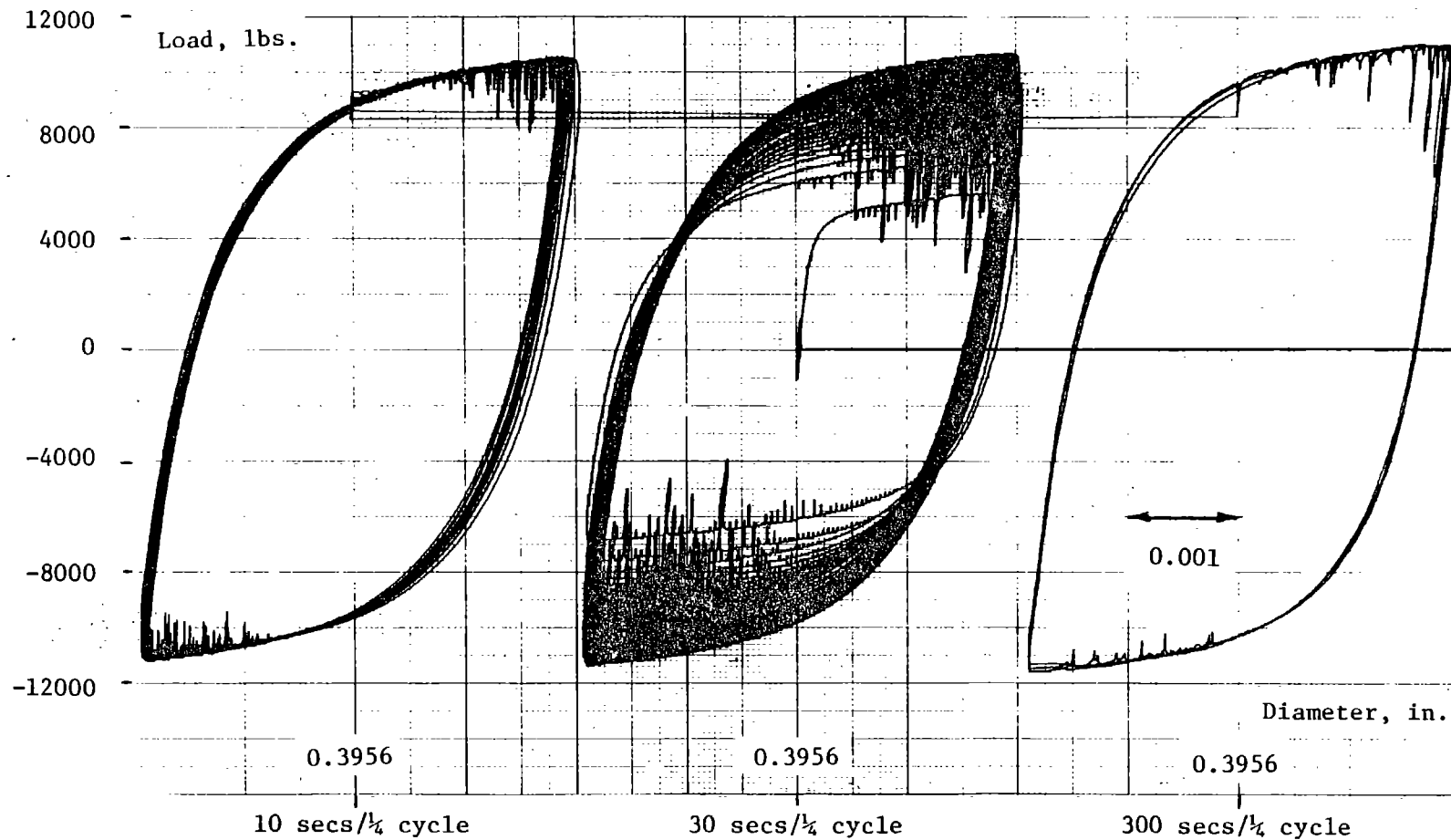


Fig. 21 Experimental hysteresis loops for hastelloy-X at 500°F

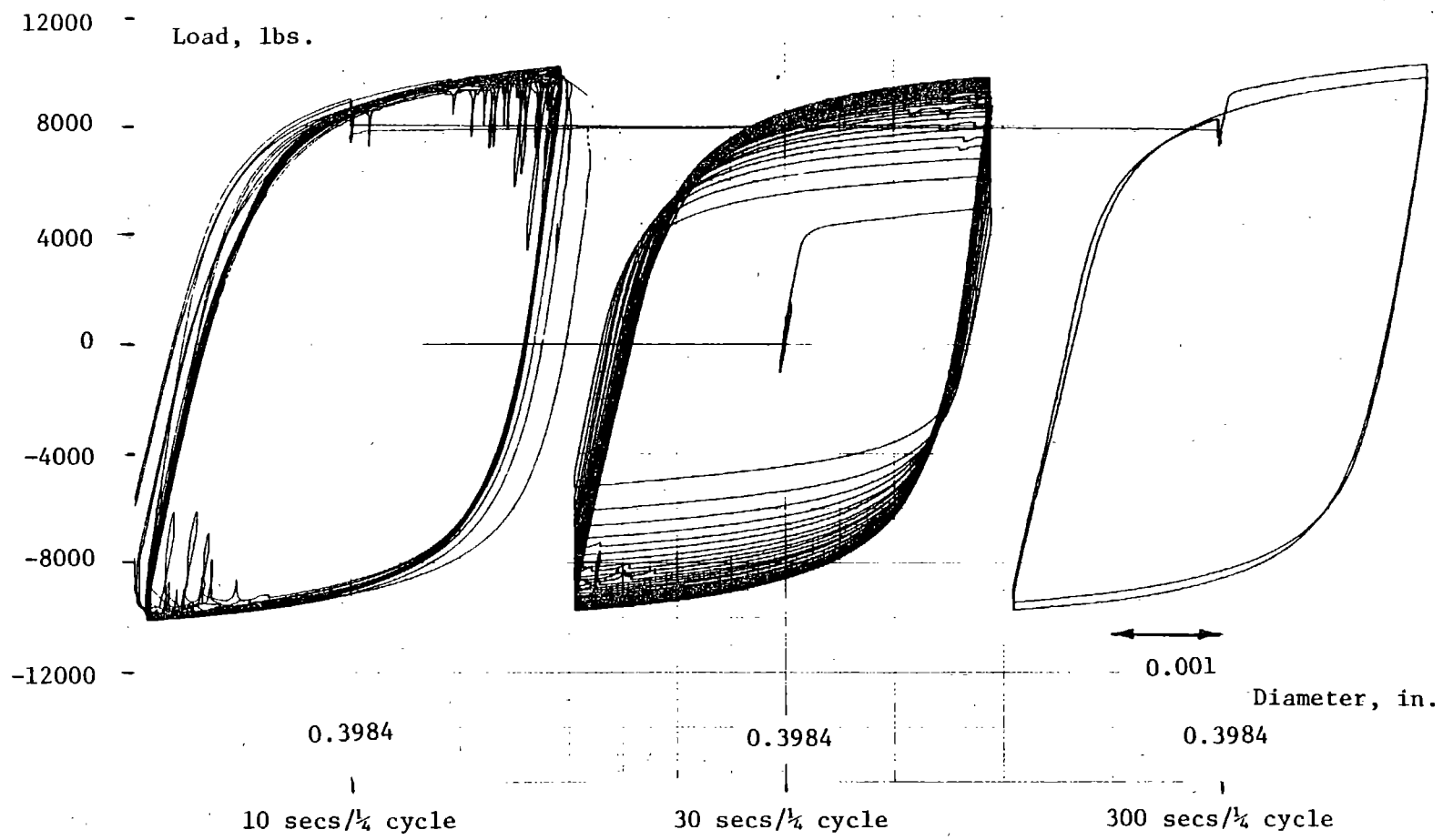


Fig. 22 Experimental hysteresis loops for hastelloy-X at 900°F

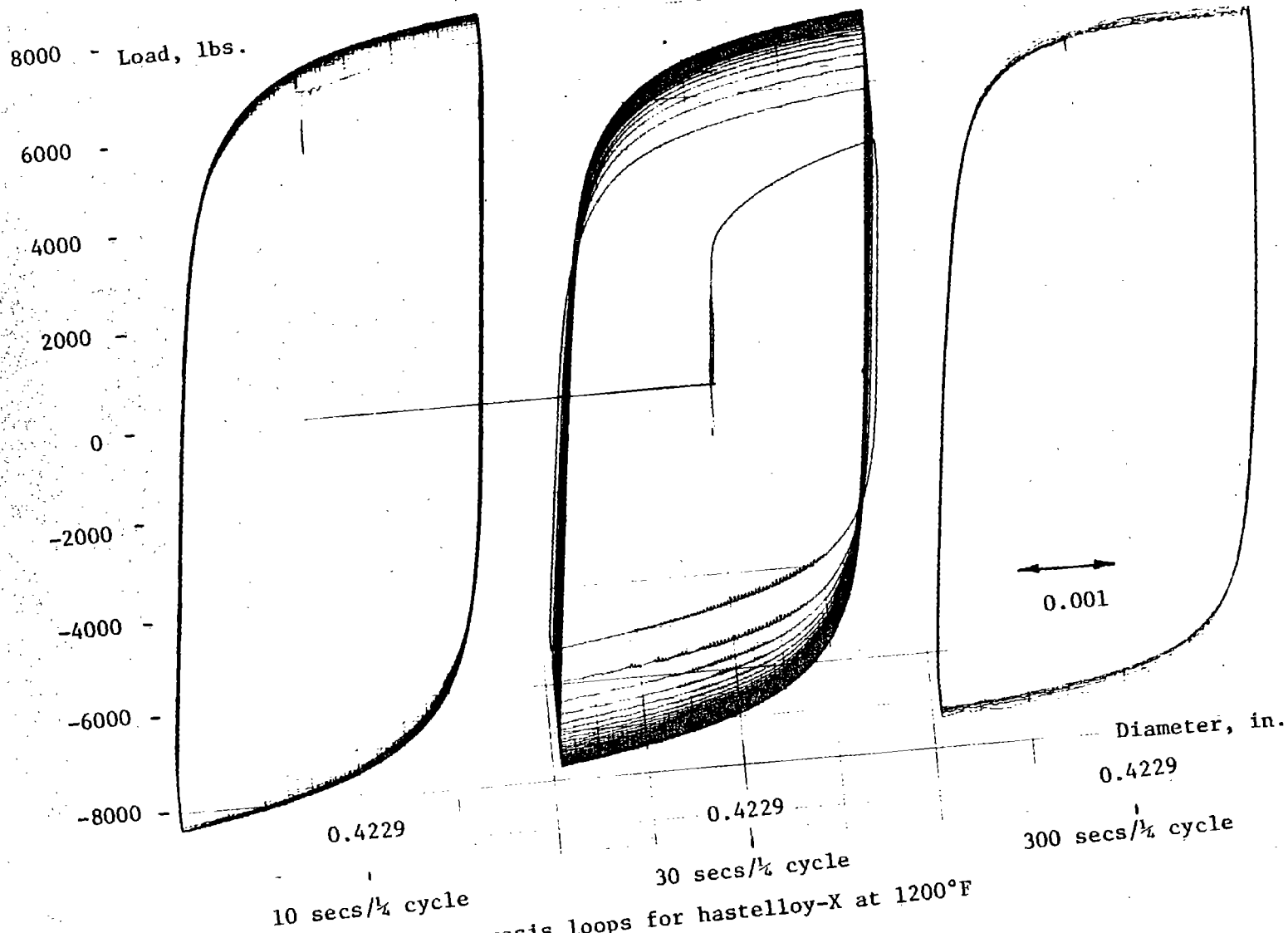


Fig. 23 Experimental hysteresis loops for hastelloy-X at 1200°F

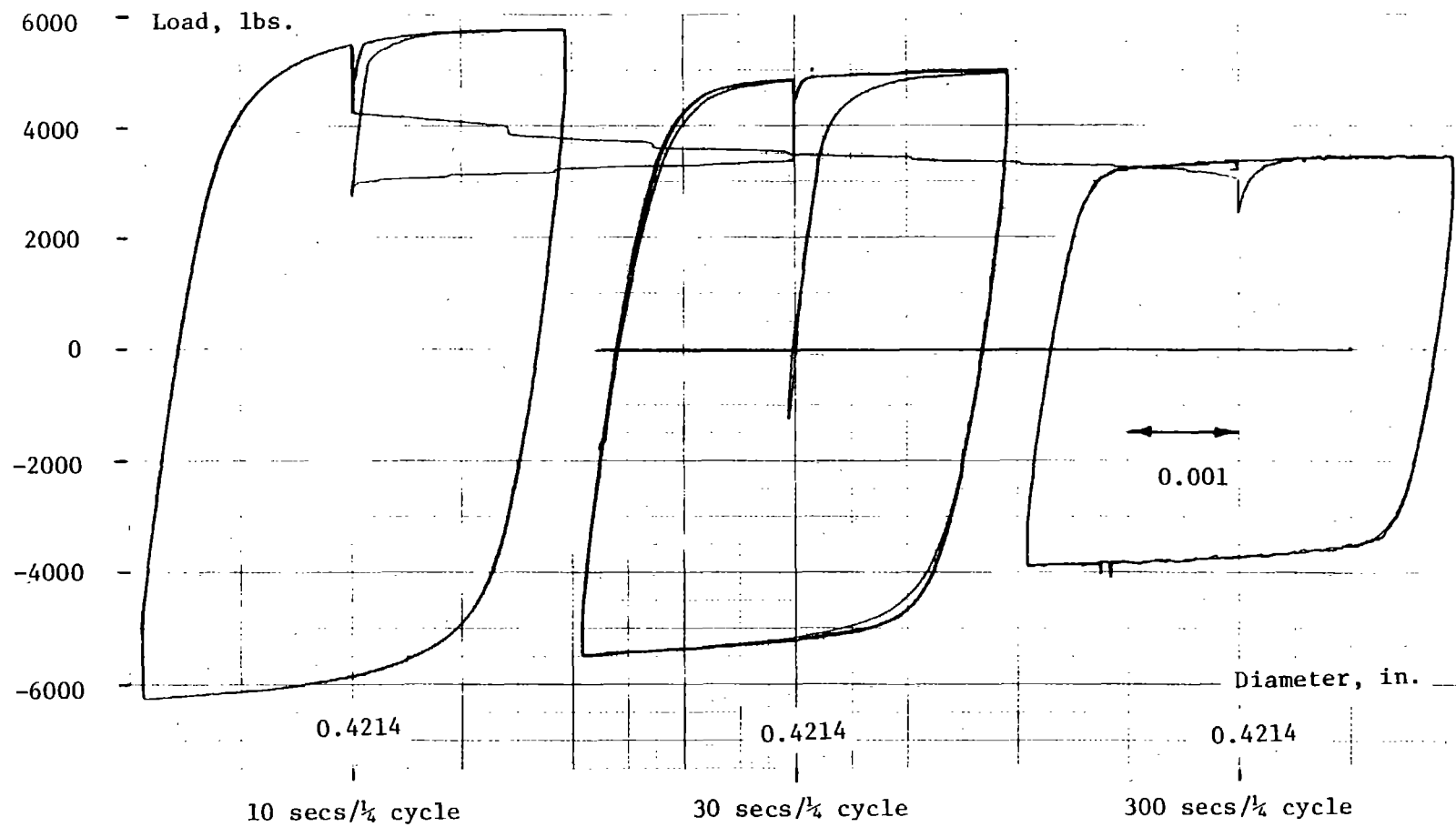


Fig. 24 Experimental hysteresis loops for hastelloy-X at 1400°F

An interesting phenomenon most clearly evident in Fig. 21 is the discontinuities or serrations seen in the curves. This is known as dynamic strain aging and is associated with interactions between moving dislocations and solute atoms [37]. Dynamic strain aging is both temperature and strain rate dependent.

At 1200°F, the rate dependent inelastic strain is no longer negligible. Fig. 23 shows the somewhat faster saturation and more "square" shape of the hysteresis loops. These effects are even more pronounced at 1400°F and 1600°F as depicted in Fig. 24 and Fig. 25. At these elevated temperatures the rate dependence dominates and can be modelled very well with an equation like equation (35). The hysteresis loops are quite square in nature, and a high rate of strain hardening upon stress reversal is not seen. A critical test of a constitutive theory would be in modelling the behavior in Fig. 23 where both rate independent plasticity and rate dependent creep are important.

Theoretical modelling of cyclic saturation of hastelloy-X was performed for the room temperature case. The results are shown in Fig. 26. Experimental stress-strain data is shown only for the first one-half cycle and the last (saturated) cycle. The model results depict the gradual saturation response as well as the limiting response. A hardening ratio of $\beta = -0.375\bar{\epsilon}^P + 0.075$ was used in tension and $\beta = -0.5\bar{\epsilon}^P + 0.10$ was used in compression. Notice that when the model predictions approach saturation, some fluctuation is seen on the compression side. This is thought to be due to increasing numerical error at this point as no equilibrium interations are performed. Most

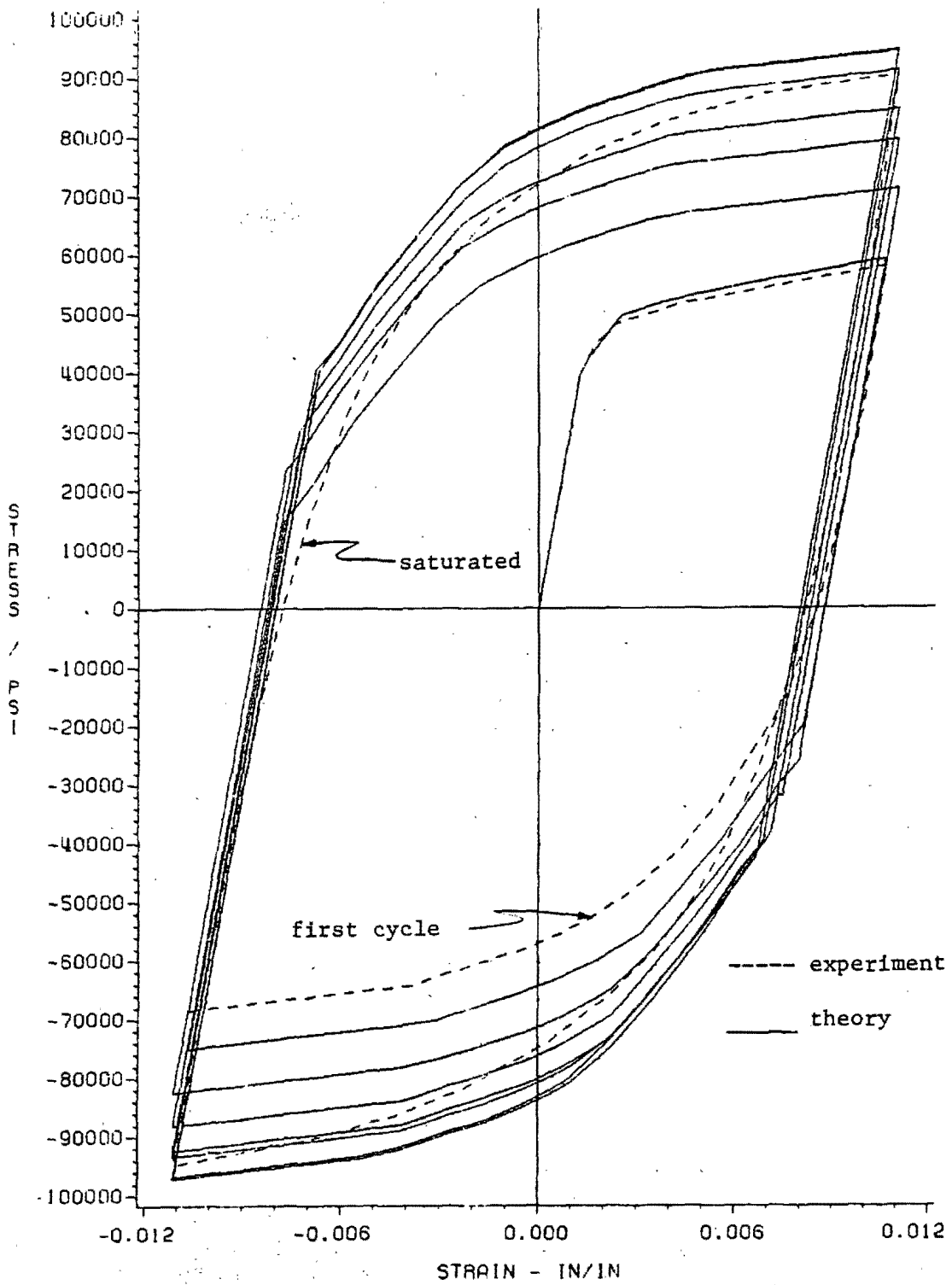


Fig. 26 Cyclic saturation of hastelloy-X at room temperature

of the difference in experiment and theory is due to difficulty in modeling of the second quarter cycle, otherwise the model predictions are quite good.

CHAPTER V

CONCLUSIONS

An uncoupled, incremental constitutive model for elastic-plastic behavior of metals at elevated temperatures has been presented. Revisions to the combined kinematic-isotropic hardening rule allow for much improved modelling of cyclic phenomenon. Also, an alternative approach to characterizing the rate dependent inelastic deformation has been proposed.

Successful evaluation of the constitutive model against experiment has been accomplished for a limited range of tests. The Bauschinger effect, change in strain hardening upon stress reversal, yield surface evolution, and cyclic saturation are all modeled well for the isothermal, rate independent case at elevated temperature. Unfortunately, no comparison of the theory to experiment have been performed at this time for the load and temperature ranges where rate dependence is a significant factor. The need to utilize an improved model like that presented herein depends on the application. For example, if the application is to life or fatigue predictions, then the detailed modelling of saturation and strain hardening observed at low temperatures may not be of utmost importance. The saturated hysteresis loop may be adequate to define long term fatigue response. Conversely, for low cycle applications, many researchers in this field are concerned with exact hysteresis loop predictions and the evolution to saturation. In this case, the improved model has important

applications. Finally, in regards to the rate dependence of the model, experimental results seem to indicate that the uncoupling presented in Chapter 3 gives acceptable predictions, but further tests are needed to verify the model.

REFERENCES

1. Tresca, H., "Notes on Yield of Solid Bodies Under Strong Pressure," Comptes Rendus del' Academie des Sciences, Vol. 59, 1864, p. 754.
2. Hill, R., The Mathematical Theory of Plasticity, Oxford University Press, London, 1950.
3. von Mises, R., "Mechanik der Festen Koerper in Plastisch Deformablen Zustant," Goettinger Nachr., Math-Phys. Kl., 1913, pp. 582-92.
4. Prandtl, L., "Spannungsverteilurg in Plastischen Koerper," Proceedings of the First International Congress on Applied Mechanics, Delft, Technische Boekhandel en Druckerij, Jr. Waltman, Jr., 1925, pp. 43-45.
5. Reuss, E., "Bereuchsichtigung der Elastischen Formaenderungen in der Plastizitaetstherie," Zeitschrift fuer Angewandte Mathematic und Mechanik, Vol. 10, 1930, pp. 266-274.
6. Drucker, D. C., "A Definition of Stable Inelastic Material," Journal of Applied Mechanics, Vol. XVII, 1959, pp. 55-65.
7. Prager, W., "The Theory of Plasticity: A Survey of Recent Achievements," Proceedings of the Institution of Mechanical Engineers, London, Vol. 169, 1955, pp. 41-57.
8. Ziegler, H., "A Modification of Prager's Hardening Rule," Quarterly of Applied Mechanics, Vol. XVII, 1959, pp. 55-65.
9. Walker, K. P., "Representation of Hastelloy-X Behavior at Elevated Temperature with a Functional Theory of Viscoplasticity," presented at ASME Pressure Vessels Conference, San Francisco, August 12, 1980.
10. Allen, David H., and Milly, Teresa M., "A Comparison of Constitutive Models for Nonlinear Rate Dependent Material Behavior of Solids," Virginia Polytechnic Institute and State University Report No. VPI-E-80.16, Blacksburg, Virginia, Sept. 1981.
11. Krieg, R. D., Swearingen, J. C., and Rohde, R. W., "A Physically-Based Internal Variable Model for Rate-Dependent Plasticity," Proceedings ASME/CSME PVP Conference, 1978, pp. 15-27.
12. Allen, David H., "A Model for Predicting Response of Nonlinear Materials Subjected to Thermomechanical Loading," Dissertation, Texas A&M University, Aug. 1980.
13. Hunsaker, B. Jr., "An Evaluation of Four Hardening Rules of the Incremental Theory of Plasticity," Thesis, Texas A&M University Dec. 1973.

14. Polakowski, N. H., and Ripling, E. J., Strength and Structure of Engineering Materials, Prentice-Hall, Inc., Englewood Cliffs, N.J., 1966.
15. Bodner, S. R., Partom, I., and Partom, Y., "Uniaxial Cyclic Loading of Elastic-Viscoplastic Materials," Journal of Applied Mechanics, Vol. 46, December 1979, pp. 805-810.
16. Miller, A. K., "Modelling of Cyclic Plasticity with Unified Constitutive Equations: Improvements in Simulating Normal and Anomalous Bauschinger Effects," Journal of Engineering Materials and Technology, Vol. 102, April 1980, pp. 215-222.
17. Kocks, U. F., "Laws for Work-Hardening and Low-Temperature Creep," Journal of Engineering Materials and Technology, Vol. 98, January 1976, pp. 76-85.
18. Walker, K. P., "Research and Development Program for Nonlinear Structural Modelling with Advanced Time - Temperature Dependent Constitutive Relationships," First Quarterly Technical Narrative, Pratt & Whitney Aircraft Group Report No. PWA-5700-6, January 1980.
19. Allen, David H., "Course Notes for MM641 - Plasticity Theory," Texas A&M University, unpublished, Summer 1980.
20. Petersson, Hans, and Popov, Egor P., "Constitutive Relations for Generalized Loadings," Journal of the Engineering Mechanics Division, ASCE, Vol. 103, No. EM4, Aug. 1977, pp. 611-27.
21. Popov, Egor P., and Petersson, Hans, "Cyclic Metal Plasticity: Experiment and Theory," Journal of the Engineering Mechanics Division, ASCE, Vol. 104, Dec. 1978, pp. 1371-87.
22. Snyder, M. D., and Bathe, K. J., "Formulation and Numerical Solution of Thermo-Elastic-Plastic and Creep Problems," National Technical Information Service, No. 82448-3, June 1977.
23. Yamada, Y., "Constitutive Modelling of Inelastic Behavior of Numerical Solution of Nonlinear Problems by the Finite Element Method," Computers and Structures, Vol. 8, 1978, pp. 533-43.
24. Yamada, Y., and Sakurai, T., "Basic Formulation and a Computer Program for Large Deformation Analysis," Pressure Vessel Technology, Part I, ASME, 1977, pp. 341-52.
25. Allen, David H., and Haisler, Walter W., "A Theory for Analysis of Thermoplastic Materials." Computers and Structures, Vol. 13, 1981, pp. 124-35.
26. Zienkiewicz, O. C., The Finite Element Method, McGraw-Hill, London, 1977.

27. Fung, Y. C., Foundations of Solid Mechanics, Prentice-Hall, Inc., Englewood Cliffs, N.J., 1965.
28. Hunsaker, B. Jr., "The Application of Combined Kinematic-Isotropic Hardening and the Mechanical Sublayer Model to Small Strain Inelastic Structural Analysis by the Finite Element Method," Dissertation, Texas A&M University, August 1976.
29. Allen, David H., "A Note on the Combined Isotropic-Kinematic Work Hardening Rule," International Journal for Numerical Methods in Engineering, Vol. 15, 1980, pp. 1724-28.
30. Pugh, C. W., Corum, J. M., Lin, K. C., and Greenstreet, W. L., "Currently Recommended Constitutive Equations for Inelastic Design Analysis of FFTF Components," ORNL TM-3602, Oak Ridge National Laboratory, Oak Ridge, Tenn., Sept. 1972.
31. Dafalias, Y. F., and Popov, E. P., "Plastic Internal Variables Formalism of Cyclic Plasticity," Journal of Applied Mechanics, Vol. 43, Dec. 1976, pp. 645-51.
32. Caulk, D. A., and Naghdi, P. M., "On the Hardening Response in Small Deformation of Metals," Journal of Applied Mechanics, Vol. 45, December 1978, pp. 755-64.
33. Swindeman, R. W., and Pugh, C. E., "Creep Studies on Type 304 Stainless Steel (Heat 8043813) Under Constant and Varying Loads," ORNL-TM-4427, June 1974, Oak Ridge National Laboratory, Oak Ridge, Tenn.
34. Haisler, W., "Application of an Uncoupled Elastic-Plastic Creep Constitutive Model to Metals at High Temperatures," to be presented at the Symposium on Nonlinear Constitutive Relations for High Temperature Applications, The University of Akron, Akron, Ohio, May 19 and 20, 1982.
35. Bradley, W. L., "A New Uncoupled, Viscoplastic Constitutive Model," to be presented at the Symposium on Nonlinear Constitutive Relations for High Temperature Applications, The University of Akron, Akron, Ohio, May 19 and 20, 1982.
36. Allen, David H., "Computational Aspects of the Nonisothermal Classical Plasticity Theory," Virginia Polytechnic Institute and State University Report No. VPI-E-80.29, Blacksburg, Virginia, Oct, 1980.
37. Reed-Hill, Robert E., Physical Metallurgy Principles, D. van Nostrand Company, New York, 1964.

APPENDIX

COMPUTER PROGRAM OUTLINE

The following outline describes a basic flowchart of the uniaxial constitutive equations for a given total strain increment. Subincrementation (forward integration) with no equilibrium iterations is the solution technique used. Note that in the setup of any problem, the yield surface size and equivalent uniaxial stress vs. plastic strain diagrams are initialized using the first set of input stress-strain curves.

- A. Set up subincrementation on strain, temperature, and time increments.
- B. Compute elastic modulus and the change in the elastic modulus due to temperature increment. Linearly interpolate between input values if necessary.
- C. Compute thermal strain increment. Linear interpolation may be necessary to obtain thermal expansion coefficient. [equation (51)]
- D. Compute creep strain increment based on stress at beginning of step and temperature at end of step. [CHAPTER III - Creep strain increment]
- E. Compute trial stress increment assuming elastic behavior. Add this to the stress at beginning of step to obtain total stress.
- F. Check for yielding
 1. Compute yield function. [equation (34)]
 2. Compute yield surface size for current value of equivalent

- uniaxial plastic strain at temperatures at start and end of load step.
3. Compare yield function value with current yield surface size.
 - a. If elastic, go to step N'.
 - b. If yielded and last step was elastic-plastic go to step J.
 - c. If yielded and last step was elastic, go to step G.
- G. Update stress and strain to yielded portion for transition step. [equations (46) and (47)]
1. Subtract assumed elastic stress increment from total since this step is elastic-plastic.
 2. Compute ζ and η factors. [equations (48) and (50)]
 3. Update total strain, elastic strain, and creep strain to yield surface.
- H. Compute creep strain increment based on yield stress and temperature at end of step.
- I. Modify global K and $\bar{\sigma}$ vs. $\bar{\epsilon}^P$ diagrams. [CHAPTER III - Construction of K and $\bar{\sigma}$ vs. $\bar{\epsilon}^P$ diagrams]
1. If the hardening ratio is a function of plastic strain, recompute the base K and $\bar{\sigma}$ vs. $\bar{\epsilon}^P$ diagrams. [equations (39) - (41)]
 2. If this is the initial yield or yield has occurred without a stress reversal, no modification is necessary. Go to step J.
 3. If reverse yielding has occurred, modify the global diagrams. The particular material of interest determines whether the first or second base curves are used.

- J. Experiencing elastic-plastic behavior.
1. Compute $\partial F/\partial \sigma$ and the gradients H' , $\partial \sigma/\partial T$, $\partial K/\partial \bar{\epsilon}^P$, $\partial K/\partial T$ for the current value of plastic strain and temperature.
[equations (42) - (45)]
- K. Compute stress increment. [equation (29)]
- In transition step from elastic to elastic-plastic behavior, only the leading term of equation (16) is used.
- L. Compute strains and update totals.
1. Elastic strain. [equation (51)]
 2. Plastic strain increment is the total minus the elastic, thermal, and creep increments.
 3. Equivalent uniaxial plastic strain is the absolute value of the plastic strain increment for the uniaxial case.
- M. Update yield surface center. In transition step the yield surface translation scalar is calculated assuming isothermal behavior for temperature at end of step.
1. Compute translation scalar. [equation (32)]
 2. Compute change in yield surface center. [equation (6)]
 3. Update yield surface center.
- N. Update values to end of subincrement.
1. Stress.
 2. Total strain.
 3. Creep strain.
 4. Thermal strain.
- N'. Update values to end of load step for elastic case.
1. Stress.

Yuen, S., "Development of an Uncoupled Viscoplastic Constitutive Model for Cyclic Plasticity of Hastelloy X at High Temperature," Thesis, Texas A&M University, College Station, Texas, May 1983.

2. Total strain.
 3. Elastic strain.
 4. Creep strain.
 5. Thermal strain.
0. Repeat above procedure for each subincrement.

DEVELOPMENT OF AN UNCOUPLED, VISCOPLASTIC
CONSTITUTIVE MODEL FOR CYCLIC PLASTICITY
OF HASTELLOY-X AT HIGH TEMPERATURE

A Thesis

by

SHIK HUNG YUEN

Submitted to the Graduate School of
Texas A&M University
in partial fulfillment of the requirement for the degree of
MASTER OF SCIENCE

May 1983

Major Subject: Mechanical Engineering

DEVELOPMENT OF AN UNCOUPLED, VISCOPLASTIC
CONSTITUTIVE MODEL FOR CYCLIC PLASTICITY
OF HASTELLOY-X AT HIGH TEMPERATURE

A Thesis

by

SHIK HUNG YUEN

Approved as to style and content by:

Walter L. Bradley
Walter L. Bradley
(Chairman of Committee)

Walter E. Haisler
Walter E. Haisler
(Member)

Richard A. Schapery
Richard A. Schapery
(Member)

Gordon R. Hopkins
Gordon R. Hopkins
(Head of Department)

May 1983

1810400

ABSTRACT

Development of an Uncoupled, Viscoplastic
Constitutive Model for Cyclic Plasticity
of Hastelloy-X at High Temperature. (May 1983)

Shik Hung Yuen, B.S., Texas A&M University

Chairman of Advisory Committee: Dr. Walter L. Bradley

An uncoupled viscoplastic model is presented based on the assumption that inelastic strain can be partitioned into rate insensitive and rate sensitive components. Unlike earlier uncoupled theories, this model recognizes that some of the inelastic strain which occurs during a load change is rate sensitive (or thermally activated). The rate insensitive, inelastic strain is defined in terms of a strain hardening function which is determined empirically from saturated hysteresis loops at room temperature. The rate sensitive inelastic strain is characterized using a standard viscoplastic model. The physical basis for the model and the experiments required to evaluate the material constants are also presented. Evaluation of the model is performed by comparing predicted hysteresis loops and stress relaxation behavior with experimental observation. The question of inelastic strain-rate continuity is addressed in terms of the uncoupled viscoplastic model as well as models developed by other

C-2

researchers. Finally, suggestions are made for further investigation.

ACKNOWLEDGEMENTS

The financial support of this work by NASA Lewis Research Center is gratefully acknowledged. I also gratefully acknowledge Dr. Walter Bradley for his support and guidance throughout this research effort. I give special thanks to Dr. Walter Haisler for his help in this work. I would also like to thank Dr. Richard Schapery for kindly consenting to join my committee. Most of all, I appreciate the endless support and encouragement from my parents throughout my college career.

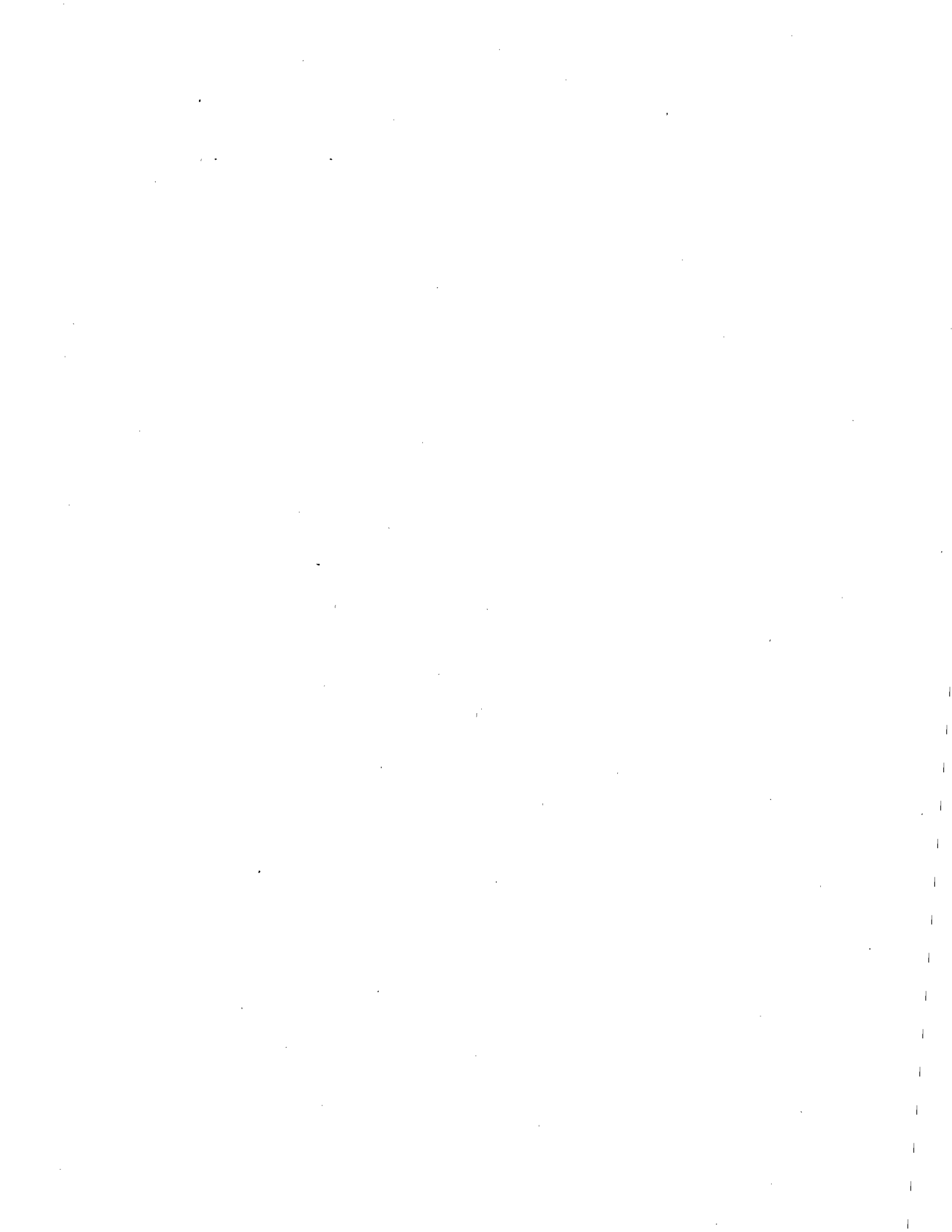


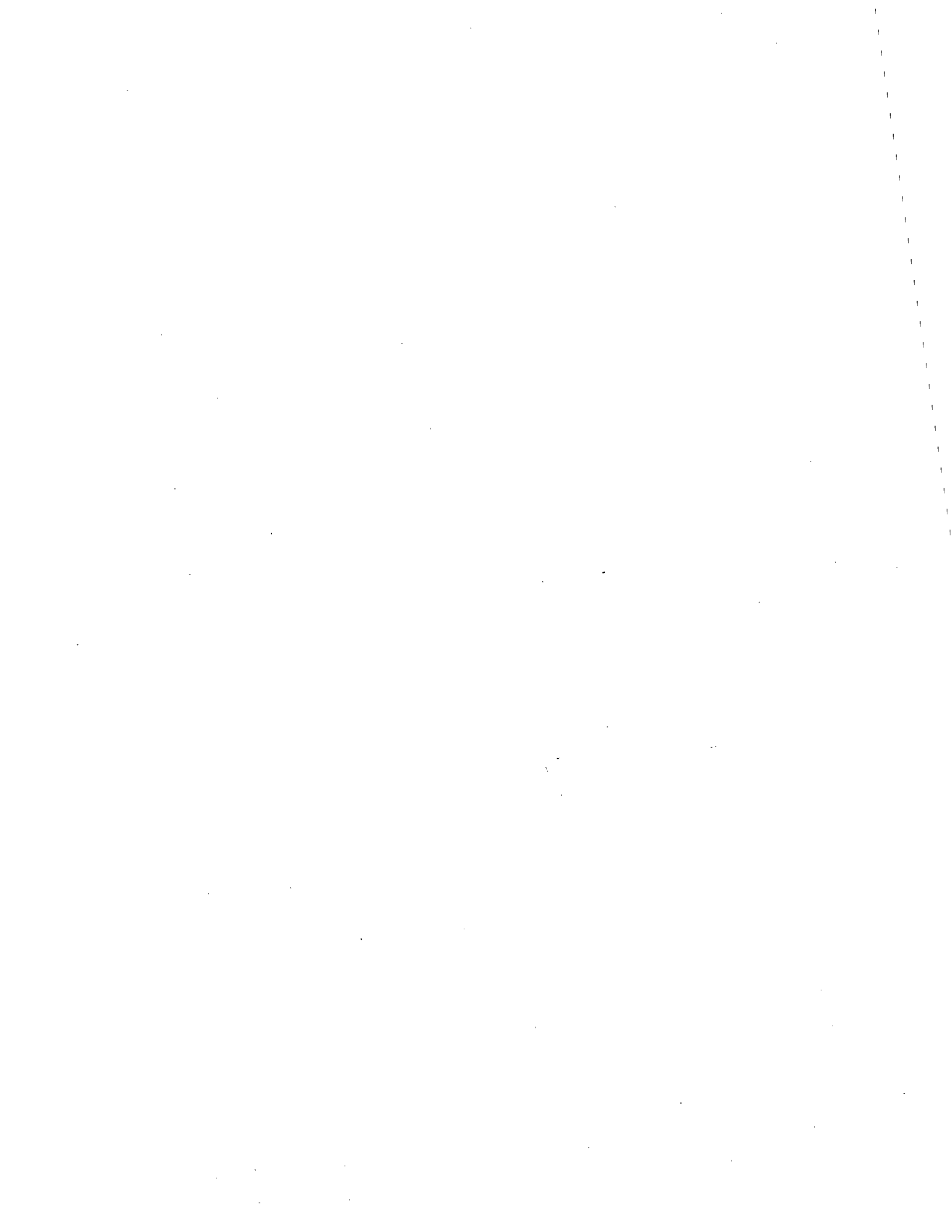
TABLE OF CONTENTS

	Page
ABSTRACT	iii
ACKNOWLEDGEMENTS	v
TABLE OF CONTENTS	vi
LIST OF TABLES	viii
LIST OF FIGURES	ix
CHAPTER I. INTRODUCTION	1
CHAPTER II. REVIEW OF EXISTING THEORIES	4
Present Status	4
Available Constitutive Theories	5
<u>Micromechanistic theories</u>	5
<u>Nonlinear viscoelastic theories</u>	6
<u>Classical plasticity theories</u>	8
Uncoupled vs. Unified Theories	10
Objectives	11
CHAPTER III. CONSTITUTIVE MODEL DEVELOPMENT	13
Physical Basis	13
Description of Constitutive Model	17
Experimental Data Requirements	23
Numerical Scheme for Theoretical Prediction	27
CHAPTER IV. EXPERIMENTAL PROCEDURE	31
Material Description	31
Specimen Preparation	31
Experimental Set Up	34
Description of Experiments	39

	page
<u>Fully reversed, strain cycling experiments</u> <u>(hysteresis loops)</u>	39
<u>Stress relaxation tests</u>	40
<u>Strain drop, stress transient tests</u>	42
<u>Strain-rate cycling tests</u>	44
CHAPTER V. EXPERIMENTAL RESULTS, ANALYSIS AND DISCUSSION . . .	46
Data Reduction	46
Hysteresis Loop Results	47
Stress Relaxation Behavior	64
Material Constants and Their Physical Significance	76
CHAPTER VI. EVALUATION OF THE MODEL	92
Justifying the Uncoupled Inelastic Strain Model	92
Comparison of Experiments with Theoretical Predictions . . .	101
<u>Saturated hysteresis loops</u>	101
<u>Stress relaxation behavior</u>	110
CHAPTER VII. CONCLUSIONS	121
CHAPTER VIII. RECOMMENDATION FOR FUTURE WORK	123
REFERENCES	125
APPENDIX A. COMPUTER PROGRAM OUTLINE FOR HYSTERESIS LOOP SIMULATION	130
APPENDIX B. COMPUTER PROGRAM OUTLINE FOR STRESS RELAXATION PREDICTION	132
APPENDIX C. DERIVATION OF EQUATIONS USED FOR DATA REDUCTION . .	133
APPENDIX D. VALUES FOR RATE INSENSITIVE, INELASTIC STRAIN FUNCTION	136
VITA	142

LIST OF TABLES

TABLE		page
I	Chemical Composition of Hastelloy-X	32
II	Values for Back Stress (Ω) (for $\sigma = \sigma_{\max}$), n, Drag Stress (K) and K^n	77
III	Values for Young's Modulus and Poisson's Ratio at Different Temperatures	78
IV	Inelastic Strain-rate Continuity at Various Temperatures	97



LIST OF FIGURES

FIGURE		page
1	Single nonlinear Maxwell element	21
2	Schematic of stress-strain behavior at three temperatures	25
3	Experimental characterization of the three strain components for the uncoupled viscoplastic model	25
4	Specimen geometry	33
5	Experimental set up	35
6	Schematic of experimental set up	36
7	Schematic for the strain drop, stress transient test	43
8	Schematic for the strain-rate cycling test	43
9	Saturated hysteresis loops for Hastelloy-X at room temperature with strain amplitudes of 0.05%, 0.1%, 0.2%, 0.3%, 0.4%, 0.5%, 0.6% 0.8% and 1.0% . . .	48
10	Saturated hysteresis loops for Hastelloy-X at room temperature	50
11	Saturated hysteresis loops for Hastelloy-X at 533K . . .	52
12	Saturated hysteresis loops for Hastelloy-X at 775K. (a) Stress vs. total strain. (b) Stress vs. rate dependent (or rate sensitive) inelastic strain	53
13	Saturated hysteresis loops for Hastelloy-X at 811K. (a) Stress vs. total strain. (b) Stress vs. rate dependent (or rate sensitive) inelastic strain	56
14	Saturated hysteresis loops for Hastelloy-X at 866K. (a) Stress vs. total strain. (b) Stress vs. rate dependent (or rate sensitive) inelastic strain	57
15	Saturated hysteresis loops for Hastelloy-X at 922K. (a) Stress vs. total strain. (b) Stress vs. rate dependent (or rate sensitive) inelastic strain	58

FIGURE		page
16	Saturated hysteresis loops for Hastelloy-X at 978K. (a) Stress vs. total strain. (b) Stress vs. rate dependent (or rate sensitive) inelastic strain	59
17	Saturated hysteresis loops for Hastelloy-X at 1033K. (a) Stress vs. total strain. (b) Stress vs. rate dependent (or rate sensitive) inelastic strain	60
18	Saturated hysteresis loops for Hastelloy-X at 1089K. Stress vs. total strain. (b) Stress vs. rate dependent (or rate sensitive) inelastic strain	61
19	Saturated hysteresis loops for Hastelloy-X at 1144K. (a) Stress vs. total strain. (b) Stress vs. rate dependent (or rate sensitive) inelastic strain	62
20	Stress relaxation tests for Hastelloy-X at room temperature executed at various points on saturated hysteresis loops	65
21	Stress relaxation tests for Hastelloy-X at 755K executed at various points on saturated hysteresis loops	66
22	Stress relaxation tests for Hastelloy-X at 811K executed at various points on saturated hysteresis loops	67
23	Stress relaxation tests for Hastelloy-X at 866K executed at various points on saturated hysteresis loops	68
24	Stress relaxation tests for Hastelloy-X at 922K executed at various points on saturated hysteresis loops	69
25	Stress relaxation tests for Hastelloy-X at 978K executed at various points on saturated hysteresis loops	70
26	Stress relaxation tests for Hastelloy-X at 1033K executed at various points on saturated hysteresis loops	71
27	Stress relaxation tests for Hastelloy-X at 1089K executed at various points on saturated hysteresis loops	72

FIGURE		page
28	Stress relaxation tests for Hastelloy-X at 1144K executed at various points on saturated hysteresis loops	73
29	Effective stress vs. rate sensitive, inelastic strain-rate at 1144K for a total strain-rate of $1 \times 10^{-3} \text{s}^{-1}$	75
30	Stress and back stress as a function of strain for Hastelloy-X at 755K	80
31	Stress and back stress as a function of strain for Hastelloy-X at 811K	81
32	Stress and back stress as a function of strain for Hastelloy-X at 866K	82
33	Stress and back stress as a function of strain for Hastelloy-X at 922K	83
34	Stress and back stress as a function of strain for Hastelloy-X at 978K	84
35	Stress and back stress as a function of strain for Hastelloy-X at 1033K	85
36	Stress and back stress as a function of strain for Hastelloy-X at 1089K	86
37	Stress and back stress as a function of strain for Hastelloy-X at 1144K	87
38	Experimental and simulated hysteresis loops for Hastelloy-X at 755K	102
39	Experimental and simulated hysteresis loops for Hastelloy-X at 811K	103
40	Experimental and simulated hysteresis loops for Hastelloy-X at 866K	104
41	Experimental and simulated hysteresis loops for Hastelloy-X at 922K	105
42	Experimental and simulated hysteresis loops for Hastelloy-X at 978K	106
43	Experimental and simulated hysteresis loops for Hastelloy-X at 1033K	107

FIGURE		page
44	Experimental and simulated hysteresis loops for Hastelloy-X at 1089K	108
45	Experimental and simulated hysteresis loops for Hastelloy-X at 1144K	109
46	Experimental and theoretical stress relaxation behavior for Hastelloy-X at 755K	111
47	Experimental and theoretical stress relaxation behavior for Hastelloy-X at 811K	112
48	Experimental and theoretical stress relaxation behavior for Hastelloy-X at 866K	113
49	Experimental and theoretical stress relaxation behavior for Hastelloy-X at 922K	114
50	Experimental and theoretical stress relaxation behavior for Hastelloy-X at 978K	115
51	Experimental and theoretical stress relaxation behavior for Hastelloy-X at 1033K	116
52	Experimental and theoretical stress relaxation behavior for Hastelloy-X at 1089K	117
53	Experimental and theoretical stress relaxation behavior for Hastelloy-X at 1144K	118
54	Experimental hysteresis loops for Hastelloy-X at 922K. Points A and B indicate where stress relaxation starts and ends. Point C indicates the flow stress upon reloading	119

CHAPTER I

INTRODUCTION

With the increasing demand for materials to function at elevated temperatures, an understanding of material behavior under such conditions is essential. Structural components in the hot section of a turbine engine experience a complex thermal-mechanical history, often leading to premature failure. Similar problems are encountered in nuclear reactors. Components in critical areas are subjected to cyclic loading conditions and possible damage due to creep-fatigue interaction. To obtain design parameters under actual service conditions is impractical in most cases due to the cost and time involved. Therefore, viscoplastic models must be developed to simulate material behavior under such conditions.

Historically, the first experimental study on "viscoplasticity" was conducted by Vicat [1] in 1834. He found that at room temperature, iron wires loaded with a stress equal to one half the breaking stress exhibited a gradual increase in length. This is the first indication of the existence of rate dependent inelastic deformation in metals, which is now referred to as creep.

Despite the fact that the first study of rate dependent inelastic deformation was performed more than a century ago, early plasticity theories were mainly concerned with rate independent inelastic

This thesis follows the style and format of the Journal of Applied Mechanics.

deformation. (For a historical review of plasticity theories one is referred to books by Hill [2] and Martin [3]).

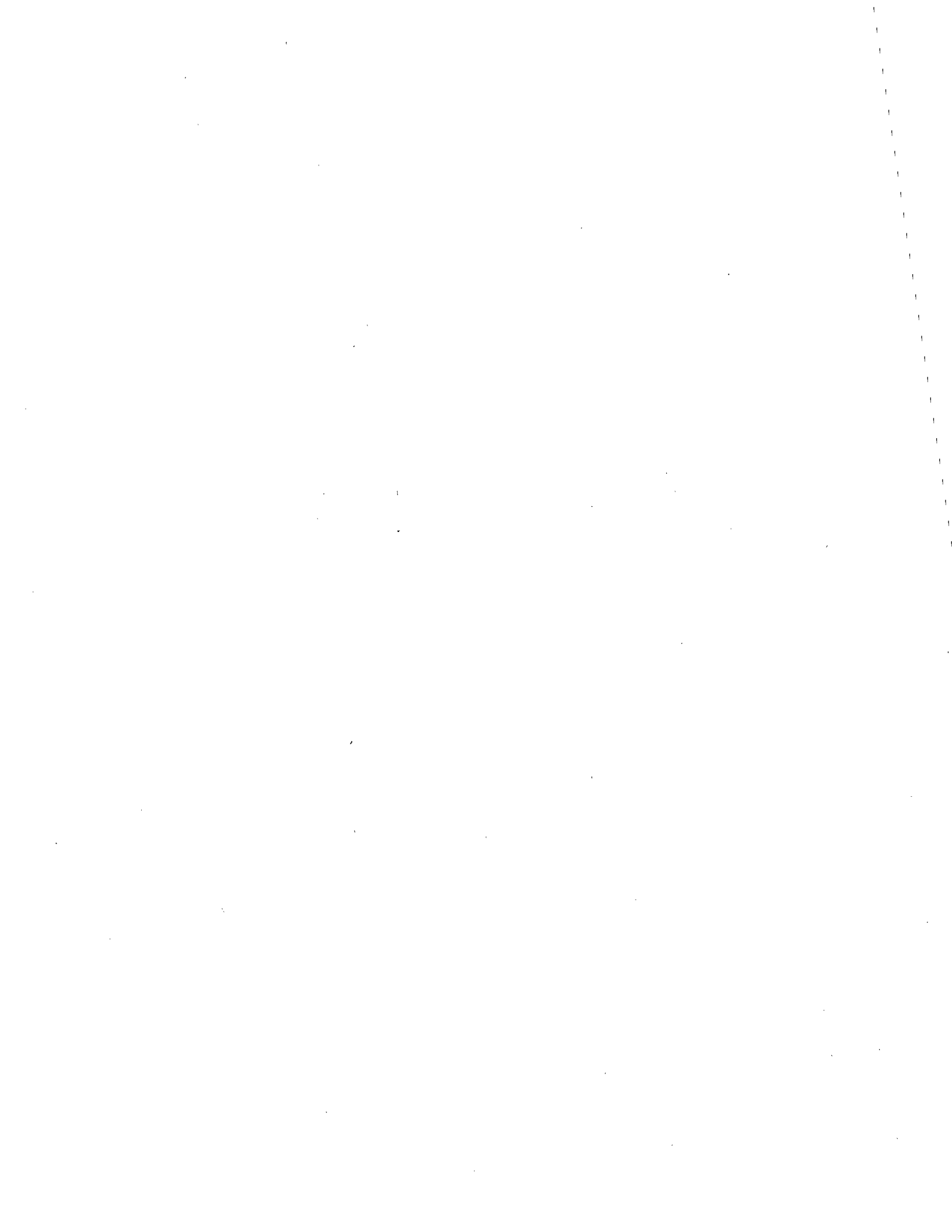
In recent years, the need to apply materials at elevated temperatures necessitates the inclusion of rate effects in plasticity studies. Considerable research efforts have been undertaken to extend classical plasticity theories to model both rate and temperature dependent phenomena [4-9]. These modifications are accomplished by introducing an uncoupled rate dependent inelastic strain component as well as temperature dependence of material properties. Constitutive models of this nature are often referred to as uncoupled theories.

More recently, there has been increasing attention toward the development of viscoplastic models which are consistent with micro-physical observation. Research efforts in this area are reflected by the proposal of a number of unified theories [10-22], many of which are still undergoing active development. The major feature of these theories is that all inelastic strain is considered to be rate dependent. Although physically appealing, many unified models fail to accurately predict cyclic behavior at lower temperatures.

This thesis will proceed in the following manner. First, a review of the existing theories will be presented along with a comparison of the uncoupled and unified theories. This will be followed by a presentation of the uncoupled viscoplastic model and the physical basis for this new model. A description of the various experiments used to evaluate the required material constants will be provided. Experimental results will be compared with theoretical predictions and the

question of inelastic strain-rate continuity will be discussed.

Finally, suggestions for future work will be outlined.



CHAPTER II

REVIEW OF EXISTING THEORIES

Present Status

As discussed in the previous chapter, the value of a constitutive model lies in its capability to predict complex thermomechanical histories. To satisfy such requirement, a model has to account for various thermally induced elastic and inelastic strains for cyclic loading as well as creep and stress relaxation responses at constant loads or strains. Furthermore, time and temperature dependent microstructural changes such as precipitation, grain growth, recrystallization, segregation, etc. have to be considered. Given the complexity of the problem, a general constitutive law which can fully describe all of the above phenomena is simply not feasible. In this research effort, we will specifically deal with cyclic plasticity and stress relaxation behavior of Hastelloy-X at various strain-rate and temperature ranges.

Three common approaches utilized in constitutive modelling include: (1) micromechanistic theories; (2) nonlinear viscoelastic theories; (3) classical incremental plasticity theories. The first approach has generally been favored by material scientists who attempt to characterize material behavior through microstructural considerations. The other two approaches are widely used in the mechanics community. Constitutive models are usually developed on the basis of continuum mechanics. Existing constitutive theories can also be classified as being "uncoupled" or "unified" depending on the way the

inelastic strain is modelled.

In the following section, the three different approaches in constitutive modelling will be discussed along with a comparison of uncoupled and unified theories.

Available Constitutive Theories

Micromechanistic theories. The thrust of the micromechanistic theories is to create a model which relates macroscopic parameters such as stress, strain-rate and temperature to underlying micromechanisms. It is generally accepted that inelastic deformation is a result of dislocation movements and interactions within a crystalline material. Constitutive laws are therefore based on various models of dislocation kinetics. For example, strain hardening is associated with the interactions of the long range stress fields of dislocations [23]. On the other hand, recovery can be explained in terms of thermally activated dislocation climb and cross-slip [24].

An example of a micromechanistic model is provided by Kreig, et al. [11]. The constitutive model takes the form of a power law function. The current microstructure is reflected by a kinematic state variable and an isotropic internal variable, which allows the model to predict combined isotropic/kinematic response. Evolutionary laws are developed for the internal variables to account for strain hardening and recovery. Since recovery is assumed to be governed by dislocation climb, the constitutive model is limited to relatively high homologous temperatures. As pointed out by the authors, a short coming of the model is that predictions of stress-strain behavior are

too "square" compared with experimental observation.

Another example is found in a unified model developed by Hart [12]. An important feature of the theory is that the inelastic strain is separated into recoverable (anelastic) and unrecoverable (plastic) components. The anelastic strain component is considered to be a state variable. The plastic strain, on the other hand, is governed by a number of internal variables. One state variable is called the "hardness" and represents isotropic strain hardening. Thermal recovery at high temperature is accounted for by modifying the "hardness" term with another function. A second state variable is used to represent the direction as well as magnitude of prior stress history and accounts for kinematic hardening. The model is based on the assumption of an isotropic material and since the internal variables are not functions of temperature, it can only be used under isotropic conditions.

Other examples of micromechanistic theories are given by Bodner and Partom [13], and Miller [14, 15].

Nonlinear viscoelastic theories. Nonlinear viscoelastic theories are generally constructed within a thermodynamic framework [25, 26] based on the First and Second Laws of Thermodynamics. These theories have been reported in both single integral and multiple integral form as well as differential equation form. In addition to thermodynamics, physical constraints must be applied to obtain a meaningful constitutive model.

One example is a viscoplastic model credited to Walker [16]. It is developed in an integral form by modifying the constitutive

relation for a standard three parameter viscoelastic solid. The model employs two state variables, the equilibrium stress and the drag stress. The equilibrium stress represents kinematic hardening and is governed by a growth law which contains both static and thermal recovery terms. The drag stress, on the other hand, represents isotropic hardening. In the original formulation, the drag stress was assumed to be constant and cyclic hardening and softening behavior was described in terms of changes in the back stress term. The drag stress term has recently been modified [17] to include a dynamic recovery term so that both internal variables can be used to describe cyclic hardening response. The evolutionary law for the back stress contains a term which allows the back stress to change with temperature during nonisothermal elastic excursions. The shortcomings of the model include its failure to accurately predict stress-strain behavior at relatively high strain-rates and the "over squareness" of its predictions in the case of cyclic response at small strain-rates.

Another example is found in a model proposed originally by Schapery [27] and later amplified by Valanis [18]. It is an endochronic theory and does not require a yield surface. The current state of stress is expressed as a function of the strain history defined with respect to a "time scale" which is itself a material property. The model has been shown to be capable of describing a number of elastic-plastic phenomena [19]. The endochronic theory has recently been modified by introducing the concept of "internal barriers" [20]. It is proposed that an internal variable will not become activated until an activation barrier is overcome. Each internal variable is

"autonomous" in the sense that it is governed by its own time scale which is defined by the internal variable itself. This version of the endochronic theory is termed an autochronic theory. The theory is used mainly in a rate independent form under isothermal conditions and has not been shown to be adequate in modelling material behavior under cyclic load conditions. Efforts have been made by Wu and Chen [28] to include strain-rate effects in the model.

Other examples are presented by Cernocky and Krempf [21], Lui and Krempf [29], and Schapery [27]. A more detailed discussion of non-linear viscoelastic theories is provided by Allen [30].

Classical plasticity theories. Classical plasticity theories are based on the concept of a yield surface. Various plastic strain histories can be described in terms of the expansion, translation and rotation of the yield surface. These theories are macrophenomenological in the sense that state variables are derived from experimental data without reference to the micromechanisms involved.

Incremental plasticity theories are generally characterized by the following features: (1) a yield function distinguishing elastic and plastic deformation, (2) a relationship between the stress increment tensor and the strain increment tensor, (3) a description of the rate independent plastic strain increment and (4) a hardening rule which describes the evolution of the yield surface during plastic flow.

There has been an enormous amount of research in this category. A majority of the work is related to the development of various hardening rules to describe different loading histories [31]. Rate

independent plasticity theories are well established and recent efforts involve the extension of these theories to include rate and thermal effects. Recent research efforts in this area have been reviewed by Allen [32, 33]. Of the classical plasticity theories discussed in reference [32], a more promising one belongs to Yamada and Sakurai [34, 35]. It includes temperature dependence of material properties, an uncoupled rate dependent inelastic strain component, and a combined hardening rule to account for the Bauehinger effect. However, the mathematical consistency of the model is questioned [32]. Another example is given by Snyder and Bathe [5]. The model is an extension of classical plasticity and has been shown to be quite accurate in modelling monotonic loadings. Since the model is a single state variable theory, it is inadequate to model combined isotropic-kinematic hardening under cyclic loading conditions. One other example is a model proposed by Sharifi and Yates [7], which accounts for creep, but does not include temperature dependence of material properties.

One of the most comprehensive models is presented by Allen and Haisler [6]. Their theory is an uncoupled, incremental, nonisothermal constitutive model based on the classical theory of plasticity. The theory is capable of modelling rate and thermal effects, the Bauehinger effect and can be extended to model multiaxial loading conditions. Recent addition of a revised hardening rule [36] results in improved capability of the theory to model cyclic behavior under various thermomechanical histories.

Uncoupled vs. Unified Theories

As discussed in the opening chapter, two distinct approaches exist in constitutive modelling with respect to the treatment of the inelastic strain component. This results in the development of the so called "uncoupled" and "unified" theories. The unified approach is relatively new but has gained considerable support in the past few years. It is therefore worthwhile at this point to discuss some of the advantages as well as drawbacks of the two approaches.

The uncoupled approach separates the total inelastic strain into a rate independent component and a rate dependent component. An example of an uncoupled theory is one proposed by Strauss [37, 38] to model "creep" and "plasticity" effects in viscoplastic materials. The model is termed a bilinear functional theory since the functional is linear in the rate dependent part as well as the rate independent part of the model. Other examples can be found in the preceding section under the category of classical plasticity theories. The uncoupled theories are widely used today in finite element structural analysis. In a recent review, Krempl [39] questioned the concept of "time independence" as a valid approach to describe material behavior at low homologous temperature since rate sensitivity is observable even at room temperature. Researchers like Walker [16], Miller [15] and Hart [12] criticized the uncoupled approach on the basis that creep and plasticity are controlled by the same physical processes. The uncoupled approach is further criticized for not taking into consideration the interaction between creep and plasticity. It is pointed out by

Krempf [40] that uncoupled models obtain their time dependent part from constant load creep tests and therefore are inadequate in modelling variable loading conditions.

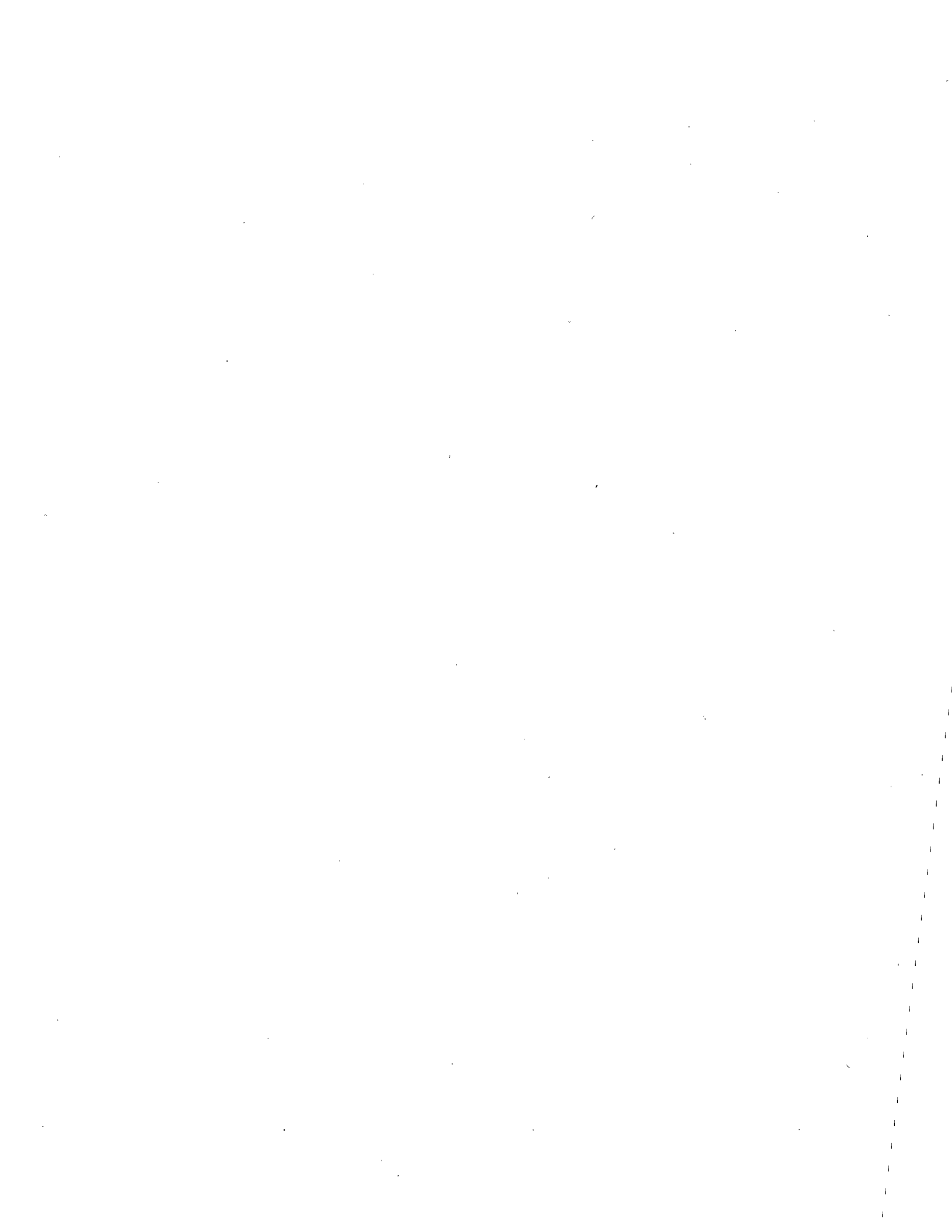
Recognizing the above shortcomings, a number of unified models [10-22] have recently been proposed which consider all inelastic strain as rate dependent. Although physically satisfying, the unified approach is not without drawbacks. In modelling cyclic response, for example, predictions made by the unified models are often too "square" compared with experimental observation [11, 15, 17]. In many cases, the evolution of the state variables is difficult to model or experimentally characterize. Furthermore, unified models produce "stiff" differential equations which often result in computational difficulties.

To summarize, neither the uncoupled nor the unified approach has shown clear advantage over the other. Since many unified models are still in a developing stage, it is possible that some of the problems discussed above will be overcome eventually. For the near future, however, it appears to be more advantageous to rely on an uncoupled theory whose form is consistent with known micromechanistic models.

Objectives

The objective of this research is to present an uncoupled viscoplastic model to characterize cyclic behavior of Hastelloy-X under different strain-rate and temperature conditions. The rate insensitive inelastic strain component is defined using hysteresis loops at room temperature. The rate sensitive inelastic strain

component will be characterized using a standard viscoplastic model. Special emphasis is placed on the modelling of saturated hysteresis loops and stress relaxation behavior at various strain-rates and temperature ranges. Evaluation of the model is performed by comparison with experimental results.



CHAPTER III

CONSTITUTIVE MODEL DEVELOPMENT

In this chapter, the physical basis and the experimental data requirements for the uncoupled viscoplastic model will be described in detail. As pointed out earlier, plasticity and creep are generally considered indistinguishable since both involve thermally assisted overcoming of various dislocation barriers. In the discussion that follows, justification for the uncoupled approach will be given in terms of the nature of dislocation barriers and the role of thermal assistance in circumventing the obstacles under various temperature and strain-rate conditions. It is the author's belief that if uncoupling is performed properly, meaningful results can be obtained.

Physical Basis

Inelastic deformation of crystalline materials occurs by dislocation movement and various forms of dislocation-obstacle interactions.

In the low temperature regions ($0-0.2 T_m$), the yield strength and flow stress are found to vary significantly with temperature. This is particularly true for body center cubic materials since the number of slip systems available decreases dramatically as the temperature falls. In this temperature range, plastic deformation is dominated by dislocation glide. The fairly small activation energy for thermally assisted dislocation movement is usually associated with the overcoming of lattice friction (i.e. Peierls stress) and

the cutting of dislocation intersections [41].

Between $0.2 - 0.4 T_m$, the thermal energy available is more than adequate to overcome such barriers, allowing dislocation glide to occur equally easily at various temperatures and strain-rates. While short range barriers such as forest dislocations and Peierls stress are easily overcome with thermal assistance at these temperatures, the thermal energy is relatively small and generally ineffective in overcoming long range barriers such as grain boundaries, cell walls and large incoherent second phase particles. The high strain hardening rate in this temperature range is generally believed to be the result of dislocation pileups against long range obstacles. Recovery in this temperature range is controlled mainly by dislocation cross-slip [24], which depends on the stacking fault energy of the material, temperature, as well as stress. The activation barriers for dislocation cross-slip is relatively large compared to the thermal energy available, making this process quite sluggish. In this case, the flow stress depends more on the long range internal stress and the resultant strain hardening it produces than the strain-rate. In summary, between 0.2 and $0.4 T_m$, thermally activated processes are either so rapid (e.g. overcoming Peierls stress) or so slow (e.g. dislocation cross-slip) that very little rate sensitivity is observed. Deformation behavior in this temperature range can be very well described as rate insensitive and over a finite range of strain-rates will be essentially rate independent. It will be shown later that Hastelloy-X specimens tested under fully reversed strain controlled conditions over a temperature range of 298 K to 533 K ($0.2 - 0.35 T_m$)

and over a 30 X strain-rate range ($3.3 \times 10^{-5} \text{ s}^{-1}$ to $1 \times 10^{-3} \text{ s}^{-1}$) have essentially identical hysteresis loops. At 755 K ($0.49 T_m$), the hysteresis loops change slightly, though rate dependence over the same strain-rate range is still not significant.

As the temperature is raised above $0.5 T_m$, rate effects on inelastic deformation becomes apparent. Numerous dislocation models have been proposed to explain thermally activated deformation in this temperature range. One example is provided by Barrett and Nix [42] based on the assumption that diffusion controlled motion of jogged screw dislocations is the rate limiting deformation process at higher temperatures. Climb and annihilation of edge dislocations have also been suggested as dominant creep mechanisms [43]. Another example is given by Nabarro [44] and Herring [45] who independently proposed two similar models describing high temperature creep in terms of stress driven atomic diffusion from one grain boundary to another. Coble [46] suggested an alternative model involving atomic diffusion along grain boundaries. Additional deformation is generally provided by grain boundary sliding. Despite the large number of theories proposed, they all recognize the importance of thermal assistance to deformation at high temperatures. It will be shown later that the stress-strain behavior of Hastelloy-X is a sensitive function of temperature and strain-rate over this temperature range.

In the following section, the rate insensitive, inelastic strain will be described in terms of dislocation pileups against long range barriers. The rate sensitive, inelastic strain will be associated with the additional increments of plastic deformation made possible

by the thermally assisted overcoming of these long range barriers to deformation. Dislocation cross-slip and climb are generally regarded as the dominant recovery processes at high temperatures. Nonetheless, thermally activated deformation resulting from other mechanisms will be implicitly included as part of the rate sensitive strain component. As discussed above, the rate sensitivity is seen principally in the circumventing of various barriers by cross-slip or climb rather than in the subsequent glide to the next barrier. Nevertheless, all of the inelastic strain that results from the combined cross-slip (or climb) and subsequent glide will be included in the rate sensitive inelastic strain.

The inelastic strain has been implicitly divided into a component which results in strain hardening and one which is associated with thermal recovery or softening. Even during the portion of the hysteresis loop where strain hardening is occurring, the inelastic strain may contain rate insensitive (strain hardening) as well as rate sensitive (thermal recovery) components. It should be noted that net strain hardening continues until the back stress reaches a level where recovery and strain hardening are balanced. This is analogous to the familiar description of high temperature creep as resulting from a balance between the processes of work hardening and recovery. It will be shown later that a constant back stress does imply steady state creep. Ideally, the stress is dependent on the rate insensitive, inelastic strain and the rate sensitive, inelastic strain-rate. A transient dependence of stress on the rate sensitive, inelastic strain (as well as strain-rate) is sometimes observed and is

equivalent to primary creep. Such transients are believed to be associated with the initial "shakedown" where dislocations are gradually being rearranged into more stable cell structures.

In the next section the constitutive model will be defined in mathematical terms and the experimental requirements to characterize the various material constants will be described.

Description of Constitutive Model

It is general practice in constitutive modelling to separate the total strain into elastic, inelastic and thermal components, i.e.

$$\epsilon_t = \epsilon_e + \epsilon_i + \epsilon_{th} \quad (1)$$

where ϵ_t , ϵ_e , ϵ_i and ϵ_{th} denote the total strain, elastic strain, inelastic strain and thermal strain respectively. Uncoupled theories further partition the inelastic strain into rate independent and rate dependent components, which can be expressed as

$$\epsilon_t = \epsilon_e + \epsilon_{ii} + \epsilon_{ir} + \epsilon_{th} \quad (2)$$

where ϵ_{ii} and ϵ_{ir} represent the rate independent (or rate insensitive) inelastic strain and the rate dependent (or rate sensitive) inelastic strain respectively. Under isothermal conditions, equation (2) can be expressed as

$$\epsilon_t = \epsilon_e + \epsilon_{ii} + \epsilon_{ir} \quad (3)$$

where ϵ_t , ϵ_e , ϵ_{ii} , ϵ_{ir} represent the total strain, elastic strain, rate insensitive inelastic strain and rate sensitive inelastic strain

respectively. Equation (3) can be rewritten in rate form as follows:

$$\dot{\epsilon}_t = \dot{\epsilon}_e + \dot{\epsilon}_{ii} + \dot{\epsilon}_{ir} \quad (4)$$

where $\dot{\epsilon}_t$, $\dot{\epsilon}_e$, $\dot{\epsilon}_{ii}$, $\dot{\epsilon}_{ir}$ denote the total strain-rate, elastic strain-rate, rate insensitive inelastic strain-rate and rate sensitive inelastic strain-rate respectively. It is assumed that at any point along the deformation path, the elastic strain-rate component can be described by the Hooke's Law as follows:

$$\dot{\epsilon}_e = \dot{\sigma}/E \quad (5)$$

where $\dot{\sigma}$ is the stress-rate and E is the modulus of elasticity of the specimen. As will be discussed later, all the experiments in this research program were conducted on a servohydraulic testing system (MTS) in the strain control mode. The rate insensitive, inelastic strain is modelled with an empirically determined strain hardening function as follows:

$$\dot{\epsilon}_{ii} = f(\sigma, \sigma_{\max}) \dot{\sigma} \quad (6)$$

where $f(\sigma, \sigma_{\max})$ denotes the hardening function which depends on the current state of stress as well as the maximum stress before load reversal. It is given by

$$f(\sigma, \sigma_{\max}) = \frac{d\epsilon_{ii}}{d\sigma} \quad (7)$$

The function is measured from saturated hysteresis loops in a

temperature range where rate sensitivity is not significant, i.e., essentially all inelastic strain is rate independent (or rate insensitive). It should be noted that the hysteresis loops even at these lower temperatures are slightly asymmetric so the sign of the σ_{\max} value before the stress reversal as well as its magnitude must be specified to define the particular f value for a given value of stress in a load reversal. The rate sensitive, inelastic strain-rate is modelled by a power law function which can be expressed as

$$\dot{\epsilon}_{ir} = \text{sgn}(\sigma - \Omega) \left| \frac{\sigma - \Omega}{K} \right|^n \quad (8)$$

where n , Ω and K represent the stress exponent, back stress and drag stress respectively. A constitutive law of the form stated above is commonly used in unified theories to model inelastic deformation behavior of crystalline materials [11, 14, 16]. It should be noted that unified theories assume all inelastic strain is rate sensitive and the constitutive law is used to model the "total" inelastic strain-rate rather than the rate sensitive inelastic strain-rate as described here. The stress exponent n is a mathematical constant which is generally a function of temperature. The back stress and drag stress represent two evolutionary parameters which are microstructure dependent. Equation (8) represents an "evolutionary material law". It is assumed that the current state of a material can be described by a number of "hidden" microstructural parameters known as internal state variables. Ideally, adequate specification of the internal state variables allows prediction of material

response without explicit knowledge of previous thermal-mechanical history. In this case, two internal state variables (i.e., Ω and K) are utilized to model microstructural changes associated with cyclic deformation. In classical plasticity theory, the drag stress reflects isotropic strain hardening and is equivalent to the expansion of the yield surface. The back stress, on the other hand, correlates with kinematic hardening and is equivalent to the translation of the yield surface. Microscopically, the back stress is associated with dislocation pileups in pure metals and/or multiple loop formation around incoherent second phase particles in alloys. The drag stress represents short range barriers to deformation, in contrast to back stress, which represents long range resistance to dislocation glide. An alternate though not contradictory interpretation of the drag stress and back stress is that they represent the respective effects of dislocation density and dislocation distribution. Equations (5), (6) and (8) can be recombined to yield the following relation:

$$\dot{\epsilon}_t = \frac{\dot{\sigma}}{E} + f(\sigma, \sigma_{\max}) \dot{\sigma} + \text{sgn}(\sigma - \Omega) \left| \frac{\sigma - \Omega}{K} \right|^n \quad (9)$$

The uncoupled model can be represented by a single Maxwell element as shown in Fig. 1. The spring represents the elastic strain which has an indirect temperature dependence through the Young's Modulus. The slider block represents the rate insensitive inelastic strain which is a function of the applied stress but is independent of time (or temperature). The rate independent nature of the slides block can be further demonstrated by rewriting equation (6) in the following

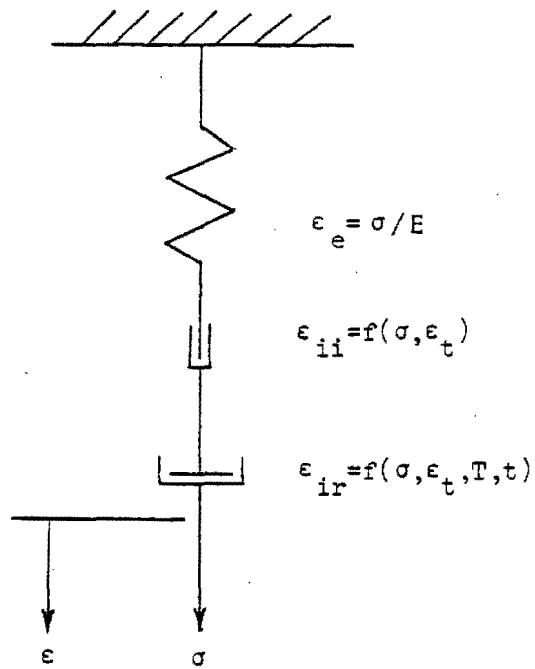


Fig. 1 Single nonlinear Maxwell element

form:

$$\left(\frac{d\sigma}{d\varepsilon_{ii}}\right)_{T_{ref}} = \left(\frac{d\sigma}{d\varepsilon_{ii}}\right)_T \quad (10)$$

where $\left(\frac{d\sigma}{d\varepsilon_{ii}}\right)_{T_{ref}} = [f(\sigma, \sigma_{max})]^{-1}$ and represents the strain hardening

rate at the reference temperature $(T_{ref})^1$ and $\left(\frac{d\sigma}{d\varepsilon_{ii}}\right)_T$ denotes the strain hardening rate for the rate insensitive inelastic strain component at a higher temperature. Equation (10) merely states that the rate insensitive inelastic strain corresponding to a given stress (or strain) remains the same regardless of the temperature (or strain-rate). At low temperatures, the "viscosity" of dashpot prevents any significant contribution from the rate sensitive inelastic component to the total deformation and the inelastic strain is essentially all rate independent. At higher temperatures and/or lower strain-rates, the dashpot becomes less viscous so that rate dependent deformation or thermal recovery occurs which results in "softening" of the material.

In summary, it is proposed that the total strain can be separated into an elastic component as well as an inelastic component which consists of rate sensitive and rate insensitive terms. The rate insensitive inelastic component results in strain hardening whereas the rate sensitive inelastic component occurs as a consequence of thermal

¹ T_{ref} in our case is taken to be room temperature.

recovery. It is important to recognize that regardless of the deformation history, the sum of the three components at any stage must equal the total strain.

In the next section, the experimental data requirements for the uncoupled model will be described.

Experimental Data Requirements

The value of a constitutive model lies mainly in its capability to predict complex thermo-mechanical histories. However, the effectiveness of a model can be severely hampered if it requires a large number of material parameters which have to be extracted from complex and lengthy experiments. A useful constitutive model should require a minimum number of material constants which can be determined by relatively simple testing procedures.

The material parameters necessary to characterize the constitutive model previously discussed includes $f(\sigma, \sigma_{\max})$, $\Omega(\sigma, T, N)$, $K(\sigma, T, N)$, $n(T)$ and $E(T)$ where N and T refer to the number of cycles and temperature respectively. For the initial phase of this program only saturated hysteresis loop behavior will be evaluated, eliminating for the time being N as a variable. It is further assumed that for a saturated hysteresis loop, K will have a constant value around the loop whereas Ω will be allowed to vary as a function of stress. The rationale for the assumption is that the drag stress is physically associated with the dislocation cell structure, which will achieve a stable configuration upon saturation. The back stress, on the other hand, is associated with metastable dislocation arrangements such as

pileups, multiple loops around particles, etc. Once a stable cell structure is formed (i.e., at saturation), it is reasonable to assume that it does not change appreciably during strain cycling.

The experiments required to evaluate the material constants are: (1) fully reversed, strain cycling experiments (i.e., hysteresis loops) at various temperatures and strain-rates; (2) stress relaxation tests at various points on the hysteresis loops; (3) strain drop, stress transient tests; (4) strain-rate cycling tests.

The strain hardening function $f(\sigma, \sigma_{\max})$ is defined by saturated hysteresis loops taken at a sufficiently low temperature ($0.2 - 0.3 T_m$) where rate sensitivity is not significant. Hysteresis loops at higher temperatures show a reduction in flow stress due to dynamic recovery (Fig. 2). The additional inelastic strain resulting from the recovery process can be obtained by simple subtraction as shown schematically in Fig. 3.

At relatively low temperatures, the back stress can be determined by stress relaxation tests performed at various points around the hysteresis loop. It is assumed that thermal recovery is negligible and the back stress is taken to be the asymptotic value approached at the end of the stress relaxation test. In our experiments, each test was carried out to the point where the stress-rate (i.e., the slope of the stress relaxation curve) approached zero. Thermal recovery becomes significant at higher temperatures and the assumption of constant back stress is no longer valid. In this case, the strain drop, stress transient test is used to evaluate the back stress. This approach is based on the observation of a "stress transient" which occurs during

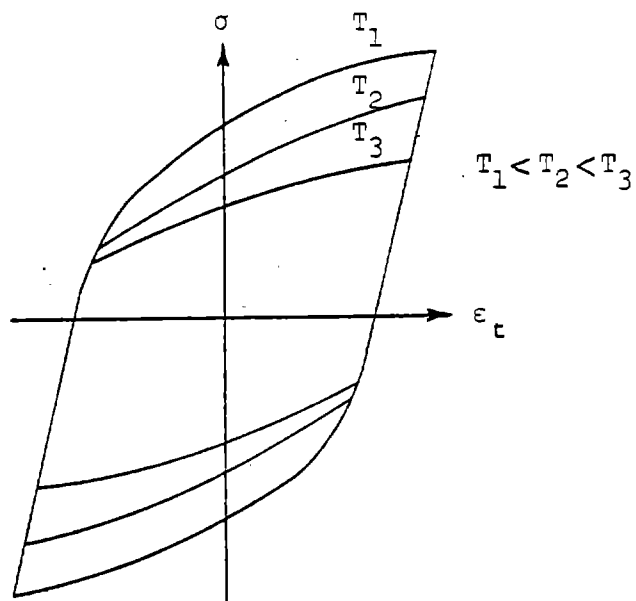


Fig. 2 Schematic of stress-strain behavior at three temperatures

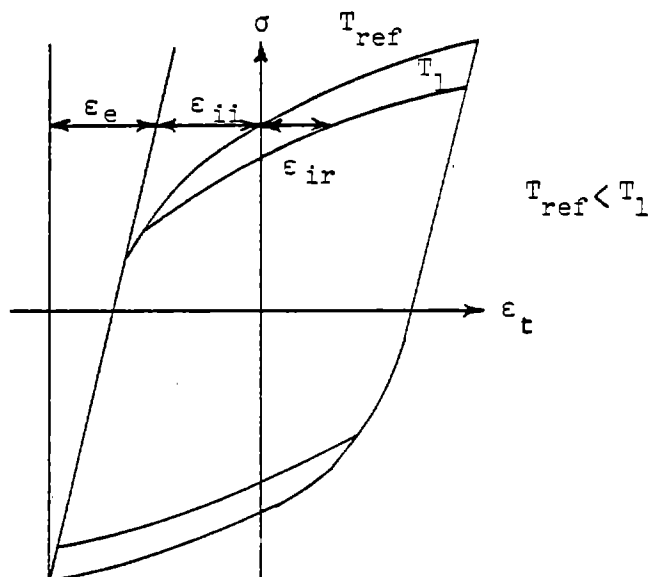


Fig. 3 Experimental characterization of the three strain components for the uncoupled viscoplastic model

load reversal when the strain is held constant momentarily. The back stress is given by the point where no transient is observed.

Other techniques have been developed for measuring internal stress and a few examples will be given here for comparative purposes. One example is an "incremental unloading technique" developed by MacEwen, et al. [47]. The test is performed by incrementally unloading the stress and observing the subsequent relaxation behavior. Positive stress relaxation will occur initially and unloading will be continued to the point where no stress relaxation is observed. The stress where this occurs is defined as the internal stress. Two alternate approaches have been summarized by Ahlquist and Nix [48]. The first one is the "stress transient dip test" which is based on the same concept as the previous technique. During a constant stress creep test, the applied stress is reduced at the point of interest and the stress transient is observed while the strain is held constant. The internal stress is given by the point where no transient is observed. The second method is referred to as the "strain transient dip test". In this case, the applied stress is reduced and held constant while the strain transient is monitored. The internal stress is indicated by the point where zero strain transient is observed. One last example is provided by Walker [17], which is based on the same concept as the strain transient dip test. In his study of cyclic behavior of Hastelloy-X specimens, the back stress was determined by holding the stress constant at various points along the unloading branch of the hysteresis loop and observe the creep rate. The back stress is defined as the point where the creep rate

goes to zero. As pointed out by Walker, the major disadvantage of this approach is that the creep strain observed in the region is very small, making an accurate assessment of the back stress difficult. He recommended the "strain drop, stress transient test" as an alternative since it is more sensitive and will allow a better estimation of the internal stress.

At lower temperatures, the stress exponent n can be obtained by plotting $\ln \dot{\epsilon}_{ir}$ vs. $\ln (\sigma - \Omega)$ from the stress relaxation tests. At higher temperatures, n is obtained from strain-rate cycling tests performed at the plateaus of the saturated hysteresis loops.

Finally, the drag stress K can be determined by substituting the known values of the back stress and the stress exponent into equation (8).

The purpose of the above discussion is to provide a general description of the experimental parameters required for the uncoupled viscoplastic constitutive model and the necessary tests for their evaluation. A more detailed discussion of the experimental procedures will be presented in the following chapter.

Numerical Scheme for Theoretical Prediction

Before a constitutive model can be used to predict complex thermo-mechanical histories, it must be able to reproduce experimental results. To first see if the uncoupled model is self consistent in being able to predict the original hysteresis loops, a numerical scheme has been devised.

The uncoupled constitutive model is represented by equation (9)

which can be rearranged in the following form:

$$\dot{\sigma} = \frac{\dot{\epsilon}_t - \text{sgn}(\sigma - \Omega) \left| \frac{\sigma - \Omega}{K} \right|^n}{\frac{1}{E} + f(\sigma, \sigma_{\max})} \quad (11)$$

or in incremental form as

$$\Delta\sigma = \frac{\Delta\epsilon_t - \text{sgn}(\sigma - \Omega) \left| \frac{\sigma - \Omega}{K} \right|^n \Delta t}{\frac{1}{E} + f(\sigma, \sigma_{\max})} \quad (12)$$

The evaluation of $\Delta\epsilon_t$ is given by $\dot{\epsilon}_t \Delta t$ where the total strain-rate (from experimental measurements) is given by

$$\dot{\epsilon}_t = \frac{-2 \frac{dD}{D_0} \frac{dt}{dt}}{1 - \frac{1}{E} \frac{d\sigma}{d\epsilon_t} (1-2\nu)} \quad (13)$$

where D_0 , $\frac{dD}{dt}$ and ν represent the initial diameter, the diametral strain-rate and the Poisson's ratio respectively. It should be noted that the total strain-rate does not remain constant during the course of deformation but instead will change with the strain hardening rate.

The point on the hysteresis loop where loading begins will be chosen as a "reference state" from which the simulation process will start. The purpose of the incremental scheme is to predict changes in material response from the preceding known state over a time interval Δt . At the reference state, the required material parameters will be specified together with the value for the initial strain hardening rate from which the initial strain-rate is determined. Next, the strain increment over the designated time interval will be computed.

The corresponding stress increment from the preceding reference state can then be calculated using equation (12). With the stress and strain increments now known, the new strain hardening rate can be computed which allows the determination of a new strain-rate value from equation (13). This will in turn enable the value of the second strain increment to be calculated. Values of the internal state variables are updated accordingly to reflect the current "micro-structural state" of the material. With the new values of internal variables and strain increment determined, the corresponding stress increment can again be computed. The procedure is then repeated for the next time increment. A program outline for this incremental procedure is presented in Appendix A.

A second numerical scheme has been designed to predict stress relaxation behavior. The "reference state" is taken to be the point on the hysteresis loop where stress relaxation commences. Once the initial conditions (i.e., initial values of the stress and internal variables) are specified, the initial rate sensitive inelastic strain-rate can be computed using equation (8), as shown below:

$$\dot{\epsilon}_{ir} = \text{sgn}(\sigma - \Omega) \left| \frac{\sigma - \Omega}{K} \right|^n \quad (8)$$

The stress relaxation tests in this research program were run under constant diameter conditions. The corresponding relation between the rate sensitive inelastic strain-rate and the stress-rate is given by

$$\dot{\epsilon}_{ir} = \frac{-2\nu}{E} \dot{\sigma} \quad (14)$$

Knowledge of the rate sensitive inelastic strain-rate will enable the stress-rate to be determined from equation (14). This will in turn allow the stress reduction over a time interval Δt to be evaluated. The same procedure is repeated by substituting the new stress value into equation (8) and assuming the back stress and drag stress remain constant. As will be discussed later, this assumption is not valid at higher temperatures and will inevitably lead to erroneous prediction. A program outline for this numerical procedure can be found in Appendix B.

CHAPTER IV

EXPERIMENTAL PROCEDURE

Material Description

The material selected for this research program is Hastelloy alloy X. It has been a successful high temperature structural material which is widely used in applications such as turbine blades in jet engines. Considerable experimental effort has been made recently to evaluate the high temperature properties of the alloy for critical applications in nuclear reactors [49] and nuclear powered rocket engines [50].

Hastelloy-X is an austenitic nickel-base superalloy that possesses good strength and oxidation resistance up to 1470 K. The alloy is solid-solution strengthened, basically by the elements Cr, Mo and W. The chemical composition of Hastelloy-X is given in Table I. The alloy used in this study was supplied in the form of 19 mm (0.75 in.) diameter bar stock in the solution heat treated condition. The standard heat treatment is performed at a temperature of 1450 K followed by rapid cooling.

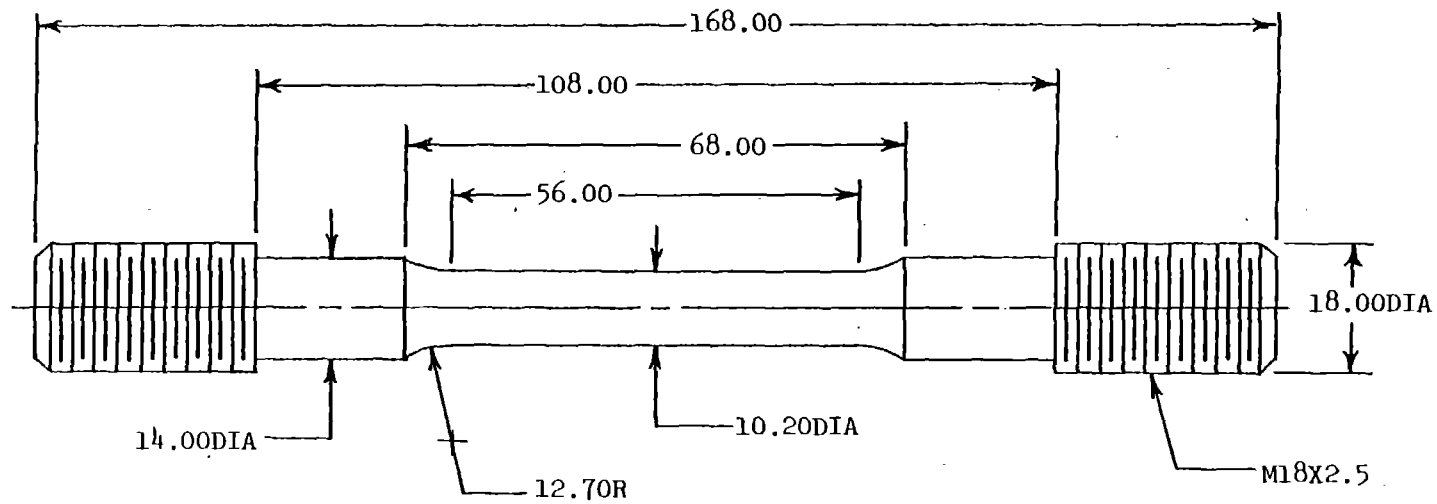
Specimen Preparation

Specimens were machined from 19 mm (0.75 in.) diameter bar stock to the configuration shown in Fig. 4. Each specimen was annealed at 1200 K for 30 minutes followed by air cooling prior to testing. The annealing process serves two purposes: (1) it will produce a more

Table I. Chemical Composition of Hastelloy-X

Alloying Element	Weight % Alloy
Cobalt	0.50 - 2.50
Chromium	20.50 - 23.00
Molybdenum	8.00 - 10.00
Tungsten	0.20 - 1.00
Iron	17.00 - 20.00
Carbon	0.05 - 0.15
Silicon	1.00*
Manganese	1.00*
Boron	0.010*
Phosphorus	0.040*
Sulfur	0.030*
Nickel	Balance

*Maximum



ALL DIMENSIONS ± 0.01
 DIMENSIONS IN MILLIMETERS
 SCALE: FULL

Fig. 4 Specimen geometry

"isotropic" microstructure, since this is an assumption made in the theoretical analysis; (2) it will provide a fully oxidized surface condition for the specimen. As will be discussed below, a stable oxidized surface condition is essential for accurate temperature measurement. The average hardness of the specimens is $54 R_A$ (Rockwell hardness number) before annealing and $52 R_A$ after annealing. Measurements were made at the gage section of the specimens.

Experimental Set Up

The experimental equipment utilized in this research program consists of four major components: (1) a 100 kip MTS Series 810 materials test system; (2) a 2.5 kW Lapel induction heating generator; (3) an LFE Series 230 temperature controller; (4) an Ircon Modline Series 6000 radiation thermometer (optical pyrometer). Picture of the experimental set up is given in Fig. 5 and a schematic is depicted in Fig. 6.

The MTS testing system is servohydraulically controlled and has considerable flexibility. It is equipped with a function generator capable of simulating complex mechanical histories under one of three control modes (load, strain or stroke). To perform high temperature experiments the MTS is equipped with special water cooled grips and a diametral extensometer utilizing quartz rods which can be used for high temperature strain measurement up to 1255 K.

The Lapel induction heater is designed to deliver to an inductively coupled load a maximum of 2.5 kW of high frequency energy in the range of 250 kHz to 800 kHz. Induction heating offers the

ORIGINAL PAGE IS
OF POOR QUALITY

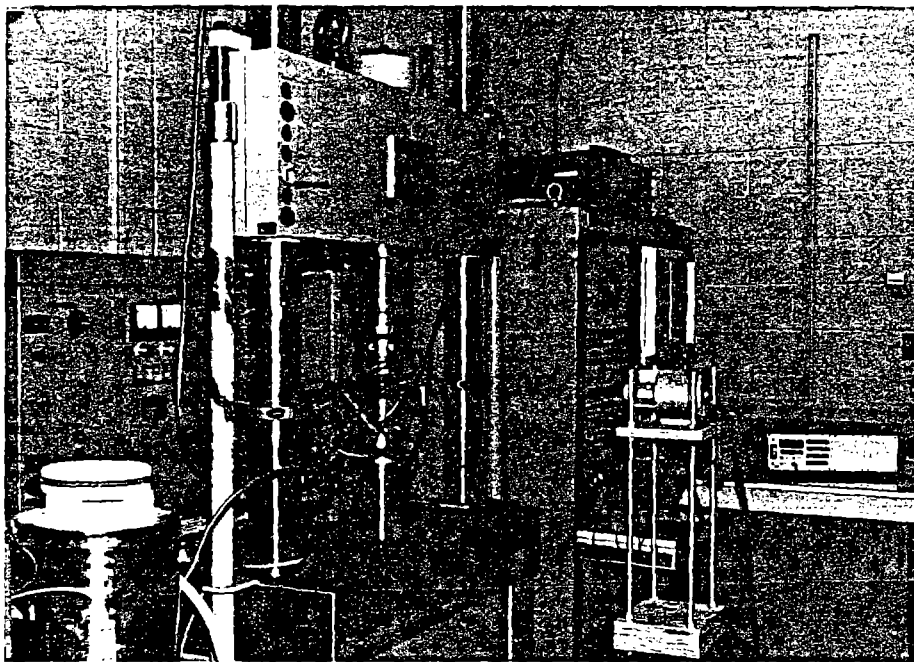


Fig. 5 Experimental set up

MPS MATERIALS TEST SYSTEM

POWER CONTROL SYSTEM

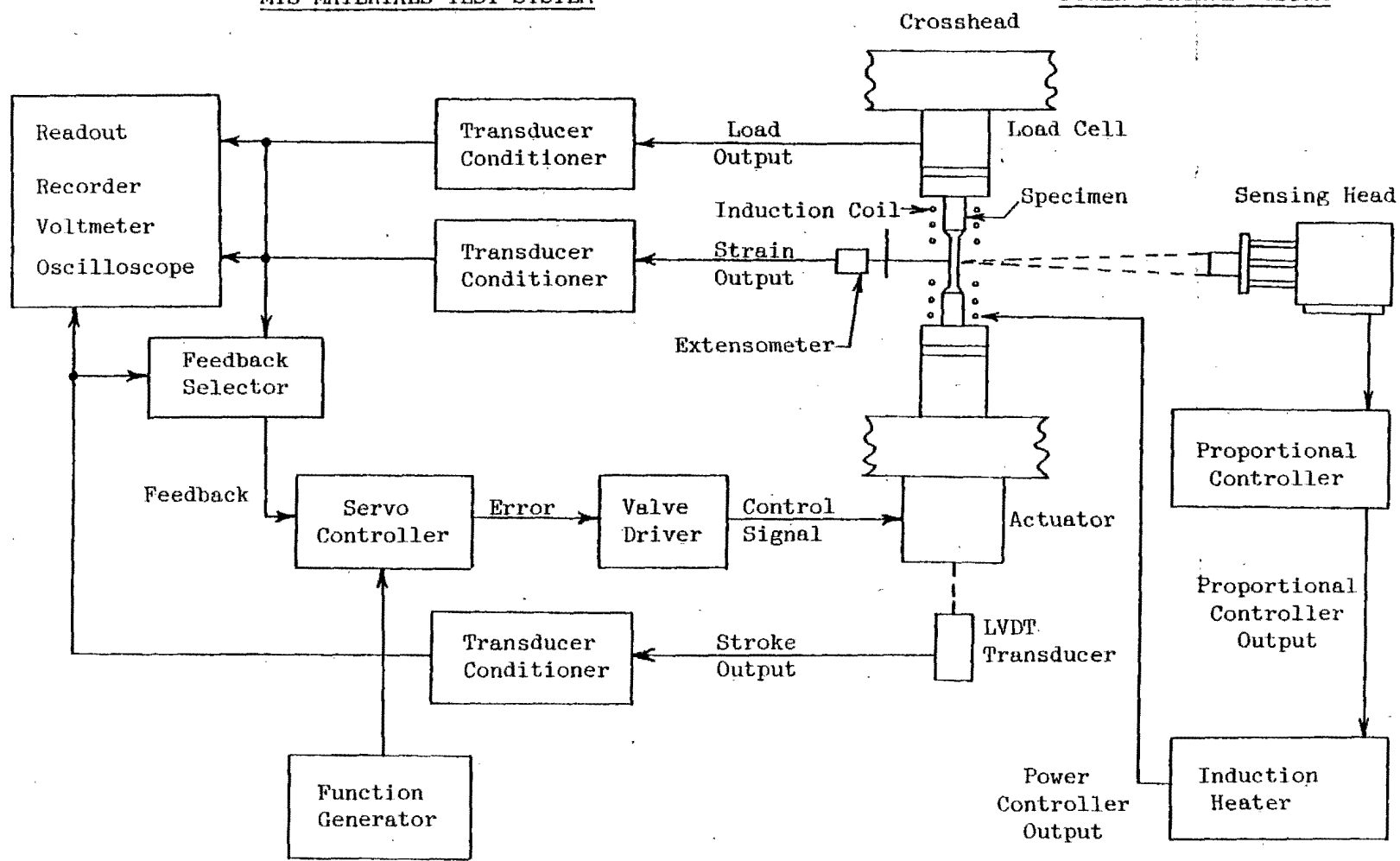


Fig. 6 Schematic of experimental set up

advantage of a rapid energy input into the specimen and is widely used for thermal or low cycle fatigue testing.

For temperature control below 700 K an LFE controller is used. It is a proportional controller which utilizes a Type J (iron-constantan) thermocouple for temperature measurement. Power output of the induction heater is adjusted by the controller in proportion to the difference between the measured and the set point temperatures. For temperature control above 700 K, an Ircon optical pyrometer is employed. It is a "noncontact" type controller which measures the temperature of an object by sensing the infrared radiation emitted from its surface. Temperature control is based on the same principle as the LFE controller. An output current is developed in the controller proportional to the deviation of the specimen temperature from the set point temperature, which governs the power output generated by the power controller inside the induction heater.

Good facilities are a necessary but not sufficient condition to produce satisfactory results. Additional steps have to be taken to minimize experimental error which might occur as a result of the limitations imposed by the testing equipment itself. In the case of high temperature materials testing under cyclic loading conditions, the most important factors to be considered include: (1) measurement and control of temperature; (2) axiality of testing machine.

In strain controlled low cycle fatigue testing, it is considered that the temperature should be controlled to within ± 2 K for reproducible results. In this research program, temperature variation at 1144 K was no more than ± 1.1 K and better temperature control was

attained at lower temperatures. The accuracy of temperature measurement by optical pyrometry depends on the emissivity of the material which is a function of both surface condition and temperature. For example, a nickel specimen with a smooth polished surface has an emittance value of 0.15 which increases dramatically to 0.90 when it becomes oxidized. Roughening of the specimen surface due to oxidation has a significant impact on the resulting emissivity value and thus poses a severe temperature control problem. To overcome this difficulty, all specimens were annealed at 1200 K for 30 minutes prior to testing to produce a stable oxidized surface condition. The emissivity has also been found to vary with temperature, which necessitates readjustment to the emittance setting on the optical controller every time the set point temperature is changed. This disadvantage is overcome by calibrating the optical pyrometer against a high precision, factory calibrated Type K (chromel-alumel) thermocouple which has an absolute accuracy of ± 3 K. Calibration was performed in a conventional furnace using a small Hastelloy-X sample cut from the gage section of one of the original specimens. Additional thermocouples were attached to the sample to verify the absence of significant thermal gradient. The thermocouples were protected with Inconel overbraid and ceramic fiber insulation against oxidation and possible contamination by the furnace atmosphere.

Induction heating offers the advantage of fast thermal response and relatively simple experimental set up. The thermal gradient at the middle of the specimen was minimized by concentrating the coil turns near the ends of the specimen at the expense of heating

efficiency.

For fully reversed low-cycle fatigue testing, it is recommended by ASTM-E606 that bending strain should not exceed 5% of the minimum axial strain range. A trial specimen equipped with three equally spaced strain gauges around the circumference was used to check the axiality of the MTS. Special alignment procedure were employed to reduce an initial variation in axial strain measurements by the strain gauges from 30% to 5% maximum.

Description of Experiments.

In this section, the various experiments necessary to determine the material constants are described. The required tests are:

- (1) fully reversed, strain cycling experiments (hysteresis loops);
- (2) stress relaxation tests; (3) strain drop, stress transient tests;
- (4) strain-rate cycling tests.

Fully reversed, strain cycling experiments (hysteresis loops).

In this research program, saturated hysteresis loops are used to characterize the behavior of Hastelloy-X under cyclic loading conditions. The experiments cover temperature range from 294 K to 1144 K ($0.2 - 0.75 T_m$) and a strain-rate range from $3.3 \times 10^{-5} s^{-1}$ to $1 \times 10^{-3} s^{-1}$. It is important that the range of temperatures and strain-rates selected for the experimental study can adequately represent the conditions encountered in actual service. Generally speaking, turbine operations typically take place between 700 K and 950 K and the strain-rate range covered in this study is consistent with those considered by other researchers [17, 50]. A triangular

waveform is used as the input function for strain cycling as recommended by ASTM-E606 since it provides a more uniform rate of straining. The waveform selected is important to the resultant stress-strain response especially at high temperatures, where inelastic deformation is extremely rate sensitive. All experiments in this research program were performed in the strain-control mode. In this control mode, a servohydraulic machine (MTS in this case) has essentially infinite stiffness, thus avoiding the complications introduced by the elastic modulus of the testing system.

Experiments were conducted at ten different temperatures and three different strain-rates. Below $0.5 T_m$, rate sensitivity is not important and hysteresis loops were run at selected temperatures (294 K, 533 K and 755 K). Above $0.5 T_m$, the material becomes more rate sensitive and experiments were conducted at 55 K intervals from 811 K to 1144 K to determine the required material constants. At each temperature, strain-cycling was performed at three different strain-rates ($1 \times 10^{-3} \text{s}^{-1}$, $3.3 \times 10^{-4} \text{s}^{-1}$, $3.3 \times 10^{-5} \text{s}^{-1}$) with a strain range of $\pm 1\%$.

As discussed previously, room temperatures hysteresis loops were used to define the rate insensitive, inelastic strain component, which has a σ_{\max} dependence. Therefore, hysteresis loops were obtained at different strain amplitudes (0.05%, 0.1%, 0.2%, 0.3%, 0.4%, 0.6%, 0.8% and 1%) which correspond to different σ_{\max} values.

Stress relaxation tests. The stress relaxation test is a technique commonly used for back stress determination. It is usually performed during a tensile test by suddenly stopping the crosshead

and monitor the stress variation with time while holding the strain constant. Initially, the total strain consists of an elastic component as well as an inelastic component. Additional rate dependent inelastic strain (i.e. creep strain) occurs at the expense of the elastic strain component. Since the elastic strain is a function of the applied stress, a stress reduction is necessary to maintain the total strain constant. As indicated by equation (8), the creep rate is governed by the stress (or effective stress) which decreases steadily during the course of stress relaxation. Ideally, creep is terminated as the effective stress drops to zero; i.e., when the applied stress equals the back stress. Thus, the back stress can simply be defined as the asymptotic value reached at the end of a stress relaxation test where the stress relaxation rate is approaching zero. The stress relaxation test offers a convenient way of determining the internal stress provided that it remains constant during the test. This condition cannot be satisfied at high temperatures where thermal recovery becomes important and can cause a substantial reduction of the internal stress. An early attempt has been made to analyze experimental stress relaxation data for Hastelloy-X using an indirect approach suggested by Gupta and Li [51]. The method failed to produce meaningful results for the back stress and stress exponent at 978 K and above, indicating the significance of recovery during stress relaxation at these elevated temperatures.

In this research program, stress relaxation tests were only used in the temperature range of 755 K to 922 K ($0.49 - 0.60 T_m$) at different points around the saturated hysteresis loops to determine

various values for the back stress. Due to the experimental set up, diametral strain rather than axial strain is held constant during stress relaxation and the resulting relation between the creep rate and the stress-rate is given by equation (14), repeated as below:

$$\dot{\epsilon}_{ir} = \frac{-2\nu}{E} \dot{\sigma} \quad (14)$$

The value of the stress exponent n can be obtained by plotting $\ln \dot{\epsilon}_{ir}$ vs. $\ln(\sigma - \Omega)$. The least square curve fitting technique can be used to give the best estimation for n . With the values for the back stress and stress exponent determined, the drag stress can be computed by rewriting equation (8) as follows:

$$K = |\sigma - \Omega| |\dot{\epsilon}_{ir}|^{\frac{-1}{n}} \quad (15)$$

Strain drop, stress transient tests. As discussed above, the stress relaxation test is unsuitable for back stress determination at high temperature due to thermal recovery. The strain drop, stress transient test is employed as an alternative in the temperature range of 978 K to 1144 K (0.64 - 0.75 T_m). A schematic of this approach is shown in Fig. 7, which is based on the same principle as the "incremental unloading technique" [47] and the "stress transient dip test" [48] described in the previous chapter. During strain cycling, the unloading strain-rate is temporarily interrupted and while the strain is held constant, the stress transient is monitored. Referring to Fig. 7 (p. 43), if strain cycling is stopped at point A, positive stress relaxation will occur, indicating that the applied stress is

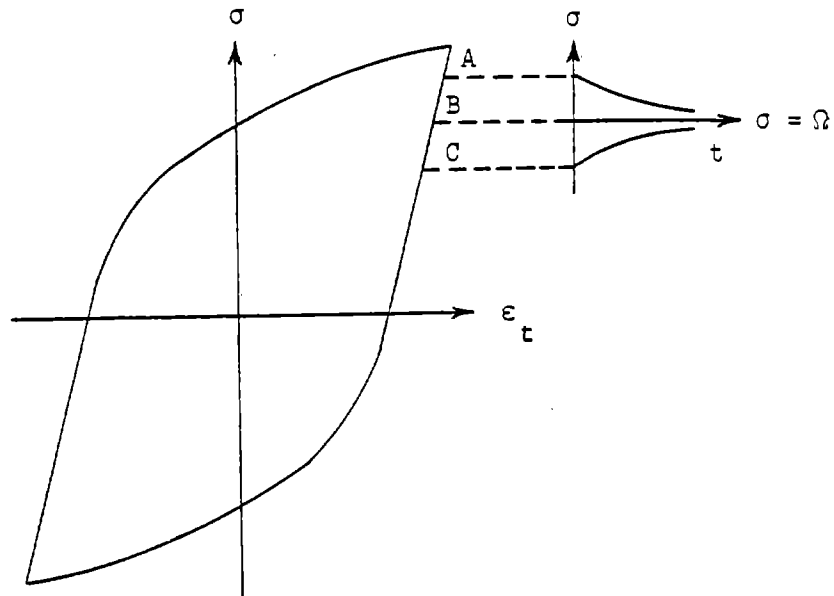


Fig. 7 Schematic for the strain drop, stress transient test

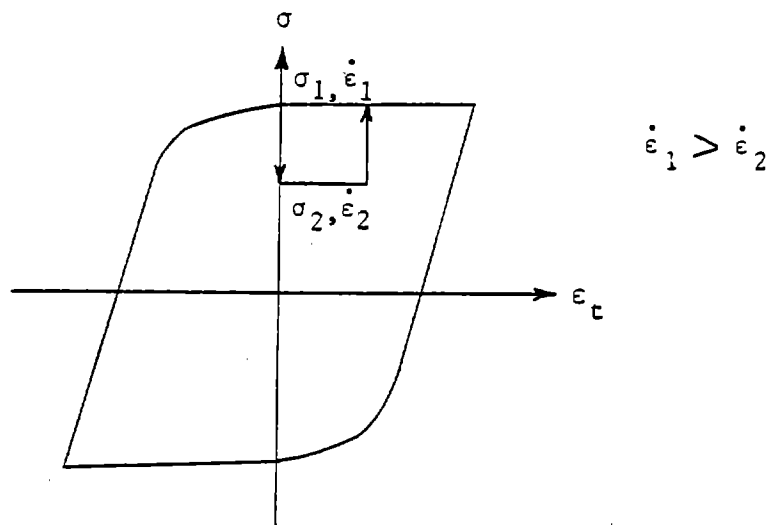


Fig. 8 Schematic for the strain-rate cycling test

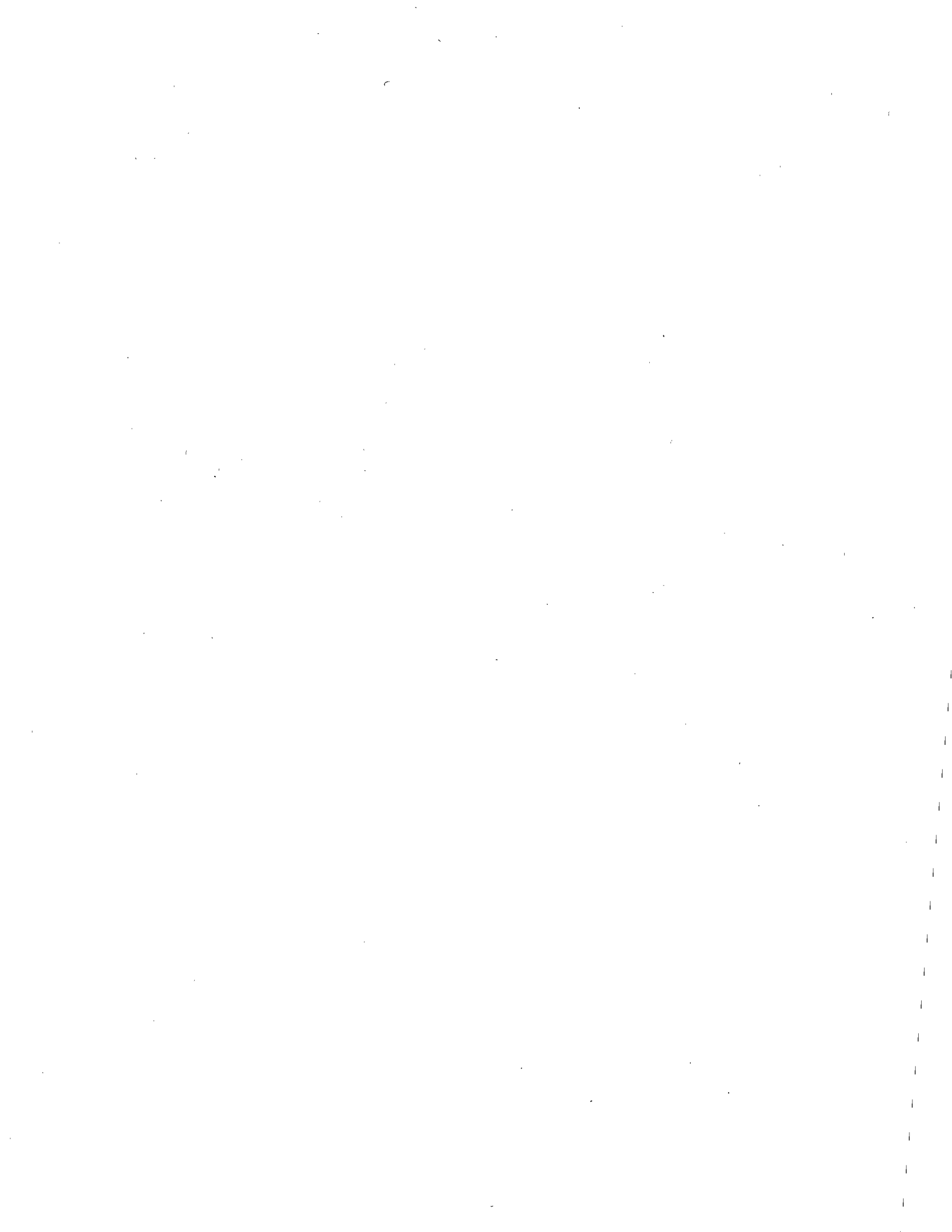
larger than the back stress. On the other hand, if the strain is held constant at point C, negative stress relaxation will occur since the back stress is now greater than the applied stress. The internal stress is given by point B where no stress transient is observed. Therefore, by introducing a series of load interruption on successive cycles at various points on the tension/compression stress reversal portion of the hysteresis loop, the internal stress value for the peak stress on the hysteresis loop can then be determined. The load transient during the first quarter second immediately after the interruption is in part due to machine characteristics and thus should be disregarded. The transient after this time is due principally to real material behavior.

Strain-rate cycling tests. The strain-rate cycling test is designed to determine the stress exponent in the temperature range of 978 K to 1144 K ($0.64 - 0.75 T_m$). The test is performed at the "plateau" of the hysteresis loop where the stress has saturated to a constant value. At the point of interest, the strain-rate is abruptly changed and the new flow stress is noted before returning to the original strain-rate. A schematic of the test is depicted in Fig. 8. It is assumed that the drag stress remains relatively constant during the strain-rate change and the reduction in flow stress is mainly a result of a decrease in the back stress. The physical basis for this assumption is that the drag stress is associated with the formation of a stable cell structure which is not expected to change appreciably during the strain-rate change. It will be shown later that the strain drop, stress transient test does indicate a decrease in back stress as

the strain-rate is reduced. The fact that the stress remains constant at the plateau region indicates a balance between strain hardening and dynamic recovery and is equivalent to steady state creep. This implies that the total strain-rate in this region equals the rate sensitive inelastic strain-rate as described by equation (8). Referring to Fig. 8 (p. 43), if σ_1 and σ_2 denote the flow stress at two different strain-rates $\dot{\epsilon}_1$ and $\dot{\epsilon}_2$, then the value of the stress exponent n can be computed as

$$n = \ln(\dot{\epsilon}_1 / \dot{\epsilon}_2) / \ln[(\sigma_1 - \Omega_1) / (\sigma_2 - \Omega_2)] \quad (16)$$

assuming K remains constant (during the period when σ_1 drops to σ_2), Ω_1 and Ω_2 being determined previously by the strain drop, stress transient test. With the value of n now known, the drag stress can be calculated from equation (15).



CHAPTER V

EXPERIMENTAL RESULTS, ANALYSIS AND DISCUSSION

The results of the experimental work for this research project will be described here in detail. The equations required for data analysis will be presented first, followed by the discussion of hysteresis loop and stress relaxation results. The various material constants and their physical significance will also be considered.

Data Reduction

Since diametral extensometer is employed in the experimental work, data reduction is performed in terms of diameter change. Engineering stress and engineering strain are employed in data analysis. Since the strain range in our experiments is limited to $\pm 1\%$, it would make little difference if true stress and true strain are used instead. Diameter measurements can be converted into axial strain using the following relationship:

$$\epsilon_t = \frac{\sigma}{E} (1-2\nu) - 2 \frac{dD}{D_o} \quad (17)$$

where σ is the applied stress, E and ν are the Young's Modulus and the Poisson's ratio, dD and D_o represent the diameter increment and the initial diameter respectively. The axial inelastic strain is calculated as the difference between the total strain and the elastic strain, or

$$\epsilon_i = - 2 \left(\frac{\nu\sigma}{E} + \frac{dD}{D_o} \right) \quad (18)$$

The total strain-rate is represented by equation (13) which is repeated as follows:

$$\dot{\epsilon}_t = \frac{\frac{-2}{D_o} \frac{dD}{dt}}{1 - \frac{1}{E} \frac{d\sigma}{d\epsilon_t} (1-2\nu)} \quad (13)$$

The inelastic strain-rate is given by

$$\dot{\epsilon}_i = \frac{-2}{D_o} \frac{dD}{dt} \left(\frac{1 - \frac{1}{E} \frac{d\sigma}{d\epsilon_t}}{1 - \frac{(1-2\nu)}{E} \frac{d\sigma}{d\epsilon_t}} \right) \quad (19)$$

where $\frac{dD}{dt}$ is the programmed diametral strain-rate and $d\sigma/d\epsilon_t$ is the strain hardening rate which is expressed as

$$\frac{d\sigma}{d\epsilon_t} = \frac{1}{\frac{(1-2\nu)}{E} - \frac{2}{D_o} \frac{dD}{d\sigma}} \quad (20)$$

where $dD/d\sigma$ is the diameter change rate with respect to stress. A complete derivation of the above equations is given in Appendix C.

Once the strain hardening function $f(\sigma, \sigma_{\max})$ is defined, the rate insensitive, inelastic strain-rate can be separated from the total inelastic strain-rate using equation (6).

Hysteresis Loop Results

The rate insensitive, inelastic strain is defined by the strain hardening function which is σ_{\max} dependent. Hysteresis loops were run at room temperature for various strain ranges which correspond to different σ_{\max} values. The experimental results are shown in Fig. 9¹

¹ Strain-rates shown in figures represent average values.

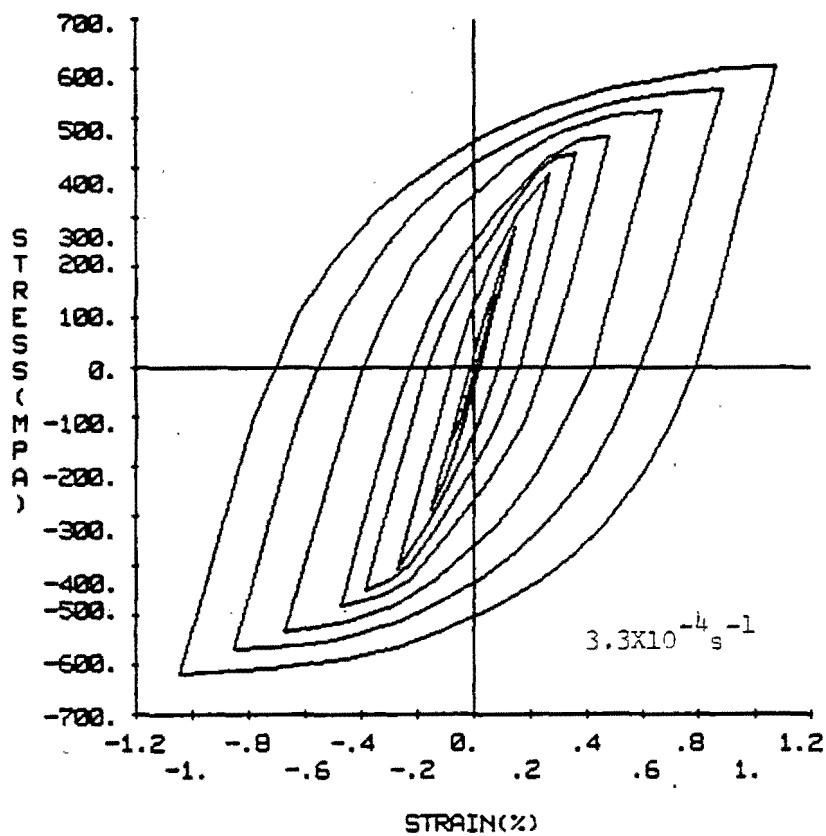


Fig. 9 Saturated hysteresis loops for Hastelloy-X at room temperature with strain amplitudes of 0.05%, 0.1%, 0.2%, 0.3%, 0.4%, 0.5%, 0.6%, 0.8% and 1.0%

with values of the strain hardening function tabulated in Appendix D. The effect of the maximum stress on the stress-strain response is apparent by comparing the values of the strain hardening function at different strain amplitudes. It can be seen that for a given stress, the value of the strain hardening function decreases as a function of σ_{\max} . In other words, the strain hardening rate at a given stress level decreases as σ_{\max} increases. As discussed in Chapter III, strain hardening is physically associated with the building up of long range internal stress, the magnitude of which depends on the total strain (or applied stress). Upon load reversal, dislocations initially stopped by dislocation barriers become mobilized, making inelastic deformation easier in the opposite direction. A higher σ_{\max} value corresponds to a higher back stress which results in a lower strain hardening rate upon load reversal, since inelastic deformation can occur easily. On the other hand, a small back stress (or σ_{\max}) will not offer much assistance upon load reversal, which accounts for the higher strain hardening rate observed. The effect of the back stress results in a lower yield strength in reverse loading. This phenomenon is referred to as the Bauehinger effect which results in "kinematic hardening" in crystalline materials.

The strain-rate dependence of Hastelloy-X at room temperature is studied by strain-cycling tests at three different strain-rates as shown in Fig. 10. The hysteresis loops at the higher strain-rates are identical while a slight reduction in the peak stress of the hysteresis loop is observed at the lower strain-rate. Nevertheless, the difference is small and the material can be considered rate

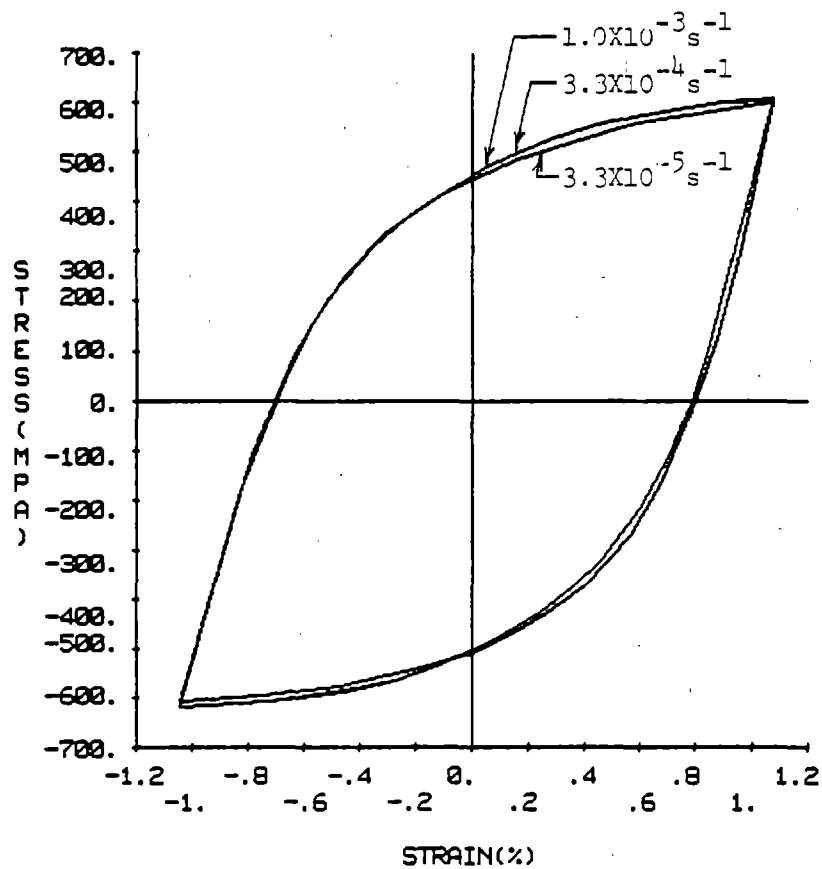


Fig. 10 Saturated hysteresis loops for Hastelloy-X at room temperature

"insensitive". Hysteresis loop results at 533 K (Fig. 11) are almost identical with those at room temperature, indicating the alloy is basically rate insensitive over these temperature and strain-rate ranges. At 755 K ($0.49 T_m$), the hysteresis loops change slightly (Fig. 12a), though the difference observed is still not significant. The higher strain hardening rate at these low temperatures are characterized by the rounded corners of the hysteresis loops, which is a good indication that inelastic deformation is mostly rate insensitive. The absence of significant dynamic recovery at 755 K is evidenced by the small amount of rate sensitive inelastic strain observed at this temperature (Fig. 12b). The rate sensitive inelastic strain component is obtained by subtracting the rate insensitive inelastic strain (defined by room temperature hysteresis loops) from the total inelastic strain. Over this temperature range, the shape of the loading portion of the hysteresis loop is similar to that of the unloading portion. This is expected to be the case if the overall deformation process remains the same during loading and unloading. At these relatively low temperatures, deformation occurs almost exclusively in the grain matrix via dislocation glide and limited recovery through dislocation cross-slip. Upon load reversal the direction of dislocation motion changes, but the relative significance of the deformation mechanisms remains the same. As will be discussed later, directionality of the loading path can affect the resulting stress-strain behavior when grain boundary sliding becomes important.

At 533 K and 755 K, Hastelloy-X has been found to exhibit inverse strain-rate sensitivity; i.e., the strain hardening rate of

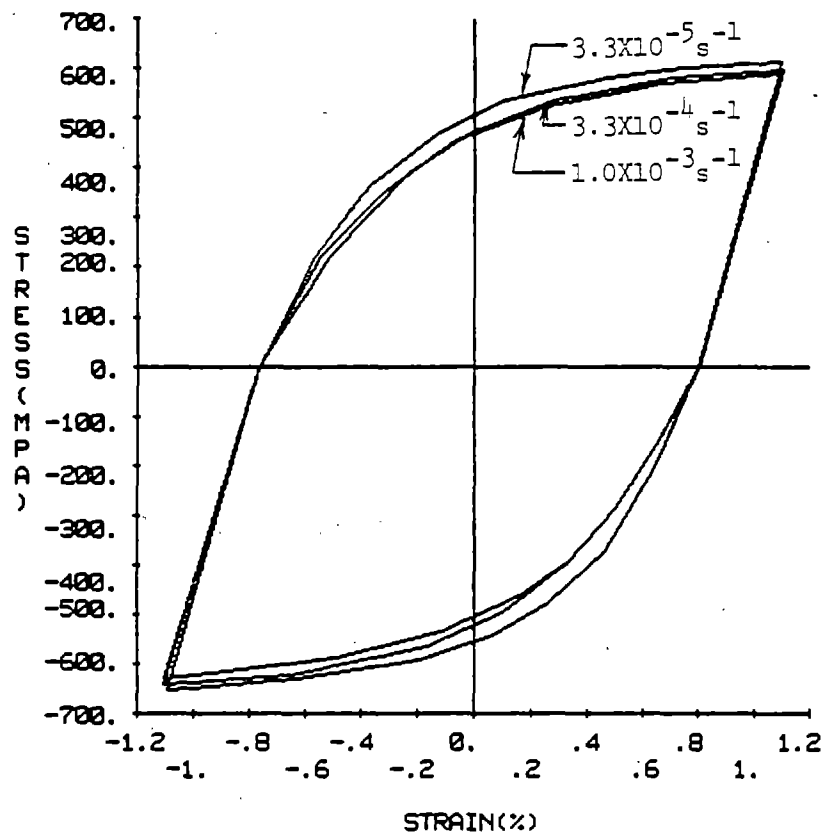
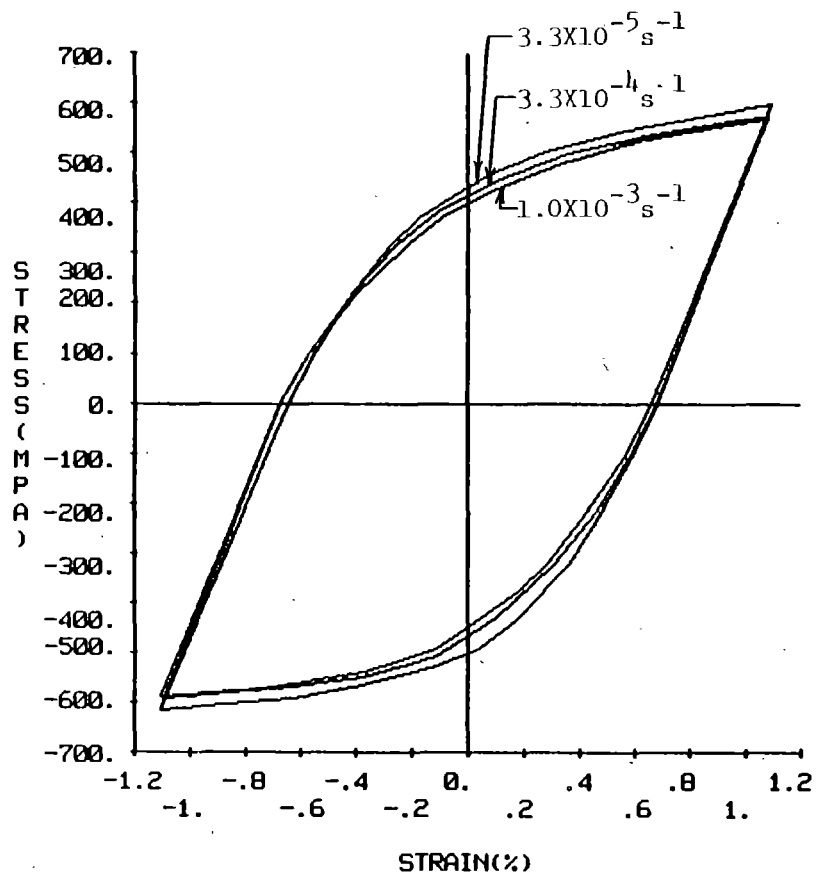
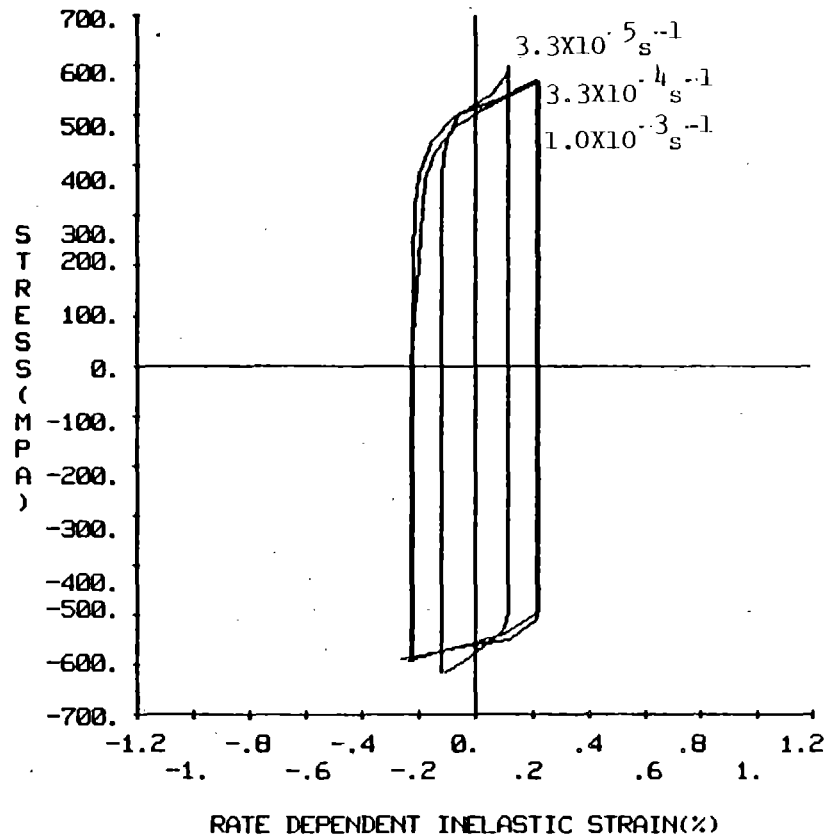


Fig. 11 Saturated hysteresis loops for Hastelloy-X at 533K



(a)



(b)

Fig. 12 Saturated hysteresis loops for Hastelloy-X at 755K. (a) Stress vs. total strain. (b) Stress vs. rate dependent (or rate sensitive) inelastic strain

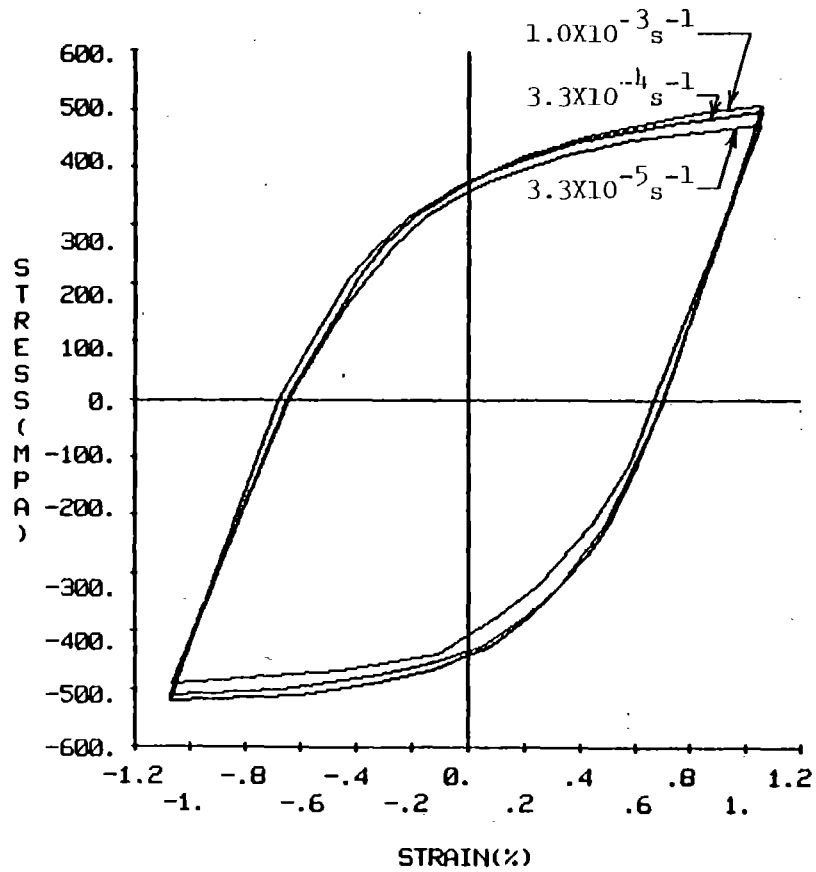
the hysteresis loop increases at reduced strain-rate, contrary to normal behavior. This phenomenon is believed to be resulted from dynamic strain aging, which is associated with the formation of solute atom atmospheres around dislocations. Dynamic strain aging involves solute diffusion to dislocation sites. This can only occur when the diffusion rate of solute atoms is similar to the dislocation velocity. Since atomic diffusion is temperature dependent and dislocation velocity is stress-rate controlled, dynamic strain aging can take place only at a suitable combination of temperature and strain-rate. At low temperatures, atomic mobility is low due to limited thermal assistance, and dynamic strain aging does not occur in general. As the temperature is raised, sufficient thermal energy will enable solute atoms to catch up with moving dislocations and the drag stress exerted by the dislocation atmospheres cause the material to strain harden. At higher temperatures, the dislocation atmospheres become dispersed as a result of an increased entropy driving force and dynamic strain aging is again unimportant. Since dynamic strain aging is possible only when the solute diffusion rate is compatible with the dislocation velocity, it will occur at different strain-rate ranges for different temperatures. The higher the temperature, the higher the strain-rate range in which dynamic strain aging will take place.

Experiments conducted on Hastelloy-X specimens reveal that inverse strain-rate sensitivity takes place in the temperature range from 533 K to 755 K ($0.35 - 0.49 T_m$) for the strain-rates used in this study. Another phenomenon associated with dynamic strain aging is the

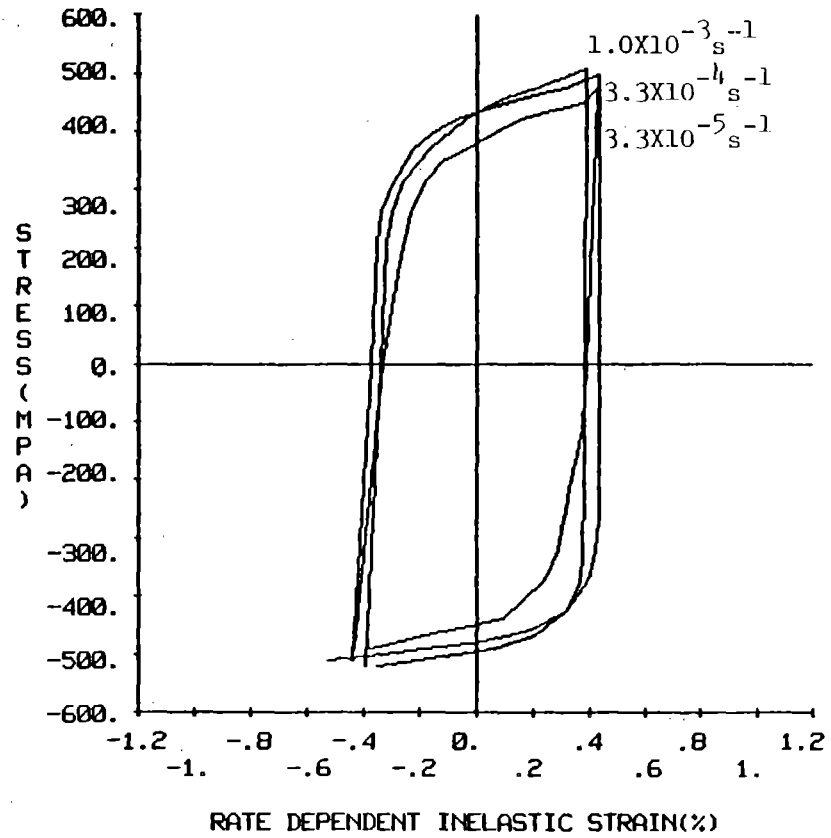
so called Portevin-LeChatelier effect . This is manifested by irregularities in the stress-strain curve which is often accompanied by sharp load drops. This effect is observed from 533 K up to 922 K ($0.35 - 0.60 T_m$) for Hastelloy-X specimens but becomes negligible above 811 K ($0.53 T_m$). It has also been found that at a given temperature the Portevin-LeChatelier effect is more pronounced at higher strain-rates for the strain-rate range considered in this research. The effects of dynamic strain aging have also been reported by other investigators [17, 50].

As the temperature is raised above $0.5 T_m$, rate effects become apparent. At 811 K and 866 K, the size of the hysteresis loops become smaller due to dynamic recovery (Fig. 13a and 14a). However, the hysteresis loops remain similar in shape to those at lower temperatures, indicating that a substantial portion of the inelastic strain is still rate insensitive. As shown by Fig. 13b and 14b, the rate sensitive inelastic strain represents about only half of the total strain. At 922 K, the more intense thermal activity is reflected by the relatively "square" appearance of the hysteresis loops (Fig. 15). At 978 K and above (Fig. 16 - 19), dynamic recovery represents a dominant deformation process and the inelastic strain is essentially all rate sensitive.

It has been observed that hysteresis loops are asymmetric; i.e. the material appears to be stronger in compression than in tension. This phenomenon can be explained in two ways: (1) material deformation is history dependent, i.e. the material has a memory of past events; (2) at high temperatures where history dependence is not significant,

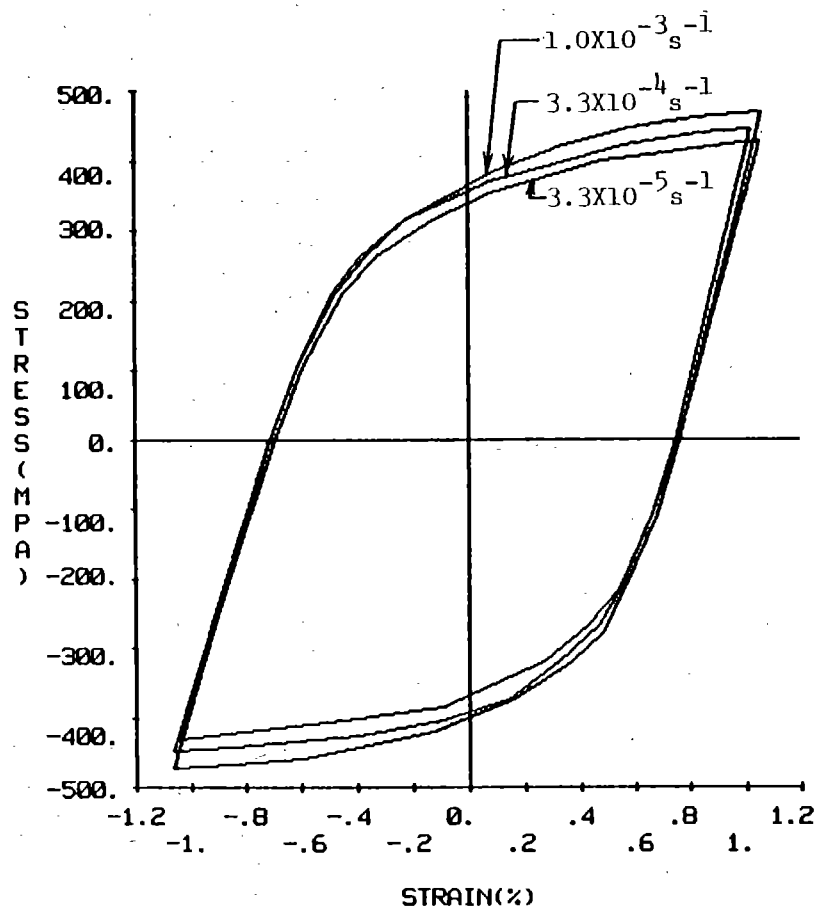


(a)

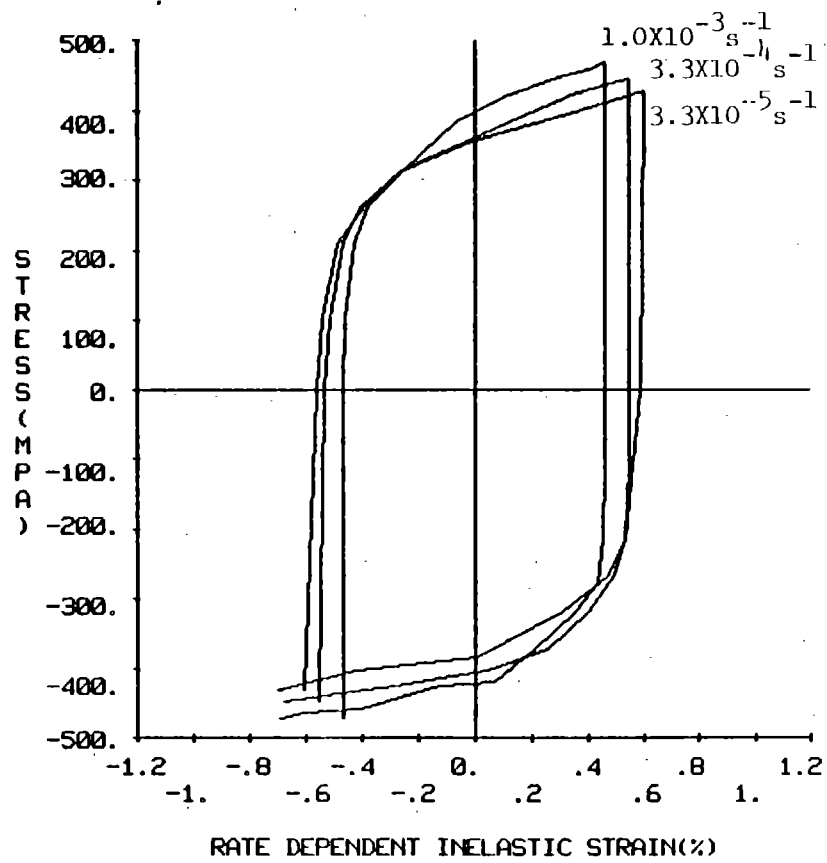


(b)

Fig. 13 Saturated hysteresis loops for Hastelloy-X at 811K. (a) Stress vs. total strain. (b) Stress vs. rate dependent (or rate sensitive) inelastic strain

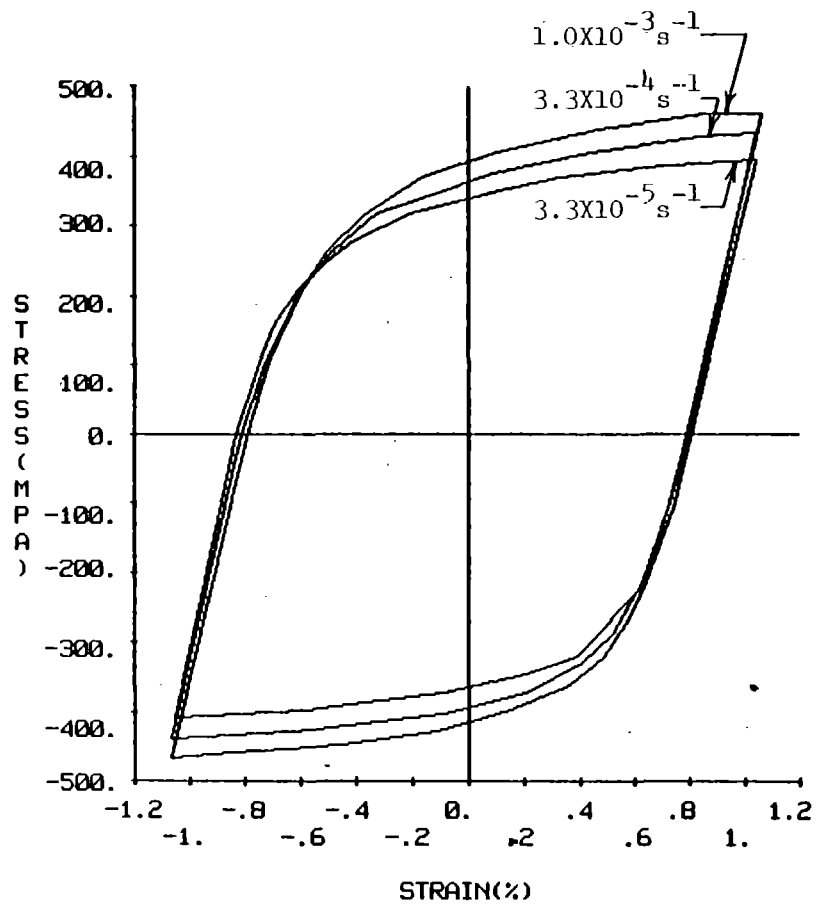


(a)

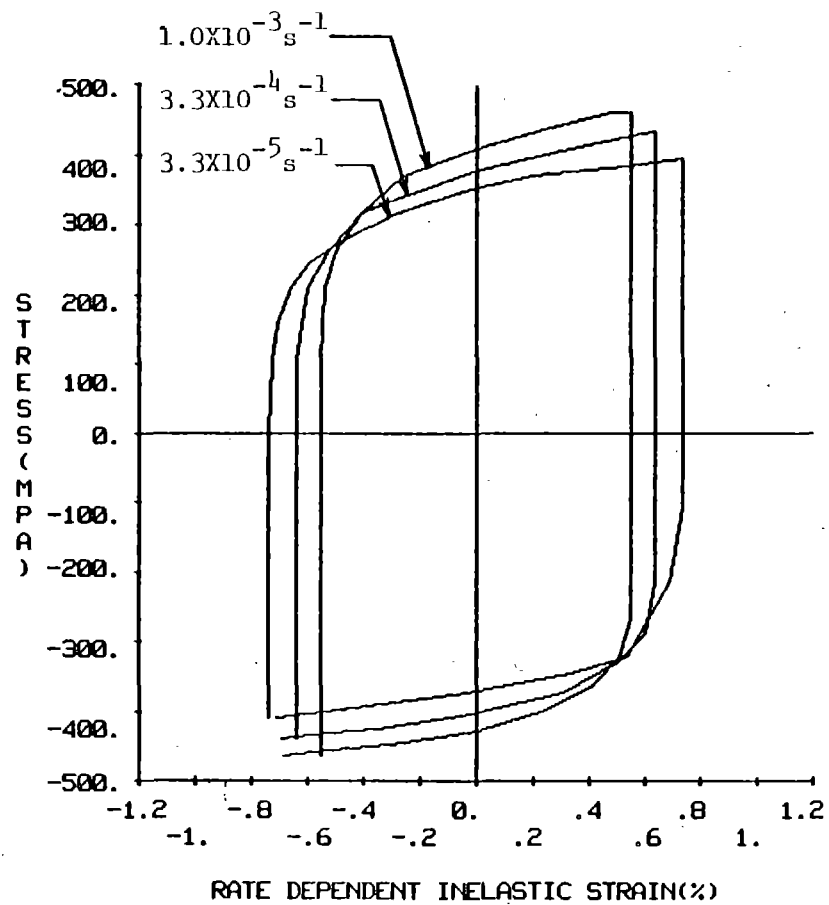


(b)

Fig. 1) Saturated hysteresis loops for Hastelloy-X at 866K. (a) Stress vs. total strain. (b) Stress vs. rate dependent (or rate sensitive) inelastic strain

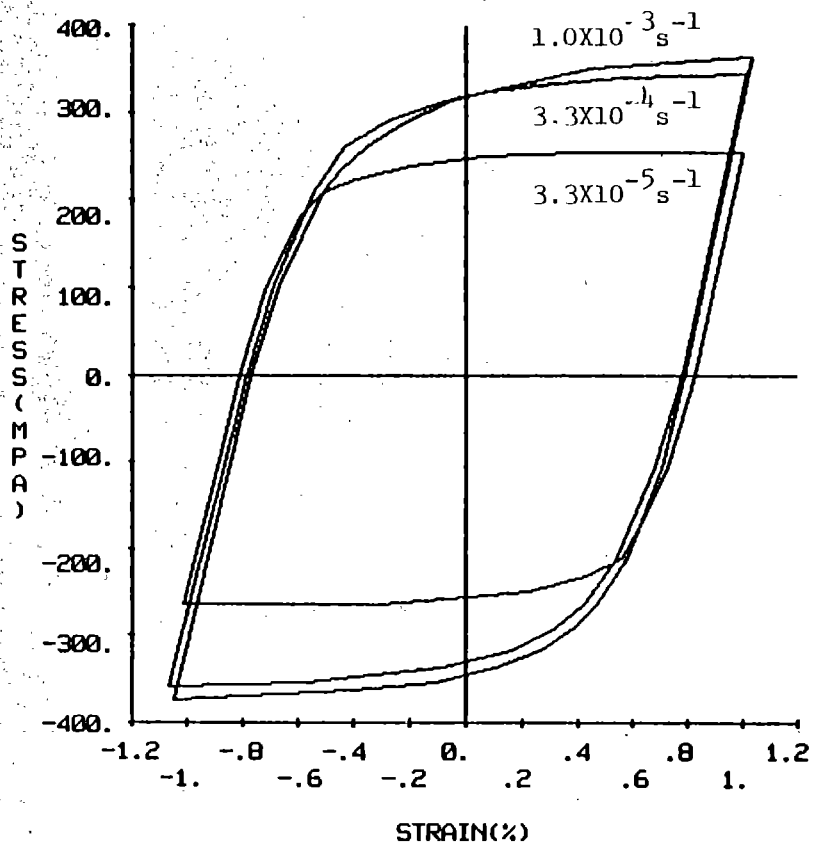


(a)

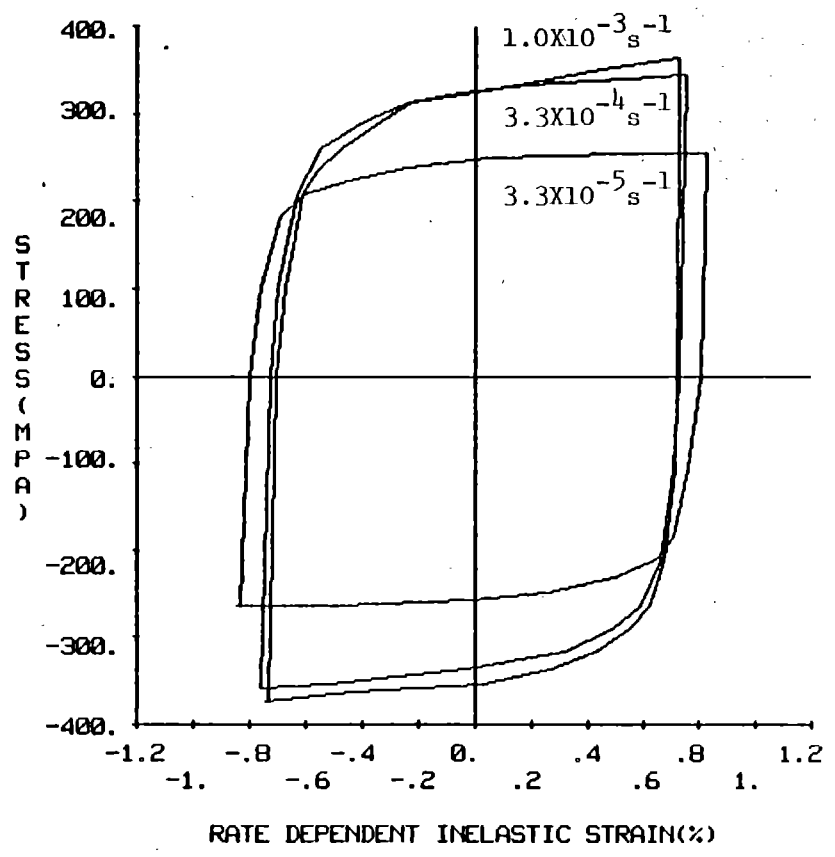


(b)

Fig. 15 Saturated hysteresis loops for Hastelloy-X at 922K. (a) Stress vs. total strain. (b) Stress vs. rate dependent (or rate sensitive) inelastic strain

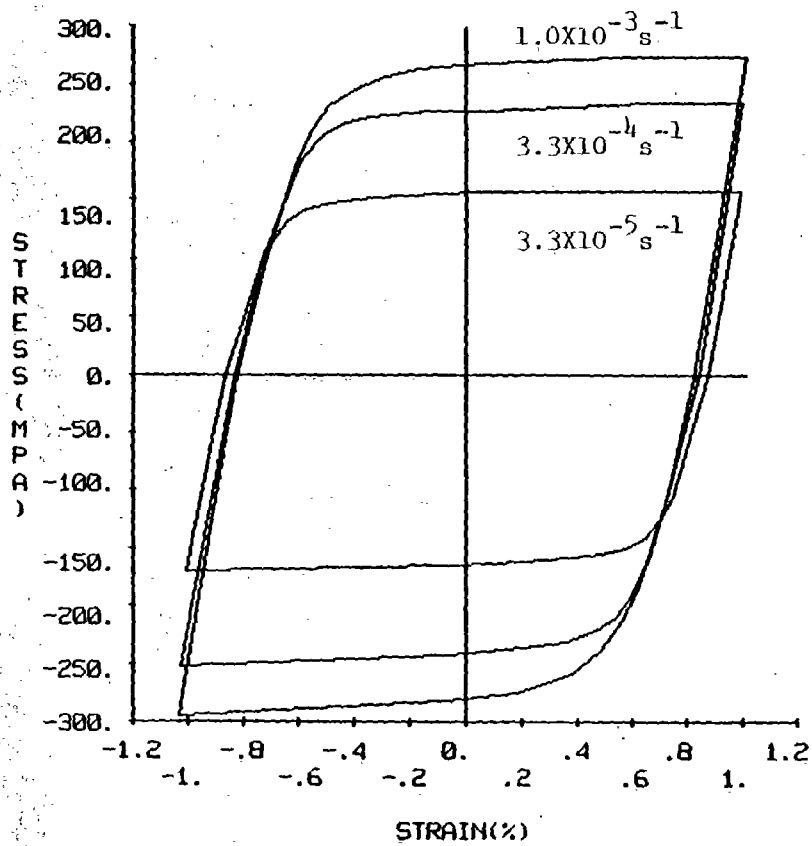


(a)

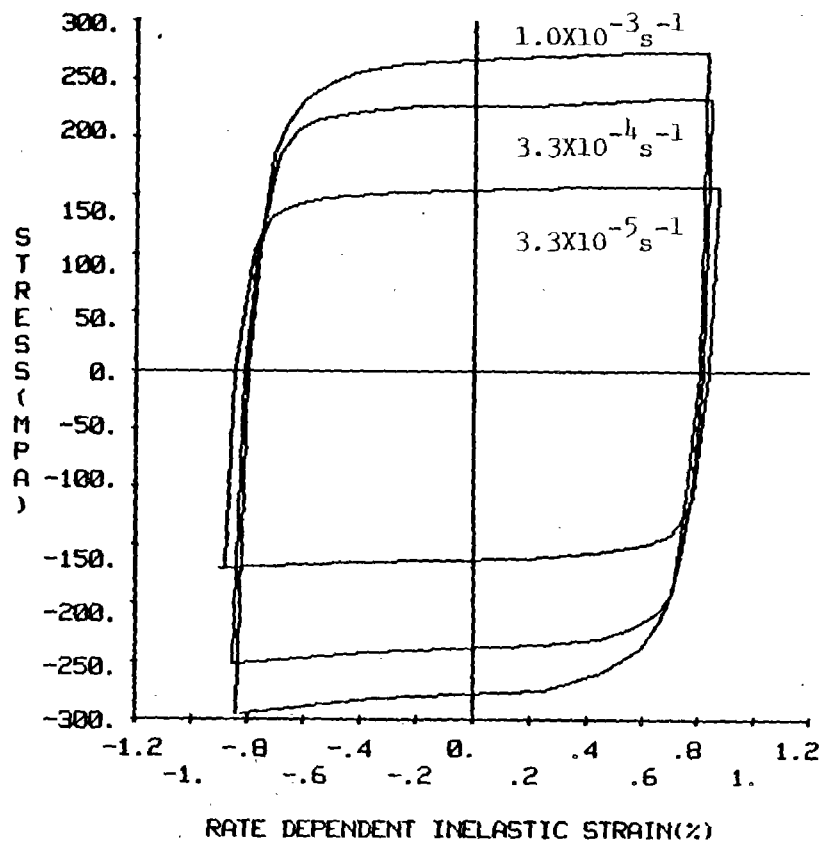


(b)

Fig. 16 Saturated hysteresis loops for Hastelloy-X at 978K. (a) Stress vs. total strain. (b) Stress vs. rate dependent (or rate sensitive) inelastic strain

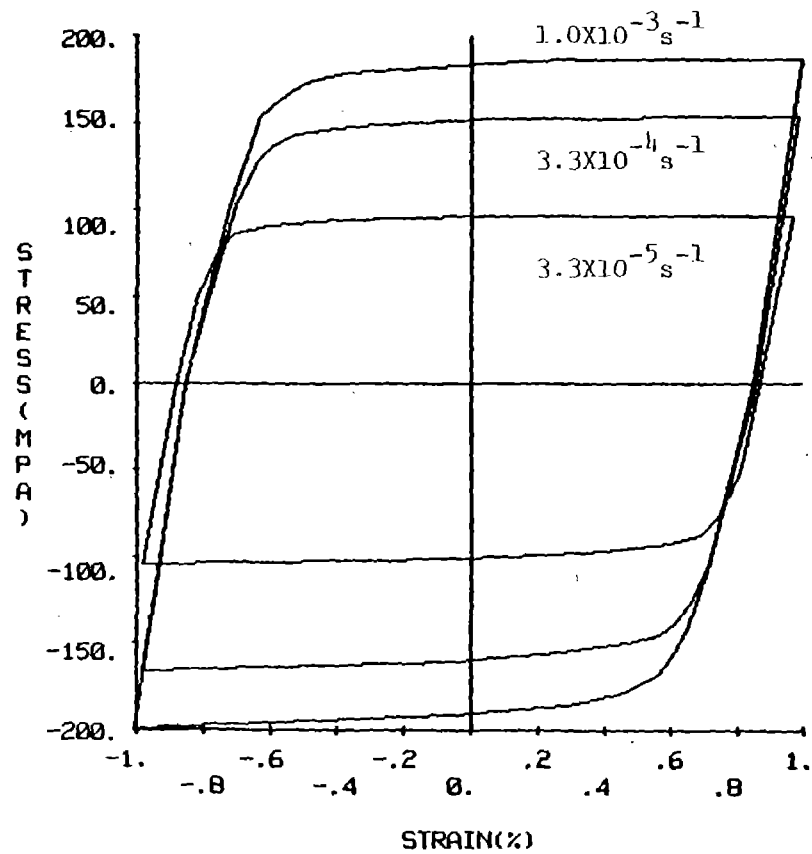


(a)

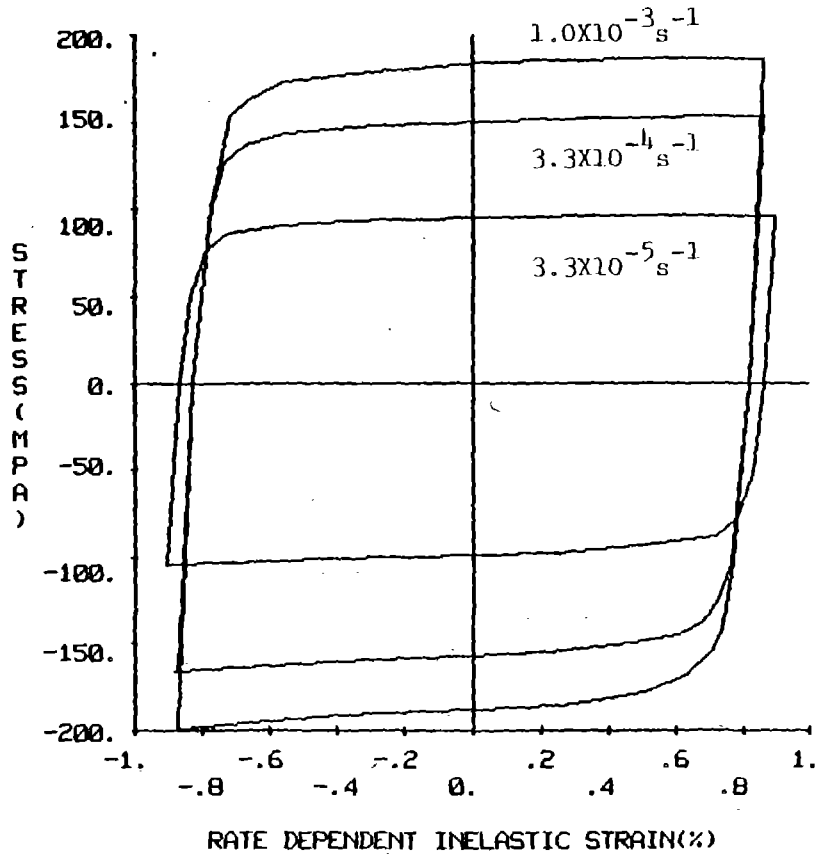


(b)

Fig. 17 Saturated hysteresis loops for Hastelloy-X at 1033K. (a) Stress vs. total strain. (b) Stress vs. rate dependent (or rate sensitive) inelastic strain

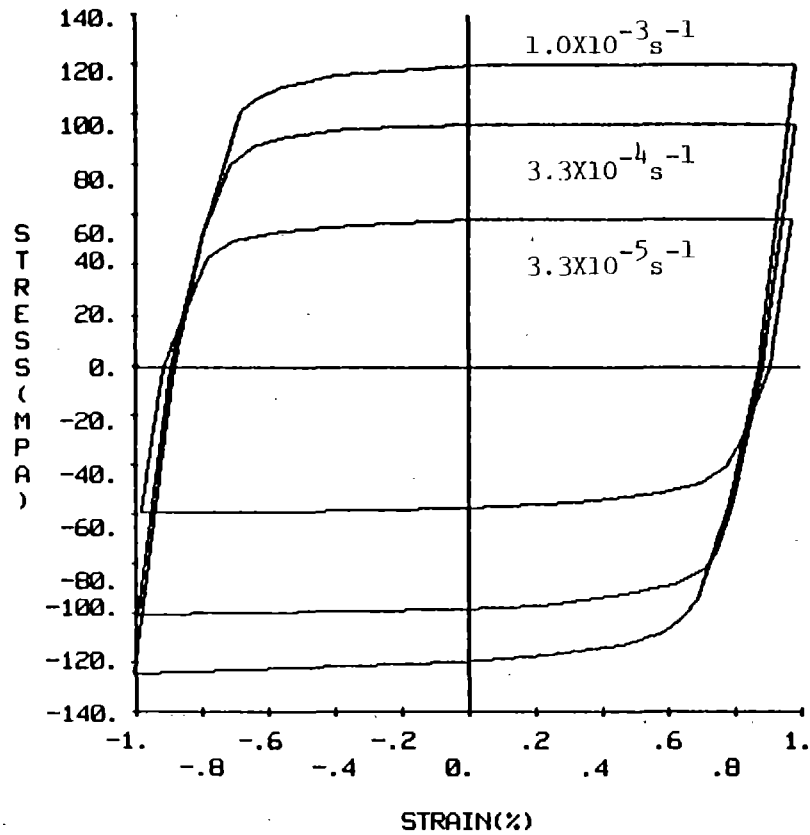


(a)

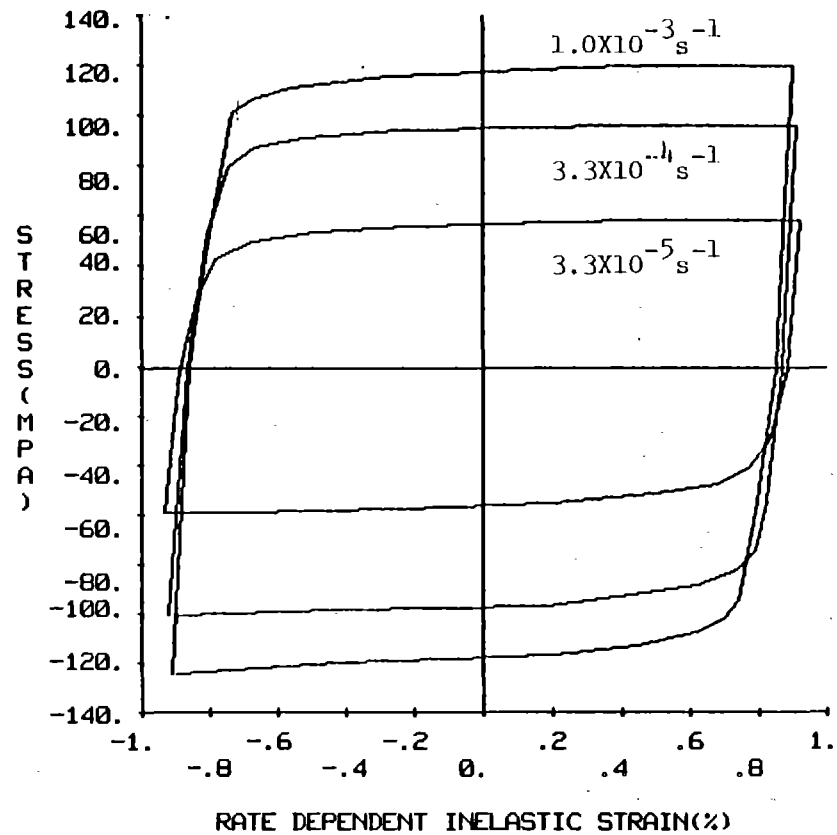


(b)

Fig. 18 Saturated hysteresis loops for Hastelloy-X at 1089K. (a) Stress vs. total strain. (b) Stress vs. rate dependent(or rate sensitive)inelastic strain



(a)



(b)

Fig. 19 Saturated hysteresis loops for Hastelloy-X at 1144K. (a) Stress vs. total strain. (b) Stress vs. rate dependent(or rate sensitive)inelastic strain

the apparent asymmetry is caused by grain boundary sliding. In this research program, all specimens were initially loaded in tension followed by compression. It is expected that if loading starts in compression, history effects will be manifested in the form of a higher peak stress in tension than in compression. Hysteresis loop tests at low temperatures reveal a considerable amount of asymmetry during the first cycle. Experimental results show that below 978 K ($0.64 T_m$), initial asymmetry may reach a maximum of about 17%. As strain cycling continues, the difference becomes progressively smaller and upon saturation, asymmetry is reduced to a minimum, though the alloy still maintains a higher peak stress in compression. The higher strain hardening rate in compression is the result of an increase in dislocation density during initial loading and their mutual interference with each other upon load reversal. As strain cycling continues, a stabilized cell structure begins to form which is equally effective against dislocation motion in either direction. As a result, the hysteresis loop becomes more symmetric upon saturation. Experimental results indicate that below 978 K ($0.64 T_m$), the degree of asymmetry of saturated hysteresis loops does not exceed 2%. At higher temperatures, the initial asymmetry is about 5% and remains relatively constant until saturation. Recall that cyclic hardening is insignificant at high temperatures and saturation can occur in as few as two cycles. It can be seen from the above discussion that saturated hysteresis loops are more symmetric at lower temperatures despite the more significant asymmetry observed in the first cycle. The greater degree of asymmetry for saturated hysteresis loops at higher

temperatures is ascribed to grain boundary sliding, which occurs more readily for tensile than for compressive loading. For example, at temperatures above 978 K a "plateau" region is generally observed at the top of the hysteresis loop while the material seldom attains a constant stress in compression. Since the amount of asymmetry is relatively small, even at these higher temperatures, grain boundary sliding is not expected to play a major role in the overall deformation process. However, triple point cracking may occur as a result which can drastically reduce the fatigue life of the material.

Stress Relaxation Behavior

Stress relaxation tests for Hastelloy-X at various temperatures and strain-rates are shown in Fig. 20 - 28. Stress relaxation tests are utilized for back stress determination from 755 K to 922 K ($0.49 - 0.60 T_m$) where thermal recovery is not significant. At higher temperatures, stress relaxation response provides a good indication of the degree of rate sensitivity the material experiences.

As discussed earlier, stress relaxation is a result of rate dependent inelastic deformation or creep that occurs at constant strain. The rate sensitive inelastic strain-rate is a function of both the effective stress and the strain-rate prior to the start of the stress relaxation test. Room temperature stress relaxation tests were conducted to evaluate the relative significance of rate sensitive inelastic strain at this temperature. As shown in Fig. 20 (p. 65), the relaxation rate is small initially and becomes insignificant after a few minutes. The low relaxation rate is a result of

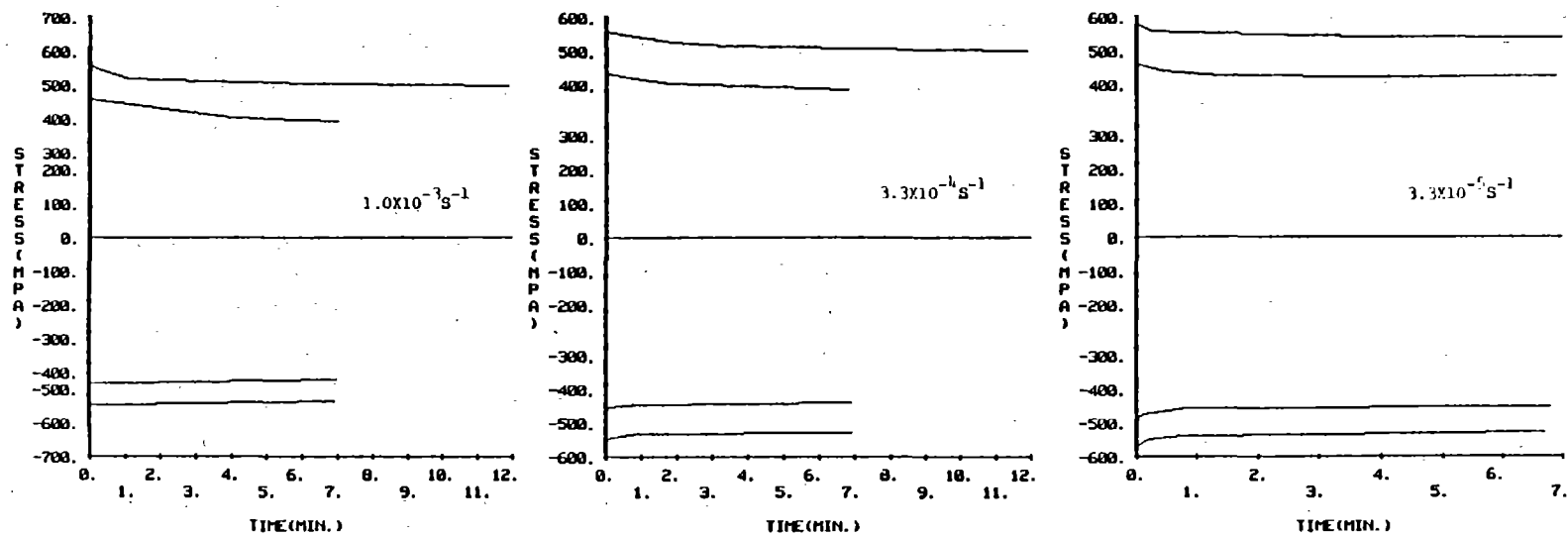


Fig. 20 Stress relaxation tests for Hastelloy-X at room temperature executed at various points on saturated hysteresis loops

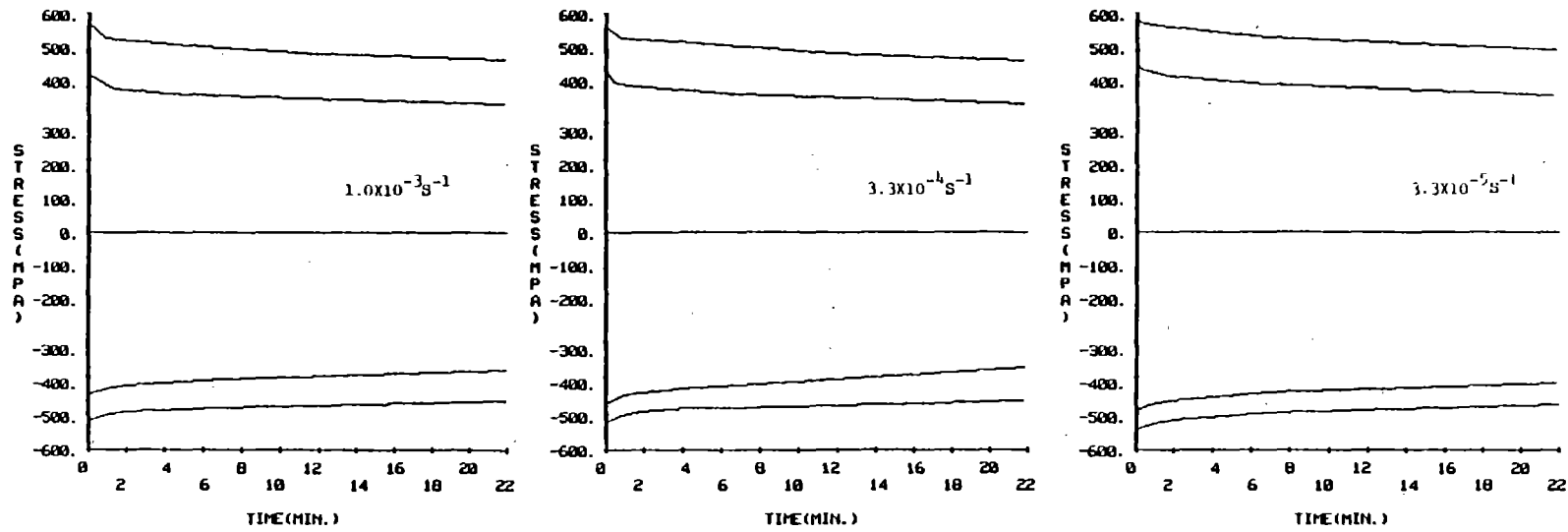


Fig. 21 Stress relaxation tests for Hastelloy-X at 755K executed at various points on saturated hysteresis loops

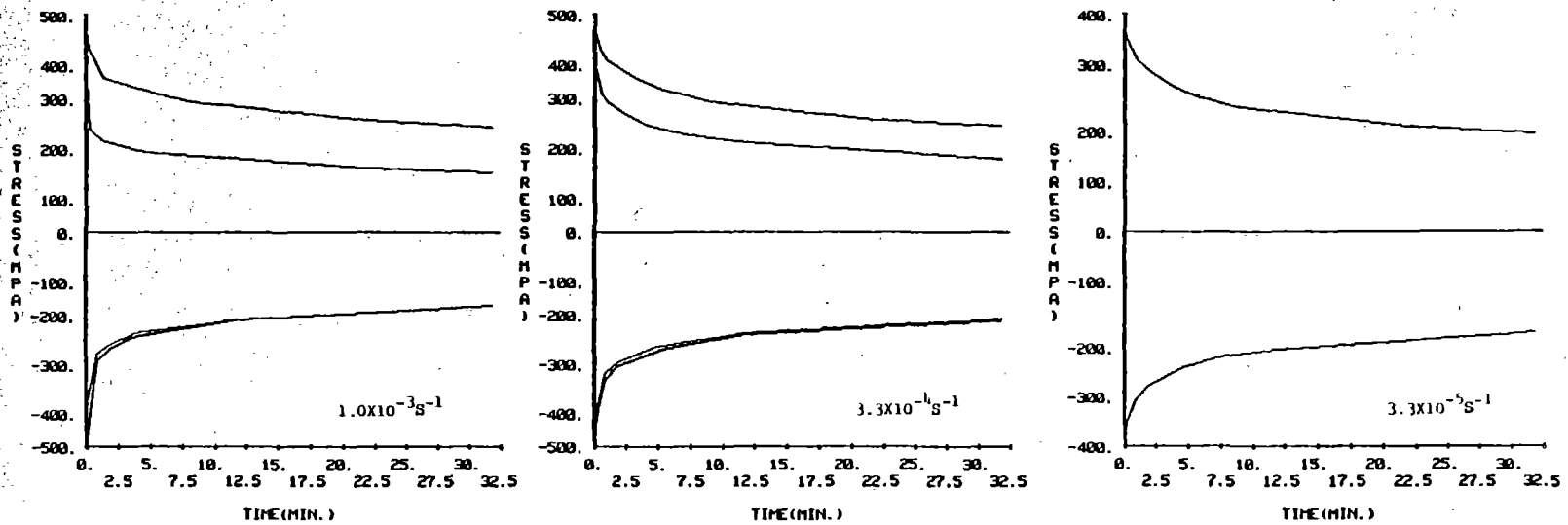


Fig. 22 Stress relaxation tests for Hastelloy-X at 811K executed at various points on saturated hysteresis loops

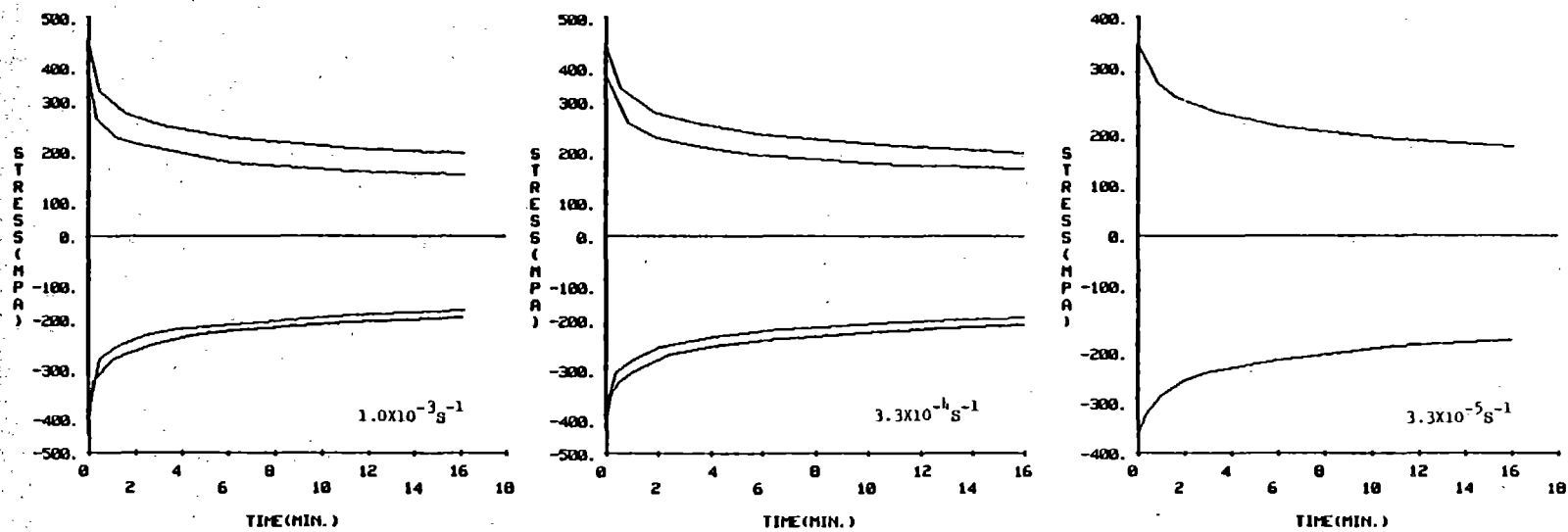


Fig. 23 Stress relaxation tests for Hastelloy-X at 866K executed at various points on saturated hysteresis loops

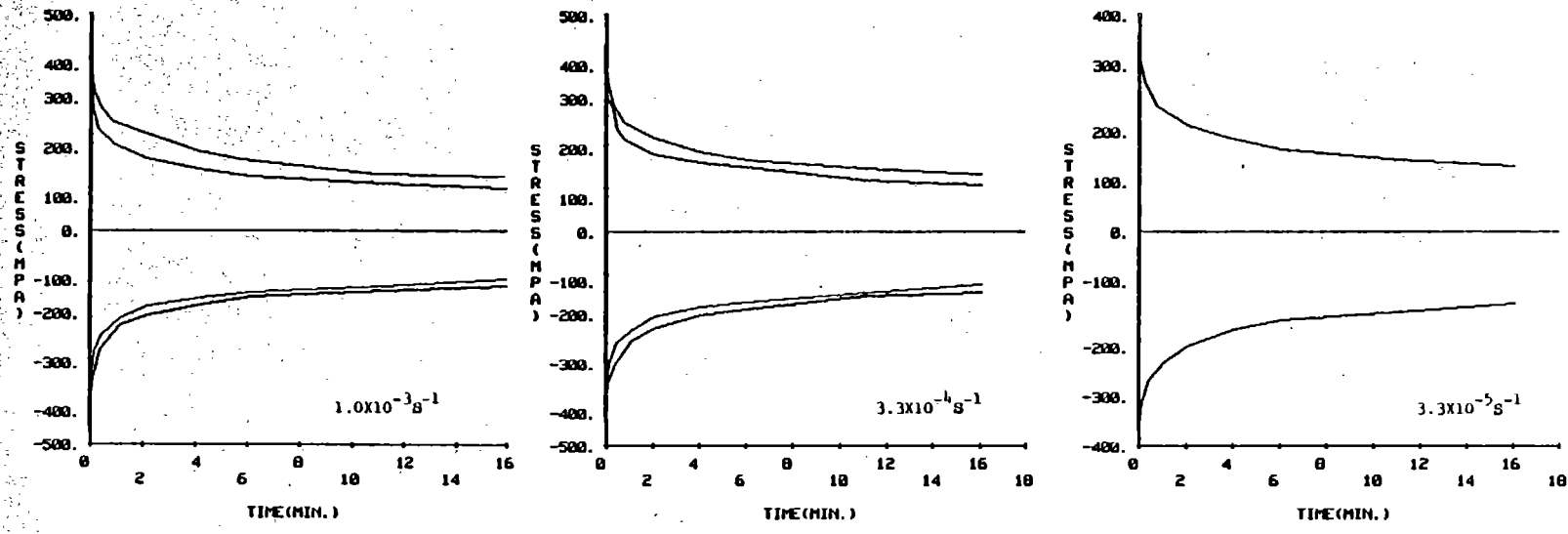


Fig. 24 Stress relaxation tests for Hastelloy-X at 922K executed at various points on saturated hysteresis loops

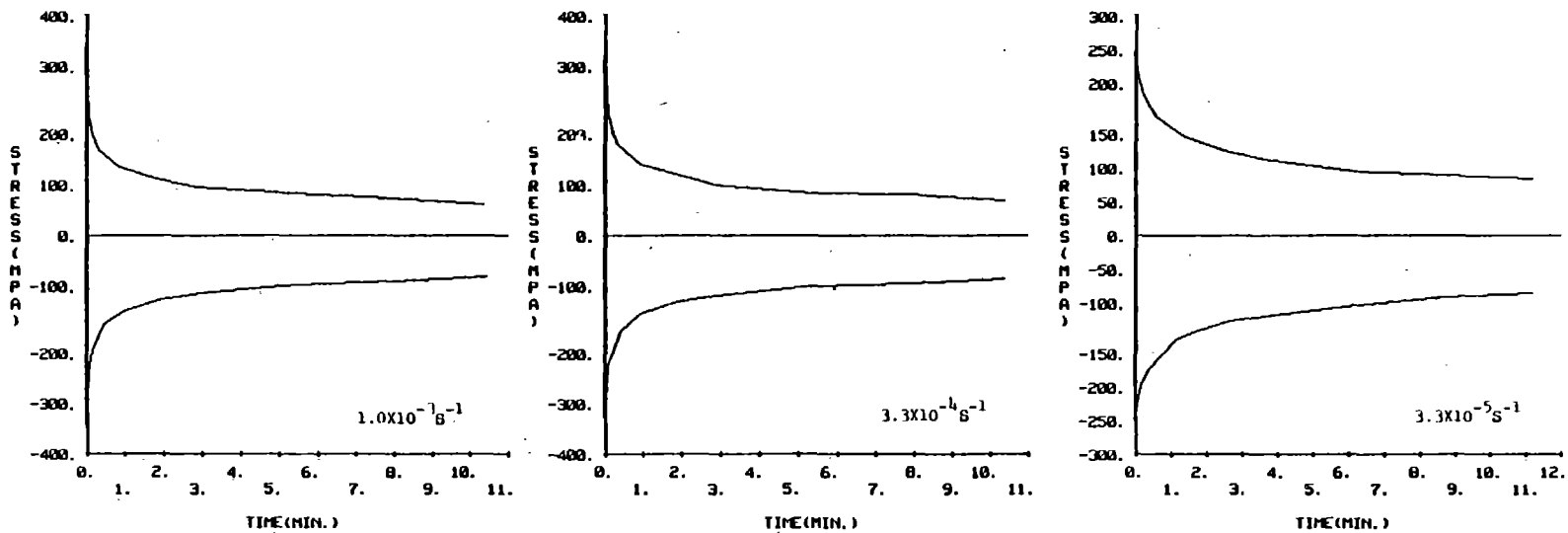


Fig. 25 Stress relaxation tests for Hastelloy-X at 978K executed at various points on saturated hysteresis loops

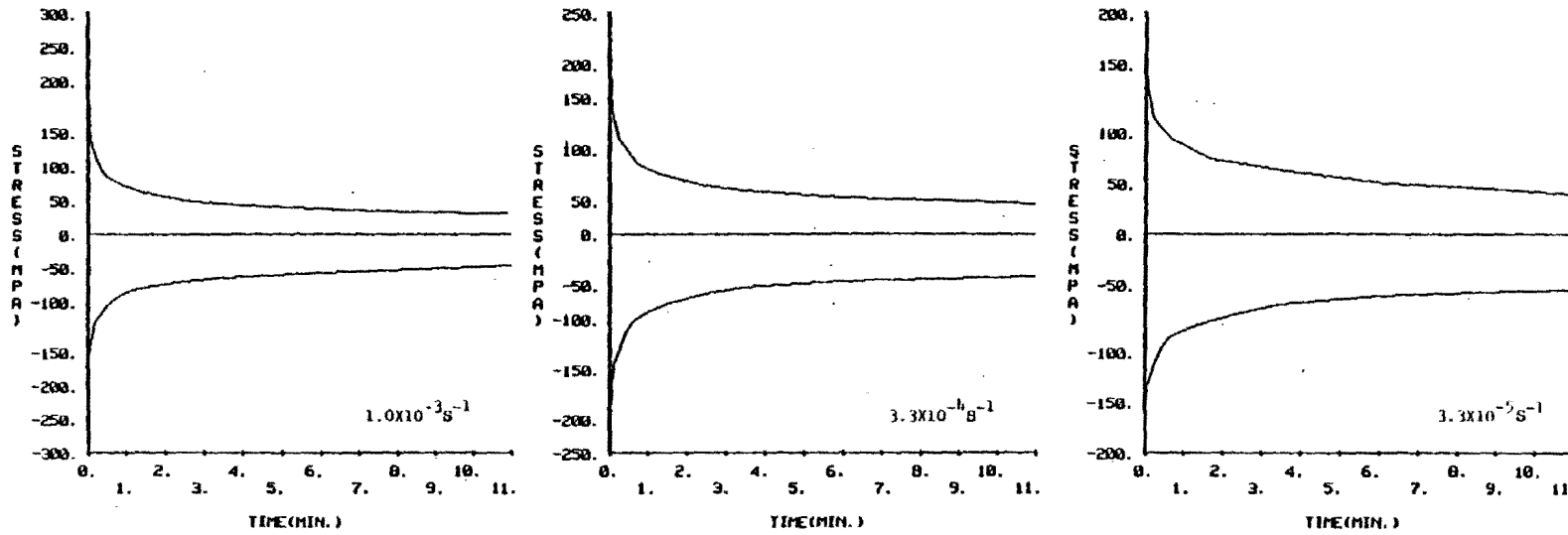


Fig. 26 Stress relaxation tests for Hastelloy-X at 1033K executed at various points on saturated hysteresis loops

ORIGINAL PAGE IS
OF POOR QUALITY

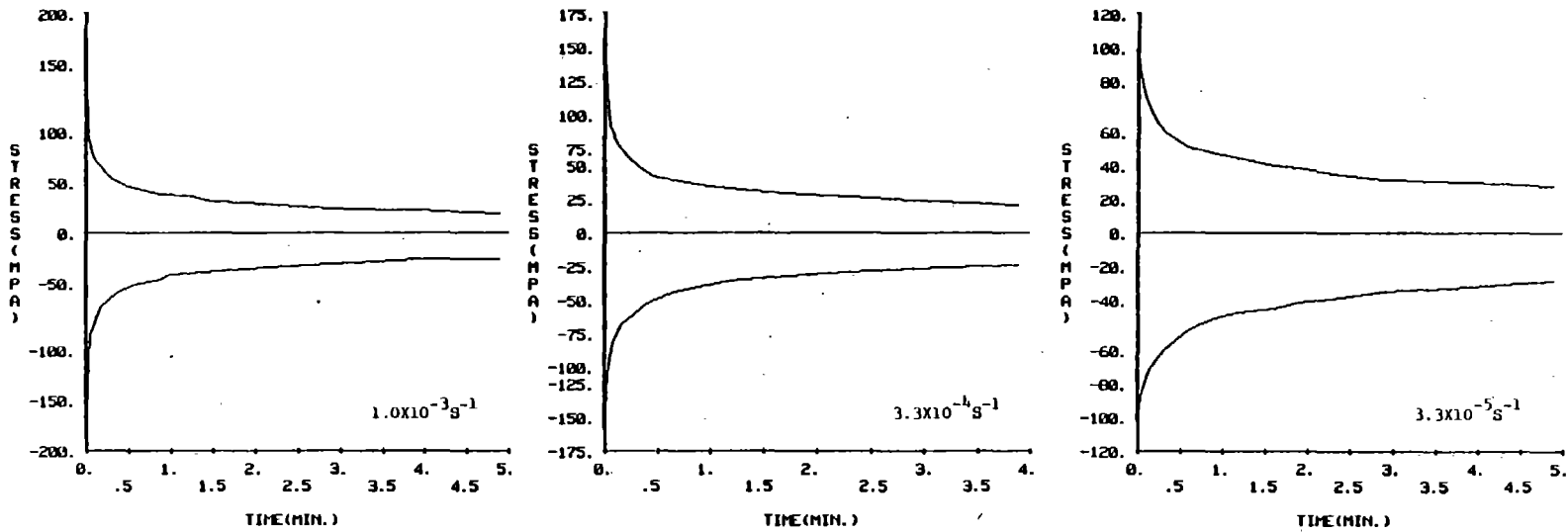


Fig. 27 Stress relaxation tests for Hastelloy-X at 1089K executed at various points on saturated hysteresis loops

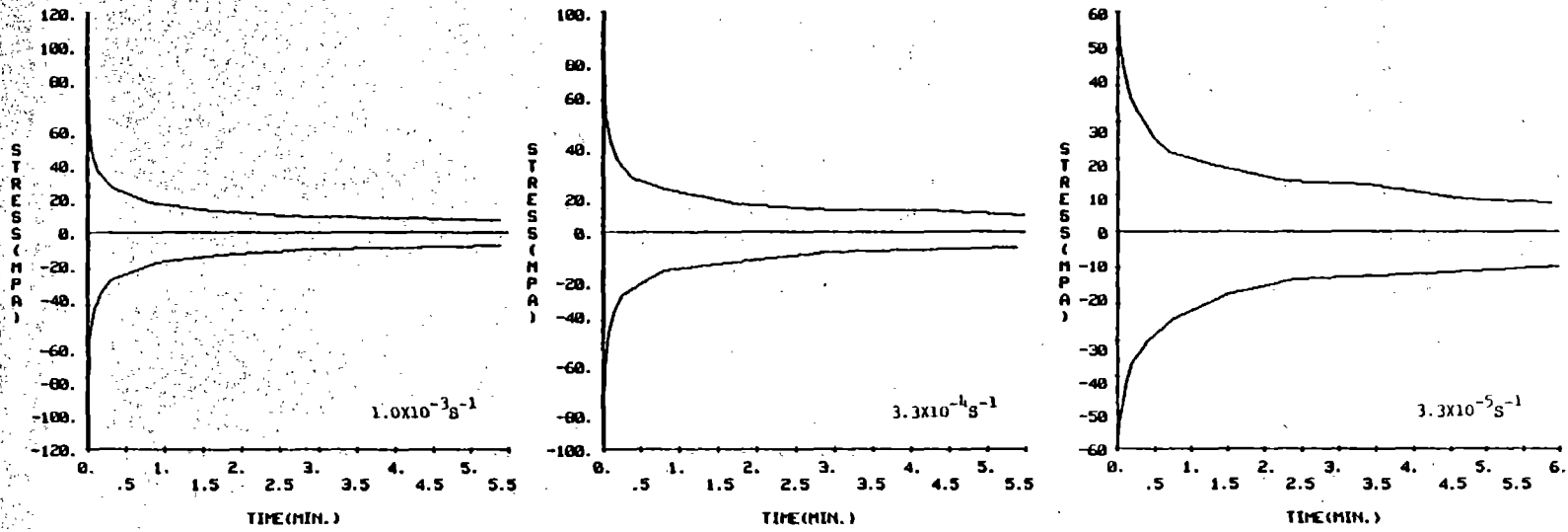


Fig. 28 Stress relaxation tests for Hastelloy-X at 1144K executed at various points on saturated hysteresis loops

the high back stress (or small effective stress) due to the absence of significant thermal effects. When one of the tests was extended for another nine hours, the stress was found to decrease by an additional 5%. At 755 K, the relaxation rate is slightly higher but not significant. The observation compares favorably with hysteresis loop data over this temperature range. The internal stress at this temperature has a magnitude equal to about 80% of the applied stress. Above 811 K the stress relaxation rate increases steadily as a result of a lower back stress due to more intense thermal activity. As the temperature rises above 978 K the significance of thermal recovery is indicated by a sharp reduction in stress during the first several minutes of stress relaxation. Experimental results show that in this temperature range, the stress can drop by 50% or more for the first 30 s of stress relaxation. In this temperature range, a plot of $\ln \dot{\epsilon}_{ir}$ vs. $\ln (\sigma - \Omega)$ often reveals a gradual reduction of the stress exponent "n" as indicated by the slope of the plot (Fig. 29). This observation indicates a possible reduction of the back stress and/or drag stress during relaxation as a result of thermal recovery. The decrease in the stress exponent may also signal a possible change of the mode of recovery during stress relaxation. The stress exponent at the beginning of the stress relaxation test usually has a value of about 4, a typical number for power law creep or dynamic recovery. Toward the end of the test, the stress exponent drops to a value of 2 or less, which is similar to values obtained for diffusional creep or static recovery. In other words, the recovery process has changed from one dominated by dislocation climb and cross-slip to one which

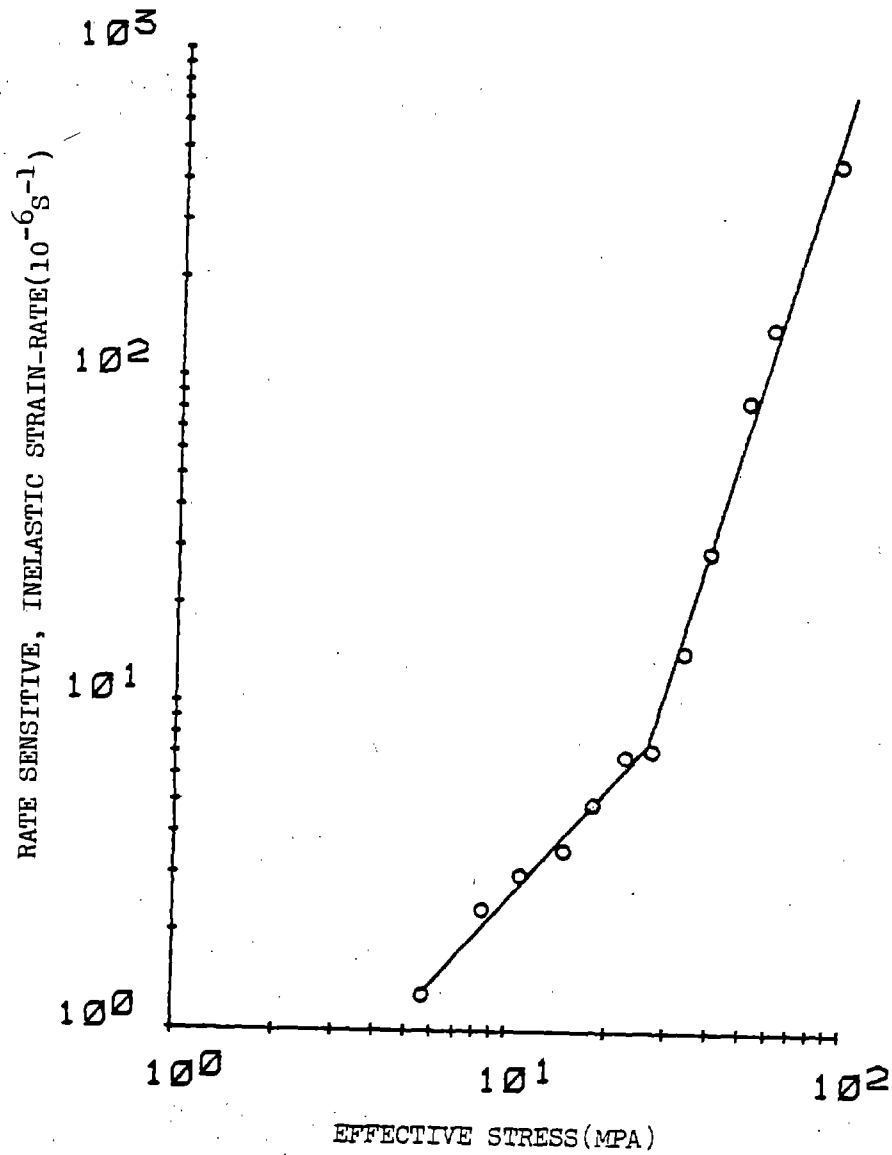


Fig. 29 Effective stress vs. rate sensitive, inelastic strain-rate at 1144K for a total strain-rate of $1 \times 10^{-3} \text{ s}^{-1}$

involves atomic diffusion across grain boundaries (or subgrain boundaries).

It is observed that the alloy experiences negative stress relaxation on the compressive side of the hysteresis loop. As shown in equation (14), negative creep occurs in compression which can only be compensated by a "positive" stress-rate. An alternative explanation can be given by the fact that the back stress is less negative than the compressive applied stress thus resulting in negative stress relaxation.

It has been found that the inelastic strain-rate at the beginning of the stress relaxation test is often less than that measured just prior to the start of the test. The "discontinuity" is more significant at lower temperatures and gradually diminishes as the temperature increases. Whether this phenomenon is real material behavior or merely the result of inaccurate measurements is a subject of much controversy. In the next chapter, arguments offered by other investigators will be discussed and an attempt will be made to explain the phenomenon in terms of the uncoupled constitutive model.

Material Constants and Their Physical Significance

The various material constants required for the characterization of the rate sensitive inelastic strain component are summarized in Table II. The elastic constants tabulated in Table III are taken from ref. [52]. The Poisson's ratio given in Table III (p. 78) is based on room temperature data and is assumed to be constant. In practice, it has a weak temperature dependence. For example, the Poisson's ratio

Table II. Values for Back Stress (Ω) (for $\sigma = \sigma_{\max}$), n , Drag Stress (K) and K^n .

Temp. (K)	Ω (MPa) Strain-rate ($10^{-4} s^{-1}$)			n	K (MPa $s^{\frac{1}{n}}$) Strain-rate ($10^{-4} s^{-1}$)			K^n (MPa s) Strain-rate ($10^{-4} s^{-1}$)		
	10	3.3	0.33		10	3.3	0.33	10	3.3	0.33
755	468	468	474	5.50	390	513	1045	1.78×10^{14}	8.05×10^{14}	4.03×10^{16}
811	252	265	318	4.96	1186	1260	1704	1.77×10^{15}	2.39×10^{15}	1.07×10^{16}
866	255	226	237	5.57	905	978	1274	2.94×10^{16}	4.53×10^{16}	1.98×10^{17}
922	161	164	163	4.31	1690	1829	2597	8.17×10^{13}	1.15×10^{14}	5.20×10^{14}
978	141	136	115	5.57	800	800	800	1.48×10^{16}	1.48×10^{16}	1.48×10^{16}
1033	118	111	82	4.75	672	672	672	2.69×10^{13}	2.69×10^{13}	2.69×10^{13}
1089	76	66	43	4.70	488	488	488	4.32×10^{12}	4.32×10^{12}	4.32×10^{12}
1144	41	38	28	3.63	532	532	532	7.85×10^9	7.85×10^9	7.85×10^9

755- 922 K: Ω , n & K obtained from stress relaxation tests.

978-1144 K: n obtained from strain-rate change tests.

Ω obtained from strain drop, stress transient tests.

K assumed to be constant for all strain-rates.

Table III. Values for Young's Modulus and Poisson's Ratio at Different Temperatures.

Temperature (K)	T/T_m^*	Young's Modulus (GPa)
294	0.19	197
533	0.35	182
755	0.49	166
811	0.53	162
866	0.57	158
922	0.60	154
978	0.64	150
1033	0.67	146
1089	0.71	142
1144	0.75	137

$\nu = 0.32$ (assumed constant for all temperatures)

*Melting range is 1533 - 1628 K

for Hastelloy-X has a value of 0.34 at 1255 K [53]. Since the change is rather small, it will have a negligible effect on the resulting strain calculations. With the strain hardening function given in Appendix D and the material constants defined in Table II (p. 77), the total strain at each temperature and strain-rate can be uncoupled into different components.

It is noted in Table II (p. 77) that the stress exponent varies from 3.63 to 5.57. The value for n does not seem to be a sensitive function of temperature although slightly higher values are generally obtained at lower temperatures. This is in contrast to unified models where the n values at lower temperatures may be as high as 60-100. Strain-rate cycling tests conducted at lower temperatures do result in higher n values if analysis is made assuming all inelastic strain as being rate sensitive (or rate dependent) as the unified theory does.

Values of the back stress measured at the peak of the hysteresis loops are shown in Table II (p. 77). At lower temperatures, the internal stress values are also evaluated at zero strain. Based on experimental data, back stress at other points can then be calculated using equation (8). The results are plotted in Fig. 30-37. At 755 K, the higher strain hardening rate observed can be seen as a result of a high internal stress due to limited thermal recovery (Fig. 30) (p. 80). The back stress at this temperature is relatively independent of strain-rate (Table II) (p. 77), which explains the rate insensitive nature of the hysteresis loops. Between 811 K and 922 K, the internal stress declines steadily as a function of temperature.

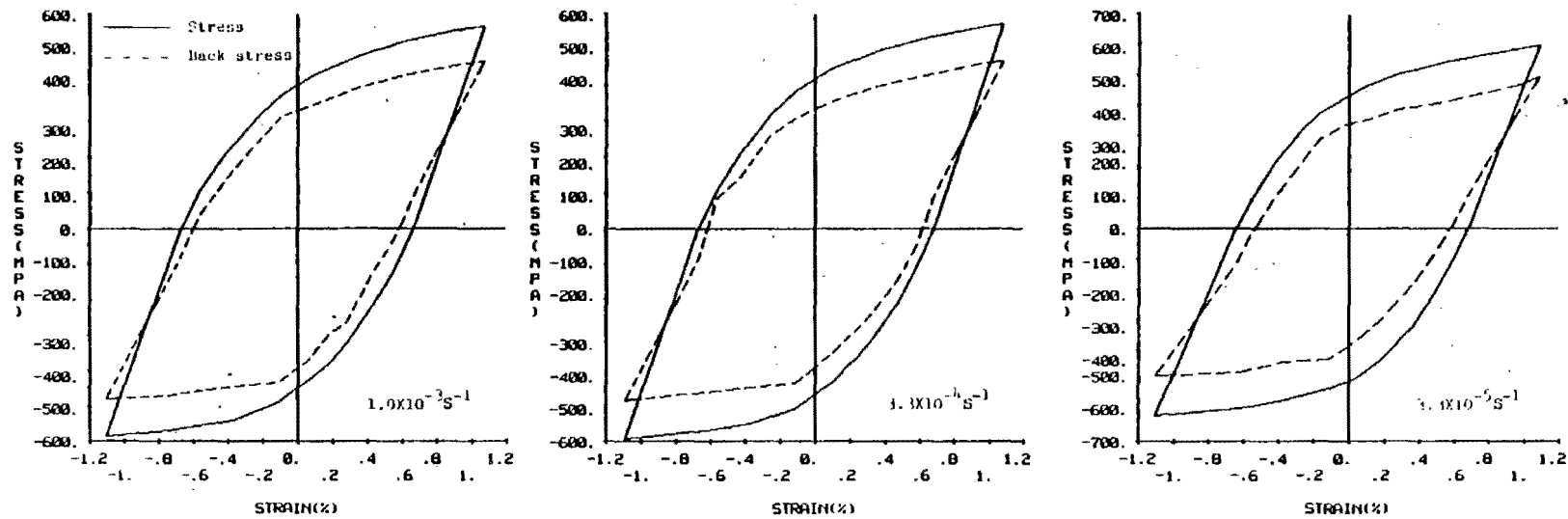


Fig. 30 Stress and back stress as a function of strain for Hastelloy-X at 755K

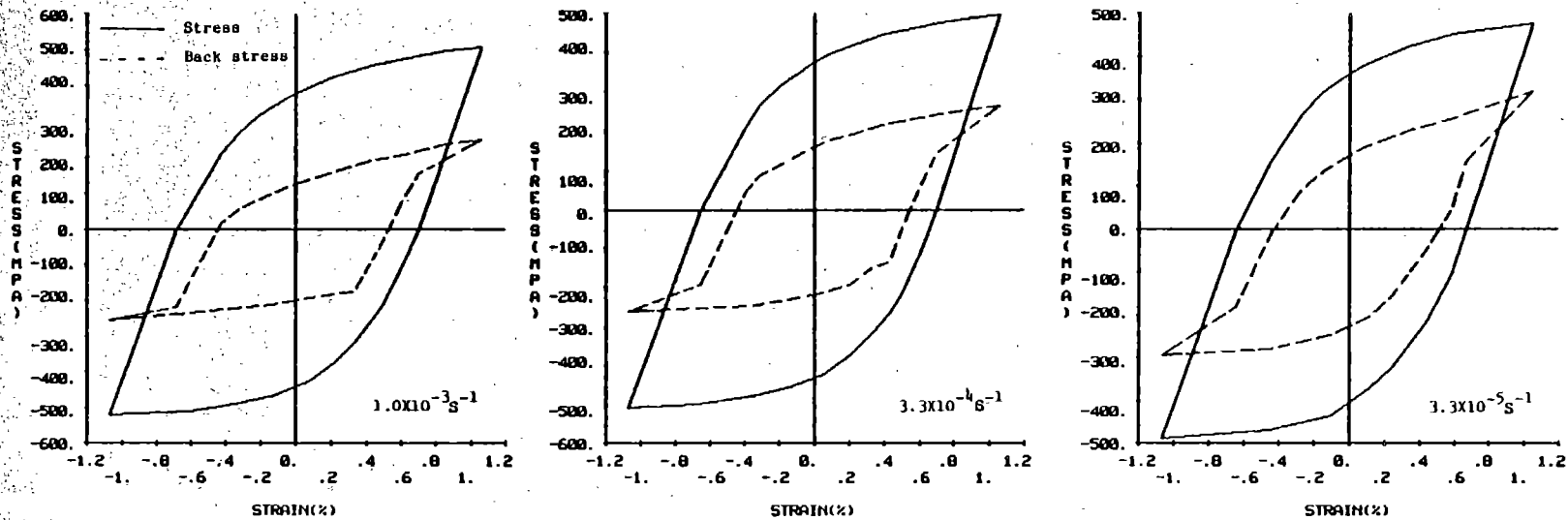


Fig. 31 Stress and back stress as a function of strain for Hastelloy-X at 811K

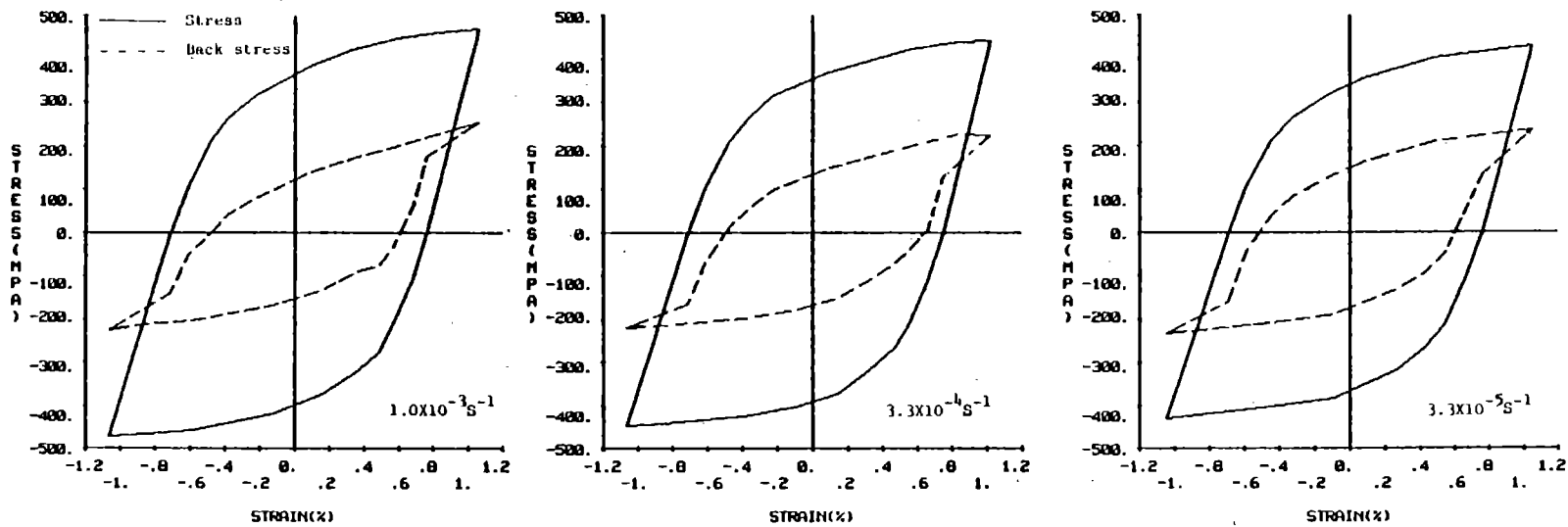


Fig. 32 Stress and back stress as a function of strain for Hastelloy-X at 866K

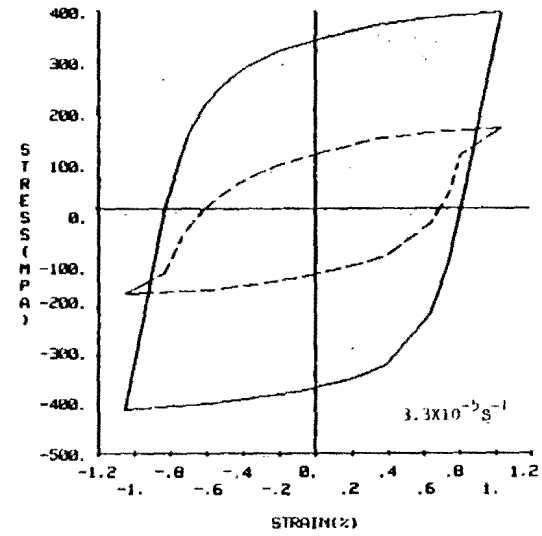
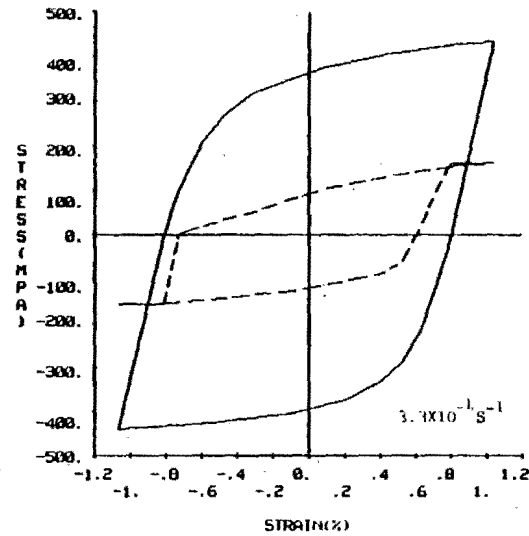
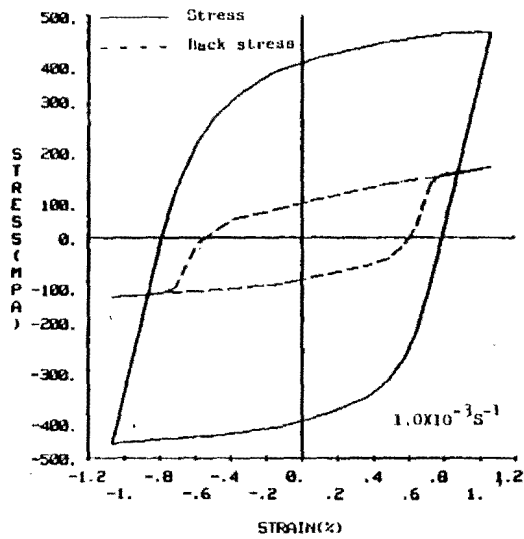


Fig. 33 Stress and back stress as a function of strain for Hastelloy-X at 922K

ORIGINAL PAGE IS
OF POOR QUALITY

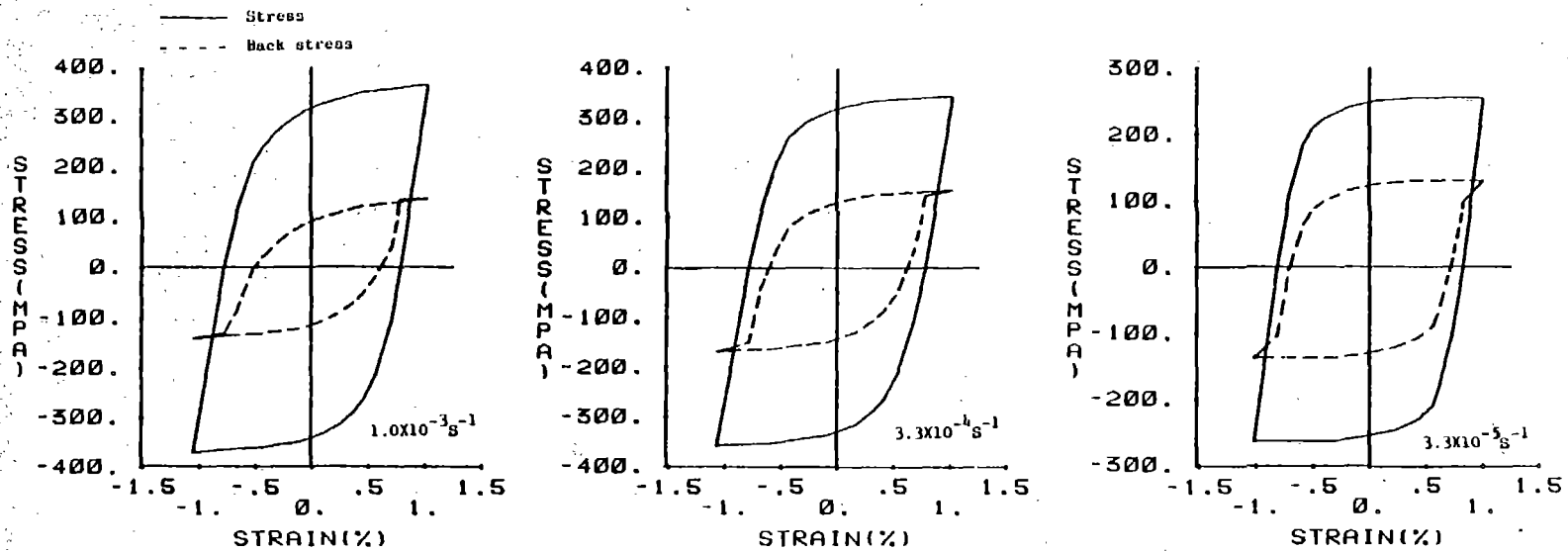


Fig. 34 Stress and back stress as a function of strain for Hastelloy-X at 978K

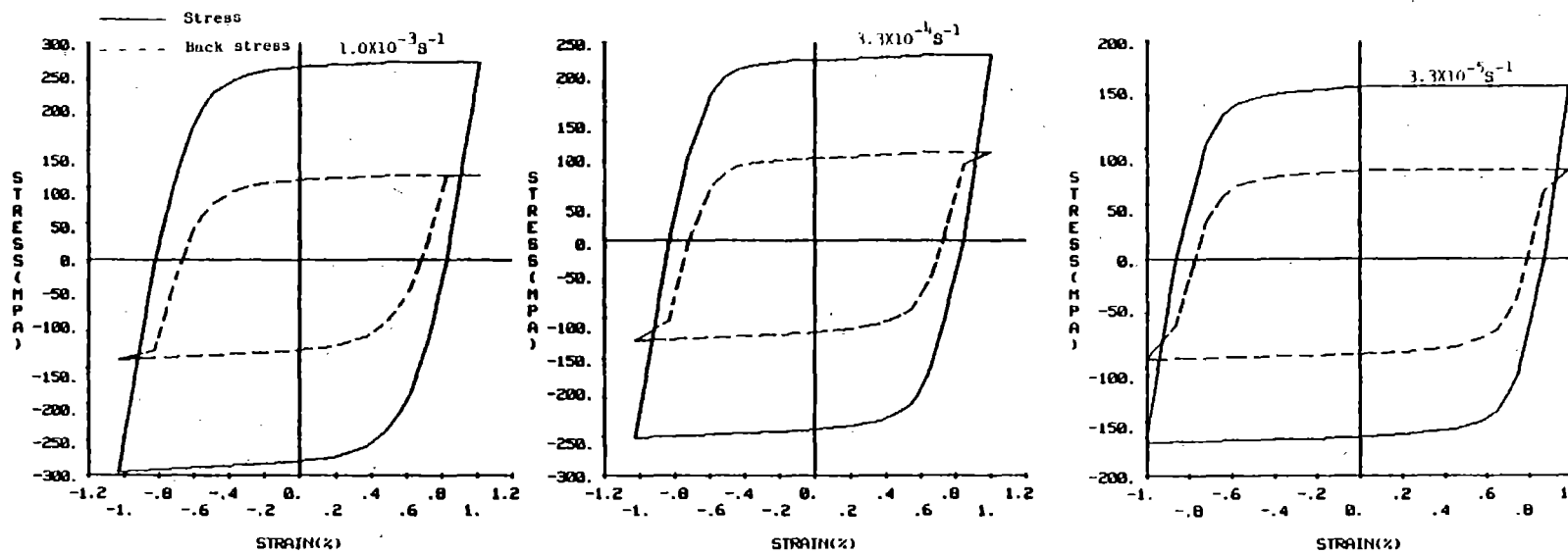


Fig. 35 Stress and back stress as a function of strain for Hastelloy-X at 1033K

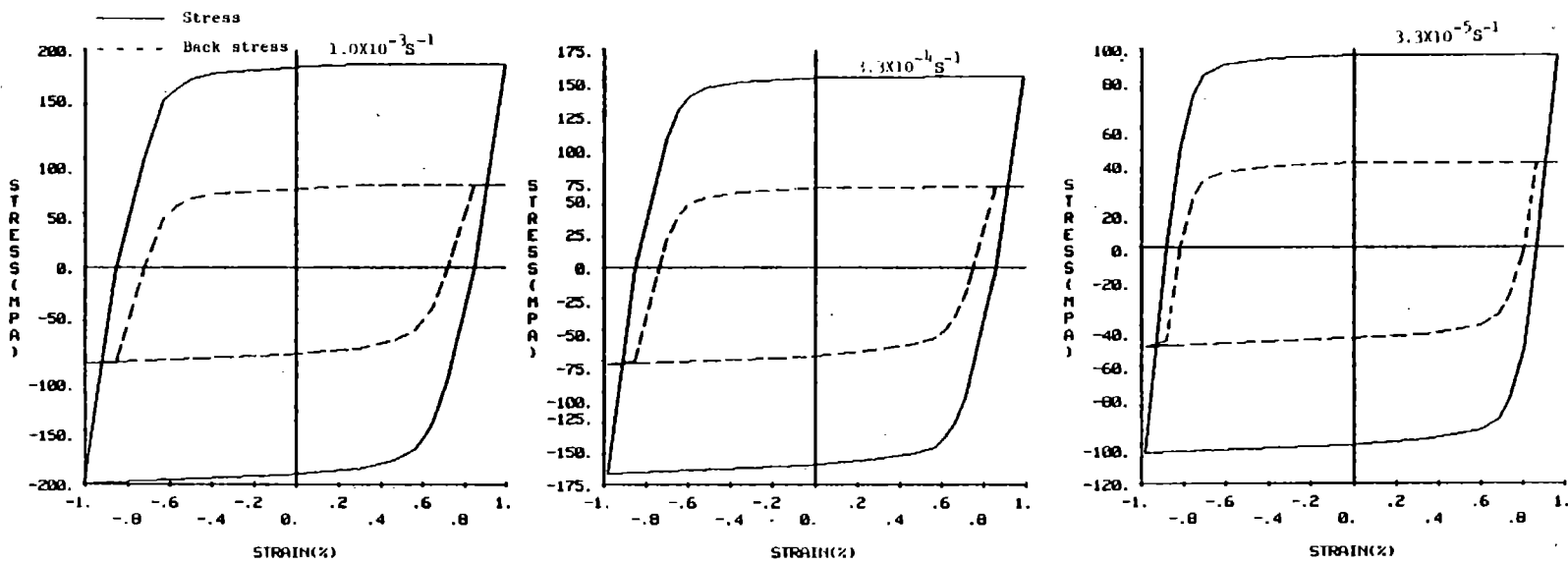


Fig. 36 Stress and back stress as a function of strain for Hastelloy-X at 1089K

ORIGINAL PAGE IS
 OF POOR QUALITY

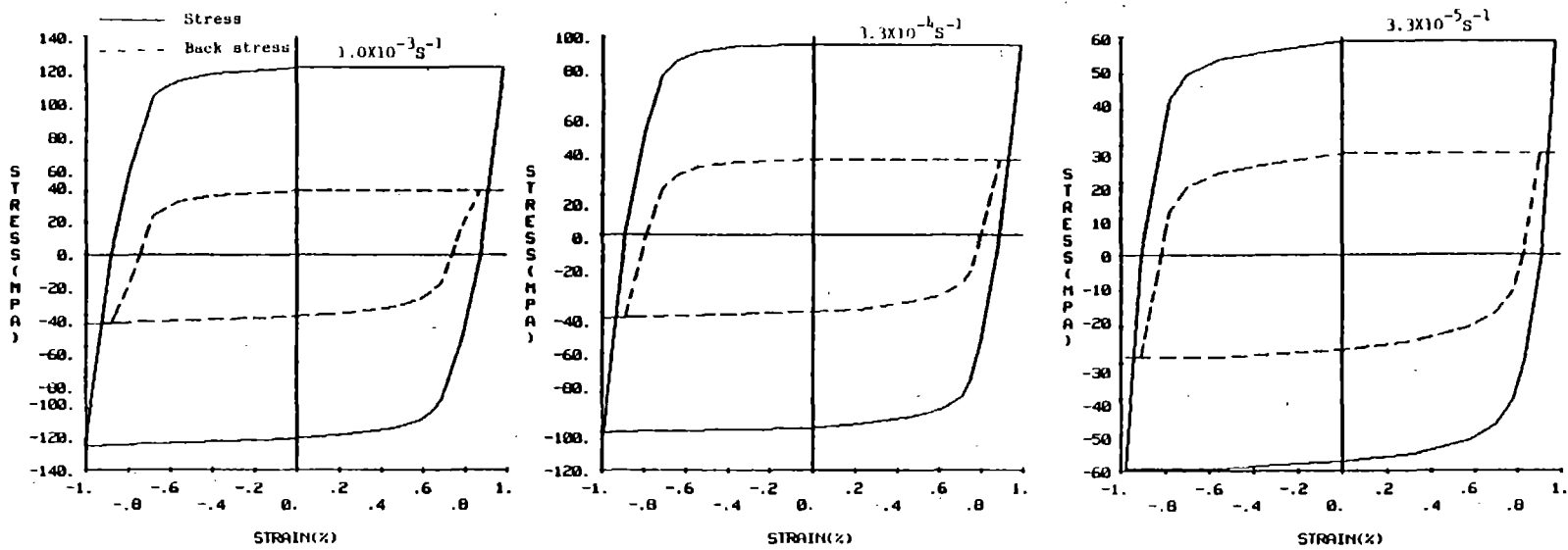


Fig. 37 Stress and back stress as a function of strain for Hastelloy-X at 1144K

The effect of increased thermal assistance is reflected by an increasing effective stress as well as a decreasing strain hardening rate (Fig. 31-33) (p.81-83). At each temperature, however, the internal stress remains relatively constant, indicating that rate effects are still not very significant. At 978 K and above, thermal effects are important and the back stress usually saturates to a constant value, accounting for the appearance of a "plateau" region at the top of the hysteresis loop. A constant back stress indicates a balance between strain hardening and dynamic recovery and is equivalent to steady state creep. It should be noted, however, that strain cycling and creep tests involve different deformation histories. Strain cycling tests are strain controlled, i.e., they are carried out at constant strain-rate while the stress is monitored. Creep tests, on the other hand, are conducted at constant stress while the resulting strain-rate (or creep rate) is monitored. A recent study on a nickel-base superalloy shows that at steady state, a tensile test (conducted at constant strain-rate) and a creep test will produce equivalent results provided the strain-rates are equal [54]. This requires that the tensile test be performed at a strain-rate equivalent to the steady-state creep rate for a given stress at a given temperature.

It can be seen that in this temperature range, slower strain-rates result in lower back stresses. At reduced strain-rate, more time will be available for dynamic recovery such as dislocation climb and cross-slip to proceed.

The values of the drag stress K are tabulated in Table II (p. 77). Despite some scattering of the data, the drag stress is found in

C-3

general to decrease with increasing temperature. This indicates an increasing mobile dislocation density, possibly resulting from an increased cell size which is both the source of mobile dislocations and a place where they may be entrapped. At lower temperatures, the drag stress increases with decreasing strain-rate, again indicating the expected lower mobile dislocation density at lower strain-rates. At higher temperatures (978 - 1144 K), it is assumed that K remains constant over the strain-rate range considered. Strain-rate cycling tests performed at these temperatures suggest that the reduction in flow stress at lower strain-rate is a result of changes in the back stress rather than the drag stress. It was subsequently confirmed by strain drop, stress transient tests that the internal stress decreases with decreasing strain-rate in this temperature range. From a physical standpoint, the abundance of thermal energy available at these temperatures justifies the assumption that the mobile dislocation density does not vary appreciably over the strain-rate range studied. The physical significance of the mobile dislocation density as well as the drag stress can be better understood in terms of the Orowan equation as shown below:

$$\dot{\epsilon}_{ir} = \phi \rho_m b \bar{v} \quad (21)$$

where ϕ is a geometrical constant, ρ_m is the mobile dislocation density, b is the Burgers vector and \bar{v} is the average dislocation velocity. \bar{v} can be expressed as a function of the effective stress as follows:

$$\bar{v} = \beta(\sigma - \Omega)^n \quad (22)$$

where β is the average dislocation velocity at unit effective stress, Ω is the internal stress and n is the stress exponent. Substituting equation (22) in equation (21) yields the following relationship:

$$\dot{\epsilon}_{ir} = \phi \rho_m b \beta (\sigma - \Omega)^n \quad (23)$$

A comparison of equation (23) with equation (8) shows that the mobile dislocation density is inversely proportional to the drag stress, i.e.,

$$\rho_m \propto K^{-n} \quad (24)$$

Values for K^n at various temperatures and strain-rates are tabulated in Table II (p. 77). The results indicated that at lower temperatures, K^n is relatively insensitive to temperature changes but increases as the strain-rate decreases. In other words, the mobile dislocation density increases with strain-rate but not a sensitive function of temperature (in the low temperature range). At higher temperatures, however, K^n is found to decrease steadily with temperature while remaining constant at various strain-rates (over the strain-rate range considered). This in turn indicates that mobile dislocation density increases with temperature but is insensitive to strain-rate change in the high temperature range. Experimental data indicates that the rate sensitive inelastic strain-rate increases both as a function of temperature and strain-rate. This observation can be explained by referring to equation (21), which implies that the rate sensitive inelastic strain-rate is controlled by the mobile dislocation density as well as the average dislocation velocity. At lower temperatures, the back stress is rate insensitive and equation (22) indicates that the average

dislocation velocity remains relatively constant, and therefore, has limited effect on the rate sensitive inelastic strain-rate. Thus, the increase in the rate sensitive inelastic strain-rate (at low temperatures) is mainly the result of higher mobile dislocation density at higher strain-rates. At high temperatures, however, the mobile dislocation density as well as the drag stress is rate insensitive and therefore has no significant impact on the rate sensitive inelastic strain-rate. In this temperature range, both the back stress and the effective stress are found to be an increasing function of strain-rate (Figs. 34-37) (p. 84 - 87), which results in a higher dislocation velocity and therefore a higher rate sensitive inelastic strain-rate.

To summarize, the rate sensitive inelastic strain-rate is controlled by the mobile dislocation density (or drag stress) at lower temperatures; whereas at higher temperatures, the average dislocation velocity becomes the controlling factor. It should be noted that despite an increase in the "magnitude" of the rate sensitive inelastic strain with increasing strain-rate, it represents a smaller "percentage" of the total inelastic strain. This is consistent with the general observation that a material is more rate insensitive at higher strain-rates.

CHAPTER VI

EVALUATION OF THE MODEL

Justifying the Uncoupled Inelastic Strain Model

It is generally accepted that inelastic deformation in crystalline materials is a result of dislocation movement on various slip planes. However, the physical processes involved are still not fully understood despite considerable experimental effort. An area still open to discussion is the role of thermal activation in dislocation dynamics under various temperature and strain-rate conditions. The question of inelastic strain-rate continuity (or discontinuity) during a change in total strain-rate has received much attention recently since it provides some important insight into the effect of thermal assistance on material deformation.

A common approach to the study of inelastic strain-rate continuity is by means of the stress relaxation test. It is performed by interrupting a constant strain-rate test, holding the strain constant while the stress is monitored as a function of time. Measurement of the inelastic strain-rate immediately before and after the start of stress relaxation should provide an answer as to whether inelastic strain-rate continuity exists. While attractive in principle, the test is difficult to conduct experimentally. In the following discussion, arguments provided by other investigators will be presented and an attempt will be made to describe the phenomenon in terms of the uncoupled constitutive model.

In a recent study, Alden [55] verified the existence of inelastic strain-rate discontinuities in aluminum single crystals over a temperature range of 77 K - 593 K. The existence of strain-rate discontinuity at the start of a stress relaxation test can also be deduced theoretically from the time-independent deformation theory (recovery-rearrangement theory) developed by the same author [56]. In the time-independent deformation theory, inelastic deformation is considered rate independent. It is assumed that stress alone is sufficient to produce strain without the direct aid of thermal activation. Thermal effect (or recovery) influences the deformation behavior indirectly through the loss and rearrangement of obstacle dislocations. The expression for the inelastic strain-rate is given in the theory as

$$\dot{\epsilon}_i = \frac{\dot{\sigma} + r}{\Theta_y} A_r \quad (\dot{\sigma} > 0) \quad (25a)$$

$$\dot{\epsilon}_i = -\frac{r}{\Theta_y} A_r \quad (\dot{\sigma} \leq 0) \quad (25b)$$

where Θ_y is the strain hardening rate in the absence of recovery (assumed to be at 0 K), r is a generalized recovery parameter associated with both loss and rearrangement of obstacle dislocations, A_r is a free area function characterizing local slip behavior. During a tensile test $\dot{\sigma} > 0$ and the inelastic strain-rate is given by equation (25a). During stress relaxation, however, $\dot{\sigma} < 0$ and equation (25b) is utilized. It can be seen from equation (25) that the inelastic strain-rate ratio (i.e., ratio of the inelastic strain-rate immediately after and before the start of stress relaxation) is given by

$$R = \frac{r}{\dot{\sigma} + r} \quad (26)$$

where R is the inelastic strain-rate ratio and $\dot{\sigma}$ denotes the stress-rate prior to stress relaxation. R will be less than unity except for the case where $\dot{\sigma}$ is equal to zero. Therefore, inelastic strain-rate discontinuity will always occur prior to saturation. It was found that R is small initially and increases with increasing stress.

Most recently, a study by Holbrook, et al. [57] on aluminum, iron and 304 stainless steel confirmed the existence of inelastic strain-rate continuity. This observation is in agreement with the thermally-activated deformation theory (reaction-rate theory) supported by the authors. In this theory, it is postulated that inelastic deformation results from the thermally assisted overcoming of local obstacles. The "thermal activation barrier" (i.e. activation energy) increases with dislocation density and decreases with stress. The expression for the inelastic strain-rate is given by

$$\dot{\epsilon}_i = \dot{\epsilon}_0 \exp\left(-\frac{\Delta G}{kT}\right) \quad (27)$$

where ΔG is the activation energy for dislocation motion past obstacles, k is the Boltzmann's constant, T is the absolute temperature and $\dot{\epsilon}_0$ is dependent on stress, temperature and the current microstructure. It can be seen from equation (27) that inelastic deformation is controlled primarily by the activation energy ΔG and is therefore rate dependent.

It is assumed that all inelastic deformation is rate dependent and the inelastic strain-rate can be represented by equation (8) as

follows:

$$\dot{\epsilon}_{ir} = \text{sgn}(\sigma - \Omega) \left| \frac{\sigma - \Omega}{K} \right|^n \quad (8)$$

None of the parameters on the right side of the equation are expected to change immediately before and after the start of stress relaxation. Although the total strain-rate experiences a sudden change from positive (or negative) to zero as the crosshead is stopped, the inelastic strain-rate will be continuous. The authors state that inelastic strain-rate discontinuity is merely the result of inaccurate measurements and continuity can be verified with improved time and load resolution provided by microprocessor digital data acquisition. Inelastic strain-rate continuities were confirmed for aluminum, iron and 304 stainless steel at low strain-rates. The apparent discontinuity at higher strain-rates was believed to be the result of experimental limitations posed by the testing system. A small number of experiments were also performed on polycrystalline nickel and 304 L stainless steel utilizing a strip chart recorder for data collecting purposes. Experimental results for nickel indicated inelastic strain-rate discontinuity, which was also considered to be a resolution problem rather than real material behavior.

In this research program, the uncoupled constitutive model can be expressed in the following form:

$$\dot{\epsilon}_i = \dot{\epsilon}_{ii} + \dot{\epsilon}_{ir} = f(\sigma, \sigma_{\max}) \dot{\sigma} + \text{sgn}(\sigma - \Omega) \left| \frac{\sigma - \Omega}{K} \right|^n \quad (28)$$

Since $\dot{\sigma}$ goes from positive to negative as the constant strain-rate is interrupted for stress relaxation and since $f(\sigma, \sigma_{\max})$ is essentially zero just after a load reversal, the rate insensitive inelastic strain-rate experiences a change from a positive value to zero. Since the stress is continuous at this point, the rate sensitive inelastic strain-rate would be expected to be continuous. Thus, a large decrease in inelastic strain-rate as one interrupts the strain cycling indicates that the inelastic strain-rate prior to stress relaxation is principally rate insensitive. If the inelastic strain-rate before and after the interruption is essentially the same, this indicates that the inelastic strain during strain cycling is mainly rate sensitive. The subject of strain-rate continuity has been studied for Hastelloy-X at three different strain-rates for a temperature range from 755 K to 1144 K. The results are summarized in Table IV. It can be seen that for a given strain-rate, the strain-rate ratio (given by $\dot{\epsilon}_1^+ / \dot{\epsilon}_1^-$) is an increasing function of temperature. For a given temperature, the strain-rate ratio is found to decrease with increasing strain-rate. At 755 K, the inelastic strain-rate after the start of stress relaxation is considerably lower than that prior to stress relaxation. Although adequate thermal assistance is available to overcome local obstacles, long range barriers such as grain boundaries and cell walls have to be overcome by dislocation climb or cross-slip, which are quite sluggish at this relatively low temperature. Thus, the inelastic strain is mostly rate insensitive which accounts for the rather significant discontinuity observed at this temperature. The rate sensitive inelastic strain-rate is increased considerably at

Table IV. Inelastic Strain-rate Continuity at Various Temperatures.

A) $\dot{\epsilon}_t = 1 \times 10^{-3} \text{ s}^{-1}$

Temp. (K)	Stress (MPa)	$\dot{\epsilon}_i^-$ (10^{-4} s^{-1})	$\dot{\epsilon}_i^+$ (10^{-4} s^{-1})	$\dot{\epsilon}_i^+ / \dot{\epsilon}_i^-$ (%)
755	434	8.76	.21	2
	558	9.57	.10	1
811	492	9.51	1.22	13
866	386	9.18	2.12	23
	455	9.57	1.01	11
922	405	9.34	2.34	25
	458	9.59	1.95	20
978	330	9.40	9.01	96
1033	277	9.80	9.80	100
1089	185	9.61	9.61	100
1144	119	9.83	9.83	100

$\dot{\epsilon}_i^-$ = plastic strain rate before the beginning of stress relaxation test

$\dot{\epsilon}_i^+$ = plastic strain rate after the beginning of stress relaxation test

Table IV. (Continued)

B) $\dot{\epsilon}_t = 3.3 \times 10^{-4} \text{ s}^{-1}$

Temp. (K)	Stress (MPa)	$\dot{\epsilon}_i^-$ (10^{-4} s^{-1})	$\dot{\epsilon}_i^+$ (10^{-4} s^{-1})	$\dot{\epsilon}_i^+ / \dot{\epsilon}_i^-$ (%)
755	450	2.95	.41	14
	568	3.19	.24	8
811	394	2.98	.40	13
	471	3.16	.69	22
866	376	3.10	.68	22
	439	3.20	.54	17
922	381	3.14	1.21	39
	431	3.22	1.38	43
978	327	3.19	3.09	97
1033	236	3.27	3.27	100
1089	154	3.21	3.21	100
1144	96	3.29	3.29	100

Table IV. (Continued)

C) $\dot{\epsilon}_t = 3.3 \times 10^{-5} \text{ s}^{-1}$

Temp. (K)	Stress (MPa)	$\dot{\epsilon}_i^-$ (10^{-5} s^{-1})	$\dot{\epsilon}_i^+$ (10^{-5} s^{-1})	$\dot{\epsilon}_i^+ / \dot{\epsilon}_i^-$ (%)
755	592	3.19	.82	26
811	373	2.97	.80	27
866	354	3.05	1.84	60
922	352	3.15	2.38	76
978	246	3.20	3.19	100
1033	163	3.27	3.27	100
1089	100	3.22	3.22	100
1144	59	3.29	3.29	100

lower strain-rates although it still represents a small fraction of the total inelastic strain-rate. The rounded corners of the hysteresis loops and the high strain hardening rates at this temperature are further evidence of the absence of significant thermally assisted flow. The rate sensitive inelastic strain-rate increases steadily with temperature, indicating the growing influence of thermal effects. At higher strain-rates, rate effects do not become important until the temperature is raised above 922 K. At the lowest strain-rate, however, the rate sensitive inelastic strain-rate component becomes dominant at temperatures above 866 K. In all cases, the inelastic strain-rate is essentially all rate sensitive at 978 K and above. The high atomic diffusion rate in this temperature range implies that dislocation climb is the dominant recovery process. Inelastic strain-rate continuity is generally observed in this temperature range due to the lack of rate insensitive inelastic strain.

It should be noted that the information provided in Table IV (p. 97) is subjected to modification for two reasons: (1) time resolution achievable by our recording system is not so good as that attained by some other investigators; (2) the effect of machine transient has not been studied in detail. To correct the first shortcoming, a high speed digital computer has been installed which can provide greatly improved time and load resolution. Before any test can be performed to confirm the existence of inelastic strain-rate continuity (or discontinuity), the complications introduced by machine characteristics have to be fully understood. Since continuity has to be studied at the point where the crosshead is stopped

"instantaneously", machine transient which lasts for even a small fraction of a second can effectively nullify any attempt to obtain a meaningful result. Until further experiments are conducted, however, our discussion will be based on the data tabulated in Table IV (p. 97).

Comparison of Experiments with Theoretical Predictions

The uncoupled constitutive model as described in Chapter III may be used to predict strain cycling, stress relaxation, creep or other phenomena if used with the proper material constants. To first see if the model is self consistent in being able to reproduce the experimental hysteresis loops, all of the input strain cycling curves were simulated using a numerical scheme discussed earlier. Stress relaxation simulations are also presented and comparisons are made with observed relaxation behavior.

Saturated hysteresis loops. Saturated hysteresis loops are simulated using equations (11) - (13) and the numerical scheme presented in Appendix A. The strain hardening function and other material constants are obtained from Appendix D, Table II (p. 77) and Table III (p. 78). The experimental and simulated hysteresis loops at various temperatures and strain-rates are presented in Figures 38 - 45. Generally speaking, the experimental hysteresis loops and the simulated curves are in good agreement over the temperature and strain-rate ranges studied. Rounded corners are well simulated at the lower temperatures where inelastic strain is mostly rate insensitive. The unified theory with its high "n" values always gives square corners at lower temperatures. At high temperatures inelastic

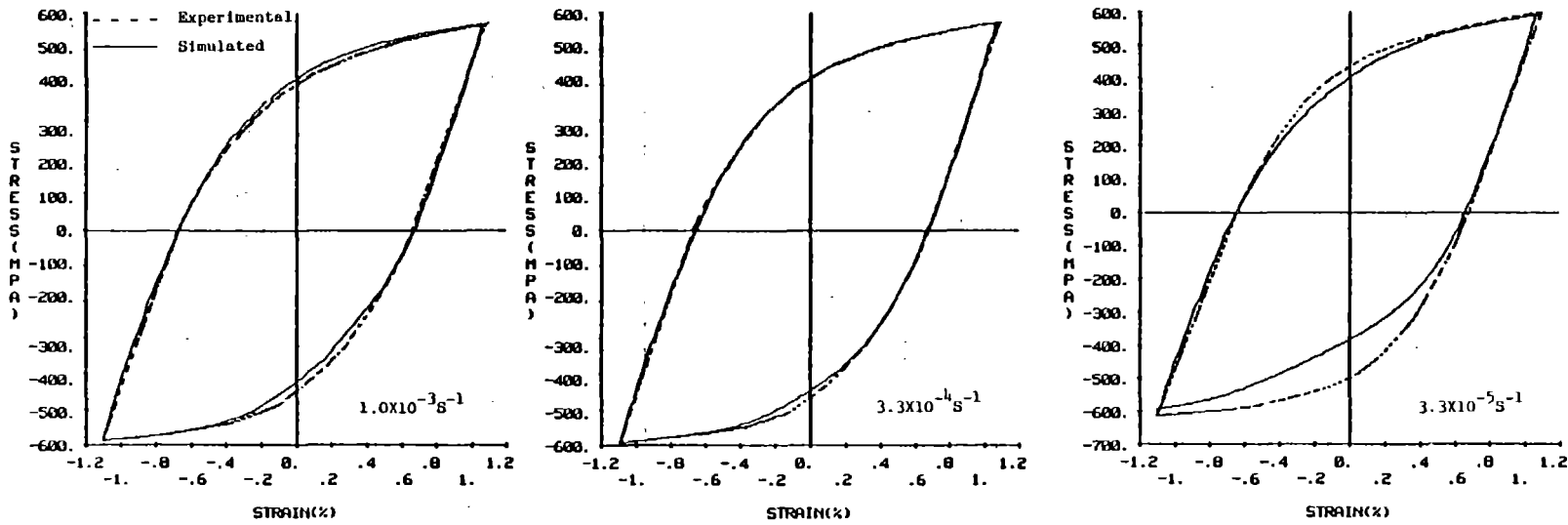


Fig. 38 Experimental and simulated hysteresis loops for Hastelloy-X at 755K

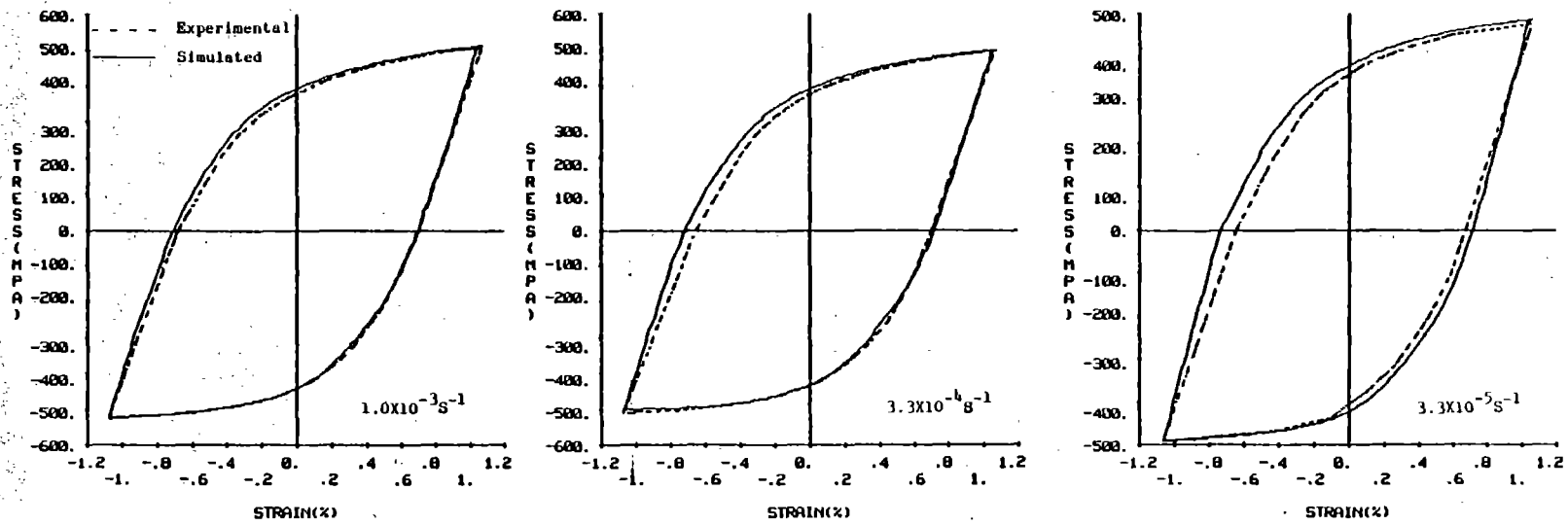


Fig. 39 Experimental and simulated hysteresis loops for Hastelloy-X at 811K

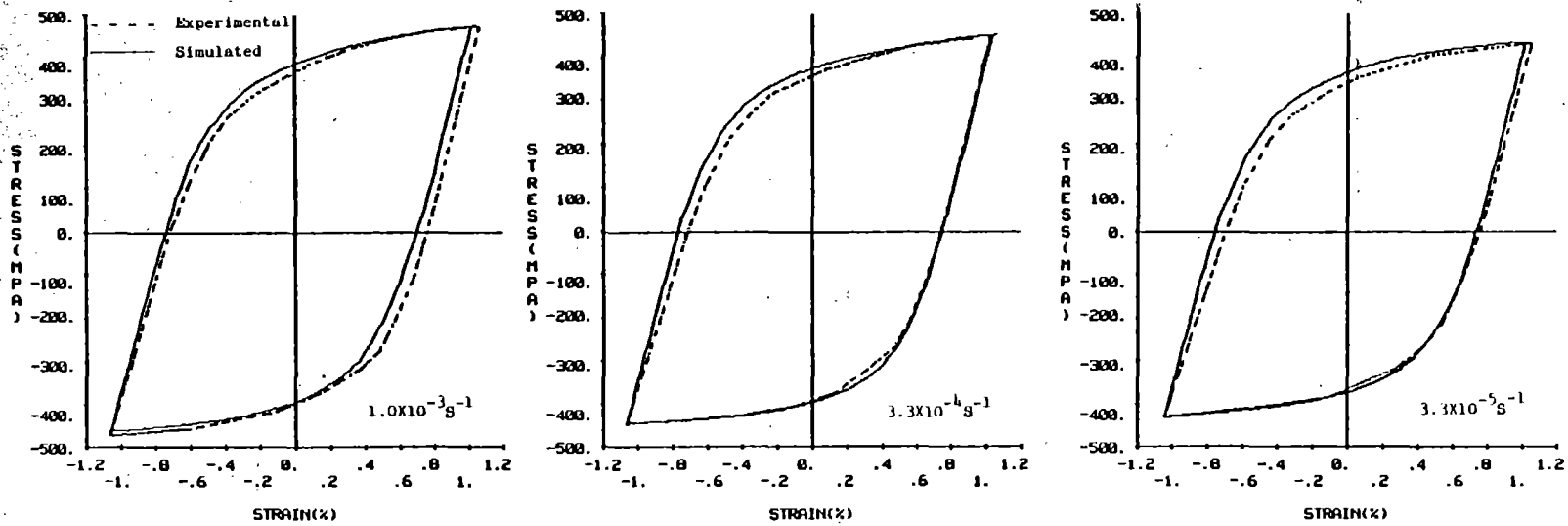


Fig. 40 Experimental and simulated hysteresis loops for Hastelloy-X at 866K

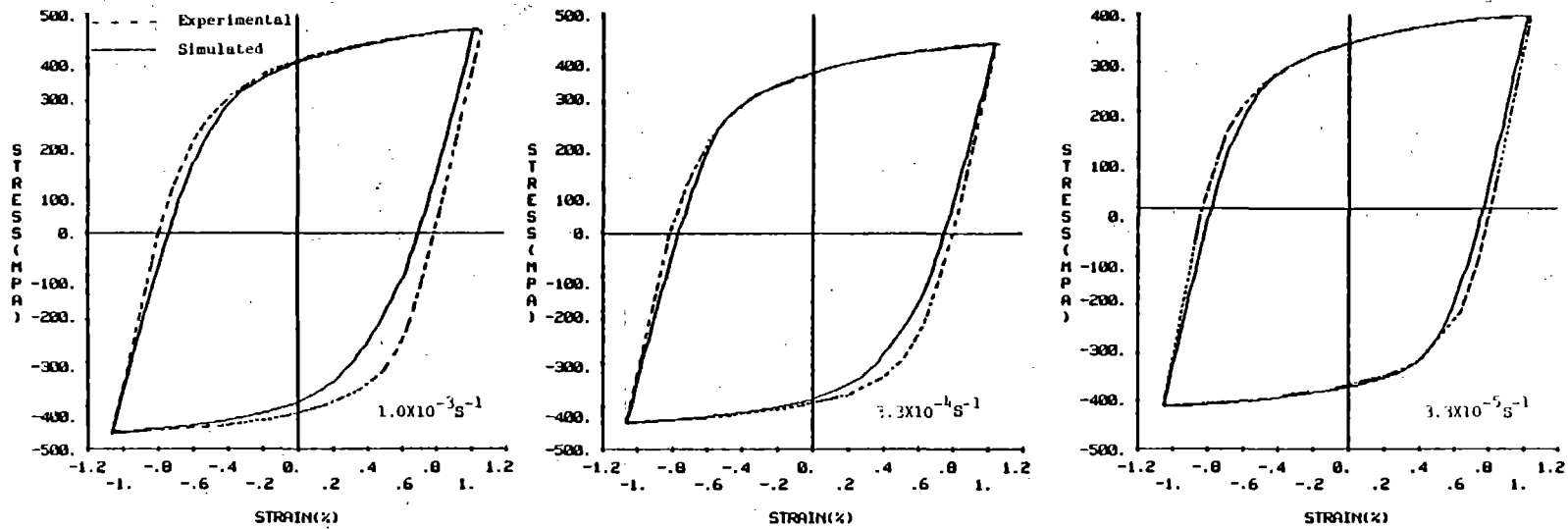


Fig. 41 Experimental and simulated hysteresis loops for Hastelloy-X at 922K

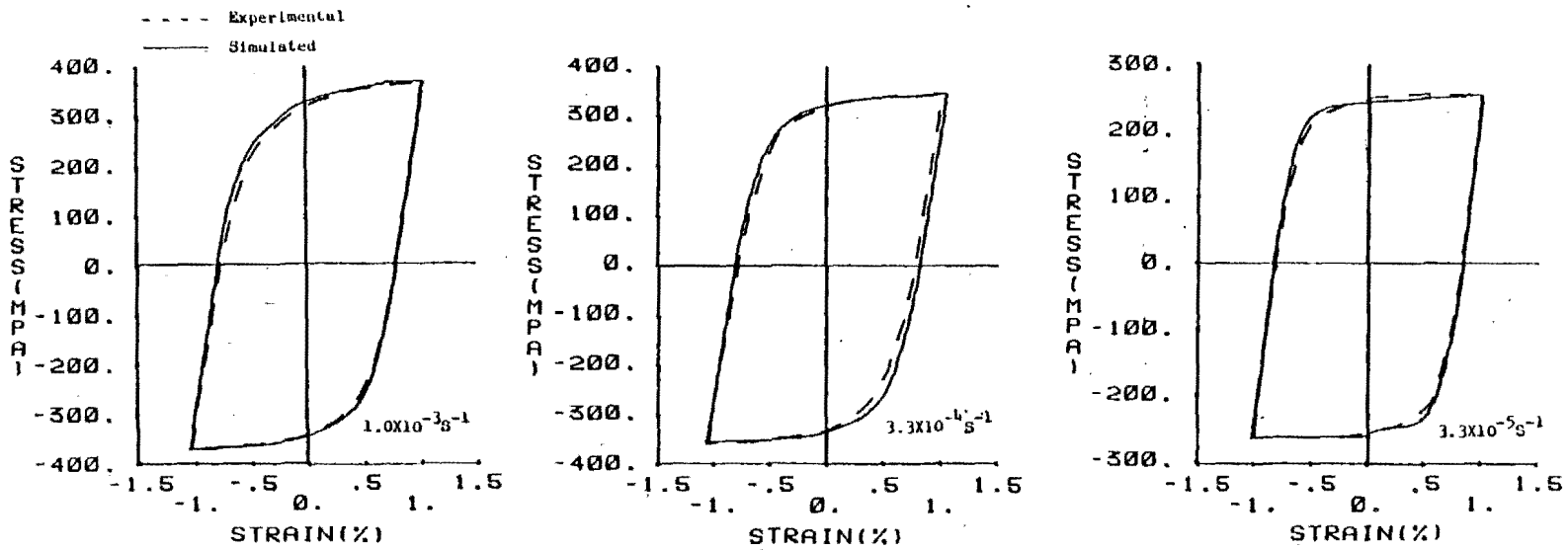


Fig. 42 Experimental and simulated hysteresis loops for Hastelloy-X at 978K

ORIGINAL PAGE IS
OF POOR QUALITY

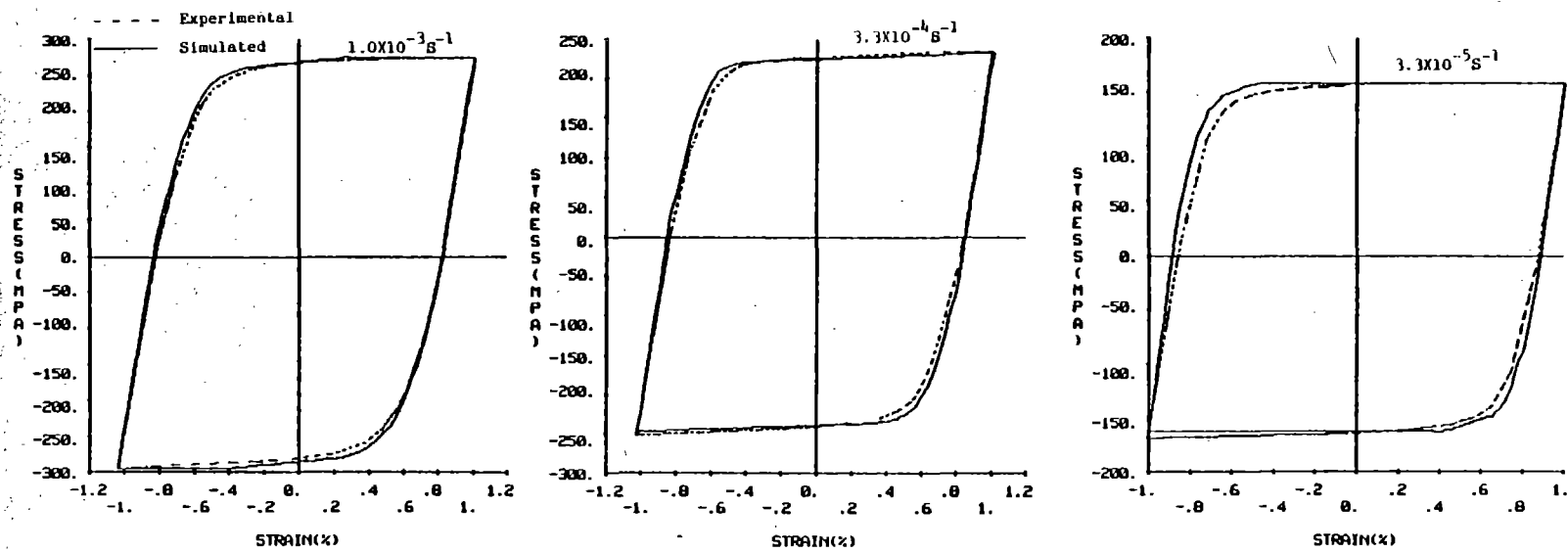


Fig. 43 Experimental and simulated hysteresis loops for Hastelloy-X at 1033K

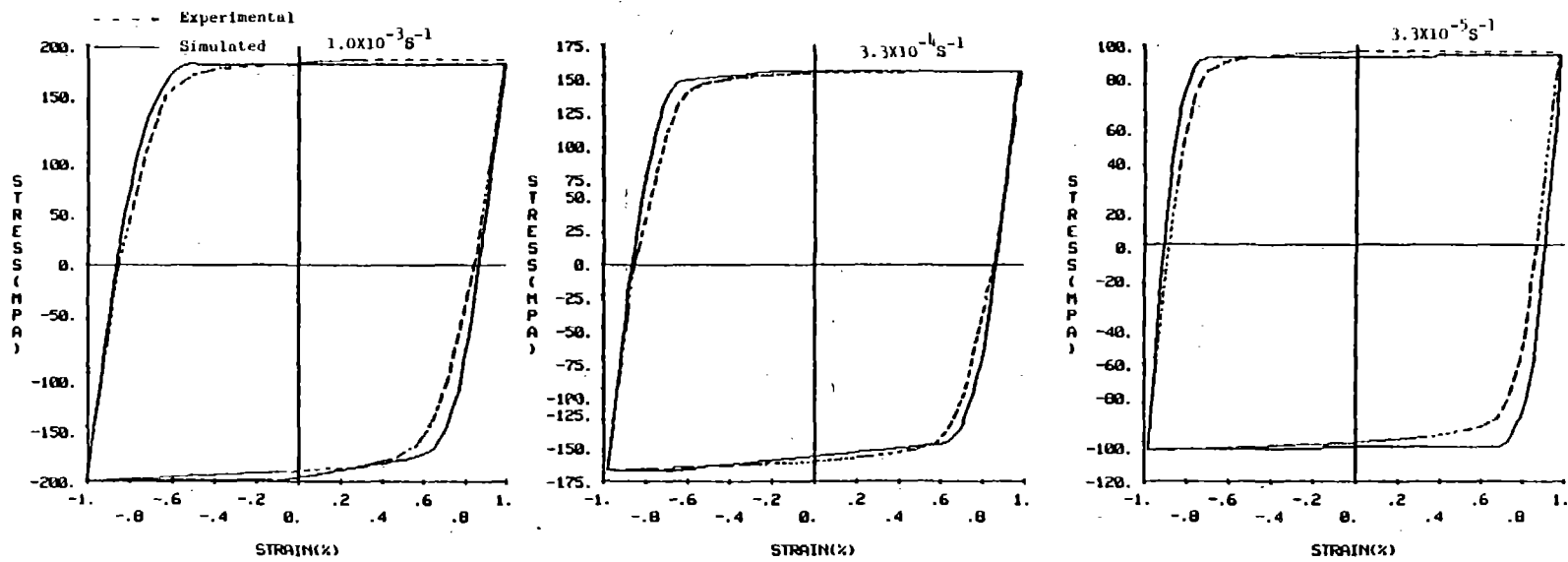


Fig. 44 Experimental and simulated hysteresis loops for Hastelloy-X at 1089K

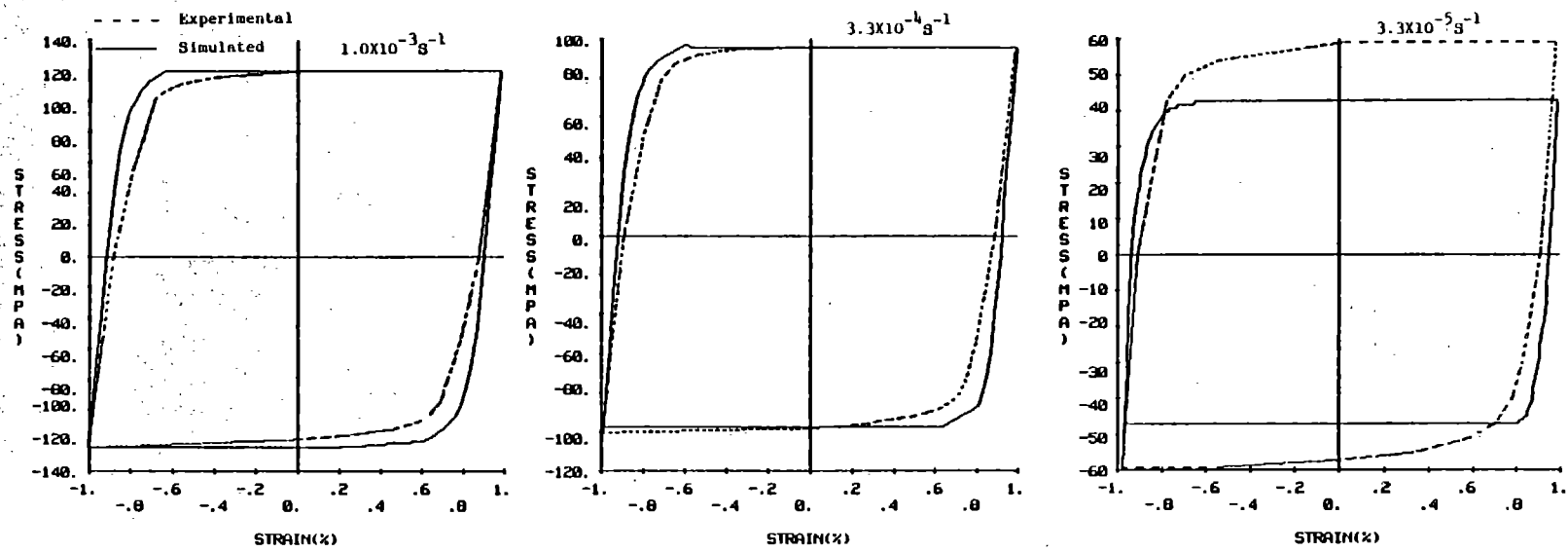


Fig. 45 Experimental and simulated hysteresis loops for Hastelloy-X at 1144K

strain is mostly rate sensitive and results obtained by the uncoupled model is the same as those obtained by the unified models. At high temperatures and low strain-rates, predicted hysteresis loops may appear to be too square compared to experimental results (Fig. 45) (p. 109). This "squareness" at low strain-rates is common among unified models. Walker [17] suggested that the "square" hysteresis loops are a result of the fact that the back stress reaches the saturated values more rapidly at low strain-rates.

Stress relaxation behavior. Theoretical stress relaxation behavior is simulated using equations (8) and (14) and the numerical scheme shown in Appendix B. Material constants utilized are tabulated in Tables II and III (p. 77 and 79). Values for the back stress " Ω " and the drag stress " K " are assumed to remain constant during the course of stress relaxation. Theoretical predictions as well as experimental results are shown in Figs. 46-53. At lower temperatures, thermal recovery is less significant and Ω and K are not expected to change appreciably during stress relaxation. Predicted relaxation behavior at the lower temperatures is reasonably close to experimental observation (Figs. 46-49) (p. 111 - 114), indicating the above assumptions are valid. At higher temperatures, however, actual asymptotic stress values are much lower than predicted values (Fig. 50 - 53) (p. 115 - 118). At these higher temperatures, recovery takes place during the course of stress relaxation which results in lower values for Ω and K . If the specimen is reloaded at the end of the relaxation test, a reduction in flow stress is generally observed. The raw data shown in Fig. 54 indicate the

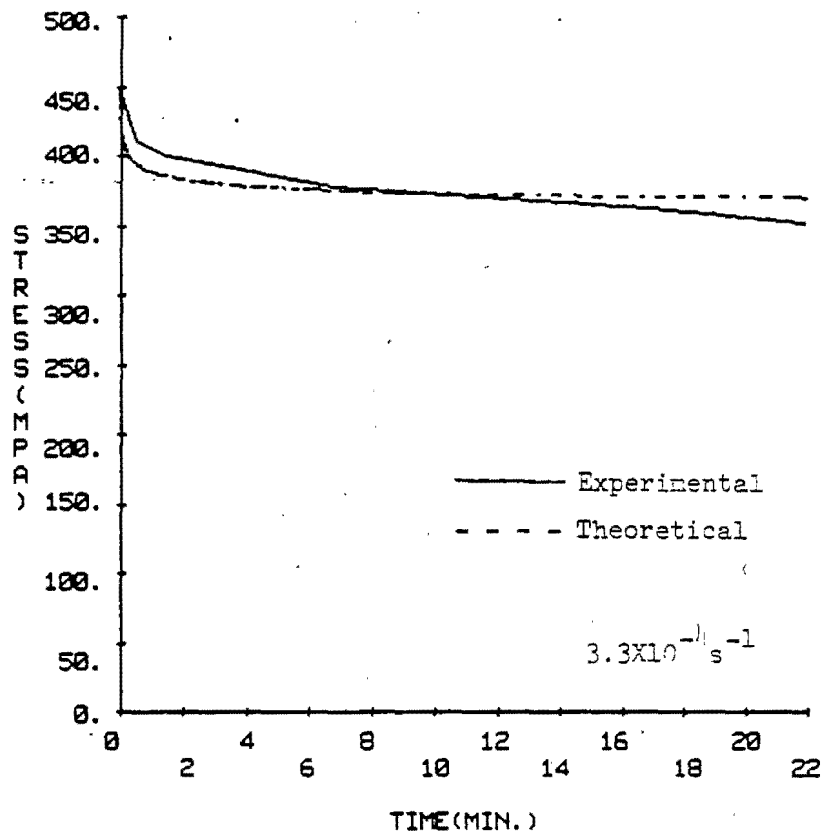


Fig. 46 Experimental and theoretical stress relaxation behavior for Hastelloy-X at 755K

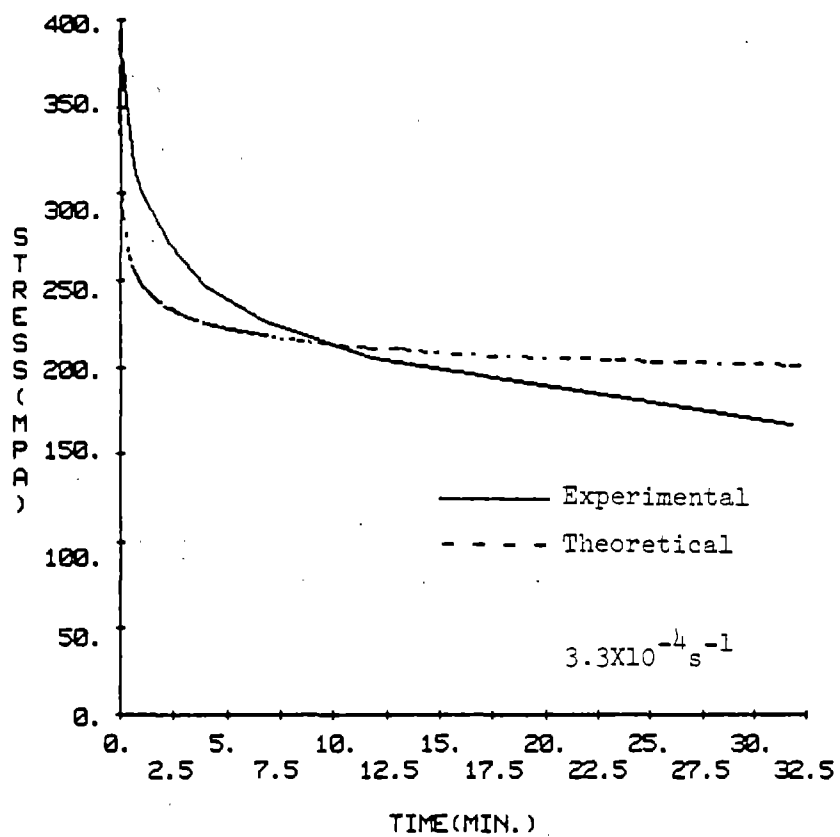


Fig. 47 Experimental and theoretical stress relaxation behavior for Hastelloy-X at 811K

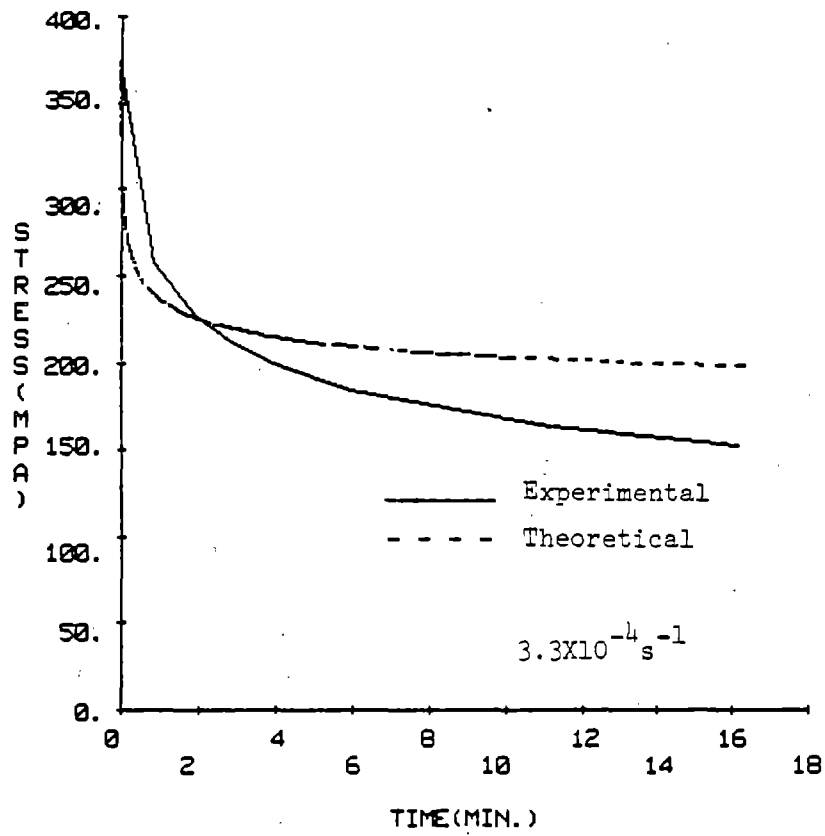


Fig. 48 Experimental and theoretical stress relaxation behavior for Hastelloy-X at 866K

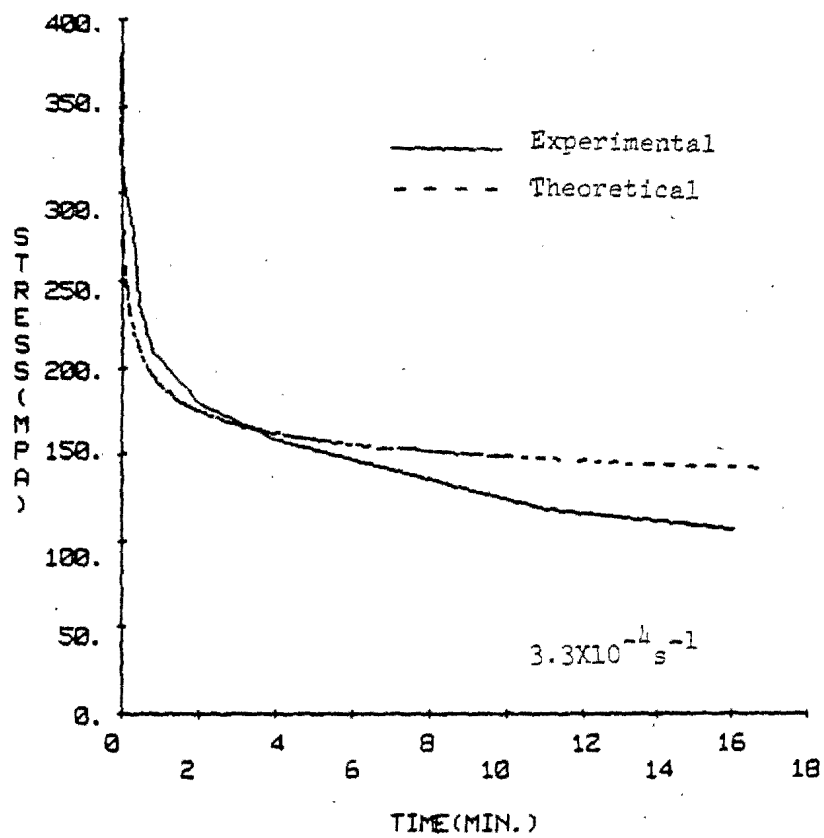


Fig. 49 Experimental and theoretical stress relaxation behavior for Hastelloy-X at 922K

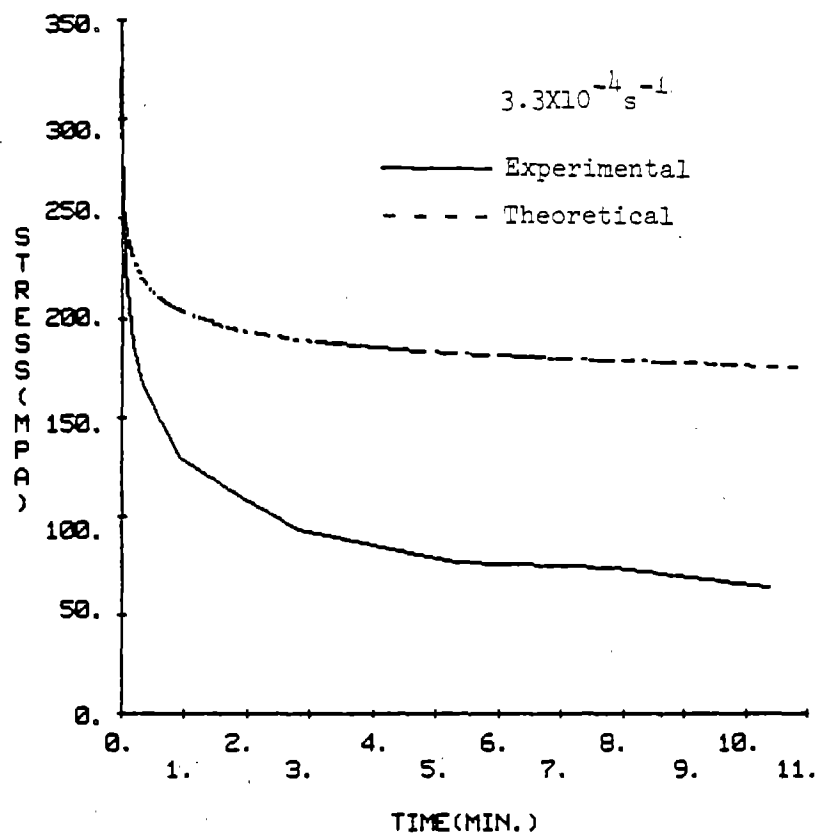


Fig. 50 Experimental and theoretical stress relaxation behavior for Hastelloy-X at 978K

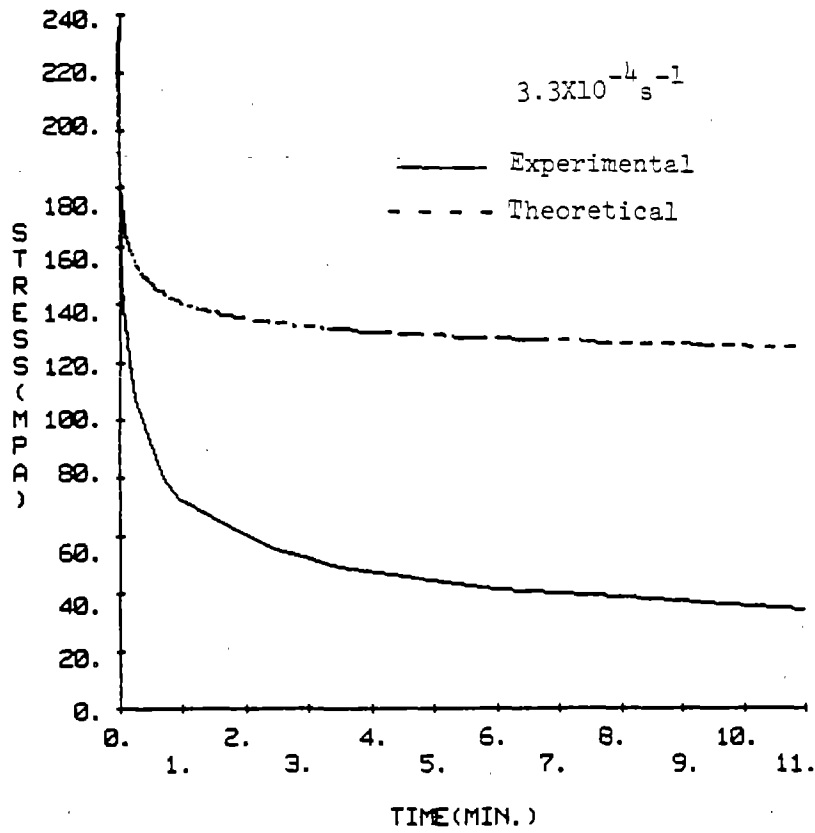


Fig. 51 Experimental and theoretical stress relaxation behavior for Hastelloy-X at 1033K

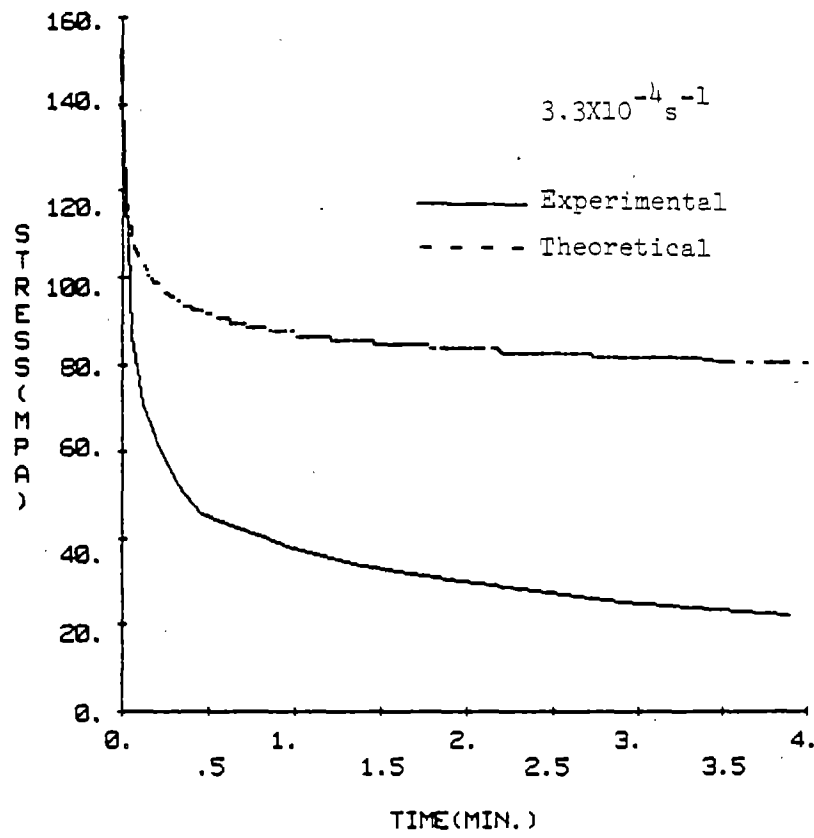


Fig. 52 Experimental and theoretical stress relaxation behavior for Hastelloy-X at 1089K

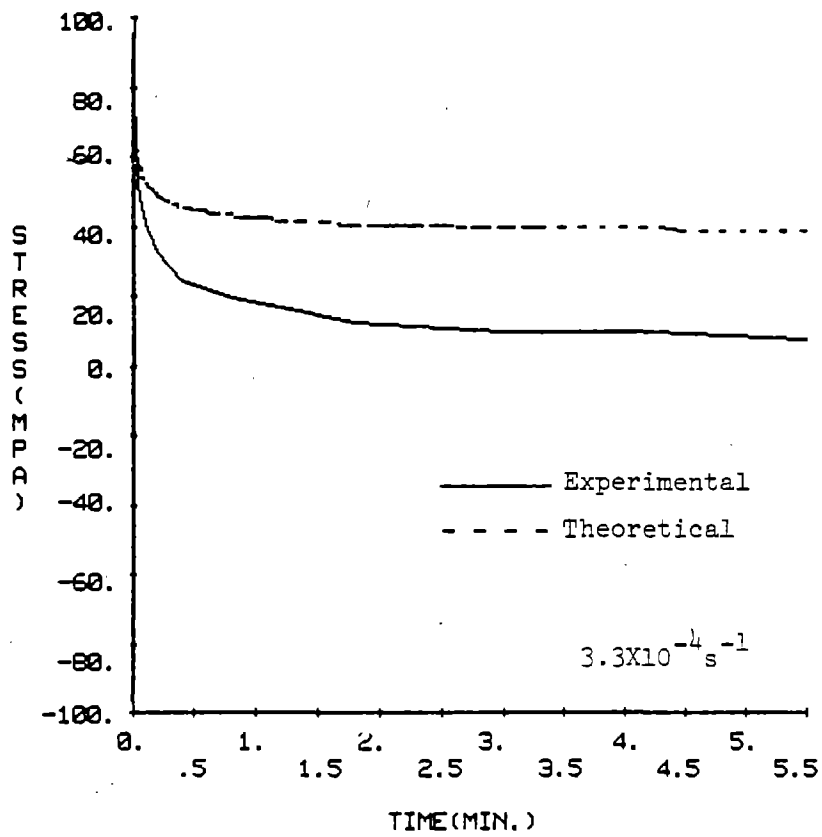


Fig. 53 Experimental and theoretical stress relaxation behavior for Hastelloy-X at 1144K

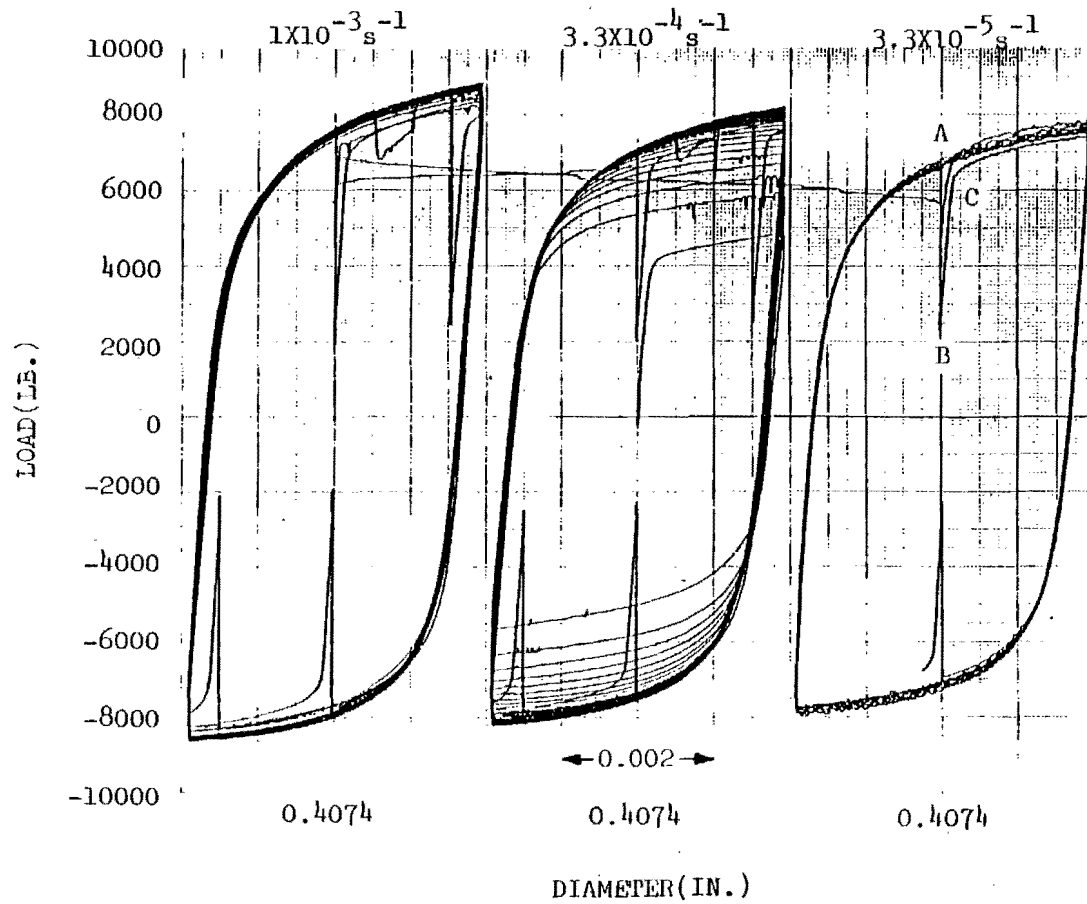


Fig. 5^h Experimental hysteresis loops for Hastelloy-X at 922K. Points A and B indicate where stress relaxation starts and ends. Point C indicates the flow stress upon reloading

ORIGINAL PAGE IS
OF POOR QUALITY

points along the saturated hysteresis loops where stress relaxation tests have been conducted. In each case, the reloading path after stress relaxation always stays below the original loading path. At point A, for example, the flow stress has a value of 349 MPa, which is reduced to 122 MPa (point B) after 16 minutes of stress relaxation. Upon reloading, the flow stress reaches a value of 328 MPa (Point C), a reduction of 21 MPa from the initial value of the flow stress. This provides direct experimental evidence that thermal recovery has taken place during stress relaxation. From a microstructural standpoint, the reduction in flow stress is mainly associated with the coarsening of the cell structure. The initial microstructural state prior to relaxation can usually be re-established after several cycles.

CHAPTER VII

CONCLUSIONS

An uncoupled viscoplastic constitutive model has been presented to describe elastic-plastic behavior of metals under a variety of temperature and strain-rate conditions. The uncoupling of the total inelastic strain into rate sensitive and rate insensitive components allows modelling of cyclic deformation behavior over a wide range of temperatures. The model is capable of describing strain cycling, stress relaxation and creep under isothermal conditions.

This model recognizes that the inelastic strain produced by a load change consists of both rate sensitive and rate insensitive components. In this regard, it is different from the models described in the preceding chapter which either assume inelastic strain is all rate independent as in the time-independent deformation theory or all rate dependent as in the thermally-activated deformation theory. Although the uncoupled approach may seem somewhat "artificial", some physical justifications are given in Chapter III. As discussed previously, the role of thermal activation at low temperatures is seen mainly in the overcoming of short range obstacles and therefore has no major effect on the overall deformation process. On the other hand, thermally activated processes such as dislocation cross-slip and dislocation climb dominate at high temperatures. A major difficulty encountered by the unified models is that at lower temperatures they often predict hysteresis loops which are too "square". The "squareness" is due to the assumption that all

inelastic strain is thermally activated. The rate sensitive inelastic strain component of the uncoupled model is described by a power law formulation which is standard to many unified models. Therefore, the two approaches are nearly the same at high temperatures where inelastic strain is essentially all rate sensitive while at lower temperatures, the uncoupled model provides more satisfactory predictions. At present, only saturated hysteresis loops have been considered. While saturated hysteresis loops may be useful for long term predictions, low cycle fatigue applications may require the modelling of cyclic response prior to saturation. Two internal variables - the back stress and the drag stress, are employed to describe the current microstructural state of the material. Growth laws have to be developed for the internal variables before cyclic hardening (or softening) can be modelled. Comparison between experimental and simulated hysteresis loops shows good agreement in general. More experiments are necessary, however, to verify the predictive capability of the model for a complex thermomechanical loading history. Stress relaxation predictions at lower temperatures are reasonable while high temperature predictions indicate significant thermal effects. Recovery terms have to be incorporated into the growth laws for the state variables if the model is to be useful for high temperature stress relaxation predictions.

CHAPTER VIII

RECOMMENDATION FOR FUTURE WORK

The uncoupled constitutive model described earlier has been shown to satisfactorily model saturated hysteresis loops under isothermal conditions over a wide range of temperatures. In this chapter, experiments necessary for further development of the model will be outlined.

As mentioned in the previous chapter, modelling of cyclic hardening prior to saturation is necessary to predict short term response such as low cycle fatigue. This will require the development of growth laws for the two internal state variables utilized in the model. Since cyclic saturation is basically associated with the formation of a stabilized cell structure, it will be reasonable to assume as a first approximation that the drag stress is mainly responsible for cyclic hardening while the back stress reaches a saturated value after the first cycle. To verify the above assumptions, tests should be conducted to measure the back stress at suitable intervals prior to saturation. It has been shown in the previous chapter that discrepancies exist between experimental and predicted stress relaxation behavior at high temperatures, indicating the need to incorporate thermal recovery into the growth laws for Ω and K . The contribution of grain boundary effects to the overall deformation process has not been considered due to insufficient information at this time. It will be interesting to consider the introduction of an additional state variable to model grain boundary sliding

as suggested by some investigators. Constant stress creep experiments should also be conducted at various points along the hysteresis loop and compared to predictions made by the model. Finally, tests have to be performed under nonisothermal loading conditions to study the capability of the model to predict more complex thermal-mechanical histories.

REFERENCES

1. Vicat, L.J., "Note Sur L'allongement Progressif Du Fil de Fer Soumis a Diverses Tensions," Annales des Ponts et Chaussees, 1^{er} semestre, 1834, pp. 40-44.
2. Hill, R.R., The Mathematical Theory of Plasticity, Oxford University Press, London, 1950.
3. Martin, J.B., Plasticity: Fundamentals and General Results, The MIT Press, Cambridge, Massachusetts, and London, England, 1975.
4. Pugh, C.E., Corum, J.M., Lin, K.C., and Greenstreet, W.L., "Currently Recommended Constitutive Equations for Inelastic Design Analysis of FFTF Components," ORNL TM-3602, Oak Ridge National Lab., Sept. 1972.
5. Snyder, M.D., and Bathe, K.J., "Formulation and Numerical Solution of Thermo-Elastic-Plastic and Creep Problems," National Technical Information Service, No. 82448-3, June 1977.
6. Allen, D.H., and Haisler, W.E., "A Theory for Analysis of Thermoplastic Materials," Computers and Structures, Vol. 13, 1981, pp. 124-135.
7. Sharifi, P., and Yates, D.N., "Nonlinear Thermal-Elastic-Plastic and Creep Analysis by the Finite Element Method," AIAA Journal, Vol. 12, 1974, pp. 1210-1215.
8. Zudans, Z., "Elastic-Plastic-Creep Response of Structures Under Composite Time History of Loadings," Third International Conference on Structural Mechanics in Reactor Technology, London, England, Sept. 1975.
9. Cailletaud, G., and Chaboche, J.L., "Macroscopic Description of the Microstructural Changes Induced by Varying Temperature: Example of IN100 cyclic Behavior," Third International Conference on Mechanical Behavior of Materials, Cambridge, Aug. 1979.
10. Lee, D. and Zaverl, F., Jr., "A Generalized Strain Rate Dependent Constitutive Equation for Anisotropic Metals," Acta Metallurgica, Vol. 26, No. 11, 1978, pp. 1771-1780.
11. Krieg, R.D., Swearingen, J.C., and Rhode, R.W., "A Physically-Based Internal Variable Model for Rate-Dependent Plasticity," Proceedings ASME/CSME PVP Conference, 1978, pp. 15-27.

12. Hart, E.W., "Constitutive Relations for the Nonelastic Deformation of Metals," Journal of Engineering Materials and Technology, Vol. 98, 1976, pp. 193-202.
13. Bodner, S.R., and Partom, Y., "Constitutive Equations for Elastic-Viscoplastic Strain-Hardening Materials," Journal of Applied Mechanics, Vol. 42, No. 2, June 1975, pp. 385-389.
14. Miller, A.K., "An Inelastic Constitutive Model for Monotonic, Cyclic, and Creep Deformation: Part I - Equations Development and Analytical Procedures and Part II - Application to type 304 Stainless Steel," ASME Journal of Engineering Materials and Technology, Vol. 98, 1976, p. 97-113.
15. Miller, A.K., "Modelling of Cyclic Plasticity with Unified Constitutive Equations: Improvements in Simulating Normal and Anomalous Bauschinger Effects," Journal of Engineering Materials and Technology, Vol. 102, April 1980, pp. 215-222.
16. Walker, K.P., "Representation of Hastelloy-X Behavior at Elevated Temperature with a Functional Theory of Viscoplasticity," presented at ASME Pressure Vessels Conference, San Francisco, Aug. 12, 1980.
17. Walker, K.P., "Research and Development Program for Non-Linear Structural Modelling with Advanced Time-Temperature Dependent Constitutive Relationships," Final Report, NASA Report NAS3-22055, Nov. 25, 1981.
18. Valanis, K.C., "A Theory of Viscoplasticity Without a Yield Surface, Part I, General Theory," Archives of Mechanics, Vol. 23, 1971, pp. 517-533.
19. Valanis, K.C., "A Theory of Viscoplasticity Without a Yield Surface, Part II, Application to Mechanical Behavior of Metals," Archives of Mechanics, Vol. 23, 1971, pp. 535-551.
20. Valanis, K.C., "Some Recent Developments in the Endochronic Theory of Plasticity-The Concept of Internal Barriers," Constitutive Equations in Viscoplasticity: Phenomenological and Physical Aspects, AMD Vol. 21, ASME, New York, 1976.
21. Cernocky, E.P., and Krempl, E., "A Nonlinear Uniaxial Integral Constitutive Equation Incorporating Rate Effects, Creep and Relaxation," International Journal of Nonlinear Mechanics, Vol. 14, 1979, pp. 183-203.
22. Delph, T.J., "A Comparative Study of Two State-Variable Constitutive Theories," ASME Journal of Engineering Materials and Technology, Vol. 102, 1980, pp. 327-336.

23. Reed-Hill, R.E., Physical Metallurgy Principles, D. Van Nostrand Company, New York, N.Y., 1973.
24. Sherby, O.D., and Burke, P.M., "Mechanical Behavior of Crystalline Solids at Elevated Temperatures," Progress in Materials Science, Vol. 13, 1968, pp. 325-390.
25. Schapery, R.A., "A Theory of Non-Linear Thermoviscoelasticity Based on Irreversible Thermodynamics," Proceedings, 5th U.S. National Congress of Applied Mechanics, ASME, 1966.
26. Biot, M.A., "Theory of Stress-Strain Relations in Anisotropic Viscoelasticity and Relaxation Phenomena," Journal of Applied Physics, Vol. 25, 1954, pp. 1385-1391.
27. Schapery, R.A., "On a Thermodynamic Constitutive Theory and Its Application to Various Nonlinear Materials," Proceedings, IUTAM Symposium, Springer-Verlag, Wien, New York, 1970.
28. Wu, H.C., and Chen, L., "Endochronic Theory of Transient Creep and Creep Recovery," Report NASA-CR-158487, NASA-Langley Research Center, 1979.
29. Lui, M.C.M., and Krempl, E., "Uniaxial Viscoplasticity Based on Total Strain and Overstress," Rensselaer Polytechnic Institute, No. RPI CS 78-4, July 1978.
30. Allen, D.H., "A Survey of Current Temperature Dependent Elastic-Plastic-Creep Constitutive Laws for Applicability to Finite Element Computer Codes," Presented at the 21st AIAA/ASCE/ASME/AHS Structural Dynamics and Materials Conference, Seattle, Washington, May, 1980.
31. Haisler, W.E., "Numerical and Experimental Comparison of Plastic Work Hardening Rules," Transactions of the 4th International Conference of Structural Mechanics in Reactor Technology, San Francisco, California, Aug. 1977.
32. Allen, D.H., "A Model for Predicting Response of Nonlinear Materials Subjected to Thermomechanical Loading," Dissertation, Texas A&M University, Aug. 1980.
33. Allen, D.H., "A Thermodynamic Framework for Comparison of Current Thermoviscoplastic Constitutive Models for Metals at Elevated Temperature," to be presented at the International Conference on Constitutive Laws for Engineering Materials: Theory and Application. University of Arizona, Tucson, Arizona, January 10-14, 1983.

34. Yamada, Y., and Sakurai, T., "Basic Formulation and a Computer Program for Large Deformation Analysis," Pressure Vessel Technology, Part I, ASME, 1977, pp. 344-352.
35. Yamada, Y., "Constitutive Modelling of Inelastic Behavior of Numerical Solution of Nonlinear Problems by the Finite Element Method," Computers and Structures, Vol. 8, 1978, pp. 533-543.
36. Cronenworth, J., "Development and Evaluation of An uncoupled, Incremental Constitutive Model for Elastic, Plastic Behavior at Elevated Temperatures," Thesis, Texas A&M University, May 1982.
37. Strauss, A.M., "A Bilinear Functional Theory of Viscoplasticity," Proc. West Virginia Acad. Sci., Vol. 44, No. 2, 1972, pp. 183-190.
38. Strauss, A.M., and Stouffer, D.C., "Sundry Aspects of Viscoplasticity," Presented at the Winter Annual Meeting of ASME, New York, Dec. 5-10, 1976.
39. Krempl, E., "Cyclic Creep - An interpretive Literature Survey," Welding Research Council Bulletin No. 195, 1974.
40. Krempl, E., "Viscoplasticity Based on Total Strain. The Modeling of Creep With Special Considerations of Initial Strain and Aging," Transactions of the ASME, Vol. 101, Oct. 1979, pp. 380-386.
41. Michalak, J.T., "The Influence of Temperature on the Development of Long-Range Internal Stress During the Plastic Deformation of High-Purity Iron," Acta Metallurgica, Vol. 13, March 1965, pp. 213-222.
42. Barret, C.R., and Nix, W.D., "A Model for Steady State Creep Based on the Motion of Jogged Screw Dislocations," Acta Metallurgica, Vol. 13, Dec. 1965, pp. 1247-1258.
43. Weertman, J., "Dislocation Climb Theory of Steady-State Creep," Transactions of the ASM, Vol. 61, 1968, pp. 681-694.
44. Nabarro, F.R.N., "Deformation of Crystals by the Motion of Single Ions," Report of a Conference on the Strength of Solids, The Physical Society, London, 1948, pp. 75.
45. Herring, C., "Diffusional Viscosity of a Polycrystalline Solid," Journal of Applied Physics, Vol. 21, 1950, pp. 437.
46. Coble, R.L., "A Model for Boundary Diffusion Controlled Creep in Polycrystalline Materials," Journal of Applied Physics, Vol. 34, 1963, pp. 1679-1682.

47. MacEwen, S.R., Kupcis, O.A., and Ramaswami, B., "An Investigation of an Incremental Unloading Technique for Estimating Internal Stresses," Scripta Metallurgica, Vol. 3, 1969, pp. 441-448.
48. Ahlquist, C.N., and Nix, W.D., "The Measurement of Internal Stresses During Creep of Al and Al-Mg Alloy," Acta Metallurgica, Vol. 19, April 1971, pp. 373-385.
49. Booker, M.K., "Evaluation of Creep and Relaxation Data for Hastelloy Alloy X Sheet," Oak Ridge National Laboratory, Report ORNL-5479, February 1979.
50. Jaske, C.E., Rice, R.C., Buchheit, R.D., Roach, D.B., and Porfilio, T.L., "Low Cycle Fatigue of Type 347 Stainless Steel and Hastelloy Alloy X in Hydrogen Gas and in Air at Elevated Temperatures," Final Report, NASA Report NAS3-20078, May 1976.
51. Gupta, I., and Li, J.C.M., "Stress Relaxation, Internal Stress, and Work Hardening in some BCC Metals and Alloys," Metallurgical Transactions, Vol. 1, August 1970, pp. 2323-2330.
52. High temperature, High Strength, Nickel Base Alloys, The International Nickel Company, Inc., New York, July, 1977.
53. Walker, K.P., "Research and Development Program for Nonlinear Structural Modelling with Advanced Time-Temperature Dependent Constitutive Relationships," Third Quarterly Technical Narrative, NASA Report NAS3-22055, Aug. 1980.
54. Jensen, R.R., Howson, T.E., and Tien, J.K., "Very Slow Strain Rate Stress-Strain Behavior and Resisting Stress for Creep in a Nickel-Base Superalloy," Superalloys 1980, Proceedings of the Fourth International Symposium on Superalloys, AMS, 1980.
55. Alden, T.H., "Load Relaxation in Aluminum: I. Theory of Plastic Deformation. II. Plastic Equation of State," Metallurgical Transactions A, Vol. 8A, Nov. 1977, pp. 1675-1679.
56. Alden, T.H., "Theory of Plastic Flow in Strain-Hardened Metals," Philosophical Magazine, Vol. 25, 1972, pp. 785-811.
57. Holbrook, J.H., Rohde, R.W., and Swearingen, J.C., "The Continuity of Plastic Strain Rate," Acta Metallurgica, Vol. 29, 1981, pp. 1099-1106.

APPENDIX A

COMPUTER PROGRAM OUTLINE FOR HYSTERESIS LOOP SIMULATION

The following outline describes the numerical scheme used to simulate saturated hysteresis loops. Simulation always starts at the point where loading begins (i.e., the point corresponding to maximum compressive stress).

- A. Enter required material constants. These include Young's Modulus, Poisson's ratio, initial diameter, programmed diametral strain-rate (dD/dt), stress exponent and drag stress.
- B. Enter initial conditons. These include initial values for dD/dP , strain hardening function, stress, total strain and back stress.
- C. Enter required time step.
- D. Calculate strain hardening rate [equation (20)].
- E. Calculate total strain-rate corresponding to strain hardening rate in step D. [equation (13)].
- F. Calculate strain increment based on strain-rate in step E and time step in step C.
- G. Calculate corresponding stress increment [equation (12)].
- H. Update stress and strain values.
 1. Add stress increment to stress.
 2. Add strain increment to strain.
- I. Check to see if total strain range is exceeded. If exceeded go to step M to start unloading.

- J. Update values for back stress and strain hardening function.
Linearly interpolate between input values if necessary.
- K. Calculate new value for dD/dP .
- L. Repeat steps D through K.
- M. Modify initial conditions corresponding to the point where unloading starts.
- N. Repeat step L. If total strain range is exceeded in step I, stop.

APPENDIX B

COMPUTER PROGRAM OUTLINE FOR STRESS RELAXATION PREDICTION

The following outline describes the numerical scheme used to predict stress relaxation behavior. Small time step is used initially to better simulate the initial portion of the stress relaxation curve. For computational efficiency, the time step is increased progressively as the stress approaches the asymptotic value.

- A. Enter material constants. These include Young's Modulus, back stress, drag stress and stress exponent.
- B. Enter initial values for stress and time limit.
- C. Calculate inelastic strain-rate [equation (8)].
- D. Calculate stress-rate corresponding to inelastic strain-rate given in step C. [equation (14)].
- E. Calculate new stress value by subtracting stress decrement (or increment) from previous stress.
- G. Check to see if increase in time step is necessary.
- H. Check to see if time limit has been exceeded. If time limit exceeded, stop.
- I. Repeat steps C through H.

APPENDIX C

DERIVATION OF EQUATIONS USED FOR DATA REDUCTION

In this appendix the equations used for data reduction will be derived. Since diametral extensometer is employed in our testing, diametral strain is measured and converted into axial strain. The equations are summarized in Chapter V.

Total diametral strain can be separated into elastic and inelastic components as follows:

$$(\epsilon_t)_D = (\epsilon_e)_D + (\epsilon_i)_D \quad (C1)$$

The diametral elastic strain can be converted into axial strain as shown below:

$$(\epsilon_e)_D = -\nu \epsilon_e = -\nu \frac{\sigma}{E} \quad (C2)$$

where ν is the elastic Poisson's ratio. Similarly, the diametral inelastic strain can be expressed in terms of the axial strain as

$$(\epsilon_i)_D = -\nu_i \epsilon_i \approx -\frac{1}{2} \epsilon_i \quad (C3)$$

where ν_i is the inelastic Poisson's ratio. Equation (C3) can be rearranged as follows:

$$\epsilon_i = -2 \left[(\epsilon_t)_D - (\epsilon_e)_D \right] = -2 \left[\frac{dD}{D_0} + \nu \frac{\sigma}{E} \right] \quad (C4)$$

The total axial strain can be given in terms of its components as

$$\epsilon_t = \epsilon_e + \epsilon_i \quad (C5)$$

Substituting equation (C4) into equation (C5) and rearranging yields

$$\epsilon_t = \frac{\sigma}{E} (1 - 2\nu) - 2 \frac{dD}{D_o} \quad (C6)$$

which is the same as equation (17). The inelastic strain can be obtained by subtracting the elastic strain from the total strain, i.e.

$$\epsilon_i = -2 \left(\frac{\nu\sigma}{E} + \frac{dD}{D_o} \right) \quad (C7)$$

which is also given by equation (18). The strain hardening rate can be expressed as follows:

$$\frac{d\sigma}{d\epsilon_t} = \frac{d\sigma}{\frac{d\sigma}{E}(1-2\nu) - 2\frac{dD}{D_o}} = \frac{1}{\frac{(1-2\nu)}{E} - \frac{2}{D_o} \frac{dD}{d\sigma}} \quad (C8)$$

Equation (C8) is identical with equation (20). Differentiation of equation (C6) gives

$$\dot{\epsilon}_t = \frac{1}{E} \frac{d\sigma}{dt} (1-2\nu) - \frac{2}{D_o} \frac{dD}{dt} = \frac{1}{E} \frac{d\sigma}{d\epsilon_t} \frac{d\epsilon_t}{dt} - \frac{2}{D_o} \frac{dD}{dt} \quad (C9)$$

Substituting equation (C8) into equation (C9) results in

$$\dot{\epsilon}_t = \frac{-\frac{2}{D_o} \frac{dD}{dt}}{1 - \frac{1}{E} \frac{d\sigma}{d\epsilon_t} (1-2\nu)} \quad (C10)$$

which is the same as equation (13). The inelastic strain-rate can be obtained from equation (C7) as

$$\dot{\epsilon}_i = -2 \left(\frac{\nu}{E} \frac{d\sigma}{dt} + \frac{1}{D_o} \frac{dD}{dt} \right) = -2 \left(\frac{\nu}{E} \frac{d\sigma}{d\epsilon_t} \frac{d\epsilon_t}{dt} + \frac{1}{D_o} \frac{dD}{dt} \right) \quad (C11)$$

Substituting equations (C8) and (C10) into equation (C11) yields

$$\dot{\epsilon}_i = \frac{-2}{D_0} \frac{dD}{dt} \left[\frac{1 - \frac{1}{E} \frac{d\sigma}{d\epsilon_t}}{1 - \frac{(1-2\nu)}{E} \frac{d\sigma}{d\epsilon_t}} \right] \quad (C12)$$

which is given by equation (19).

APPENDIX D

VALUES FOR RATE INSENSITIVE, INELASTIC STRAIN FUNCTION

$$\sigma_{\max} = 149 \text{ MPa}$$

Stress (MPa)	$f(\sigma, \sigma_{\max})$ (MPa ⁻¹)
Loading	
-149	0
-106	0
106	0
149	0
Unloading	
149	0
106	0
-106	0
-149	0

$$\sigma_{\max} = 286 \text{ MPa}$$

Stress (MPa)	$f(\sigma, \sigma_{\max})$ (MPa ⁻¹)
Loading	
-286	0
0	0
106	0.187E-6
212	0.406E-6
286	0.161E-5
Unloading	
286	0
0	0
-106	0.275E-6
-212	0.580E-6
-286	0.148E-5

$$\sigma_{\max} = 392 \text{ MPa}$$

Stress (MPa)	$f(\sigma, \sigma_{\max})$ (MPa ⁻¹)
Loading	
-403	0
0	0.319E-6
106	0.165E-5
212	0.259E-5
318	0.435E-5
392	0.124E-4
Unloading	
392	0
0	0.232E-6
-106	0.186E-5
-212	0.270E-5
-318	0.417E-5
-403	0.107E-4

$$\sigma_{\max} = 435 \text{ MPa}$$

Stress (MPa)	$f(\sigma, \sigma_{\max})$ (MPa ⁻¹)
Loading	
-446	0
0	0.652E-6
106	0.258E-5
212	0.432E-5
318	0.620E-5
392	0.126E-4
424	0.246E-4
435	0.680E-4
Unloading	
435	0
0	0.551E-6
-106	0.214E-5
-212	0.441E-5
-318	0.694E-5
-392	0.108E-4
-424	0.184E-4
-446	0.522E-4

$$\sigma_{\max} = 467 \text{ MPa}$$

Stress (MPa)	$f(\sigma, \sigma_{\max})$ (MPa ⁻¹)
Loading	
-477	0
-106	0.145E-6
0	0.113E-5
106	0.255E-5
212	0.559E-5
318	0.880E-5
424	0.187E-4
461	0.455E-4
467	0.134E-3
Unloading	
467	0
106	0.145E-7
0	0.104E-5
-106	0.294E-5
-212	0.546E-5
-318	0.890E-5
-424	0.165E-4
-459	0.329E-4
-477	0.913E-4

$$\sigma_{\max} = 520 \text{ MPa}$$

Stress (MPa)	$f(\sigma, \sigma_{\max})$ (MPa ⁻¹)
Loading	
-530	0
-106	0.681E-6
0	0.164E-5
106	0.330E-5
212	0.732E-5
318	0.114E-4
424	0.197E-4
477	0.333E-4
509	0.754E-4
520	0.196E-3
Unloading	
520	0
106	0.127E-6
0	0.135E-5
-106	0.383E-5
-212	0.723E-5
-318	0.110E-4
-424	0.177E-4
-477	0.310E-4
-509	0.541E-4
-530	0.157E-3

$$\sigma_{\max} = 562 \text{ MPa}$$

Stress (MPa)	$f(\sigma, \sigma_{\max})$ (MPa ⁻¹)
Loading	
-567	0
-106	0.986E-6
0	0.225E-5
106	0.394E-5
212	0.658E-5
265	0.862E-5
318	0.126E-4
371	0.164E-4
424	0.220E-4
477	0.328E-4
509	0.461E-4
530	0.600E-4
552	0.111E-3
562	0.291E-3
Unloading	
562	0
106	0.783E-6
0	0.174E-5
-106	0.388E-5
-212	0.677E-5
-318	0.120E-4
-371	0.164E-4
-424	0.217E-4
-477	0.314E-4
-509	0.403E-4
-530	0.565E-4
-546	0.796E-4
-557	0.132E-3
-567	0.388E-3

$$\sigma_{\max} = 610 \text{ MPa}$$

Stress (MPa)	$f(\sigma, \sigma_{\max})$ (MPa ⁻¹)
Loading	
-615	0
-106	0.141E-5
0	0.288E-5
106	0.429E-5
212	0.723E-5
318	0.126E-4
371	0.175E-4
424	0.232E-4
477	0.307E-4
530	0.448E-4
562	0.629E-4
583	0.868E-4
605	0.162E-3
610	0.229E-3
Unloading	
610	0
106	0.681E-6
0	0.188E-5
-106	0.367E-5
-212	0.630E-5
-318	0.103E-4
-371	0.159E-4
-424	0.194E-4
-477	0.274E-4
-530	0.416E-4
-562	0.572E-4
-583	0.894E-4
-605	0.186E-3
-615	0.372E-3

VITA

Shik Hung Yuen was born [REDACTED], in [REDACTED], the son of Yin W. Yuen and Lau W. Yuen. He attended elementary and high school in Kowloon. His high school diploma was obtained from the Maryknoll Fathers' School in May 1976. He was enrolled in the Southeastern Oklahoma State University in the fall of 1976.

Shik entered Texas A&M University in September 1977 and majored in Mechanical Engineering. His B.S. degree was awarded in May of 1980. He began graduate study in July 1980 and will receive his M.S. degree in May 1983.

Shik's permanent address is 1317 Ching Yung House, Cheung Ching Estate, Tsing Yi Is., N.T., Hong Kong.